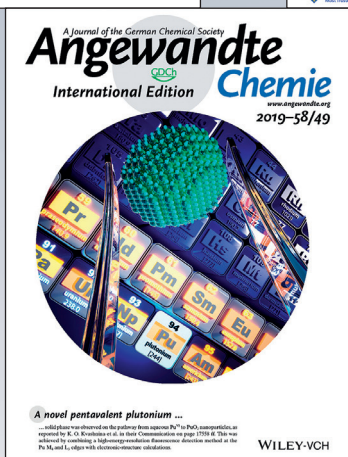
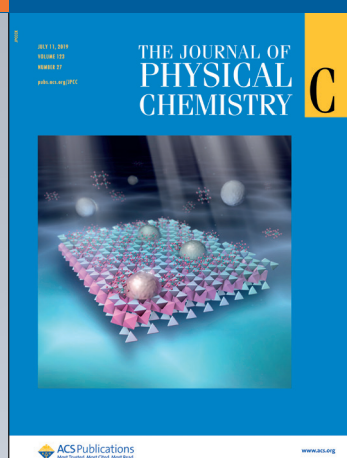
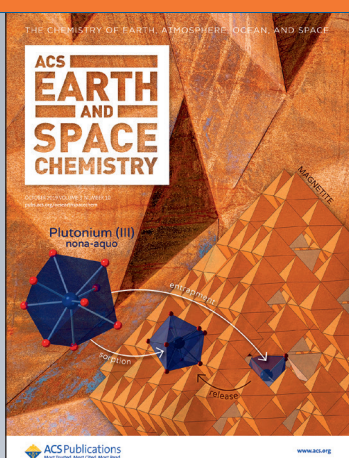


ANNUAL REPORT 2019

Institute of Resource Ecology



Wissenschaftlich-Technische Berichte
HZDR-110

Annual Report 2019

Institute of Resource Ecology

Editorial board:

Prof. Dr. Thorsten Stumpf
Dr. Harald Foerstendorf
Dr. Frank Bok
Dr. Anke Richter

HZDR

 **HELMHOLTZ**
ZENTRUM DRESDEN
ROSSENDORF

Impressum

Print edition: ISSN 2191-8708

Electronic edition: ISSN 2191-8716

The electronic edition is published under Creative Commons License (CC BY-NC-ND):

<https://www.hzdr.de/publications/Publ-30774>

<urn:nbn:de:bsz:d120-qucosa2-386344>

Published by Helmholtz-Zentrum Dresden–Rossendorf e.V.

Contact

Helmholtz-Zentrum Dresden–Rossendorf e.V.

Institute of Resource Ecology

Bautzner Landstraße 400

D-01328 Dresden

Germany

Phone: +49 (0) 351 260 3210

Fax: +49 (0) 351 260 3553

e-mail: contact.resourceecology@hzdr.de

<https://www.hzdr.de/fwo>

This report is also available at <https://www.hzdr.de/fwo>

Cover picture

In 2019, for the first time members of the Institute of Resource Ecology were holding responsible authorships of more than 100 articles in peer-reviewed journals within one year. The cover picture displays cover arts of six articles published in high-ranked journals.

Drobot, B.; Schmidt, M.; Mochizuki, Y.; Abe, T.; Okuwaki, K.; Brulfert, F.; Falke, S.; Samsonov, S.; Komeiji, Y.; Betzel, C.; Stumpf, T.; Raff, J.; Tsushima, S.: *Cm³⁺/Eu³⁺ Induced Structural, Mechanistic and Functional Implications for Calmodulin*. *Physical Chemistry Chemical Physics* (2019) 21, 21213-21222. Reproduced with permission.

Dumas, T.; Fellhauer, D.; Schild, D.; Gaona, X.; Altmaier, M.; Scheinost, A.: *Plutonium retention mechanisms by magnetite under anoxic conditions: Entrapment versus sorption*. *ACS Earth and Space Chemistry* (2019) 3, 2197-2206.

Kumar, S.; Creff, G.; Hennig, C.; Rossberg, A.; Steudtner, R.; Raff, J.; Vidaud, C.; Oberhaensli, F. R.; Bottein, Y.; Den Auwer, C.: *How do actinyls interact with hyperphosphorylated yolk protein Phosvitin?* *Chemistry - A European Journal* (2019) 25, 12332-12341 (2019). Copyright Wiley-VCH Verlag GmbH & Co. KGaA. Reproduced with permission.

Kvashnina, K.; Romanchuk, A.; Pidchenko, I.; Amidani, L.; Gerber, E.; Trigub, A.; Roßberg, A.; Weiß, S.; Popa, K.; Walter, O.; Caciuffo, R.; Scheinost, A.; Butorin, S.; Kalmykov, S.: *A novel metastable pentavalent plutonium solid phase on the pathway from aqueous Pu(VI) to PuO₂ nanoparticles*. *Angewandte Chemie - International Edition* (2019) 58, 17558-17562. (2019). © 2019 The Authors. Published by Wiley-VCH Verlag GmbH & Co. KGaA

Rossberg, A.; Abe, T.; Okuwaki, K.; Barkleit, A.; Fukuzawa, K.; Nakano, T.; Mochizuki, Y.; Tsushima, S.: *Destabilization of DNA through interstrand crosslinking by UO₂²⁺*. *Chemical Communications* (2019) 55, 2015-2018. Reproduced with permission.

Yuan, K.; Bracco, J. N.; Schmidt, M.; Soderholm, L.; Fenter, P.; Lee, S. S.: *Effect of Anions on the Changes in the Structure and Adsorption Mechanism of Zirconium Species at the Muscovite (001) – Water Interface*. *Journal of Physical Chemistry C* (2019) 123, 16699-16710.

Cover created by WERKSTATT X. Michael Voigt (www.werkstatt-x.de)

Preface

THE INSTITUTE OF RESOURCE ECOLOGY (IRE) IS ONE OF the eight institutes of the Helmholtz-Zentrum Dresden-Rossendorf (HZDR). Our research activities are mainly integrated into the program “Nuclear Waste Management, Safety and Radiation Research (NUSAFE)” of the Helmholtz Association (HGF) and focused on the topics “Safety of Nuclear Waste Disposal” and “Safety Research for Nuclear Reactors”. The program NUSAFE, and therefore all work which is done at IRE, belong to the research field “Energy” of the HGF.

Our research objective is the protection of humans and the environment from hazards caused by pollutants resulting from technical processes that produce energy and raw materials. Treating technology and ecology as a unit is the major scientific challenge in assuring the safety of technical processes and gaining their public acceptance. We investigate the ecological risks exerted by radioactive and non-radioactive metals in the context of nuclear waste disposal, the production of energy in nuclear power plants and in processes along the value chain of metalliferous raw materials. A common goal is to generate better understanding of the dominating processes essential for metal mobilization and immobilization on the molecular level by using advanced spectroscopic methods. This in turn enables us to assess the macroscopic phenomena, which determine the transport and distribution of contaminants in the environment, including their implementation into models, codes, and data for predictive calculations.

The extraordinary broadness of research topics and activities is illustrated below by some selected highlights:

For several years, the HZDR reactor dynamics program is being extended to liquid metal cooled reactors. As part of this qualification program, HZDR participates in a coordinated research project of the IAEA on the post-test calculation of reactivity measurements at the Fast Flux Test Facility representing a 400 MW reactor core of a Sodium cooled fast reactor. The obtained results with the updated DYN3D code are in very good agreement with the experimental data (→ p. 69). This validation activity is an important step towards the use of DYN3D for safety analyses of liquid metal cooled reactors.

The method of small angle neutron scattering (SANS) contributed significantly to the understanding of solute atom clustering and nm-scale precipitation in three classes of ferromagnetic Fe-based nuclear materials: (i) Reactor pressure vessel steels (effect of neutron irradiation); (ii) Ferritic/martensitic chromium steels (effect of neutron irradiation, Fe-Cr phase diagram); (iii) Nanostructured ferritic alloys (effect of mechanical alloying). The publication record over a decade resulted in an invitation to contribute to a top-ranking review article on magnetic SANS by covering the applications on steels (→ p. 64).

Irrespective of the site selection for the final disposal of nuclear waste in Germany, fission products (amongst them ⁹⁹Tc) will play an essential role in the safety assessment. Here, new findings were published in high-ranked journals that pointed out how efficient solids with Fe(II) moieties are in Tc retardation. Pyrite (→ p. 34) and Layered Double Hydroxides (→ p. 35) showed excellent Tc removal and low Tc re-mobilization into the aqueous phase. The work also revealed the basic processes behind these retardation phenom-

ena by coupling various spectroscopies with microscopy and batch experiments.

Current results are highlighting the need for new approaches to reactive transport modeling in terms of both reactivity and transport. Usually, transport control is employed solely to explain differences in reactivity. In a combined approach using a Vertical Scanning Interferometer (VSI) and X-ray microcomputed tomography, it has been confirmed that VSI dissolution rate heterogeneity resolved in 2D is also characteristic of distributions in 3D, persisting over considerably longer reaction periods. The results underscore the competition between surface- and transport-controlled mechanisms as a function of disequilibrium. (→ p. 40).

Research aiming at an improved understanding of actinide properties in metal-organic compounds found interesting effects of halide exchanges on the electronic and magnetic properties of actinides in amidinate complexes. A charge compensating chloride ligand is accessible for exchange by (pseudo)halogenides, which can lead to a complete inversion of the magnetic tensors of the molecule. (→ p. 19)

In 2019, the biochemistry of the trivalent *f*-elements also moved into the focus of the institute’s research. Using the model protein calmodulin, we investigated the Ca(II) exchange by Eu(III) and Cm(III) with a combination of spectroscopy, calorimetry, enzymology and computational chemistry. We could show that this effective substitution affects the protein structure and thus the enzymatic activity. This is an important step towards understanding the chemotoxicity of *f*-elements at the molecular level. (→ p. 48).

The extensive upgrade of The Rossendorf Beamline (ROBL) at the European Synchrotron Radiation Facility (ESRF) in Grenoble was endowed with a budget of EUR 4.5 million and completed as scheduled in 2019. In parallel, the ESRF constructed its new electron storage with an award-winning hybrid multi-bend achromat design, and produced already a stable beam at 5 mA in January 2020. After ramping up the current to 200 mA, a process taking several months of time, ROBL can restart its user operation at the worldwide first 4th generation synchrotron-light source as foreseen in September 2020. Four experimental stations will then be available for research on radionuclides, including a 5-crystal spectrometer for high-energy-resolution X-ray absorption and emission spectroscopy, a Pilatus 2M diffractometer for single-crystal and in situ diffraction, a 6-circle Huber diffractometer for surface and high-resolution powder diffraction, and an EXAFS station with the world’s first multielement Ge detector with CUBE amplifiers, lowering the detection limit by at least one order of magnitude to 1 ppm.

Beside these highlights, we obtained many other new scientific results in the past year, which are presented in this annual report. Furthermore, 107 original papers were published in peer-reviewed international scientific journals with an average impact factor of 5.07. In the last year, more than 140 scientists, technicians, and students working on their Ph.D., diploma, master, or bachelor thesis, were employed at the Institute of Resource Ecology. Thereof, 41 Ph.D. students worked at the institute in 2019. Support of young scientists is an important tool to ensure the competence and further scientific excellence in future times. Therefore, we are pleased that Jenny Jessat got the “Women in Nuclear Germany Prize 2019” for her master thesis “Studies on the interaction of

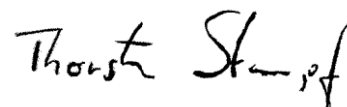
plant cells with U(VI) and Eu(III) and on stress-induced metabolite release.”

Another highlight in 2019 was the success of Kristina Kvashnina who applied for a “Megagrant” funding from the Ministry of Research and High Education in Russia. The subsidy of EUR 1.3 million will be used to build up a new group at the Chemistry Department of the Moscow State University (MSU). The funding will be combined with a professorship status at MSU.

In November 2019, the HGF strategic program evaluation for “NUSAFE” took place in Berlin. I would like to address cordial thanks to the high-ranked international review panel of this evaluation for taking the time and of course, for the given supporting remarks and the good rating. As a result, we will be able to focus on our research with a planning reliability until 2028.

In retrospect of a successful year 2019, I would like to thank the visitors, German and international ones, for their interest in our research and for their participation in the institute seminars. We would also like to thank our scientific collabo-

rators and the visiting scientists for coming to Dresden/Rossendorf in 2019 to share their knowledge and experience with us. We will continue to strongly encourage the collaborations and visits by scientists in the future. Special thanks are due to the executive board of the HZDR, the Ministry of Science and Arts of the Free State Saxony (SMWK), the Federal Ministry of Education and Research (BMBF), the Federal Ministry of Economics and Energy (BMWi), the Deutsche Forschungsgemeinschaft (DFG), the European Commission, and other organizations for their support.



Prof. Dr. Thorsten Stumpf
Director of the
Institute of Resource Ecology

Contents

SCIENTIFIC CONTRIBUTIONS

Part I: The Chemistry of Long-Lived Radionuclides

Towards the Pu(V) solid phase formation	11
K. O. Kvashnina, A. Y. Romanchuk, I. Pidchenko, L. Amidani, E. Gerber, A. L. Trigub, A. Rossberg, S. Weiss, K. Popa, O. Walter, R. Caciuffo, A. C. Scheinost, S. M. Butorin, S. N. Kalmykov	
Magnetite incorporates plutonium through formation of pyrochlore-like islands	12
T. Dumas, D. Fellhauer, D. Schild, X. Gaona, M. Altmaier, A. C. Scheinost	
Trivalent actinide incorporation into m-ZrO ₂	13
M. Eibl, N. Huittinen	
Towards the surface hydroxyl species in CeO ₂ nanoparticles.....	14
S. Bauters, T. V. Plakhova, A. Y. Romanchuk, S. M. Butorin, A. D. Konyukhova, A. V. Egorov, A. A. Shiryaev, A. E. Baranchikov, P. V. Dorovatovskii, T. Huthwelker, E. Gerber, M. M. Sozarukova, A. C. Scheinost, V. K. Ivanov, S. N. Kalmykov, K. O. Kvashnina	
Deciphering the crystal structure of a scarce 1D polymeric thorium peroxo sulfate	15
L. Bonato, M. Virost, T. Dumas, A. Mesbah, P. Lecante, X. Le Goff, C. Hennig, N. Dacheux, P. Moisy, S. I. Nikitenko, D. Prieur	
Combining factor analysis with <i>ab initio</i> multiple scattering calculations of the X-ray absorption fine structure: Tc(IV) complexes with layered double hydroxide	16
A. Rossberg, N. Mayordomo	
Complexation of tetravalent uranium with iminophosphonamide ligands.....	17
L. Köhler, P. Kaden, J. März, T. Stumpf	
Multi-reference methods help to improve the understanding of An-ligand bonding	18
R. Kloditz, M. Patzschke, S. Knecht	
Synthesis and characterization of tetravalent actinide amidinates of [AnXL ₃] type with different halide substituents (X = F, Cl, Br)	19
S. Fichter, J. März, M. Patzschke, P. Kaden	
Temperature-dependent complexation of Cm(III) with H ₂ PO ₄ ⁻ : insights from luminescence spectroscopy and quantum chemical calculations.....	20
I. Jessat, F. Réal, V. Vallet, N. Huittinen, N. Jordan	
Structural aspects of the aqueous U(IV) sulfate species	21
H. Foerstendorf, M. Patzschke, S. Lehmann, P. Dullies, R. Steudtner	
Interaction between UO ₂ ²⁺ and α-isosaccharinic acid: alteration of the ligand reactivity	22
H. Brinkmann, P. Kaden, M. Patzschke, R. Kloditz, H. Moll	
ESI-MS investigation on the aqueous U(VI)-H ₄ SiO ₄ system.....	23
H. Lösch, M. Raiwa, M. Steppert, N. Huittinen	
Extraction of molybdenum by bis(2,4,4-trimethylpentyl)phosphinic acid (Cyanex 600) – Radiotracer technique <i>vs.</i> ICP-OES	24
T. Helbig, A. Mansel	
Production and purification of n.c.a. ⁴⁸ V at the Leipzig cyclotron for extraction studies	25
A. Mansel, K. Franke	
First-time production of Na-22 at the cyclotron Cyclone 18/9 in Leipzig	26
K. Franke, A. Mansel	
The new single-crystal diffractometer at ROBL	27
C. Hennig, A. Ikeda-Ohno, T. Radoske, S. Findeisen, J. Claussner, J. Exner, D. Naudet, N. Baumann, A. C. Scheinost	

Part II: Long-Lived Radionuclides & Transport Phenomena in Geological Systems

The influence of bentonite colloids on Np(V) transport in granitic rock	31
O. Elo, P. Hölttä, P. Kekäläinen, M. Voutilainen, N. Huittinen	
Insight into the mechanism of U(VI) sorption on graphene oxide.....	32
L. Amidani, A. S. Kuzenkova, A. Y. Romanchuk, A. L. Trigub, A. V. Talyzin, S. N. Kalmykov, K. O. Kvashnina	
Sorption of trivalent REEs (Eu, La, Lu, Nd, Y) and actinides (Cm) onto K-feldspar.....	33
J. Neumann, H. Brinkmann, S. Britz, M. Stockmann, T. Stumpf, M. Schmidt	
Spectroscopic analysis of the ⁹⁹ Tc removal by synthetic pure pyrite.....	34
D. M. Rodríguez, N. Mayordomo, A. C. Scheinost, V. Brendler, K. Müller, T. Stumpf	
⁹⁹ Tc retention promoted by Fe ^{II} -Al ^{III} -Cl layered double hydroxide	35
N. Mayordomo, D. M. Rodríguez, A. Rossberg, H. Foerstendorf, K. Heim, A. C. Scheinost, V. Brendler, K. Müller	
On the chemistry and diffusion of hydrogen in the interstitial space of layered crystals h-BN, MoS ₂ , and graphite.....	36
Y. An, A. Kuc, P. Petkov, M. Lozada-Hidalgo, T. Heine	
Spatially-resolved sorption studies on Bukov diorite	37
M. Demnitz, K. Molodtsov, A. Schierz, S. Schymura, M. Schmidt, T. Stumpf	
Flow field characterization in an unaltered granite fracture from the geothermal project Soultz-sous-forets.....	38
J. Pingel, J. Kulenkampff, C. Fischer, M. Stoll, T. Schäfer	
Coupled transport processes across a claystone-concrete interface: results of a combined X-ray CT and PET experiment.....	39
J. Kulenkampff, U. Mäder, E. Bernard, A. Jenni	
Dissolution rate maps and rate spectra based on X-ray micro-computed tomography data quantify transport- and surface-controlled rate portions.....	40
W.-A. Kahl, T. Yuan, T. Bollermann, W. Bach, C. Fischer	
Modelling radionuclide transport through a sedimentary rock system with the reactive transport code OpenGeoSys#Phreeqc-3.5.0	41
M. Stockmann, R. Lu, V. Brendler	
Thermodynamic reference database THEREDA: 9. Solubility of selenate compounds in ternary systems at high ionic strengths.....	42
F. Bok	
Detection of manufactured nanomaterials in complex environmental compartments – An expert review	43
S. Schymura, H. Hildebrand, K. Franke, C. Fischer	
Mobility of radionuclides enhanced by complexants used in a repository: full description by reactive transport modeling.....	44
L. Karimzadeh, H. Lippold, M. Stockmann, C. Fischer	

Part III: Long-Lived Radionuclides in Biological Systems

Lanthanide-induced folding of an intrinsically disordered protein.....	47
E. Hoyer, J. Knöppel, M. Liebmann, M. Steppert, M. Raiwa, O. Herczynski, E. Hanspach, S. Zehner, M. Göttfert, S. Tsushima, K. Fahmy, J. Oertel	

Interaction of Eu(III) with calmodulin.....	48
B. Drobot, M. Schmidt, Y. Mochizuk, T. Abe, K. Okuwaki, F. Brulfert, S. Falke, S. A. Samsonov, Y. Komeiji, C. Betzel, T. Stumpf, J. Raff, S. Tsushima	
Transport studies of uranium, europium, caesium and strontium in the mycelium of <i>S. commune</i> by microcosm experiments.....	49
A. Wollenberg, L. Freitag, A. Günther, J. Raff	
Interactions of an extremely halophilic archaeon with Eu(III)	50
M. Bader, H. Moll, R. Steudtner, H. Lösch, B. Drobot, T. Stumpf, A. Cherkouk	
Cm(III) interaction with a Spanish bentonite yeast isolate	51
M. Lopez-Fernandez, H. Moll, M. L. Merroun	
Antibacterial activity of selenium nanoparticles studied by microcalorimetry and electron microscopy	52
S. Schäfer, K. Fahmy, M. L. Merroun	
First results of U retention studies on <i>Magnetospirillum magneticum</i> AMB-1.....	53
E. Krawczyk-Bärsch, S. Kluge, J. Raff	
Interaction of <i>Brassica napus</i> with U(VI): Extension of the experiments from plant cell cultures to plants	54
J. Jessat, S. Sachs	
Initiation and establishment of a <i>Daucus carota</i> callus cell culture for the study of the interaction of radionuclides with plants	55
S. Sachs, J. Jessat	
Microcosms as tool for analyzing the microbial influence on metal corrosion	56
M. Dressler, S. Kluge, A. Schierz, N. Matschiavelli	
Thickness of polyelectrolyte layers of separately confined bacteria alters key physiological parameters on a single cell level.....	57
I. Rybkin, D. Gorin, G. Sukhorukov, A. Lapanje	

Part IV: Nuclear Reactor Safety Research

Grain boundary analysis in a VVER-440 type reactor pressure vessel steel by electron backscatter diffraction.....	61
P. Chekhonin, F. Bergner, C. Heintze	
On the role of Ni, Si, and P on the microstructural evolution of FeCr alloys under irradiation.....	62
C. Heintze, B. Gómez-Ferrer, C. Pareige	
Effect of anisotropic microstructure of ODS steels on small punch test results.....	63
E. Altstadt, F. Bergner, A. Das, M. Houska	
Novel and established applications of magnetic small-angle neutron scattering.....	64
A. Ulbricht, F. Bergner	
Neutron fluence calculations and experimental validation for the dismantling of a German PWR.....	65
R. Rachamin, A. Barkleit, J. Konheiser	
Uniform fission source method in coupled Monte Carlo/Thermo-Hydraulic calculation	66
Y. Bilodid	
Analysis of In-Vessel Melt Retention for Konvoi Pressurized Water Reactor for selected severe accident scenarios	67
M. Jobst	
The efficiency of sequential accident management measures for a German PWR under prolonged station blackout conditions	68
Y. Kozmenkov, M. Jobst, S. Kliem, K. Kosowski, F. Schäfer, P. Wilhelm	

Neutronic modeling of the FFTF isothermal physics tests with DYN3D.....	69
E. Nikitin, E. Fridman	
Extension of the DYN3D/ATHLET code system to SFR applications	70
V. A. Di Nora, E. Fridman	

PUBLICATIONS

○ Articles (peer-reviewed).....	73
○ Oral Presentations	80
○ Reports.....	86
○ Theses	86

SCIENTIFIC ACTIVITIES

○ 14 th workshop of the European Cyclotron Network – CYCLEUR 2019.....	91
○ Workshop of the ALLIANCE Topical Roadmap Working Group NORM.....	92
○ GDCh – Jahrestagung der Fachgruppe Nuklearchemie 2019.....	93
○ Awards	94
○ Sessions (co)organized by IRE.....	94
○ Seminars (Talks of Visitors)	96
○ Teaching Activities.....	97
○ Further Events	99

PERSONNEL 101

ACKNOWLEDGEMENTS 107

INDEX OF AUTHORS 110

SCIENTIFIC CONTRIBUTIONS (PART I)

The Chemistry of
**LONG-LIVED
RADIONUCLIDES**

Towards the Pu(V) solid phase formation

K. O. Kvashnina, A. Y. Romanchuk,¹ I. Pidchenko, L. Amidani, E. Gerber, A. L. Trigub,² A. Rossberg, S. Weiss, K. Popa,³ O. Walter,³ R. Caciuffo,³ A. C. Scheinost, S. M. Butorin,⁴ S. N. Kalmykov¹

¹Department of Chemistry, Lomonosov Moscow State University, Moscow, Russia; ²National Research Centre “Kurchatov Institute”, Moscow, Russia; ³Directorate for Nuclear Safety and Security, European Commission, Joint Research Centre, Karlsruhe, Germany; ⁴Department of Physics and Astronomy, Molecular and Condensed Matter Physics, Uppsala University, Uppsala, Sweden

The formation of PuO₂ nanoparticles from oxidized Pu(VI) under alkaline conditions proceeds through the formation of an intermediate Pu(V) solid phase, similar to NH₄PuO₂CO₃, which is stable over a period of several months. State-of-the-art experiments at Pu M₄ and L₃ absorption edges combined with theoretical calculations unambiguously allowed to determine the oxidation state and the local structure of this intermediate phase.^[1]

The most debated question in properties of PuO₂ nanoparticles (NPs) is the structural nature of these NPs (crystalline *vs.* amorphous, surface *vs.* bulk), as well as the presence of Pu(V) and other oxidation states in small NPs (<3 nm). Various studies used different synthetic approaches and different solution conditions to examine the precipitated product, leading to unresolved controversies. For example, Walther *et al.* found evidence for multiple Pu oxidation states (III, IV, V) in the early stages of hydrolysis and polymerization of PuO₂ colloids at pH 0.5–1.0, while Rothe *et al.* reported only Pu(IV) during Pu(IV) oxyhydroxide-colloid formation.^[2,3] Conradson *et al.* examined solid precipitates prepared by a variety of synthetic approaches and argued for the presence of Pu(V) in nonstoichiometric PuO_{2+x} solids.^[4] Indeed, one of the most fundamental properties of the chemical behaviour of Pu is the variety of its oxidation states. We employ here High-Energy Resolution Fluorescence-Detection X-ray Absorption Near-Edge Structure (HERFD-XANES) spectroscopy at the PuM₄ edge, which allows probing the Pu oxidation state with unprecedented sensitivity as compared to conventional XANES.^[1]

RESULTS. Figure 1a shows the first experimental HERFD data at the PuM₄ edge for Pu^{IV}O₂ and KPu^VO₂CO₃(s) (solid) systems with Pu(IV) and Pu(V) oxidation states, respectively. In comparison with PuO₂, the HERFD XANES edge of KPuO₂CO₃(s) shifts towards higher incident energy and shows a narrow profile with an asymmetric shape and a shoulder at the higher incident energy side. Theoretical calculations based on the Anderson Impurity Model are in fairly good agreement with the experimental KPuO₂CO₃(s) and PuO₂ HERFD-XANES spectra (Fig. 1b).

Moreover, Fig. 1a shows experimental HERFD data recorded at different stages during the synthesis of PuO₂ NPs from the aqueous Pu(VI) precursor. For this purpose, a solution of Pu(VI) was added to an excess of ammonia. The measured pH value of the solution was 11. The kinetics of the Pu(VI) to PuO₂ transformation reveals a two-step process: during the first minutes, we observed the formation of an intermediate Pu phase consisting of a yellow sludge. Later, during the formation of PuO₂ NPs, this intermediate phase dissolved and the final phase formed. The PuM₄ HERFD spectrum recorded at the intermediate stage of the reaction is shown by the blue curve in Fig. 1a. The spectrum clearly indicates the presence of the Pu(V) oxidation state. Surprisingly, the dried NH₄PuO₂CO₃ phase was found to be stable over months. We recorded additional HERFD spectra after three months and the spectral shape remains the same. The final state of the reaction - the PuO₂ NPs - contains only Pu in the

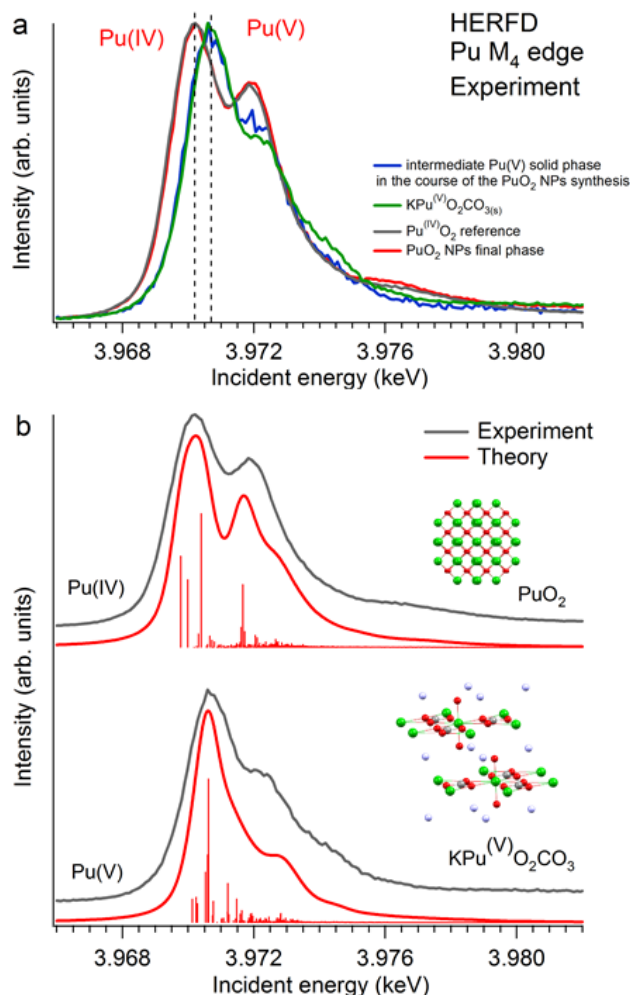


Fig. 1: Experimental HERFD data at the Pu M₄ edge from two plutonium phases (blue and red curves) obtained during the synthesis of PuO₂ nanoparticles (NPs) from a Pu(VI) precursor at pH 11 (a). The spectra of a PuO₂ bulk sample (grey curve) and of KPuO₂CO₃(s) (green curve) are also shown as references for Pu(IV) and Pu(V) oxidation states, and compared with the results of Anderson Impurity Model calculations (b).

pentavalent oxidation state. We show here for the first time that while Pu(V) solid state complexes are always viewed as exotic compounds, a thermodynamically meta-stable Pu(V) solid phase is formed during the reductive precipitation of PuO₂ NPs from the Pu(VI) precursor at pH 11.^[1]

[1] Kvashnina, K. O. *et al.* (2019) *Angew. Chemie - Int. Ed.* **58**, 17558–17562.

[2] Walther, C. *et al.* (2009) *Radiochim. Acta* **97**, 199–207.

[3] Rothe, J. *et al.* (2004) *Inorg. Chem.* **43**, 4708–4718.

[4] Conradson, S. D. *et al.* (2004) *J. Am. Chem. Soc.* **126**, 13443–13458.

Magnetite incorporates plutonium through formation of pyrochlore-like islands

T. Dumas,¹ D. Fellhauer,^{2,3} D. Schild,² X. Gaona,² M. Altmaier,² A. C. Scheinost

¹CEA Marcoule, Bagnols sur Cèze, France; ²Institute for Nuclear Disposal, KIT, Karlsruhe, Germany; ³Joint Research Centre, European Commission, Karlsruhe, Europe

Radionuclide incorporation by Fe oxides forming as corrosion product on waste containers may very efficiently reduce the migration of radionuclides by intruding ground water and, hence, increase the safety of waste repositories across millennia. Here, we show that this process is not as relevant for one of the most long-lived and radiotoxic radionuclides, plutonium, since it is reduced during this process to its trivalent oxidation state. Although Pu(III) can be partly incorporated by magnetite by rapid coprecipitation, it is expelled by recrystallization. The reason for this is its large ionic radius of 1.0 Å, which prevents that Pu(III) substitutes for one of the Fe sites in magnetite, but rather forms pyrochlore-like islands in the cubic spinel structure.^[1]

EXPERIMENTAL. Pu(V) or Pu(III) solutions were coprecipitated with Fe(II)/Fe(III) solutions to obtain magnetite with two different doping levels (samples Pu-Mag-1300 and Pu-Mag-4400, the numbers indicating solid-state associated Pu in ppm). The samples were further subjected to an Fe(II)-induced recrystallization procedure to mimic long-term aging (samples Pu-Mag-1300-rec and Pu-Mag-4400-rec).^[2] The oxidation state and local structure of Pu was investigated by Pu L_{III} edge XANES and EXAFS spectroscopies at The Rosendorf Beamline (Grenoble, France).

RESULTS. No matter if the starting solution contained Pu in tri- or pentavalent oxidation state, the final Pu oxidation state after coprecipitation was solely Pu(III) (Fig. 1A). The EXAFS spectra of the fresh precipitates are similar to each other, revealing no significant influence of Pu doping level (Fig. 1B). After the Fe(II)-induced recrystallization procedure, however, the spectra are remarkably different, and resemble those of the previously determined Pu(III) sorption complex shown at the bottom.^[3] We analyzed the EXAFS data with ITFA to decipher the number of spectral components, to derive their fractions, and to extract the endmember spectra (Comp. 1 in Fig. 1B).^[4] The fresh precipitates retain Pu(III) to about 50 % as the tridentate sorption complex on the oxygen-terminated{111} faces of the octahedrally shaped magnetite nanoparticles.^[3] After recrystallization, this fraction even increases to about 70 %. Analysis by shell fitting of Comp. 1, which represents the extracted, unknown species, showed that plutonium did not simply substitute for iron in magnetite. It adopted a split eight-fold coordination to oxygen with a distance of 3.68 Å to the nearest Fe atoms, arising from the edge-sharing linkage between Pu-hosting polyhedra and the nearest Fe-hosting octahedra in pyrochlore. This peculiar coordination environment suggests that Pu creates a pyrochlore-like environment in its neighborhood, out to a radial distance of 5 Å. Beyond this value, Pu-Fe paths of 5.17 and 5.47 Å with coordination numbers of 12 and 8, respectively, correspond reasonably well with Fe-Fe distances in magnetite (0.05 to 0.06 Å longer). Therefore, Pu(III) forms a pyrochlore-like local structure, but the longer-range environment of Pu is clearly that of magnetite. Pyrochlores are notorious host phases for lanthanides, hence it is obvious that Pu with its similar, large ionic radius of 1.0 Å, fits well in such an environment. Quite surprising is, however, that pyrochlore did not form as a separate phase,

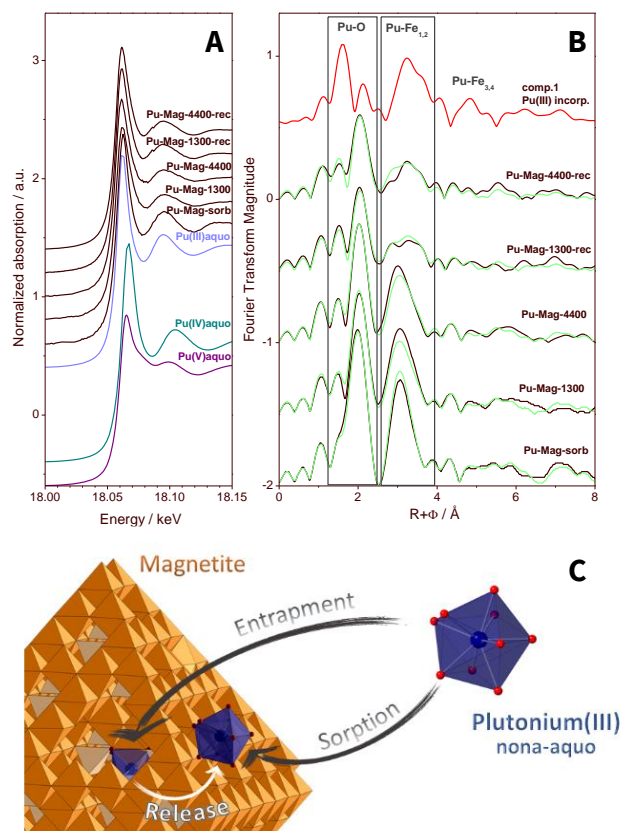


Fig. 1: Pu L_{III} XANES (A) and EXAFS (B) spectra of co-precipitation sample and references. Green lines are ITFA reconstructions by two components (B). Comp. 1 represents the Pu(III) species incorporated by magnetite, (B, red trace) and Comp. 2 is represented by the Pu(III) sorption complex at magnetite {111} faces (B, lower trace). Schematic presentation of the processes of Pu uptake and release by magnetite (C).

but rather as tiny islands within the already small (5 nm) magnetite nanoparticles. The adoption of a pyrochlore-like local environment within the magnetite long-range structure is most likely induced by the rapid coprecipitation procedure, a process named kinetic entrapment (Fig. 1, bottom). These small pyrochlore islands are, however, structurally incompatible with the magnetite structure and may present only a metastable thermodynamic state. In contrast, the sorption complex seems to be the stable phase relevant for predicting plutonium migration across geologic timescales.

- [1] Dumas, T. et al. (2019) *ACS Earth Space Chem.* **3**, 2197–2206.
- [2] Boland, D. D. et al. (2011) *Environ. Sci. Technol.* **45**, 1327–1333.
- [3] Kirsch, R. et al. (2011) *Environ. Sci. Technol.* **45**, 7267–7274.
- [4] Rossberg, A. et al. (2003) *Anal. Bioanal. Chem.* **376**, 631–638.

Trivalent actinide incorporation into m-ZrO₂

M. Eibl, N. Huittinen

The incorporation of trivalent actinides into monoclinic zirconia has been studied by means of PXRD as well as luminescence spectroscopy. It was observed that only partial incorporation into the monoclinic phase is possible, likely due to the large mismatch of the host and dopant cation radii and the small site volume of this solid phase. Doping levels high enough to stabilize the tetragonal or cubic zirconia phases are necessary to allow for complete incorporation of the dopant.

Zirconia is the main corrosion product of the Zircaloy cladding material surrounding nuclear fuel rods.^[1] Therefore, studies of the interactions of zirconia with actinides, such as structural incorporation, are necessary to enable predictions about the long term safety of final repositories for nuclear waste.

EXPERIMENTAL. To study the incorporation of Cm³⁺ into ZrO₂, ZrOCl₂ was dissolved in dilute HCl together with varying amounts of Cm³⁺ to obtain doping fractions of 25, 50, and 100 ppm. For one sample, 300 ppm of Cm³⁺ and 22 mol-% Gd³⁺ was added to the ZrOCl₂ solution to stabilize the cubic ZrO₂ phase in the final product. The solutions were dropwise added to an alkaline solution of NaCl (0.5 M, pH12) leading to the precipitation of Cm³⁺/Gd³⁺-doped hydrous zirconia. After addition of the Zr/Cm/Gd precursor solution, the resulting suspension was stored at 80 °C for 16 h to allow for complete precipitation. Thereafter, the solid phase was separated *via* centrifugation and the resulting wet paste was washed with water. Calcination was performed at 1,000 °C for 5 h to receive a crystalline solid, which was then mortared into a fine powder. A reference sample of 50 ppm Cm³⁺ doped Gd₂O₃ was prepared by the same co-precipitation method described above. PXRD measurement was performed on a Rigaku MiniFlex 600 diffractometer. Laser luminescence data was obtained with a pulsed Nd:YAG (Continuum Surelite II) pump laser coupled to a dye-laser setup (Radian Dyes) with an Exalite 398 dye. The excitation of Cm³⁺ was carried out at 396.6 nm.

RESULTS. The PXRD results of the three Cm³⁺ doped ZrO₂ samples with doping fractions of 25, 50, and 100 ppm, show a pure monoclinic crystal phase. This is in line with previous studies, which have shown that the phase transformation from monoclinic (m) to tetragonal (t) and cubic (c) ZrO₂ phases occurs for much higher trivalent dopant concentrations.^[1–3] In agreement with these studies, the zirconia sample co-doped with 300 ppm Cm³⁺ and 22 mol-% Gd³⁺ is purely cubic, owing to the high overall amount of dopant in the sample. The Cm³⁺ luminescence emission spectra of all synthesized solid compositions are presented in Fig. 1. The three ZrO₂ samples with low concentrations of Cm³⁺ (25, 50, and 100 ppm) show comparable emission behavior where the main emission peak is found at 650 nm. In addition, a hot-band is resolved at approximately 631 nm for all compositions. Both the hot-band and the main transition peak in these ZrO₂ samples are very comparable to the spectrum obtained for Gd₂O₃ doped with 50 ppm Cm³⁺. In contrast to Gd₂O₃, however, an increasing amount of luminescence signal can be seen in the m-ZrO₂ samples between the hot-band and main transition peaks with increasing Cm³⁺ concentration. A comparison of these low doped samples with the c-ZrO₂ sample shows that the incorporation in the cubic

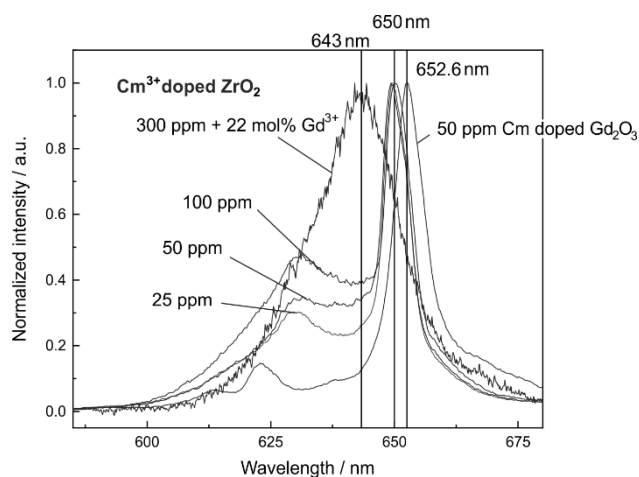


Fig. 1: Emission spectra of Cm³⁺ doped ZrO₂ for various doping fractions (25, 50, and 100 ppm) are presented together with a Gd³⁺ co-doped c-ZrO₂ sample (22 mol-% Gd³⁺, 300 ppm Cm³⁺). Additionally, a Cm³⁺ doped (50 ppm) Gd₂O₃ sample is presented.

phase results in a very broad emission peak at 643 nm. This peak coincides with the intensity between the two aforementioned peaks in the low doping samples.

Therefore, we assume that only partial incorporation takes place into the m-ZrO₂ phase, which is a result of the large cation radius mismatch of the host (78 pm) and dopant (97 pm) as well as the small site volume in monoclinic ZrO₂.^[4] Further, we assume that Cm³⁺ which is not incorporated into the m-ZrO₂ forms a Cm₂O₃ like structure within the solid phase. This assumption is based on the observed similarities of the Cm³⁺ emission signal in the m-ZrO₂ samples and in Gd₂O₃. Both Cm₂O₃ and Gd₂O₃ can form the same cubic crystal structure (IA $\bar{3}$). The unit cell volume in Gd₂O₃, however, is slightly smaller than in Cm₂O₃ due to the differences of the host cation radii (94 *vs.* 97 pm).^[4] This manifests itself as a red-shift of the Cm³⁺ emission signal in the smaller Gd₂O₃ host in comparison to the presumed Cm₂O₃ environment in m-ZrO₂ as seen in Fig. 1.

[1] Eibl, M. *et al.* (2020) *Chem. Mater.*, in prep.

[2] Li, P. *et al.* (1994) *J. Am. Ceram. Soc.* **77**, 118–128.

[3] Andrievskaya, E. R. and Lopato, L. M. (1995) *J. Mater. Sci.* **30**, 2591–2596.

[4] Shannon, R. D. (1976) *Acta Cryst.* **A32**, 751–767.

Towards the surface hydroxyl species in CeO₂ nanoparticles

S. Bauters, T. V. Plakhova,¹ A. Y. Romanchuk,¹ S. M. Butorin,² A. D. Konyukhova,¹ A. V. Egorov,¹ A. A. Shiryaev,^{1,3} A. E. Baranchikov,^{1,4} P. V. Dorovatovskii,⁵ T. Huthwelker,⁶ E. Gerber, M. M. Sozarukova,⁴ A. C. Scheinost, V. K. Ivanov,^{1,4} S. N. Kalmykov,^{1,3} K. O. Kvashnina

¹Lomonosov Moscow State University, Department of Chemistry, Moscow, Russia; ²Molecular and Condensed Matter Physics, Uppsala University, Sweden; ³Frumkin Institute of Physical Chemistry and Electrochemistry of Russian Academy of Science, Moscow, Russia; ⁴Kurnakov Institute of General and Inorganic Chemistry, Russian Academy of Sciences, Moscow, Russia; ⁵National Research Centre “Kurchatov Institute”, Moscow, Russia; ⁶Paul Scherrer Institute Swiss Light Source, Villigen, Switzerland

The surface structure and composition of Ce nanoparticles (NPs) was investigated using a multitude of analytical and spectroscopic techniques. The debated presence of Ce^{III} was successfully disproven. Moreover, with the help of electronic structure calculations, we show here that the pro/anti-oxidant properties of nanoceria are affected by the presence of hydroxyl ligands at the surface.^[1]

CeO₂ nanoparticles display excellent size-dependant pro (>10 nm) or anti (2–10 nm) oxidant properties due to their specific surface chemistry, making them highly attractive in the rapidly growing field of nanomedical products.^[1,2] Commonly, this activity is attributed to the oxygen nonstoichiometry (~ Ce^{IV}/Ce^{III} ratio) and the presence Ce^{III} species at the particle surface.^[3,4] However, spectroscopic techniques, such as XPS, EELS, EMS and RPES, employed to obtain this information often affect the particles substantially due to high-vacuum conditions and X-ray exposure, leading to elevated levels of Ce^{III} and ambiguity in general.^[5] In this study, an investigation was made combining XAS, HERFD-XAS, XRD, HRTEM, and SAXS to further clarify the exact nature of CeO₂ and its surface chemistry.^[6]

EXPERIMENTAL. Aqueous solutions of cerium nitrate Ce(NO₃)₃·6H₂O were used as stock solutions with concentrations of 0.001 M, 0.1 M and 0.8 M. For NP precipitation, the cerium stock solution was added to a fivefold excess of 3 M aqueous ammonia at room temperature under continuous stirring. The precipitate formed was allowed to age for 12 h, leading to CeO₂ NPs of 2 nm, 5 nm and 8 nm respectively. After that the yellow precipitate was separated by centrifugation and washed three times with MilliQ water to remove soluble admixtures. For further characterization, CeO₂ sam-

ples were prepared in three different ways. “As-prepared sample”: CeO₂ NPs after washing procedure without any thermal treatment; “sample dried at 40 °C”: as-prepared NP after drying overnight under ambient environment at 40 °C; “sample dried at 150 °C”: as prepared NP after drying overnight under an ambient environment at 150 °C. HERFD-XAS experiments were performed at the ROBL beamline BM20 of the European Synchrotron Radiation Facility in Grenoble.⁷ The Ce M₅ XAS edge spectra were measured at the PHOENIX beamline located at the Swiss Light Source (SLS) in Villigen, Switzerland.

RESULTS. The Ce L₃ edge HERFD spectra shown in Fig. 1 probe mainly (i) the quadrupole 2p-4f transition (pre-edge), which here indicates the presence of Ce^{IV}, and (ii) 2p-5d dipole-allowed transitions, which are sensitive to electron delocalization at the surface level of the NPs. The latter produces less pronounced features for the smallest NPs (with the highest surface to volume ratio), as can be seen in both the calculated as experimental data for the 2 nm NPs. Thermogravimetric analysis confirms the release of water when heated. Combined with the complete lack of Ce^{III} presence in the more surface sensitive Ce M₄ edge XAS spectra, we conclude the Ce NPs consist of Ce^{IV} with strongly coordinated hydroxyl ligands at the surface.

- [1] Plakhova, T. *et al.* (2019) *Nanoscale* **11**, 18142–18149.
- [2] Wills, L. A. *et al.* (2017) *Nat. Commun.* **8**, 15852.
- [3] Gliga, A. R. *et al.* (2017) *Sci. Rep.* **7**, 9284.
- [4] Pirmohamed, T. *et al.* (2010) *Chem. Commun.* **46**, 2736–2738.
- [5] Tsai, Y. *et al.* (2007) *Nanomedicine* **2**, 325–332.
- [6] Shang, F. *et al.* (2004) *Surf. Sci.* **563**, 74–82.
- [7] Kvashnina, K. *et al.* (2016) *J. Synchrotron Radiat.* **23**, 836–841.

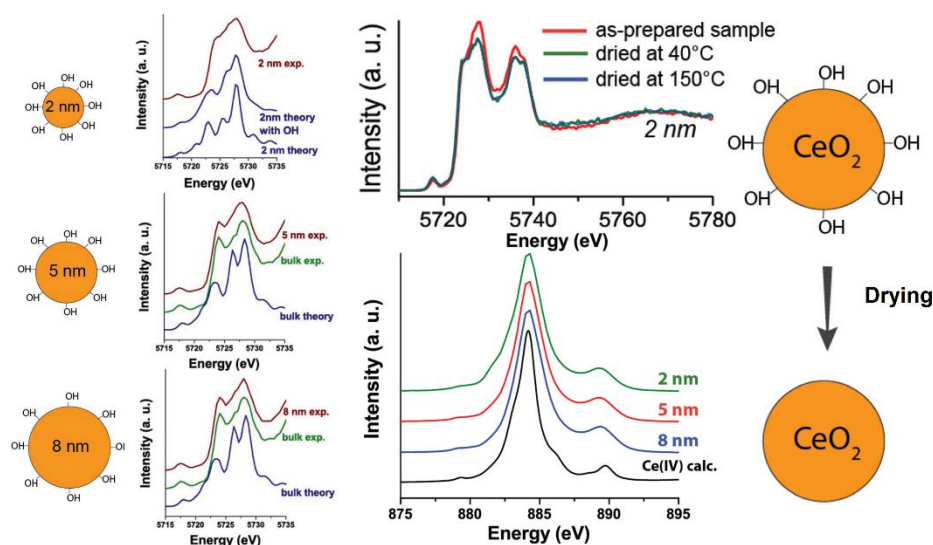


Fig. 1: Schematic drawing of the CeO₂ NPs together with their respective HERFD-XAS spectra at the Ce L₃ edge, compared to bulk CeO₂ and theoretical calculations. The differences between (non-) drying methods are shown in the Ce L₃ HERFD-XAS data on the right together with the Ce M₄ XAS spectra, both of which strongly support the presence of hydroxyl groups at the NP surface in favor of Ce^{IV}.

Deciphering the crystal structure of a scarce 1D polymeric thorium peroxo sulfate

L. Bonato,¹ M. Virost,¹ T. Dumas,² A. Mesbah,¹ P. Lecante,³ X. Le Goff,¹ C. Hennig, N. Dacheux,¹ P. Moisy,² S. I. Nikitenko,¹ D. Prieur

¹The Institute for Separation Chemistry in Marcoule (ICSM), University of Montpellier, Bagnols sur Cèze, France; ²Department of Mining and Fuel Recycling Processes (DMRC), Atomic and Alternative Energies Commission (CEA), Nuclear Energy Division, Bagnols sur Cèze, France; ³Groupe SINanO, CEMES-CNRS, Toulouse, France

The preparation and structural characterization of an original Th peroxo sulfate dihydrate, crystallizing at room temperature in the form of stable 1D polymeric microfibers, is described. A combination of laboratory and synchrotron techniques allowed resolving the structure of the $\text{Th}(\text{O}_2)(\text{SO}_4)(\text{H}_2\text{O})_2$ compound, which crystallizes in a new structure type.^[1]

The structure of thorium peroxides is still puzzling coordination chemists; the few publications reported so far often deal with highly insoluble and ill-defined compounds integrating inorganic anions from the solution in the solid species.^[2] This work describes the unprecedented structure of a mixed Th(IV) complex coordinated by peroxo and sulfate ligands.

EXPERIMENTAL. The sample preparation was performed at ICSM (France) and is detailed elsewhere.^[1] Extended X-ray Absorption Fine Structure (EXAFS) analysis and Synchrotron Powder X-ray Diffraction (SPXRD) were performed at the HZDR-operated Rossendorf Beamline (ESRF, Grenoble, France).

RESULTS. SPXRD allowed to unravel the structure (Fig. 1). The indexing of the diffraction peaks leads to the refinement of the $\text{Th}(\text{O}_2)(\text{SO}_4)(\text{H}_2\text{O})_2$ compound in an orthorhombic system in $\text{Pna}2_1$ space group with four formula units per unit cell with lattice parameters of $a = 10.2600(5) \text{ \AA}$, $b = 16.3746(7) \text{ \AA}$, $c = 4.2696(1) \text{ \AA}$ and $V = 717.31(5) \text{ \AA}^3$. The asymmetric unit is composed of one Th atom surrounded by one sulfur atom and eight oxygen atoms. Four of them belong to the sulfate group (labeled O_s), two O-atoms form the peroxo group (labeled O_p) and two others stand for water molecules (labeled O_w). A general view of the structure down the c-axis is presented in Fig. 2.

The formed polyhedra are connected together by edge or face sharing through the peroxo groups to form infinite polymeric chains oriented along the c-axis. The 3D cohesion is ensured by hydrogen bonds between water molecules and one oxygen from the sulfate groups. The presence of coordi-

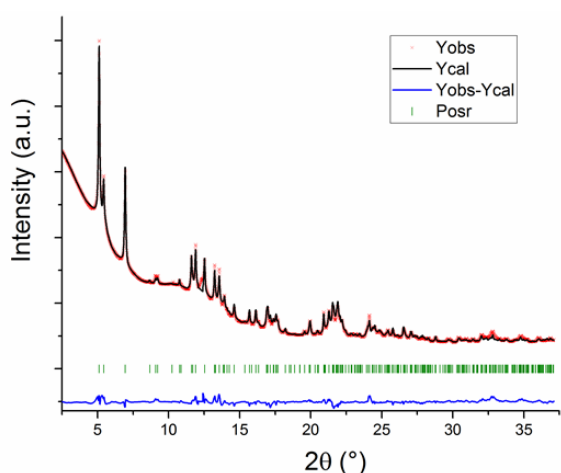


Fig. 1: Experimental and calculated patterns, and their difference, obtained from Rietveld refinement of $\text{Th}(\text{O}_2)(\text{SO}_4)(\text{H}_2\text{O})_2$.

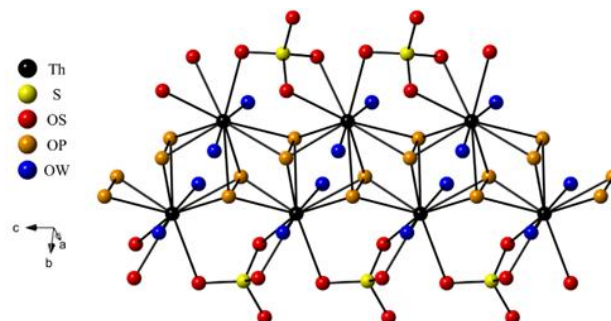


Fig. 2: Arrangement of the asymmetric unit $\text{Th}(\text{O}_2)(\text{SO}_4)(\text{H}_2\text{O})_2$ forming polymeric chains along the c-axis, showing the presence of bridging $\mu_3\text{-}\eta^2\text{:}\eta^2\text{:}\eta^2$ peroxo ligands, coordinated water molecules, and simultaneous monodentate and bidentate sulfato ligands.

ated water, peroxo, monodentate and bidentate sulfato ligands agrees with structural hypotheses obtained with FT-IR and Raman spectroscopies (not shown). Peroxo groups are found to be coordinated in a fairly scarce bridging $\mu_3\text{-}\eta^2\text{:}\eta^2\text{:}\eta^2$ mode recently reported in the crystal structure of lanthanide complexes.^[3]

The validity of the structural model is supported by simulating the experimental EXAFS signal (Fig. 3). In detail, the eleven oxygen atom distances observed in the first shell are ranging from 2.29 \AA to 2.55 \AA . The second shell contains one short distance of an S-atom from a bidentate sulfato ligand at 3.13 \AA and a longer one at 3.23 \AA from a monodentate sulfato group.

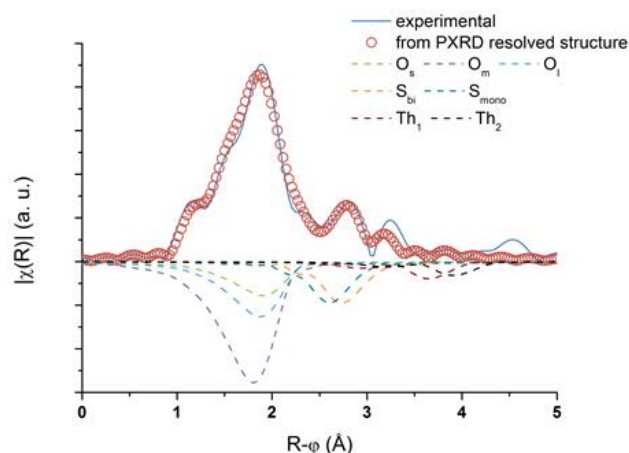


Fig. 3: FT magnitude of the experimental k^2 -weighted EXAFS spectrum (solid blue curve) compared to that obtained by an EXAFS simulation of the structure resolved by SPXRD (red circles).

- [1] Bonato, L. *et al.* (2019) *Chem. Eur. J.* **25**, 9580–9585.
- [2] Seaborg, G. T. *et al.* (1949) *The transuranium elements*.
- [3] Habash, J. *et al.* (1992) *J. Crystallogr. Spectrosc. Res.* **22**, 21–24.

Combining factor analysis with *ab initio* multiple scattering calculations of the X-ray absorption fine structure: Tc(IV) complexes with layered double hydroxide

A. Rossberg, N. Mayordomo

Factor analysis, *e.g.* Iterative Target Factor Analysis (ITFA), has proven its virtues to decompose EXAFS spectral mixtures into their components and has often allowed to derive precise chemical speciation.^[1] An important prerequisite are, however, the availability of suited experimental reference spectra. Here we develop a new method, where the experimental spectra can be replaced by more easily available structure data. The method combines to this end target transformation factor analysis (TFA) with *ab initio* multiple scattering calculations (FEFF).^[2,3] We applied the method to elucidate the Tc endmember components after the redox reaction of Tc(VII) with Fe(II)-Al(III)-Cl layered double hydroxide (LDH).^[4]

EXPERIMENTAL. The fluorescent Tc-K edge EXAFS spectra of ten Fe(II)Al(III)-Cl LDH sorption samples were measured at 77 K at the KARA synchrotron facility at KIT. The samples were prepared under different atmosphere (O₂ or N₂), pH 4.5–9.5 and Tc loading from 400 to 1,000 ppm.

In the first step of the analysis, we use ITFA in order to decompose the spectral mixtures into the eigenvectors and to determine the number of structurally different Tc(IV) complexes. This information is used for TFA. With TFA, spectra can be tested (test spectra) if they would enable a reproduction of the spectral mixtures by their linear combination, hence TFA allows for the identification of the spectra of the pure metal complexes. Moreover, TFA measures the quality of the test spectra in reproducing the spectral mixtures. However, the spectra of the pure metal complexes are often unavailable. Provided that structural models of the assumed complexes are available, FEFF can be used to calculate theoretical EXAFS spectra which can then serve as a test spectrum subjected to TFA.

We apply here the following procedure to derive the Tc speciation in the LDH system: (1) generation of a structural model based on fragments taken from XRD, (2) calculation of a theoretical test spectrum with FEFF, where the unknown Debye-Waller terms are replaced by an amplitude function gained by a recently developed Fourier filtering technique, (3) TFA by using the test spectrum, (4) Monte-Carlo target transformation factor analysis (MCTFA) of the best matching structural model.^[5,6] The structural model (step 1) is optimized successively by repeating steps 1–3. The resulting best matching structural model is subjected to MCTFA for further structural refinement. For step 1 we tested several structures which consisted in different sorbed and non-sorbed mononuclear and polynuclear arrangements of Tc. Furthermore, different Fe sites in hematite were replaced by Tc and tested.

RESULTS. Two components were detected by ITFA. The two structurally refined molecular environments of Tc(IV) and their corresponding EXAFS spectra, which reconstruct best the ten EXAFS spectral mixtures by their linear combination, are shown in Fig. 1 and Fig. 2. Regardless of Tc loading or the atmosphere (N₂ or O₂), at low pH Tc(IV) forms a corner sharing inner sphere complex with hematite and at high pH Tc(IV) incorporates in the hematite structure. In the corner sharing Tc(IV) sorption complex with hematite, Tc is surrounded by six O-atoms at 2.00 Å, one Tc atom at 2.56 Å

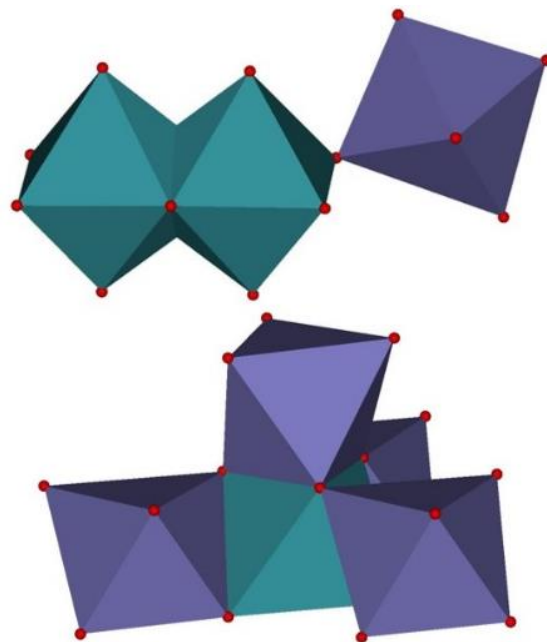


Fig. 1: Tc(IV) corner sharing sorption complex on hematite (top) and Tc(IV) incorporated into hematite (bottom). Tc (cyan), Fe (blue).

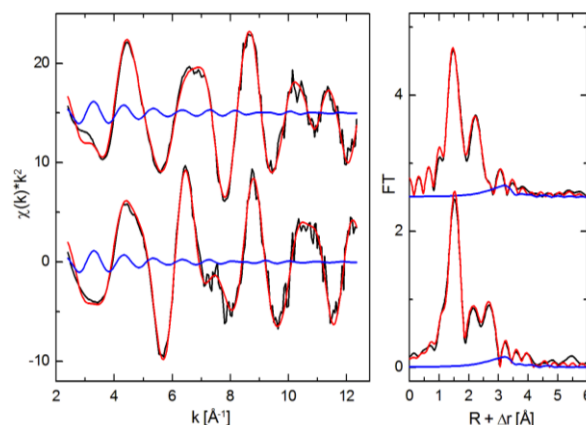


Fig. 2: Tc K edge EXAFS spectra of the Tc(IV) corner sharing sorption complex on hematite (top) and Tc(IV) incorporated into hematite (bottom). Corresponding Fourier transform (FT) (right). Isolated spectra (black), MCTFA fit (red), total multiple scattering (blue).

and 0.5 Fe-atoms at 3.55 Å. For Tc(IV) incorporated in hematite, Tc is surrounded by six O-atoms at 2.00 Å, one Fe-atom at 2.56 Å and three Fe atoms at 3.07 Å.

With our example we demonstrate that the proposed method enables a structural analysis of spectral mixtures even if the spectra of the pure metal complexes cannot be isolated by ITFA prior to a structural analysis.

[1] Rossberg, A. *et al.* (2003) *Anal. Bioanal. Chem.* **376**, 631–638.

[2] Malinowski, E. R. (1991) in: *Factor Analysis in Chemistry*, John Wiley & Sons, New York.

[3] Ankudinov, A. *et al.* (2009) *Phys. Rev. B.* **56**, 1712–1715.

[4] Majordomo, N. *et al.* (2019) this report, p. 35.

[5] Taube, F. *et al.* (2019) *Inorg. Chem.* **58**, 368–381.

[6] Rossberg, A. *et al.* (2005) *Anal. Bioanal. Chem.* **383**, 56–66.

Complexation of tetravalent uranium with iminophosphonamide ligands

L. Köhler, P. Kaden, J. März, T. Stumpf

Complex formation of tetravalent uranium with the iminophosphonamide (NPN) ligands *P,P*-diphenyl-*N,N'*-bis(*R*)-1-phenyl-ethyl phosphine-imidic amide HL¹ and *P,P*-diphenyl-*N,N'*-bis(*R*)-(2,6-diisopropylphenyl) phosphinimidic amide HL² was investigated. Upon addition of base (butyllithium or lithium hexamethyldisilazide (LiHMDS)), U complex species could be identified in solution by NMR and UV-vis spectroscopy. Due to very low complex concentration no single crystal formation is observed, indicating U complexation is prevented by intermediately formed Li species.

Within the family of NXN ligands, the group of iminophosphonamides (X = P) is of particular interest (Fig. 1), because long N–X bonds and wide N–X–N angles establish greater ligand backbone flexibility. This enables the ligand to adopt to different ion sizes.^[1,2] Principally, this allows the synthesis of complex series with U in different oxidation states (+III to +VI) and thus very different ionic radii in similar or identical chemical environments. From trends in such series we can then derive information on the binding properties of the actinides as a function of their number of *f*-electrons.

EXPERIMENTAL. UCl₄ was added to a [Li(L¹)₂] THF solution, and the reaction mixture was stirred at room temperature for one day. After centrifugation the solvent was removed *in vacuo*, the solid was washed with pentane and toluene and a brownish powder was obtained.

HL², LiHMDS and UCl₄ were dissolved in THF and stirred at ambient temperature for 24h. Afterwards the same work up procedure as for the ligand L¹ was applied. Colorless crystals were grown *via* diffusion experiments.

RESULTS. For UV-vis investigations, the method of continuous variation was applied: The molar fractions of ligand ([Li(L¹)₂] in THF) and metal (UCl₄ in THF) are varied throughout the measured series, whereas the sum of their molar concentrations stays constant. The following Job plot analysis showed favored U:ligand ratios of 1:1 and 1:3. Furthermore, absorption around 630 nm and 1,106 nm indicate the presence of an additional complex species (Fig. 2).

To investigate the complex structure in solution, NMR spectroscopy was applied. In the ¹H NMR spectrum sharp signals could be assigned to [LiL¹]₂, whereas the broad signals show the existence of at least one U complex species. Signal broadening is caused by the paramagnetic influence of U, proven by a temperature series, where both, the signal position and width were found to be temperature dependent (Fig. 2).

Moreover, in the ³¹P spectrum a broad and strongly shifted signal was detected at –282 ppm, in the same range as a similar U–NPN complex (–230 ppm).^[3] In the spectra of various

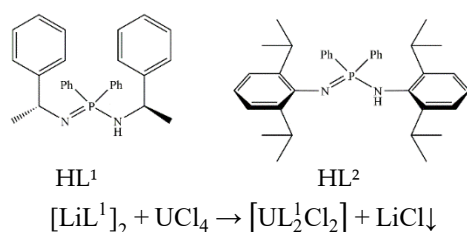


Fig. 1: For the studies used ligands and exemplary reaction equation for L¹.

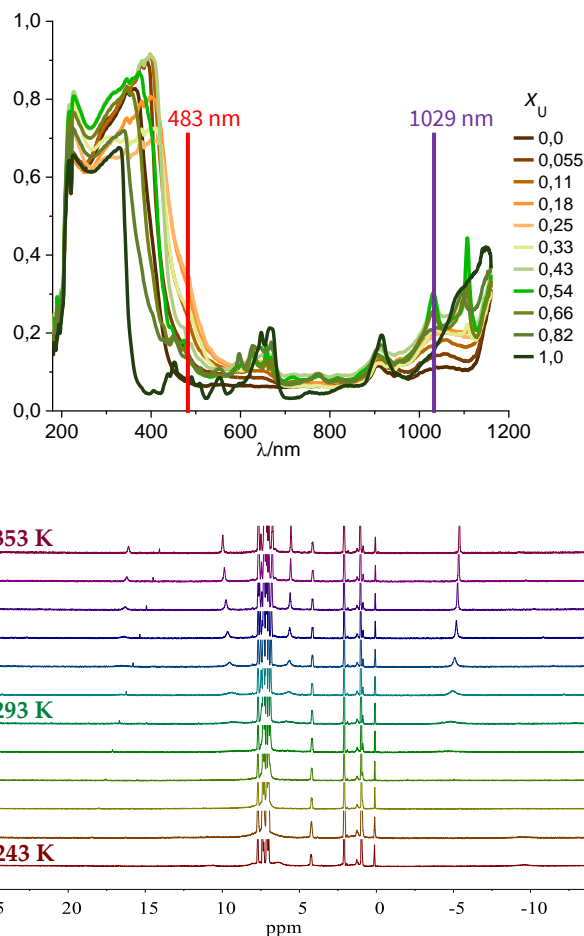


Fig. 2: Top: UV-vis spectra of different U:ligand ratios, with marked spots suitable for Job plot analysis. Bottom: ¹H NMR temperature series in the range of 243–353 K.

nuclei (¹³C, ³¹P, ⁷Li, ¹H), the width of the complex signals differs, showing a dependence on the respective NMR time scale. This behavior points to a dynamic process in solution. To conclude, the complex is forming in solution, but it is labile. Thus, the equilibrium of the complex formation is on the educt side, yielding a very low average complex concentration.

The colorless crystals formed in the reaction with HL², were revealed to be a [LiL²(THF)₂] complex by SC-XRD. Even though U was present in the reaction mixture, the actinide complex was not formed. This confirms the assumption that has been made for L¹:Li⁺ has a higher affinity to the NPN binding site in the specifically used ligands and is not replaced by U⁴⁺.

Future work will focus on using the analogous K⁺ salts as precursors, which have previously been applied in the synthesis of analogous lanthanide complexes.^[4] The K⁺ salts of L¹ exhibit a greater cavity for U to enter the alkali metal dimer. In the case of L² substituting K⁺ widens the N–P–N angle resulting in U possibly reaching better onto the binding site.^[4]

- [1] Prashanth, B. and Singh, S. (2014) *Dalton Trans.* **43**, 16880–16888.
- [2] Peganova, T. A. et al. (2018) *Eur. J. Inorg. Chem.*, 5098–5107.
- [3] Recknagel, A. (1989) *J. Organomet. Chem.* **371**, C40–C44.
- [4] Feuerstein, T. J. et al. (2019) *Chem. Sci.* **10**, 4742–4749.

Multi-reference methods help to improve the understanding of An-ligand bonding

R. Kloditz, M. Patzschke, S. Knecht¹

¹ETH Zürich, Department of Chemistry and Applied Bioscience, Zürich, Switzerland

High-level multi-reference calculations have been performed on a series of actinide salen complexes in order to assess the role of the f-electrons in actinide bonding.

Calculations of actinide-bearing molecules carry high computational costs for a number of reasons, which only partly can be mitigated by advanced methods. Firstly, actinides introduce a large number of electrons to the system and require the incorporation of relativistic effects, this can be improved by using relativistic effective core potentials (RECPs). Spin-orbit coupling makes it necessary to perform calculations not based on the Schrödinger equation, but on the Dirac equation. While these effects are normally less important for structural parameters, they are crucial for the determination of spectroscopic properties like excitation energies. In addition, actinides have an open f-shell and for a proper description of all possible spin states one has to perform multi-reference calculations, typically as complete-active-space (CAS) calculations. On top of these, electron correlation is treated *via* many-body perturbation theory. Finally, for all calculated states a spin-orbit coupling calculation is performed.

The problem in this approach is the large number of states to be optimized. The number of these, so called, configuration state functions (CSF) can be calculated using Weyl's formula:

$$K(n, N, S) = \frac{2S+1}{n+1} \binom{n+1}{\frac{1}{2}N-S} \binom{n+1}{\frac{1}{2}N+S+1} \quad (1)$$

Where n is the number of orbitals, N is the number of electrons and S is the spin quantum number. In Tab. 1, the number for CSFs for different f-occupations can be found.

Tab. 1: CSF for different f-occupations. For details see text.

N/N	Spin State (2S+1)							
	1	2	3	4	5	6	7	8
0/14	1							
1/13	–	7						
2/12	28	–	21					
3/11	–	112	–	35				
4/10	196	–	210	–	35			
5/9	–	490	–	224	–	21		
6/8	490	–	588	–	140	–	7	
7/7	–	784	–	392	–	48	–	1

The large number of states limits the practically accessible size of the active space, which may introduce inaccuracies if a too small active space is chosen.

A relatively recent addition to the theoretical chemist's toolbox to mitigate this problem are density-matrix renormalization-group (DMRG) calculations, which allow larger active spaces (more than 40 electrons in 40 orbitals).

Here we report results of such a state-of-the-art calculation on the [U(IV)(salen)₂] complex (Fig. 1) using OpenMolcas1. We first performed a Hartree-Fock calculation with a subsequent orbital localization. This helped us to identify a set of 44 orbitals of interest, containing the U s/p/d and f valence orbitals, O 2s and 2p as well as N 2s and CN as well as CO

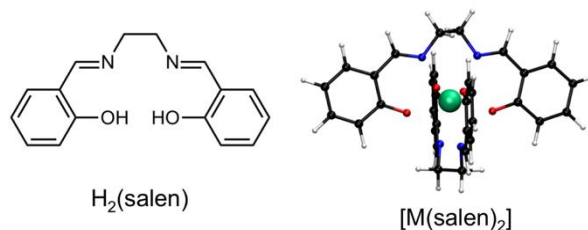


Fig. 1: Left: schematic drawing of the salen ligand. Right: optimized structure of the [U(IV)(salen)₂] complex.

π -orbitals and CN π^* -orbitals. 50 electrons are in these orbitals. From the DMRG-CI calculation one can extract an entanglement diagram that provides information on the interaction of those orbitals (Fig. 2). Lines between different orbitals reveal mutual information exchange, such orbitals correlate. Additionally, spheres at the start of the lines show one-orbital entanglement. For [U(IV)(salen)₂], it is quite clear that the f-orbitals do exhibit significant entanglement amongst each other. Furthermore, one sees important contributions (dotted lines) from CN π - and π^* -orbitals (#13–18 and 32–35, respectively). The thin black lines show entanglement between O p-orbitals and U d-orbitals.

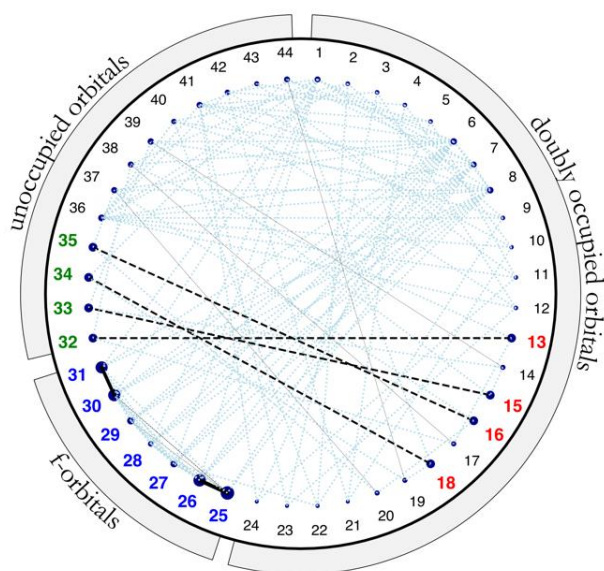


Fig. 2: Entanglement plot for [U(IV)(salen)₂]. Red: doubly occupied CN π orbitals, green: unoccupied CN π^* orbitals, blue: uranium 5f orbitals (two electrons in seven orbitals).

Based on this information of active orbitals further CAS calculations can be performed. More directly, the diagram illustrates that the U f-orbitals are not entangled with the ligand orbitals from N and O. Any covalency in this compound would be a dative bond between the O 2p and empty U 6d.

[1] Galván, I. *et al.* (2019) *J. Chem. Theory Comput.* **15**, 5925–5964.

[2] Boguslawski, K. *et al.* (2012) *J. Phys. Chem. Lett.* **3**, 3129–3135.

Synthesis and characterization of tetravalent actinide amidinates of [AnXL₃] type with different halide substituents (X = F, Cl, Br)

S. Fichter, J. März, M. Patzschke, P. Kaden

A series of enantiopure tetravalent actinide tris-amidinate complexes [AnX((S)-PEBA)₃] (An = Th, U, Np; (S)-PEBA: (S,S)-N,N-Bis-(1-phenylethyl)-benzamidinate) featuring different halide ligands (X = F, Cl, Br) have been synthesized and characterized in solution and in solid state. The neptunium amidinates [NpX((S)-PEBA)₃] represent the first transuranic amidinates and include the first structurally characterized Np–Br bond in a metal-organic compound.

The chemistry of neptunium has always lacked behind that of its lighter neighbor uranium due to its higher radiotoxicity and the restrictions of handling Np by only a few dedicated research facilities worldwide. We aim to expand the rich uranium chemistry to neptunium, plutonium, and beyond. Amidinates are a well-known class of N-donor ligands which have been successfully used to synthesize lanthanide and actinide complexes.^[1] The (S)-PEBA ligand was synthesized only recently and features chiral centres next to the nitrogen donors.^[2] This enables the synthesis of enantiopure metal complexes.^[3]

EXPERIMENTAL. The enantiopure tris-amidinate chloro complexes [AnCl((S)-PEBA)₃] (An = Th (**1a**), U (**2a**), Np (**3a**)) were prepared as reported in the literature.^[4] Halide substitution was obtained using Ag[PF₆] and (CH₃)₃SiBr, respectively, in THF. After workup [AnX((S)-PEBA)₃] compounds (An = Th (X = F, **1b**; Br, **1c**), U (X = F, **2b**; Br, **2c**), Np (X = F, **3b**; Br, **3c**)) were obtained in good yields.

RESULTS. A schematic representation of the tris-amidinate tetravalent actinide compounds **1a–3c** is shown in Fig. 1 together with the molecular structure of [NpBr((S)-PEBA)₃] (**3c**) representing the first structurally characterized metal-organic complex featuring a Np–Br bond. All compounds crystallize in the chiral space group *P*2₁2₁ with similar cell parameters showing the enantiopurity of these compounds in solid state. The distances towards the amidinate moieties (2.50 Å (**1**); 2.44 Å (**2**), 2.43 Å (**3**)) do not vary when changing the halide ligand whereas the distances to the halide increases in the order F < Cl < Br as anticipated by the ionic radii of the respective anions.

All complexes were studied in solution by means of NMR spectroscopy (δ_{obs}). The presence of paramagnetic metal centres in **2a–3c** causes additional paramagnetic shifts which can be described in terms of the hyperfine shift δ_{HF} .^[5] Furthermore, the diamagnetic contribution δ_{dia} to the NMR

chemical shift of the paramagnetic complexes **2a–3c** is expected to be similar to the chemical shifts of the diamagnetic Th compounds **1a–1c**. The pure hyperfine contribution δ_{HF} can be obtained for all compounds (see Fig. 2) according to equation 1.

$$\delta_{HF} = \delta_{obs} - \delta_{dia} \quad (1)$$

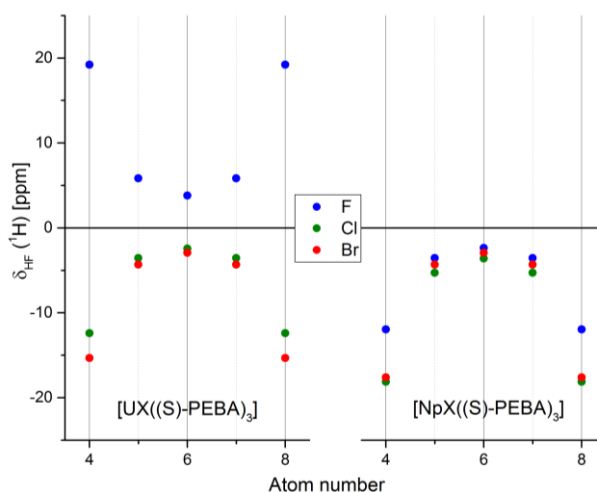


Fig. 2: Plot of hyperfine shift δ_{HF} for protons 4–8 of [AnX((S)-PEBA)₃] (An = U (left), Np (right); X = F (blue), Cl (green), Br (red)).

The absolute value of δ_{HF} is similar for all compounds and decreases with increasing distance from the paramagnetic centre. However, the complexation of F⁻ in **2b** (left, blue) resulted in an opposite sign of δ_{HF} indicating a change of the magnetic susceptibility for the 5f² (U^{IV}) configuration but not the 5f³ (Np^{IV}) system. The elucidation of this unprecedented behaviour is part of ongoing investigations including high-level quantum chemical calculations to estimate the electronic influence of the fluoride anion on the spectroscopic properties of **2b** and **3b**.

Within this study we could show that although the chemistry of uranium and neptunium is similar in terms of reactivity the electronic structure as characterized by paramagnetic NMR spectroscopy may differ substantially.

ACKNOWLEDGEMENTS. This work was supported by the German Federal Ministry of Education and Research (BMBF) under the project number 02NUK046B (FENABIUM). We thank Prof. Dr. P. Roesky (Karlsruhe Institute of Technology) for providing the benzamidinate ligand.

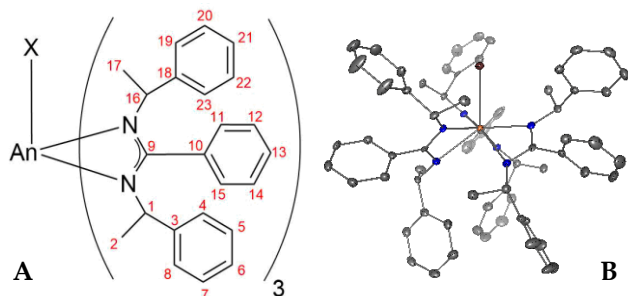


Fig. 1: Schematic drawing of **1a–3c** (A). Molecular structure of [NpBr((S)-PEBA)₃] (**3c**) (B). Color code: Np, orange; Br, brown; N, blue; C, grey. Hydrogen atoms are omitted for clarity.

- [1] Edelmann, F. T. (2013) *Adv. Organomet. Chem.* **61**, 55–374.
- [2] Benndorf, P. et al. (2011) *J. Organomet. Chem.* **696**, 1150–1155.
- [3] Benndorf, P. et al. (2012) *Chem. Eur. J.* **18**, 14454–14463.
- [4] Schöne, S. et al. (2016) *Report HZDR-079*, p. 18.
- [5] Parigi, G. et al. (2019) *Prog. Nucl. Magn. Res. Spect.* **114–115**, 211–236.

Temperature-dependent complexation of Cm(III) with H_2PO_4^- : insights from luminescence spectroscopy and quantum chemical calculations

I. Jessat, F. Réal,¹ V. Vallet,¹ N. Huittinen, N. Jordan

¹Université Lille, CNRS, UMR 8523, PhLAM, Lille, France

The complexation of Cm(III) with H_2PO_4^- was investigated between 25 and 90 °C and at $-\log[\text{H}^+] = 2.52$ using laser-induced luminescence spectroscopy. Two complexes namely $\text{CmH}_2\text{PO}_4^{2+}$ and $\text{Cm}(\text{H}_2\text{PO}_4)_2^+$ could be identified. The extended van't Hoff equation was used to obtain molal reaction enthalpies and entropies for both complexes. Computational studies indicated changes in the coordination number of Cm(III) in the presence and absence of H_2PO_4^- -ligands.

EXPERIMENTAL. For the luminescence spectroscopy ($\lambda_{\text{exc}} = 396.6 \text{ nm}$), sample series with $I = 0.5, 1.0$ and 2.0 mol L^{-1} were prepared using NaClO_4 as background electrolyte. The concentration of ^{248}Cm was 8.76×10^{-7} or $1.15 \times 10^{-7} \text{ mol L}^{-1}$. In all samples, the proton concentration was $3 \times 10^{-3} \text{ mol L}^{-1}$. The phosphate concentrations varied between zero and 0.08 mol L^{-1} . In addition, temperature dependent measurements between 25 and 90 °C at $I = 1 \text{ mol L}^{-1}$ were performed. Computational studies were achieved using the MOLCAS and Turbomole programs. *Ab initio* simulations were obtained from the unrestricted MP2 level using VTZ basis sets and an effective core potential for curium. Solvation effects were included using COSMO-RS. Multireference CASPT2 calculations with spin-orbit coupling yielded ground and excited states (all $5f^7$ spin states).

RESULTS. With increasing phosphate concentrations the emission spectra of Cm(III) at 25 °C were shifted to higher wavelengths indicating an increasing complexation (data not shown). After deconvolution,^[1] the pure spectral components of the Cm^{3+} aquo ion, the $\text{CmH}_2\text{PO}_4^{2+}$ and the $\text{Cm}(\text{H}_2\text{PO}_4)_2^+$ complexes (Fig. 1) were obtained, as well as their species distributions (considering luminescence intensity factors). Conditional stability constants at 25 °C were determined on the molal scale assuming the following chemical reaction ($n = 1$ and 2):



as confirmed by slope analysis.^[2] The conversion of molar to molal scale and the derivation of molal concentration of the free H_3PO_4 was performed as described elsewhere.^[1,2] By applying the SIT equation,^[3] the following values at infinite dilution were derived: $\log \beta^0 = 0.45 \pm 0.09$ ($\text{CmH}_2\text{PO}_4^{2+}$) and $\log \beta^0 = 0.08 \pm 0.17$ ($\text{Cm}(\text{H}_2\text{PO}_4)_2^+$). An increased complexation with increasing temperature was observed (data not shown). The extended van't Hoff equation provided positive

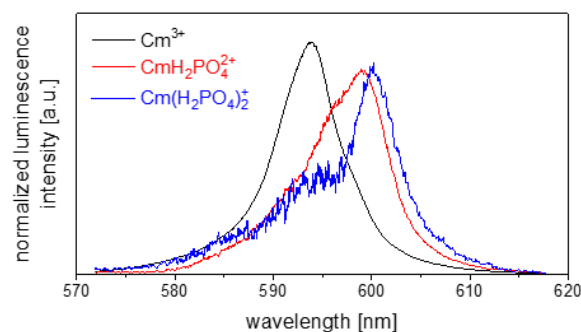


Fig. 1: Pure component spectra of the Cm^{3+} aquo ion, the $\text{CmH}_2\text{PO}_4^{2+}$ and the $\text{Cm}(\text{H}_2\text{PO}_4)_2^+$ complex.

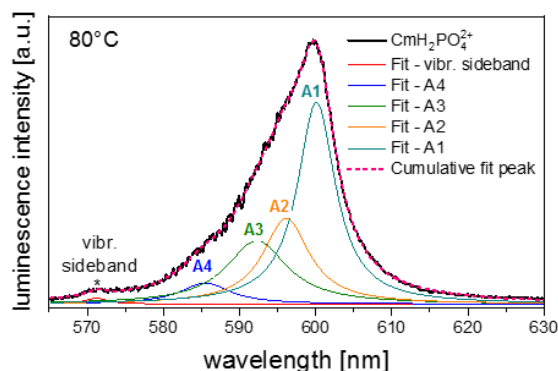


Fig. 2: Pure component spectrum of the $\text{CmH}_2\text{PO}_4^{2+}$ complex at 80 °C fitted with four Lorentzian peaks (A1–A4) describing the emissions from the four crystal states (${}^6\text{D}_{7/2}$) to the ground state (${}^8\text{S}_{7/2}$).

standard enthalpies and entropies of reaction for both complexes.^[2,4] To shed light on potential changes occurring in the Cm(III)-coordination environment with increasing temperature, such as a decrease of the coordination number (CN) from 9-fold to 8-fold as observed for the Cm^{3+} aquo ion,^[5] electronic level calculations were performed for the $\text{CmH}_2\text{PO}_4^{2+}$ complex. Here, the relative energies of the four relevant emissions of the 9-fold and 8-fold coordinated $\text{CmH}_2\text{PO}_4^{2+}$ complexes compared to the main transition (A1) were calculated and compared to experimental results. The experimental pure component spectrum of $\text{CmH}_2\text{PO}_4^{2+}$ at 80 °C was fitted with four Lorentzian peaks (Boltzmann distribution used to constrain area under peak, Fig. 2). The best agreement between the computed and fitted experimental results was obtained for the 9-fold coordinated $\text{CmH}_2\text{PO}_4^{2+}$ complex (Tab. 1).

Tab. 1: Fitted experimental energies and computed results for the four main emissions of the $\text{CmH}_2\text{PO}_4^{2+}$ complex at 80 °C. All values are given in cm^{-1} .

Transition	CN = 9		$\Delta\Delta E$ ($\Delta E_{\text{comp.}} - \Delta E_{\text{exp.}}$)	
	$E_{\text{exp.}}$	$\Delta E_{\text{exp.}}$		$\Delta E_{\text{comp.}}$
A4	17,080	416	432	16
A3	16,884	220	291	71
A2	16,775	111	112	1
A1	16,664	0	0	0

Thus, in contrast to the Cm^{3+} aquo ion, the CN of the $\text{CmH}_2\text{PO}_4^{2+}$ complex is not impacted by the temperature. Further studies will be conducted to explain this behavior.

- [1] Jordan, N. *et al.* (2018) *Inorg. Chem.* **57**, 7015–7024.
- [2] Huittinen, N. *et al.* (2020) *Env. Int.*, in preparation.
- [3] Lemire, R. J. *et al.* (2013) *Chemical Thermodynamics of Iron: Part I*, OECD Publications, Paris.
- [4] Puigdomènech, I. *et al.* (1999) *Temperature Corrections to Thermodynamic Data and Enthalpy Calculations*, TDB-4, Issy-Les-Moulineaux, France: OECD Nuclear Energy Agency.
- [5] Lindqvist-Reis, P. *et al.* (2005) *J. Phys. Chem. B*, **109**, 3077–3083.

Structural aspects of the aqueous U(IV) sulfate species

H. Foerstendorf, M. Patzschke, S. Lehmann, P. Dullies, R. Steudtner

A combined approach of infrared (IR) spectroscopy and quantum-chemical calculations based on density functional theory (DFT) was applied to resolve the binding motif of sulfate anions to the U(IV) cation in aqueous solution. From the results, a predominant monodentate coordination of the anions was consistently derived.

It is important to predict the environmental behavior of uranium in dilute to highly saline aquifer systems based on reliable thermodynamics with a realistic species set. One important ligand to consider is sulfate (SO_4^{2-}), both in dilute and in highly saline solutions. For instance, sulfate is encountered in technological steps for both the mining and enrichment of uranium.

This study addresses the structural characteristics of the uranium(IV) complexes with sulfate in the aqueous phase focusing on the conformational orientation of the ligand ions in the U(IV) complex.

EXPERIMENTAL. The experimental setup of IR spectroscopy and the basic data set used for DFT calculation can be found in detail elsewhere.^[1]

RESULTS. The vibrational modes of small molecules observed in vibrational spectra intrinsically correlate with the overall molecule's symmetry. At pH 1, the reference spectrum of the aqueous sodium sulfate showed five S–O stretching modes representing the tetrahedral and C_{3v} molecule symmetries of the prevailing SO_4^{2-} and HSO_4^- anions, respectively (Fig. 1A).^[2]

The spectrum of the U(IV) containing solution revealed a significantly changed spectrum (Fig. 1B). All major bands can be ascribed to the $\nu_{3,as}$, $\nu_{3,sr}$ and ν_1 modes of the sulfate

ions, strongly suggesting a predominant C_{3v} symmetry of the ligand, *i.e.* a monodentate coordination to the U^{4+} ion. This is supported by the excellent reproduction of the spectrum by the components necessary for the C_{3v} symmetry of the sulfate ions including the presence of uncoordinated $\text{HSO}_4^-/\text{SO}_4^{2-}$ according to the reference spectrum given above.

With the obtained IR results it is possible to compare the computed IR spectra of suggested structures. For the calculations, a rather large cluster consisting of 100 water molecules and one sulfate ion was necessary to circumvent polarization effects of the water molecules when adding the highly charged U^{4+} ion. It was made sure that the first and second solution shells for the uranium and sulfate ions were intact. Three different starting geometries were considered: mono-, bi- and tridentate bonding of the sulfate ion. Upon optimization, no true minimum for the tridentate or bidentate motif could be found. Following the computed imaginary frequencies led to monodentate structures (Fig. 2). The calculated vibrational frequencies of the sulfate modes in the optimized complex are indicated as grey bars in the U^{IV}sulfate spectrum (Fig. 1B)

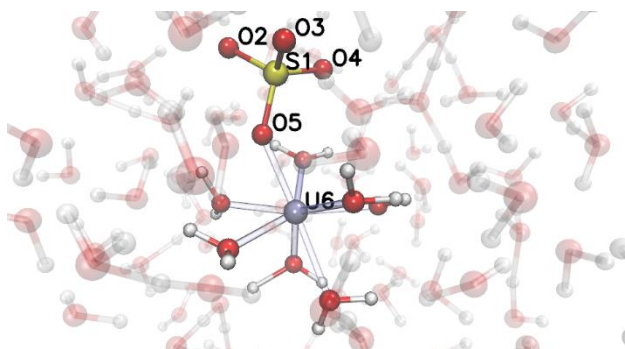


Fig. 2: Best computational guess for the structure of the $\text{U}^{\text{IV}}\text{SO}_4^{2+}$ complex in aqueous solution. The surrounding extra water molecules are rendered transparent in order to improve the clearness of the picture. Numbering of atoms is consecutive.

Our speciation shows that for the concentrations used in this work $\text{U}^{\text{IV}}\text{SO}_4^{2+}$ should be the dominant species and for this species clear monodentate binding should be the preferred mode.

ACKNOWLEDGEMENT. This work was partially funded by the German Ministry of Economic Affairs and Energy under the grants 02E11334B within the EDUKEM project.

[1] Lehmann, S. *et al.* (2019) *Dalton Trans.* **48**, 17898–17907.

[2] Nakamoto, K. (2002) *Handbook of Vibrational Spectroscopy*, p. 1872–1892.

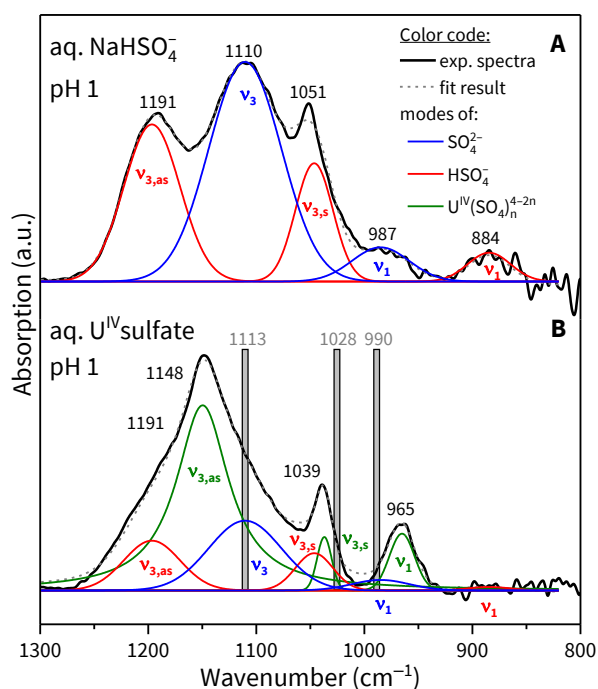


Fig. 1: IR spectra of aqueous solution of sulfate (A) and the corresponding U(IV) species (B) including the components of the S–O stretching modes of prevailing HSO_4^- and SO_4^{2-} species as given in the legend. Calculated frequencies of the optimized aqueous U^{IV}sulfate species are given as grey bars. [Sulfate] = 1 mmol L⁻¹; [U] = 2 mmol L⁻¹; pH 1. Values are given in cm⁻¹.

Interaction between UO_2^{2+} and α -isosaccharinic acid: alteration of the ligand reactivity

H. Brinkmann, P. Kaden, M. Patzschke, R. Kloditz, H. Moll

The impact of UO_2^{2+} on the transformation of α -isosaccharinic acid (HISA) to α -isosaccharinate-1,4-lactone (ISL) has been investigated by NMR-spectroscopy. Theoretical calculations were used to explain ongoing processes on the molecular level.

Isosaccharinic acid is the main product of alkaline cellulose degradation.^[1] Information concerning the interaction of this polyhydroxycarboxylic acid with UO_2^{2+} are scarce and no structural information were given in the literature. HISA transforms to ISL under very acidic conditions. As experiments towards the characterization of complexes formed in the UO_2^{2+} -ISA system were performed under acidic conditions, the impact of UO_2^{2+} on the transformation from HISA to ISL had to be assessed.

EXPERIMENTAL. Two 60 mM NaISA solutions were prepared. One solution contained 15 mM UO_2^{2+} . After adjusting the pH to 2.2 (start of the experiment), ^1H -NMR spectra of both samples were collected over a period of approximately nine days. Integration of well separated ^1H -signals were used to calculate the relative concentrations of HISA and ISL as described by Brinkmann *et al.*^[2]

RESULTS. The transformation kinetics of HISA to ISL was investigated by ^1H -NMR spectroscopy. Figure 1 shows the relative concentrations of HISA and ISL. According to the first order of the lactone-formation reaction, the data were fitted with a monoexponential function ($R^2 > 0.99$). The kinetics are significantly faster in the presence of UO_2^{2+} . This reflects in the decreased half-life ($t_{1/2}$) of the reaction from 3,294 to 2,058 min. Calculated equilibrium concentrations of HISA and ISL were not affected by the presence of UO_2^{2+} . Comparison of ^1H -NMR spectra from different points in time (data not shown), revealed the interaction between UO_2^{2+} and HISA.^[2]

There is no interaction with ISL. Consequently, the faster kinetics of the lactone formation must be caused by the changed reactivity of HISA upon interaction with UO_2^{2+} . To further understand the mechanism on the molecular level, the structure of a $[\text{UO}_2(\text{ISA})(\text{HISA})]^+$ -complex was optimized by DFT-calculations. Moreover, changes in the electron density, which is caused by the interaction of the single components, were calculated and are shown in Fig. 2. Elec-

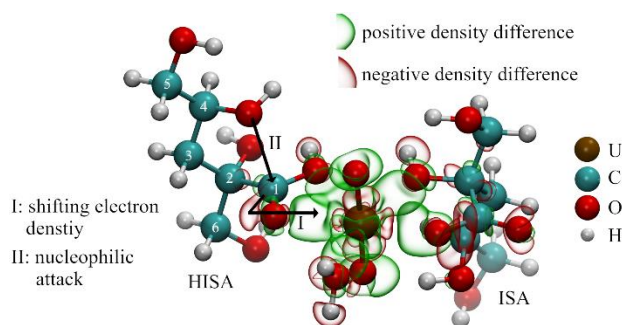


Fig. 2: Calculated electron density changes in a $[\text{UO}_2(\text{ISA})(\text{HISA})]^+$ -complex and the impact on the lactone formation reaction (isovalues for the representation of electron densities were -0.005 (red) and $+0.005$ (green).

tron density is withdrawn from the coordinating O-atoms by the central U-atom. This causes a decrease of electron density at the C_1 -atom of the HISA carboxylic group. Once C_1 is activated, the nucleophilic attack by the secondary alcohol ($\text{C}_4\text{-OH}$) can occur, resulting in a tetrahedral transition state. This is the rate limiting step of the lactone formation.^[2] The results clearly show the changed reactivity of the HISA molecule, caused by the electron withdrawing effect of the UO_2^{2+} unit. This does improve the general understanding with respect to the interaction of UO_2^{2+} with organic ligands. Furthermore, unveiling the interaction between UO_2^{2+} and the protonated form of isosaccharinic acid was a requirement to understand the complex formation mechanisms in the UO_2^{2+} -ISA system, as described by Brinkmann *et al.*^[2]

MISCELLANEOUS. Figures were taken directly from the original publication.^[2]

ACKNOWLEDGEMENTS. This project has received funding from the Euratom research and training programme 2014–2018 under Grant Agreement no. 61880.

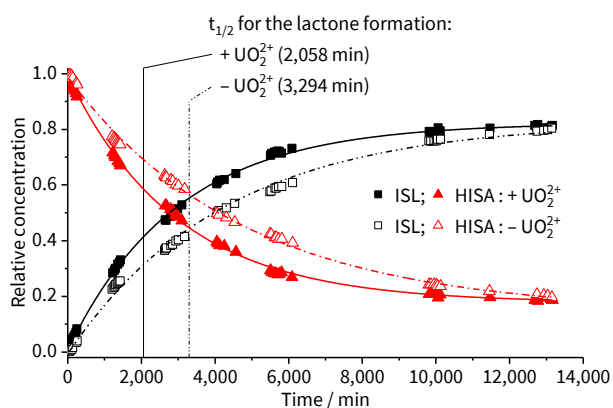


Fig. 1: Transformation of HISA to ISL in the presence (+) and absence (-) of UO_2^{2+} at pH 2.2. Relative concentrations of HISA and ISL were determined based on the ratio of their integrated ^1H -NMR signals. Experimental data were fitted with a monoexponential function.

ESI-MS investigation on the aqueous U(VI)-H₄SiO₄ system

H. Lösch, M. Raiwa,¹ M. Steppert,¹ N. Huittinen

¹Institute of Radioecology and Radiation Protection, Leibniz Universität Hannover, Hannover, Germany

The aqueous speciation of the U(VI)-H₄SiO₄ system was investigated using electrospray ionisation mass spectrometry (ESI-MS) at pH 3.5 and 5.0. The results reveal the formation of the known UO₂OSi(OH)₃⁺ complex in undersaturated silicate solutions. In addition the formation of oligomeric U-Si and Na-Si complexes were obtained in under- and oversaturated silicate solutions. At pH 3.5 as well as pH 5.0 the formation of the U-hydroxo complex UO₂OH⁺ was identified.

EXPERIMENTAL. For the solution preparation sodium meta-silicate was dissolved in milli-Q water and the pH was adjusted with HClO₄ and NaOH to 3.5 and 5.0. No additional NaClO₄ for ionic strength adjustments were added to avoid clogging of the ESI needle and to reduce artefacts during the measurements. Two different silicate concentrations of 1 × 10⁻³ (undersaturation with respect to SiO_{2,am}) and 5 × 10⁻³ M (oversaturation) were used with a fixed uranyl(VI) concentration of 1 × 10⁻⁵ M. The measurements were performed with a Velos Pro Orbitrap Elite (Thermo Fisher Scientific Inc.) using a Nanospray Flex source.

RESULTS. In the absence of silicates in solution at pH 3.5 the signals of the free uranyl "UO₂⁺⁺" were obtained at an m/z ratio of 270.04 (Fig. 1). Hence, reduction of U^{VI}O₂²⁺ to U^VO₂⁺ takes place as a result of collision with other gas molecules in the ESI process.^[1]

Moreover, the formation of the hydroxo complex UO₂OH⁺ can be seen already at pH 3.5 with different amounts of water at m/z 287.04, 305.05, and 323.06 attached.

Furthermore, the spectrum is dominated by signals from [Na(NaClO₄)_n]⁺ chains (n = 1–9) associated with different quantities of H₂O, reflecting the natural abundance of the two chlorine isotopes ³⁵Cl (75.75 %) and ³⁷Cl (24.24 %) (Fig. 1, gray). Small signals of UO₂OSi(OH)₃⁺ (Fig. 1, green) can be found in the mass spectrum which can be related to the measurement of artefacts produced by the ESI-needle.

In the presence of silicates under the solubility limit of amorphous silica additional signals in the m/z ratio 400–800 can be obtained in the mass spectrum (Fig. 2, top). The signal for UO₂OSi(OH)₃⁺ at 365.02, 383.03, and 401.04 (in green) with different amounts of water show a significant increase in comparison to the blank, revealing the formation of the expected U(VI) complex in the presence of silicates. Especial-

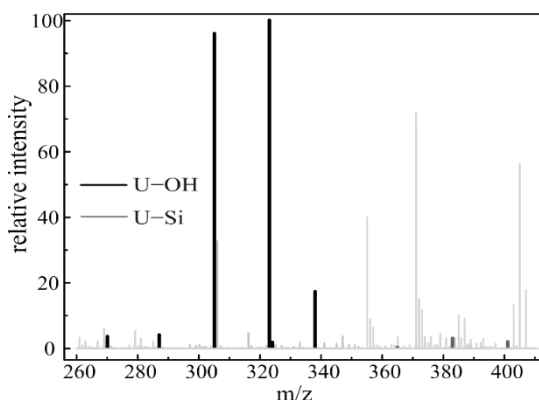


Fig. 1: Mass spectrum of a uranyl(VI) reference solution in absence of silicate at pH 3.5 with [U(VI)] = 1 × 10⁻⁵ M, m/z = 260–410. The abbreviation U-OH in the figures stands for free uranyl(VI) and uranyl(VI)-hydroxo species.

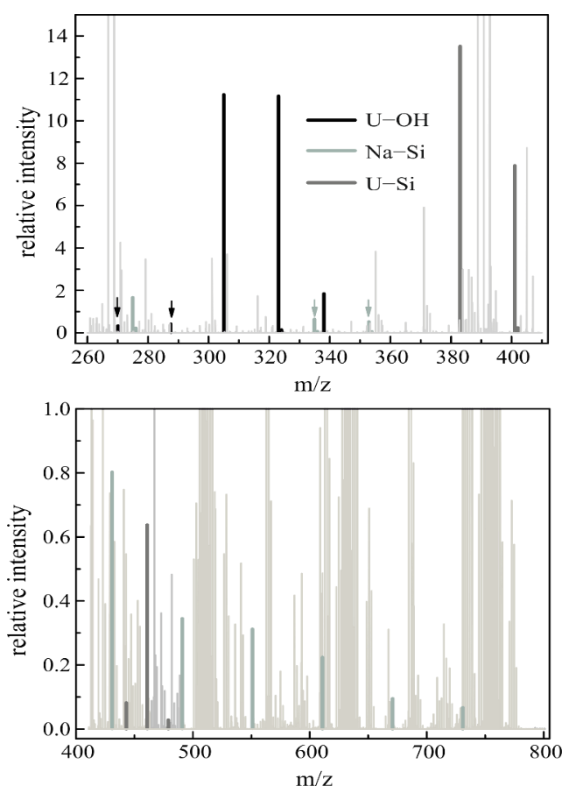


Fig. 2: Mass spectra of an uranyl(VI) silicate solution at pH 3.5 with [U(VI)] = 1 × 10⁻⁵ M, [Si] = 1 × 10⁻³ M, m/z = 260–410 and m/z = 400–800.

ly at higher m/z ratios, additional signals appear, which can be assigned to oligomeric Na-Si up to 10 silica units as well as a dimeric U-Si complex (in olive). In a moderately oversaturated silica solution, the signals at higher m/z ratio become more pronounced and U-Si complexes up to 4 silica units can be determined in the mass spectrum (Fig. 2, bottom). The ratio between monomeric and polymeric species in solution observed in the ESI-MS approach shifted from 16 to 5 at these mild oversaturation conditions of 5 × 10⁻³ M. Silica reference samples without uranyl show a similar formation of oligomeric Na-Si species.^[2] Vercouter *et al.* also identified the oligomerisation of silica units in the Eu-Si system.^[3]

These results clearly show that silica oligomerisation already occurs in moderate oversaturated solutions and has to be taken into account in metal complexation studies with aqueous silicates.

[1] Spears, K. G. *et al.* (1972) *J. Chem. Phys.* **56**, 2562–2566.

[2] Lösch, H. *et al.* (2020) *Environ. Int.* **136**, 105425.

[3] Vercouter, T. *et al.* (2008) 4th annual workshop proceedings of the integrated project "Fundamental Processes of Radionuclide Migration", (6th EC FP IP FUNMIG) November 24–27, 2008, Karlsruhe, Germany.

Extraction of molybdenum by bis(2,4,4-trimethylpentyl)phosphinic acid (Cyanex 600) – Radiotracer technique vs. ICP-OES

T. Helbig,¹ A. Mansel

¹Helmholtz Institute Freiberg for Resource Technology, Freiberg, Germany

Molybdenum is mainly used in steel alloys, such as stainless, high-strength or high-temperature steels. In most of its applications, Mo is hardly substitutable.^[1] In order to secure a constant supply of Mo, the recovery from primary and secondary resources needs to be adapted to the increasing complexity of the materials. The background of these investigations is the solvent extraction (SX) of low concentrated Mo from complex aqueous solutions.^[2] The active component of the applied reagent “Cyanex 600” is bis(2,4,4-trimethylpentyl)phosphinic acid. Radiotracer technique (RTT) using ^{99m}Mo was applied to confirm the results obtained by inductively coupled plasma optical emission spectroscopy.

EXPERIMENTAL. *SX experiments:* Equal volumes of aqueous and organic phase were mixed in PP centrifuge tubes for 60 min using an overhead shaker (Heidolph Reax 2). The pH was measured with a Mettler Toledo pH electrode (InLab Micro).

RTT: ^{99m}Mo was eluted from a ^{99m}Tc radionuclide generator using 1 M NaOH and doped to the aqueous Mo solutions. Gamma spectroscopy was used to determine the 740 keV gamma emission in the organic and the aqueous phases which allowed the direct calculation of the distribution coefficient.

ICP-OES: The aqueous phase was analyzed before and after the phase contact using an Analytik Jena ICP-OES (Plasma-Quant PG9000). Matrix adaption was performed using H₂SO₄, Na₂SO₄ or (NH₄)₂CO₃, respectively. The Mo concentration was determined with the spectral lines at 202.030 nm and 203.844 nm. The distribution coefficient was calculated from mass balance.

RESULTS. The advantage of RTT over ICP-OES is the possibility to directly analyze the distribution of Mo between the organic and the aqueous phase without additional preparation. The comparisons of RTT and ICP-OES show that the results are very similar in terms of Mo extraction (Fig. 1: Maximum extractability at pH ≈ 2; Fig. 2: Negative influence of sulfate concentration) and stripping (Fig. 3: Quantitative stripping at pH >7). A slight deviation can only be noticed for the Mo stripping at pH <5. These results demonstrate that RTT can be used to determine the Mo distribution in SX processes and that the concentrations obtained by ICP-OES with matrix adaption are reliable.

ACKNOWLEDGEMENTS. The authors thank Stefanie Schubert for the ICP-OES measurements and Dr. Norman Kelly for his support and helpful discussions.

[1] Espinoza, L. T., Erdmann, M. (2018) *r⁴-Rohstoffprofil: Molybdän.*

[2] Helbig, T. et al. (2018) Proceedings of Hi-Tech Metals '18, Cape Town.

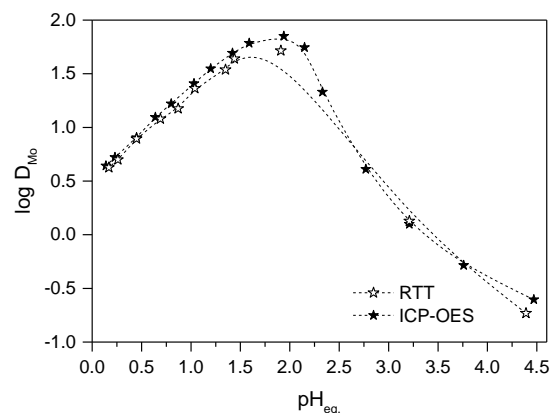


Fig. 1: pH dependence of the distribution coefficient of Mo(VI); $c_{\text{initial}} = 10 \text{ g L}^{-1} \text{ Mo}$, 0.3 M Na₂SO₄, 0.2 M Cyanex 600 in kerosene.

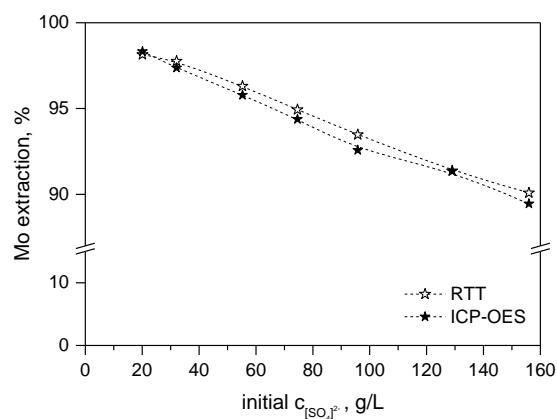


Fig. 2: Influence of the initial sulphate concentration on the extraction of Mo(VI); $\text{pH}_{\text{eq}} = 1$, $c_{\text{initial}} = 10 \text{ g L}^{-1} \text{ Mo}$, 0.3 M Cyanex 600 in kerosene.

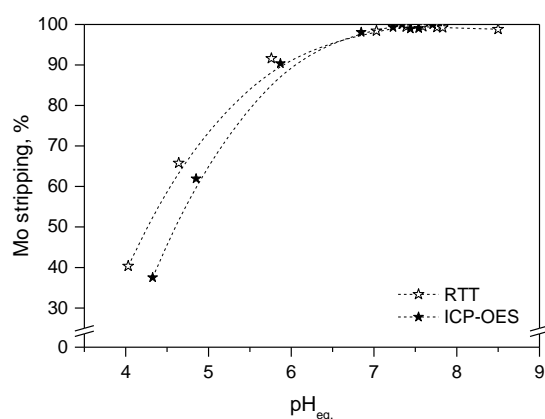


Fig. 3: pH dependence of stripping of Mo(VI) with (NH₄)₂CO₃; 0.3 M Cyanex 600 in kerosene loaded with 10 g L⁻¹ Mo(VI).

Production and purification of n.c.a. ^{48}V at the Leipzig cyclotron for extraction studies

A. Mansel, K. Franke

In Europe is a very high need for critical and strategic metals (e.g. Cr, V, Mo, Nb). The recycling of iron-chromium slags is a promising alternative for the supply of such metals. Therefore, new approaches using specific chemical and physical processes are investigated for recovering such metals from slags. One approach is the use of the liquid-liquid extraction technique. Here, radiotracers offer the unique opportunity to study and optimize the complex extraction procedure. The radionuclide ^{48}V can be used as an isotopic tracer for the elucidation of the vanadium liquid-liquid extraction. Aim of this study was to produce this radionuclide at the Leipzig cyclotron facility and to establish the radiochemical target processing providing n.c.a. (no carrier added) ^{48}V .

EXPERIMENTAL.

Production at the cyclotron: The irradiation of ~140 mg titanium foil at the cyclotron was done by the nuclear reaction $^{nat}\text{Ti}(p,n)^{48}\text{V}$ ($\sigma_{\text{max}} \sim 400 \text{ mbarn}$) (Fig. 1).^[1]

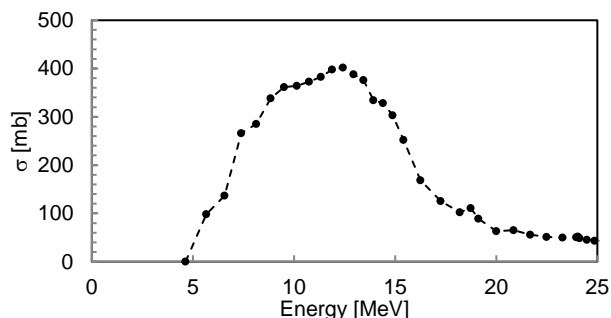


Fig. 1: Cross section of the nuclear reaction $^{nat}\text{Ti}(p,n)^{48}\text{V}$.^[1]

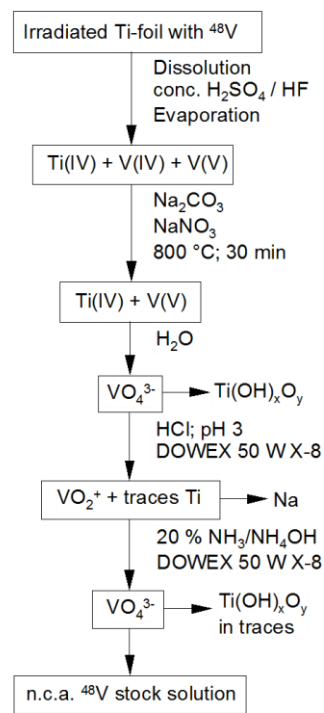
The proton energy E_p was 12 MeV at a current I_p of 22 μA . The beam time was $t_{\text{beam}} = 2 \text{ h}$. At the end of the bombardment (EOB) an activity of 245 MBq was measured. The half-life of ^{48}V is 15.97 d. The radioactive signal was measured at an gamma energy of 984 keV (99.97%).^[2] The decay of the by-product ^{47}V ($T_{1/2} = 32.6 \text{ min}$) was realized overnight.

Separation of the radionuclide ^{48}V (Fig. 2).^[3]

The Ti-foil was dissolved in conc. H_2SO_4 /conc. HF. After evaporation, an alkaline decomposition with Na_2CO_3 / NaNO_3 at 800 °C for 30 min was performed. After multiple dissolving steps with water the soluble species VO_4^{3-} and $\text{VO}_3(\text{OH})^{2-}$ were received. The insoluble species TiO_2 , $\text{TiO}(\text{OH})_2$ and $\text{Ti}(\text{OH})_4$ were separated by centrifugation. After evaporation, the V-species were dissolved with 10^{-3} M HCl (pH3). Cation exchange with DOWEX 50 W X-8 was performed at pH3 for Ti^{4+} and VO_2^+ and the sodium was separated. V was eluted as VO_4^{3-} with 20% ammonia. The Ti remains as hydroxide on the ion exchanger (separation of traces Ti).

γ -spectrometry: A HPGe-detector ORTEC GEM15180-P) was used together with a DSPEC 502 system (ORTEC) for γ -spectrometry measurements.

RESULTS. The radiochemical yield of the separation process is $95\% \pm 8\%$. The radiochemical purity of the ^{48}V was proven by γ -spectrometry (Fig. 3). The γ -spectrum shows 4 prominent peaks at 511 keV (annihilation), 944.13 keV, 983.53 keV and 1,312.1 keV, which are characteristic for ^{48}V . No other radionuclidic impurities were detected. With the established method, ^{48}V is available as a highly sensitive isotopic



95 % \pm 8 % Radiochemical yield

Fig. 2: Separation scheme for the separation of n.c.a. ^{48}V from an irradiated titanium target.

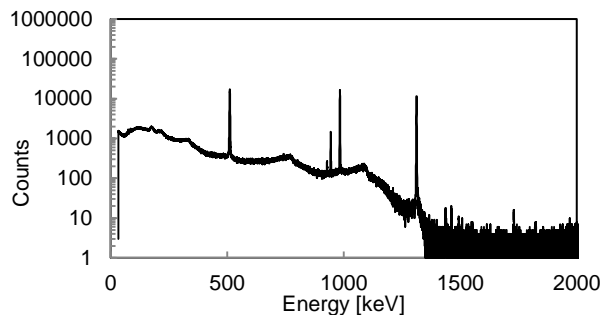


Fig. 3: γ -spectrum of ^{48}V after the separation.

tracer (n.c.a.) for the investigation of the vanadium liquid-liquid extraction from iron-chromium slags down to a detection limit of 8 fM ($\sim 0.4 \text{ pg L}^{-1}$). ^{48}V can be used as a tracer for extraction studies concerning recycling of V and as a radiotracer for GeoPET ($\beta^+ = 49.9\%$).

ACKNOWLEDGEMENTS. We gratefully acknowledge funding by European Union's Horizon 2020 Research and Innovation program „CHROMIC“ under Grant Agreement No°73047.

- [1] Zarie, K. et al. (2006) *Radiochim. Acta* **94**, 795–799.
- [2] NuDat 2.7 database (2015), <https://www.nndc.bnl.gov/nudat2/>.
- [3] Bonardi, M. L. et al. (2005) *J. Radioanal. Nucl. Chem.* **263**, 23–28.

First-time production of Na-22 at the cyclotron Cyclone 18/9 in Leipzig

K. Franke, A. Mansel

Positron emission tomography (PET) is used for non-destructive quantitative visualization of transport processes of inert and reactive species in porous materials including rocks. This task requires suitable radiotracers with appropriate half-life and decay properties. Na-22 is considered as a conservative tracer for the analysis of low-permeability rocks composed mainly of sheet silicates.

Na-22 ($T_{1/2} = 2.6018$ a) decays by the emission of positrons with an average energy of 215.54 keV (90.326 %). The resulting annihilation radiation of 511 keV (180.76 %) is only disturbed by 1,274.537 keV (99.94 %) γ -radiation.^[1] Possible production routes of Na-22 are Ne-22(p,n), Na-23(p,pn), Mg-24(d, α) and Mg-25(p, α). The cross sections of the nuclear reactions are shown in Fig. 1. Considering the abundance of the isotopes in target material with a natural composition, the Mg-24(d, α) reaction is the preferential production route of Na-22.

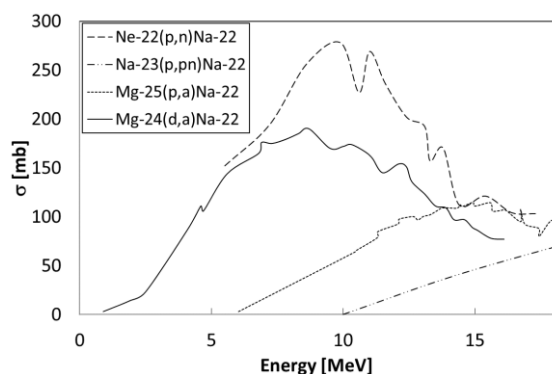


Fig. 1: Cross section of the nuclear reactions Ne-22(p,n),^[2] Na-23(p,pn),^[3] Mg-24(d, α),^[4] and Mg-25(p, α).^[5]

EXPERIMENTAL. Cyclotron: The cyclotron Cyclone 18/9 (iba) provides deuterons with an energy of 9 MeV with a maximum current on target of 40 μ A. **Target station:** The irradiation of solid targets was done at the COSTIS solid target irradiation station (iba) at port 4 of the cyclotron, mounted directly at the yoke. The target is cooled with helium on the front and water on the back side.

Windows: 25 μ m Ti foil was used as vacuum window, 125 μ m Al foil was used as entrance window of the target capsule.

Target capsule: The target was hold in a target capsule. It consists of an Al-backing and Al-cover which served as window holder (Fig. 2).

Target: Metallic Mg (foil Alfa Aesar, diameter of 10 mm, thickness of 250 μ m) with natural isotopic composition was used as target material.

Irradiation: Irradiation was done with deuterons with an initial energy of 9 MeV and a current on target of 8 μ A for 500 μ Ah.



Fig. 2: Target capsule (from left to right: Al backing, Mg foil, Al foil, cover).

γ -spectrometry: A HPGe-detector ORTEC GEM15180-P) was used together with a DSPEC 502 system (ORTEC) for γ -spectrometry measurements.

RESULTS. One day after end of bombardment (EOB), the target capsule was opened and measured with γ -spectrometry (Fig. 3, blue spectrum). Na-22 was identified by means of the 1,274.54 keV γ -emission (Fig. 3: peak2) and the proportional annihilation radiation (511 keV: 180.76 %) (Fig. 3: peak1). Additional peaks were identified at 1,368.67 keV, 1,732.1 keV and 2,243.1 keV (Fig. 3: peak 3, 4, 6). These peaks belong to Na-24.^[6] The γ -emission at 1,368.67 keV is part of decay of Na-24. 1,732.1 keV and 2,243.1 keV are the detected double escape and single escape events of the 2,754.1 keV (99.85 %) γ -emission of Na-24 in the detector. The 2,754.1 keV peak itself is above the observed energy range in the spectrum and not part of it.

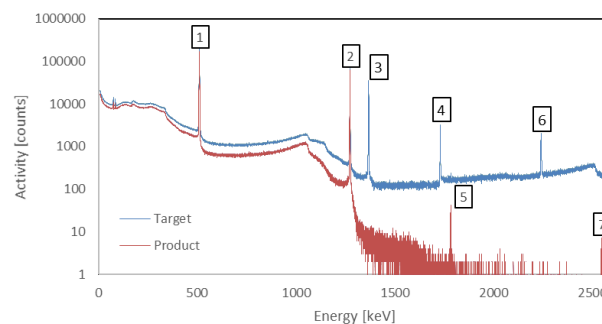


Fig. 3: γ -spectrum 1 d after EOB (blue) and 14 d after EOB (red).

Na-24 was formed by the nuclear reaction Mg-26(d, α). Mg-26 is with 11 % part of target material. Na-24 has a half-life of 15,031 h. The γ -spectrometry measurements were repeated after $> 10 \times$ the half-life of Na-24 (Fig. 3, red spectrum). The characteristic peaks for Na-24 vanish from the spectrum. Two other peaks at 1,758.6 keV and 2,548.8 keV (Fig. 3: peak 5, 7) become visible. These peaks belong to the sum peaks of peak 1 and 2 and to $2 \times$ peak 2. After the decay of Na-24, a radionuclide pure product was obtained, which can be processed and utilized for PET application.^[7]

- [1] Shamsuzzoha Basunia, M. (2015) *Nucl. Data Sheets* **127**, 69–190.
- [2] Takacs, S. et al. (1996) *Appl. Rad. Isotop.* **47**, 303–307.
- [3] Meadows, J. W. et al. (1951) *Phys. Rev.* **83**, 47–49.
- [4] Roehm, H. F. et al. (1969) *J. Inorg. Nucl. Chem.* **31**, 3345–3356.
- [5] Cohen, B. L. et al. (1954) *Phys. Rev.* **96**, 1617–1620.
- [6] Firestone, R. B. (2007) *Nucl. Data Sheets* **108**, 2319–2392.
- [7] Rightmire, R. A. et al. (1957) *Int. J. Appl. Rad. Isot.* **2**, 274–279.

The new single-crystal diffractometer at ROBL

C. Hennig, A. Ikeda-Ohno,¹ T. Radoske, S. Findeisen,² J. Claussner,² J. Exner, D. Naudet, N. Baumann, A. C. Scheinost

¹Japan Atomic Energy Agency, Sector of Fukushima Research and Development, Collaborative Laboratories for Advanced Decommissioning Science, Fuel Debris Science Group, Tokai-mura, Naka-gun, Ibaraki, Japan; ²HZDR, Mechanical Engineering, Dresden, Germany

This report summarizes the technical features of the new single-crystal diffractometer at the Rossendorf Beamline (ROBL) at the European Synchrotron Radiation Facility (ESRF) in Grenoble/France.

The Rossendorf Beamline undergoes currently a refurbishment which includes the installation of two diffractometers: a 6-circle diffractometer and a single crystal diffractometer with a large Pilatus 2D detector.^[1] The single crystal diffractometer is based on a design developed by SNBL.^[2] Measurements at the single crystal diffractometer comprise small and large molecule crystallography, mainly structures with heavy metals. The diffractometer is equipped with a Pilatus3 X2M detector (Dectris), with a pixel size of $172 \times 172 \mu\text{m}$ and up to 250 Hz and 0.95 ms readout time. The detector is mounted on a support frame (Instrument Design Technology Ltd.), which allows its rotation on a goniometer (Huber) as well as lateral and vertical movements (see Fig. 1). The support frame and the goniometer support are placed on an optical bench in order to ensure accurate and reproducible positioning with respect to the beam.

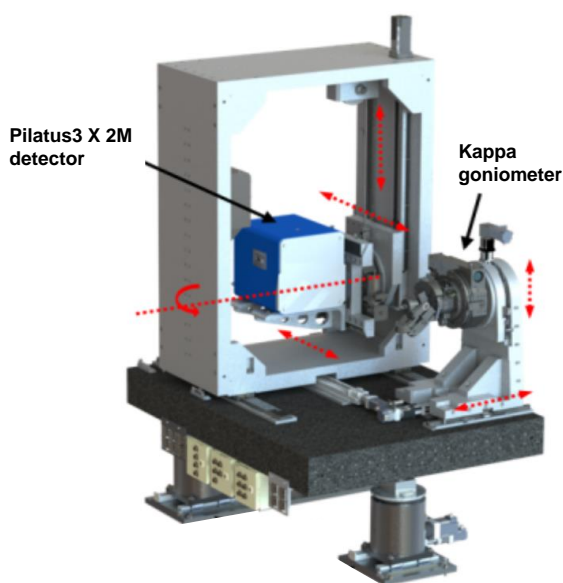


Fig. 1: View on the single crystal diffractometer. Possible movements of the support frame and the goniometer support are indicated with red arrows.

The sample-to-detector distance can be varied between 140 and 600 mm. Three goniometers are available to mount single crystals: a Huber Kappa goniometer 512.410, an Arinax Kappa goniometer MK3, and a Huber uniaxial goniometer 410. The available energy range of 5–35 keV supports measurements with anomalous dispersion. *In situ* experiments on single crystals and powder samples are possible. Diffraction measurements can be combined simultaneously with XANES and XRF spectroscopy using a Vortex X90 CUBE silicon drift detector with FalconX1 processor. A beam conditioning unit in front of the sample (Fig. 2) comprises an entrance slit, a small ionization chamber to monitor the incoming beam intensity, and a collimation unit to suppress parasitic scattering. The long-distance microscope K2 (Infinity Photo-Optical GmbH) permits optical sample alignment. A macro camera serves to align additional sample environ-

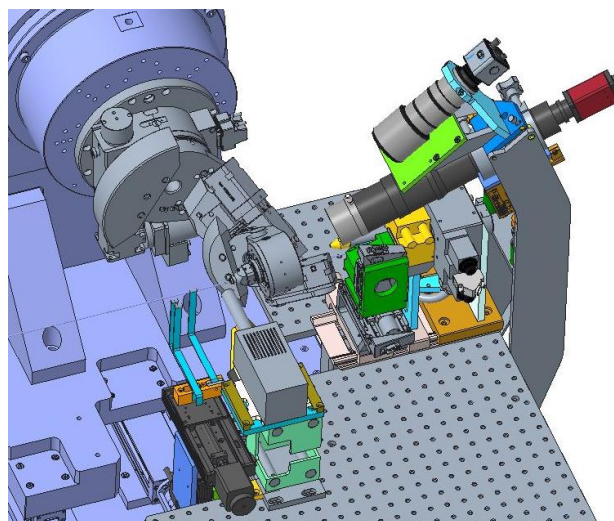


Fig. 2: Beam conditioning unit, goniometer support with Huber Kappa goniometer, and Vortex X90 CUBE silicon drift detector.

ments like the heat chamber HTK 1200N (Anton Paar, up to $1,200^\circ\text{C}$). The setup includes a cryo cooler (80–400 K) (Oxford Cryosystems Ltd). The diffractometer is operated with the GUI-based software Pylatus.^[2]

Figure 3 shows the result of a feasibility test performed with beam from the old experimental setup before the EBS upgrade of the ESRF.^[3] The U(IV) sample was housed in a sealed Kapton capillary for radioprotection. The excitation energy was set to 17,038 eV to reduce the sample absorption and to avoid fluorescence arising from the uranium L_3 absorption edge at 17,162 eV. The sample was mounted on the Huber uniaxial goniometer 410, which restricted the accessible space to 80 % of the full scattering sphere. The observed data were extracted with the CrysAlis software.^[4] The structure of $\text{UCl}_2\text{Salen}(\text{MeOH})_2$ was solved with Olex2 with an R1 of 2.99 %.^[5]

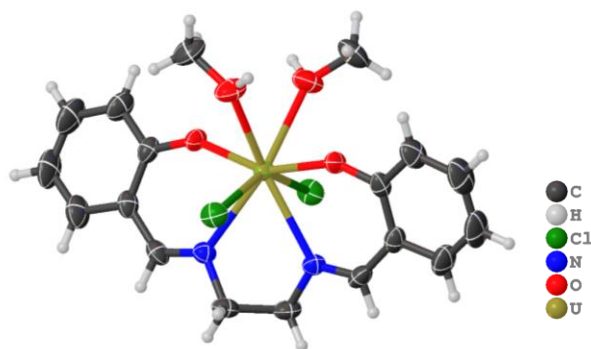


Fig. 3: Molecule picture of $\text{UCl}_2\text{Salen}(\text{MeOH})_2$, space group $P 4_32_12$.

- [1] Hennig, C. et al. (2019) Report HZDR-096, p. 62.
- [2] Dyadkin, V. et al. (2016) *J. Synchrotron Rad.* **23**, 825–829.
- [3] <https://www.esrf.eu/about/upgrade>.
- [4] Meyer, M. (2019) CrysAlisPro 40. *ECM32 Abstract booklet*, 750.
- [5] Dolomanov, O. V. et al. (2009) *J. Appl. Cryst.* **42**, 339–341.

SCIENTIFIC CONTRIBUTIONS (PART II)

Long-Lived Radionuclides & Transport Phenomena in

GEOLOGICAL SYSTEMS

The influence of bentonite colloids on Np(V) transport in granitic rock

O. Elo,¹ P. Hölttä,¹ P. Kekäläinen,¹ M. Voutilainen,¹ N. Huittinen

¹University of Helsinki, Department of Chemistry, Radiochemistry, Helsinki, Finland

In the present study Np(V) (NpO₂⁺) uptake by crystalline granitic rock and the role of stable and mobile bentonite colloids on the migration of Np(V) has been investigated.

Bentonite is considered as potential buffer material in several spent nuclear fuel repository concepts due to its low hydraulic conductivity, swelling ability, and high specific surface area. At low ionic strengths following *e. g.* a glacial period, stable and mobile colloids may form from the buffer material. Therefore, studies involving bentonite colloids in various host rock environments and their role as mobilizers of colloid-borne radionuclides with flowing ground water should be investigated in detail. In the present work we have conducted batch sorption studies of Np(V) sorption on crystalline granitic rock (Kuru grey granite) and MX-80 bentonite colloids under various conditions. Additional granite column experiments have been conducted in the presence and absence of colloids and the resulting Np(V) breakthrough curves have been modeled using an analytical solution of advection–matrix diffusion equation.^[1]

EXPERIMENTAL. Colloid solutions for the batch sorption experiments were prepared from the MX-80 bentonite under constant rotation for 7 days followed by colloid separation from the solid by centrifugation (12,000 g/20 min). The granite material was crushed and sieved, and the size fraction ranging from 0.1 to 1 mm in diameter was used. The final colloid concentration in the batch sorption samples ranged from 0.06 to 0.8 g L⁻¹ depending on the experiment, while a granite concentration of 40 g L⁻¹ was used. The Np(V) concentration and ionic strength were kept constant at 10⁻⁶ M and 10 mM NaClO₄, respectively. The granite column experiments were conducted under flowing water conditions (flow rates of 0.3 mL h⁻¹ and 0.8 mL h⁻¹) in a 28 cm long drill core column with a diameter of 1.4 cm. A conservative tracer (³⁶Cl) was used to determine flow properties of the drill core column. 2 × 10⁻⁴ M Np(V) was injected into the 10 mM NaClO₄ feed solution with a pH of either 8 or 10, in the absence and presence of 0.08–0.32 g L⁻¹ bentonite colloids.

RESULTS. The obtained pH-edges for 10⁻⁶ M Np(V) sorption on 0.8 g L⁻¹ bentonite and 40 g L⁻¹ granite under ambient conditions are presented in Fig. 1.

Sorption on the colloidal material was found to be pH-independent speaking for a large fraction of outer-sphere electrostatic attachment of Np(V) on the colloids. For crushed granite, pH dependent sorption can be seen above pH7, however, the maximum sorption percentage (80%)

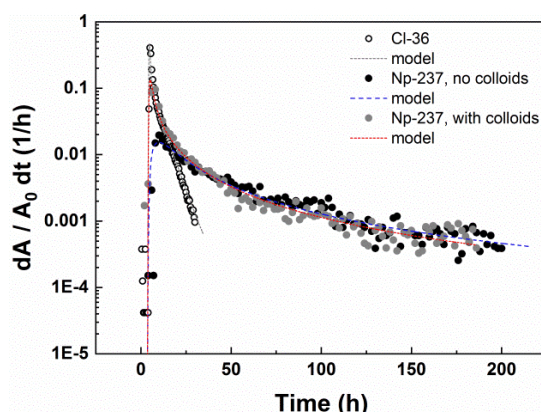


Fig. 2: Experimental and modelled ³⁶Cl and ²³⁷Np(V) breakthrough curves in the absence and presence of bentonite colloids at a flow rate of 0.8 mL h⁻¹ and pH = 10.

and K_d (100 L kg⁻¹) remain rather low even at pH > 10. The experimental and modelled breakthrough (BT) curves at 0.8 mL h⁻¹ and pH = 10 for ³⁶Cl and ²³⁷Np in the presence and absence of bentonite colloids are presented in Fig. 2. The higher tail of the BT curves for Np(V) in comparison to our conservative tracer implies that Np(V) sorbs on the granite surface. The obtained K_d values from our modelled curves, however, are between 10 and 200 times lower than the K_d values obtained in our batch sorption experiment on the crushed granite material. This may be related to the difference in the specific surface area of the intact granite column and the crushed material. However, other factors such as a high reversibility of the Np(V) sorption reaction under flowing water conditions may also influence the uptake behavior. The detachment of Np(V) under flowing water conditions was shown in our previous study for Np(V) sorption on montmorillonite purified from the MX-80 bentonite material.^[2] When comparing the BT curves in the absence and presence of bentonite colloids, an almost identical BT behavior can be deduced. This implies that the influence of colloids on the Np(V) mobility is almost negligible under the chosen experimental conditions. With respect to conditions in a crystalline host-rock repository environment where the pH ranges from circumneutral to slightly alkaline, and the groundwater is mildly oxidic, *e. g.* due to the glacial melt waters, migration of Np(V) is likely to occur due to low sorption onto granite.

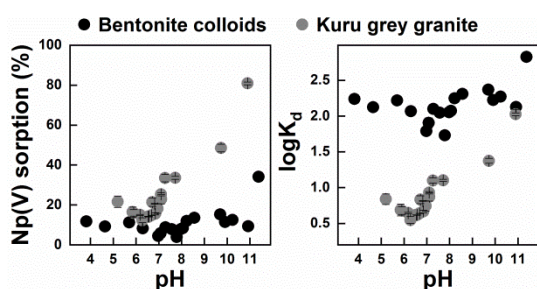


Fig. 1: Np(V) uptake by MX-80 bentonite colloids and crushed granite as a function of pH under ambient atmosphere. Results presented as sorption percentage (left) and as log K_d (K_d in L kg⁻¹) (right).

[1] Elo, O. *et al.* (2019) *Appl. Geochem.* **103**, 31–39.

[2] Elo, O. *et al.* (2017) *Geochim. Cosmochim. Acta* **198**, 168–181.

Insight into the mechanism of U(VI) sorption on graphene oxide

L. Amidani, A. S. Kuzenkova,¹ A. Y. Romanchuk,¹ A. L. Trigub,² A. V. Talyzin,³ S. N. Kalmykov,¹ K. O. Kvashnina

¹Department of Chemistry, Lomonosov Moscow State University, Moscow, Russia; ²Kurchatov Institute, Moscow, Russia; ³Department of Physics, Umeå University, Umeå, Sweden

To elucidate the interaction mechanism of graphene oxide (GO) with U(VI), we studied the sorption of U(VI) on GO sheets having different functional groups and density of defects.^[1] The insight on the local structure of sorbed U obtained by spectroscopic techniques reveals that GO's interaction with U(VI) takes place on small holes in the GO sheets and not at edges or on top of GO sheets. Promoting high defect densities and high concentrations of carboxyl groups is hence the best strategy to optimize GO-based sorbents for radionuclide waste treatment.

Graphene oxide (GO) demonstrated high sorption ability towards various cations of radionuclides and heavy metals. However, little is known about the chemistry behind the cation-GO interaction, a knowledge that could guide the technological improvement of GO's sorption capabilities. Different synthesis methods for GO result in different abundance of defects and different functional oxygen-containing groups. We performed a systematic study of the sorption capabilities *vs.* composition of GO and investigated the local structure of sorbed U(VI) with Extended X-ray Absorption Fine Structure (EXAFS) and High-energy Resolution Fluorescence-Detected X-ray Absorption Near-Edge Structure (HERFD XANES) spectroscopies. Data analysis was based on DFT optimized structures of U sorbed at different locations of the GO sheet. The results are consistent with the adsorption of U(VI) favored by carboxyl groups and taking place in small holes of the GO sheet.

EXPERIMENTAL. GO obtained by Hummers's (HGO), Brodie's (BGO) and Tour's (TGO) methods have different structures and were selected for sorption experiments. EXAFS and HERFD XANES at U L₃ edge were acquired on the Rossendorf Beamline (BM20) at the ESRF. DFT model structures for U(VI) sorbed on GO in different parts of the GO sheet were calculated with Quantum ESPRESSO and used for EXAFS analysis and FDMNES simulations of HERFD XANES.^[2]

RESULTS. Pristine GO's sheets were measured with XPS and FTIR to characterize the defect densities and the nature of functional groups associated with the synthesis method used. The abundance of C=O bonds, estimated from XPS, correlates with holes and small defects. The results indicate that HGO and TGO have more carboxylic groups compared to BGO which shows nearly complete absence of double bonded oxygen. The dependence of the sorption capacity of GO on pH as well as in the presence of competing cations were measured for the three GOs. In both cases experimental results show that HGO and TGO have higher affinity towards radionuclides.

To understand where U(VI) binds to the GO sheet, EXAFS and HERFD XANES at U L₃ edge were measured. Both spectroscopies found that the position of sorbed U is sample independent. The analysis of the first coordination shell of EXAFS shows that U(VI) is adsorbed in the form of uranyl ion. Comparing U–O and U–C distances extracted from EXAFS with the DFT models reveals that U(VI) preferential-

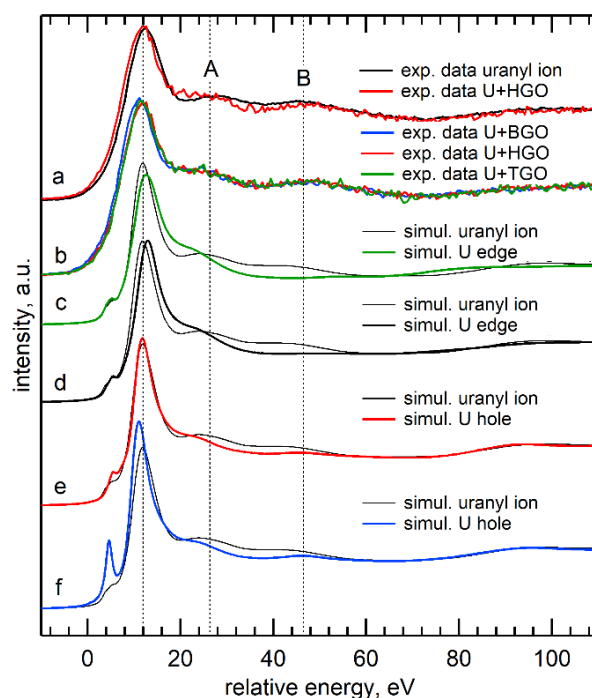


Fig. 1: U L₃ edge HERFD XANES data of uranyl ion compared to U(VI) sorbed onto HGO (a); U in BGO, HGO and TGO (b). FDMNES simulations of uranyl reference (black thin line) compared with simulation of U at the edge of a flake (c–d) U in a hole of GO (e–f).

ly interacts with carboxyl groups located in the holes of the sheet rather than at the edge.

The HERFD XANES spectra for the three GO samples are shown in Fig. 1 together with reference spectrum of uranyl ions prior to sorption. The three samples have the same spectral shape and present significant differences compared to uranyl ion prior to sorption, especially in the post-edge region. To assess which local configuration of U corresponds to the HERFD XANES spectra, we performed XANES simulations with the FDMNES code. We considered DFT optimized structures with U bound at the edge or in holes of the GO sheet. Results in Fig. 1 show that the simulated spectra for both configurations reproduce the general features of the data. However, only the models featuring U in a hole reproduce correctly the intensity ratio and the energy position of the post-edge features relative to the main absorption edge. In accordance with EXAFS results, HERFD XANES confirms that U(VI) is adsorbed in holes of the GO sheet and not at the edges.

In the perspective of using GO as a sorbent for radionuclides waste treatment, efforts have to be devoted to the optimization of the density of defects and of carboxyl functional groups to maximize the U(VI)-GO interaction.

[1] Kuzenkova, A. S. *et al.* (2019) *Carbon*, in press.

[2] Bunao, O. and Joly, Y. (2009) *J. Phys.: Condens. Matter* **21**, 345501–345511.

Sorption of trivalent REEs (Eu, La, Lu, Nd, Y) and actinides (Cm) onto K-feldspar

J. Neumann, H. Brinkmann, S. Britz,¹ M. Stockmann, T. Stumpf, M. Schmidt

¹Gesellschaft für Anlagen- und Reaktorsicherheit (GRS) gGmbH, Braunschweig, Germany

Here, we study the sorption of trivalent rare earth elements (REEs: Eu, La, Lu, Nd, Y) and the actinide Cm on K-feldspar. Batch sorption experiments are combined with Time-Resolved Laser Fluorescence Spectroscopy (TRLFS) to quantify and gain a fundamental understanding of sorption processes on the molecular level. The results show, that the sorption behavior of the investigated trivalent metal ions is very similar. Sorption occurs as outer sphere (OS) complex at pH < 5. Additionally, two species could be identified as an inner sphere (IS) complex (pH ≥ 5) and its hydrolysis form (pH ≥ 7). The species distribution for a broad pH range (2–12) was obtained. The results will be used to develop a robust surface complexation model (SCM) using a generic approach, covering a broad range of experimental conditions.

The mobility of radionuclides (RN) in the environment is strongly influenced by sorption processes. In a repository for radioactive waste, the host rock is the main barrier to reduce transport of RN. One potential host rock type for a repository, which is considered in many countries (e.g. Sweden, Finland, and Germany), is crystalline rock, e.g. granite. In this study we investigate sorption of RN on one main component of granite, feldspars. The trivalent rare earths are often used as analogues for the trivalent actinides, e.g. Am and Cm. Here, we combine quantitative batch experiments with molecular level investigations using TRLFS to describe the sorption process and test the applicability of this analogy. The results will then be used to develop a SCM and to expand the data base for the Smart-K_d concept.^[1]

EXPERIMENTAL. For batch experiments, samples of 3, 10, 12.5 g L⁻¹ K-feldspar (<21 μm) in 1–100 μM Eu, La, Lu, Nd, and Y at an ionic strength of 0.01, 0.1 M NaCl or NaClO₄ (pH 2–12) were prepared under atmospheric conditions. After shaking for 24h, the samples were centrifuged and the remaining metal concentration was measured using ICP-MS. For TRLFS measurements, the Cm concentration was adjusted to 1 μM. Excitation was performed 396.6 nm for Cm using a pulsed Nd:YAG-OPO laser system Powerlite Precision II 9020 Laser, coupled with a PANTHER EX OPO Continuum.

RESULTS. Sorption edges of Eu, La, Lu, Nd, and Y on K-feldspar are plotted in Fig. 1. Constant, low sorption is detected for pH < 5. The amount of sorption in this pH range depends on ionic strength, indicating OS sorption. A stark increase in sorption was observed between pH 6 and 7, leading to complete sorption at pH ≥ 7.5. At higher pH, sorption remains constant at ~100%. For high metal concentrations (100 μM), surface precipitation cannot be excluded at high pH. The emission spectra of the Cm samples show a strong red shift with increasing pH, indicating the formation of an IS sorption complex. Peak deconvolution shows two species besides the Cm aquo ion (593.8 nm, FI: 1.0). The first species occurs at pH > 5 at a band position of 599.0 nm (FI: 1.65), which indicates an IS sorption complex. A second species was observed at pH ≥ 7 at 602.5 nm (FI: 1.48), with the same luminescence lifetime as species 1. Therefore, we conclude that the second species is the hydrolyzed form of the IS complex. Luminescence lifetimes could only be analyzed qualitatively due to quenching effects, induced by Fe and

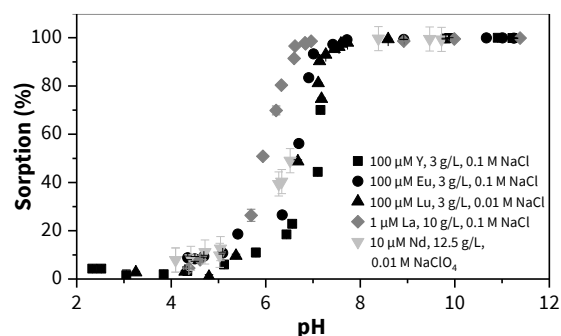


Fig. 1: Sorption edges of Eu, La, Lu, Nd, and Y on K-feldspar under atmospheric conditions.

Mn impurities in the natural mineral. An additional species was observed at very high pH with a peak position of ~607 nm, but its contribution to the species distribution is only minor.

The obtained species distribution is displayed in Fig. 2. For pH < 5, only the Cm aquo ion is detected, confirming that the low amount of sorption is caused by OS sorption. From pH ≥ 5, the formation of the IS complex is observed. This result is in very good agreement with the increase of sorption obtained in the batch experiments at the same pH. At near neutral pH, the hydrolysis of the IS species begins.

In the next step, the batch sorption and species distribution data will be used for the development of a SCM to obtain thermodynamic data for sorption of trivalent lanthanides and actinides on K-feldspar.^[2]

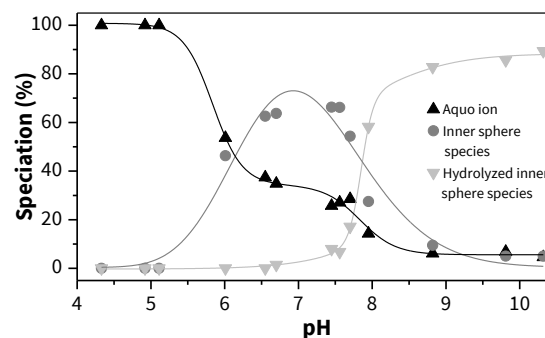


Fig. 2: Species distribution of 1 μM Cm in 3 g L⁻¹ K-feldspar under inert conditions obtained by peak deconvolution of the Cm spectra.^[2]

[1] Stockmann, M. et al. (2017) *Chemosphere* **187**, 277–285.

[2] Neumann, J. et al. (2020), in preparation.

Spectroscopic analysis of the ^{99}Tc removal by synthetic pure pyrite

D. M. Rodríguez, N. Mayordomo, A. C. Scheinost, V. Brendler, K. Müller, T. Stumpf

^{99}Tc is a fission product of high concern for nuclear waste management due to its long half-life (2.14×10^5 a) and the high mobility of TcO_4^- , its most stable compound under aerobic conditions. Fe(II) minerals have shown a remarkable ability to immobilize ^{99}Tc . We performed batch experiments to study the ^{99}Tc removal from solution by synthetic pure pyrite and used X-ray absorption spectroscopy, XAS, to determine the molecular mechanisms involved. Pyrite removes Tc quantitatively from water in a wide pH range through the incorporation of Tc(IV) into magnetite (pH 10) and the formation of Tc(IV)-Tc(IV) dimers sorbed on hematite (pH 6).

EXPERIMENTAL. All experiments were performed under N_2 atmosphere. Pure synthetic pyrite purchased from Alfa Aesar ($2.0 \text{ m}^2 \text{ g}^{-1}$ SSA, $\text{pH}_{\text{iep}} = 7.9$) was characterized by powder XRD and Raman microscopy. For the batch experiments suspensions with $1.3 \pm 0.2 \text{ g L}^{-1}$ of pyrite in Milli-Q water were used. Table 1 summarizes the experimental conditions for all the experiments carried out. Tc concentration in solution was measured by liquid scintillation counting, LSC. X-ray absorption spectroscopy, specifically X-ray absorption near edge structure, XANES, and extended X-ray absorption fine structure, EXAFS, was performed on samples at pH 6 and 10 containing 600 and 1,000 ppm of Tc.

Tab. 1: Experimental conditions of the ^{99}Tc sorption experiments.

Experiment	$[\text{Tc(VII)}]_0$ (M)	pH	Time (days)
Kinetics	5×10^{-6}	3.5–10.5	1–42
pH effect	5×10^{-6}	3.5–10.0	1–42
Isotherm	2×10^{-7} – 2×10^{-3}	6.0 / 10.0	14

RESULTS. Figure 1 shows the pH effect on the ^{99}Tc removal by pyrite during 42 days. At pH > 5.5, 97–100% Tc removal from solution was reached after 1 day, whereas at pH < 5.5 the Tc retention kinetics were significantly slower, being complete only after 35 days. This is explained by the higher solubility of pyrite at pH 4.5 determined by ICP-MS (not shown) as Tc(VII) reduction by Fe^{2+} in solution is not kinetically favored.^[1]

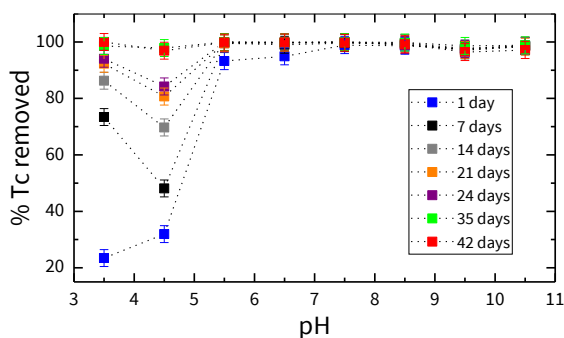


Fig. 1: pH effect on the $^{99}\text{Tc(VII)}$ uptake by pyrite at different contact times.

Figure 2 presents the K-edge XAS spectra of the pyrite samples after interacting with Tc for one month under N_2 atmosphere. Samples 1 and 2 contain 600 and 1,000 ppm of Tc respectively at pH 6; samples 3 and 4 contain 600 and 1,000 ppm of Tc respectively at pH 10.

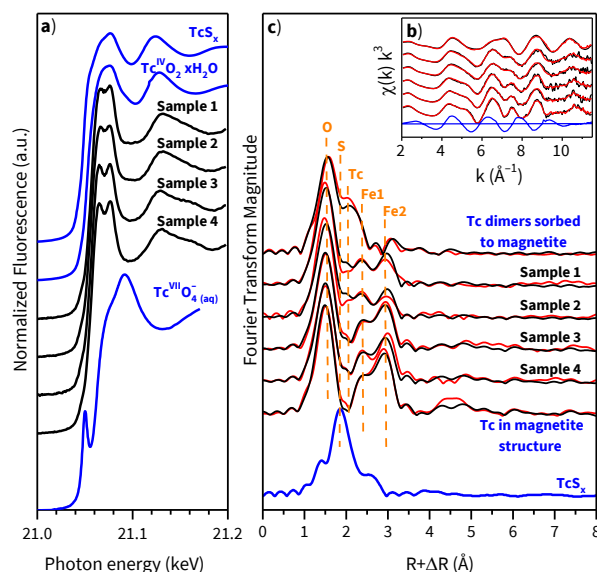


Fig. 2: Tc-K edge XAS spectra of Tc sorbed on pyrite. XANES (a), k^3 -weighted EXAFS spectra (b), Fourier-transform magnitude (c). Black lines represent the experimental data; the red lines in (b) and (c) represent their ITFA reconstruction with two principal components. Reference spectra not used for ITFA are shown in blue.

The XANES spectra indicate that Tc is fully reduced to Tc(IV) (< 2% of Tc(VII)) and that it is prevalently coordinated to oxygen and not to sulfur in all four samples.

EXAFS spectra of the four samples could be reconstructed with two principal components (ITFA analysis [2]), indicating that Tc occurs in two local structures depending on the pH. Adding selected reference spectra to ITFA of the four samples,^[3,4] we found that Tc(IV) replacing Fe at the octahedral site in magnetite is one of the two components. This species prevails at pH 10, with magnetite evidently formed from pyrite by the Tc/Fe redox reaction.

ITFA could then be used to extract the spectrum of the second component. This species prevailing at pH 6 was elucidated as a dimeric Tc(IV)–Tc(IV) inner-sphere sorption complex at a secondary iron oxide phase. By scanning electron microscopy and Raman microscopy we identified this phase as hematite (not shown). Thermodynamic calculations confirmed formation of hematite at pH < 7.5 and of magnetite at pH > 7.5 (not shown).

ACKNOWLEDGEMENTS. Funding from the German Federal Ministry of Economic Affairs and Energy (BMWi) is acknowledged (02E11607B). We thank Jörg Rothe and Kathy Dardenne from the KARA Synchrotron Radiation Source at KIT for their help during the XAS measurements.

- [1] Cui, D. *et al.* (1996) *Environ. Sci. Technol.* **30**, 2259–2262.
- [2] Roßberg, A. *et al.* (2003) *Anal. Bioanal. Chem.* **376**, 631–638.
- [3] Yalçıntaş, E. *et al.* (2016) *Dalton Trans.* **45**, 17874–17885.
- [4] Saeki, M. *et al.* (2012) *Inorg. Chem.* **51**, 5814–5821.

⁹⁹Tc retention promoted by Fe^{II}-Al^{III}-Cl layered double hydroxide

N. Mayordomo, D. M. Rodríguez, A. Rossberg, H. Foerstendorf, K. Heim, A. C. Scheinost, V. Brendler, K. Müller

The removal of Tc by Fe^{II}-Al^{III}-Cl layered double hydroxide (LDH) has been studied by batch experiments, *in situ* attenuated total reflection Fourier-transform infrared (ATR FT-IR) and X-ray absorption spectroscopy (XAS). Tc is quantitatively removed by Fe^{II}-Al^{III}-Cl LDH from solution, especially under low ionic strengths. The Tc retention is predominantly due to the reductive immobilization of Tc^{VII} to Tc^{IV}, while anion exchange of Tc^{VII}O₄⁻ contributes only little (<1%).

LDHs are commonly known as “cationic clays” and they sorb anions mainly by anion exchange,^[1] allowing for their interaction with the highly mobile Tc^{VII}O₄⁻, which is the most stable Tc species under oxidizing conditions. In addition, the LDH selected contains Fe^{II} that potentially immobilizes Tc by reduction of Tc^{VII} to Tc^{IV}, whose main species are generally low soluble.

EXPERIMENTAL. All experiments were performed in a N₂ glove box (O₂ <0.5 ppm). Fe^{II}-Al^{III}-Cl LDH was synthesized by co-precipitation of AlCl₃ and FeCl₂ at pH9. For batch sorption studies, LDH suspensions (0.5 g L⁻¹) were exposed to 5 μM Tc^{VII}O₄⁻. *In situ* IR experiments were carried out as reported earlier.^[2,3] XAS experiments were performed at the Tc K-edge with samples prepared at various pH (4.5, 6 and 9.5) containing 600 ppm Tc under N₂ or normal atmosphere conditions.

RESULTS. Figure 1 shows the Tc uptake by Fe^{II}-Al^{III}-Cl LDH as a function of ionic strength ranging from 0 to 0.1 M at three different pH values. At pH 6 and pH 9.5, Tc was quantitatively removed, regardless of the ionic strength, whereas Tc removal increased with decreasing ionic strength at pH 4 suggesting outer-sphere complexation or ion exchange.

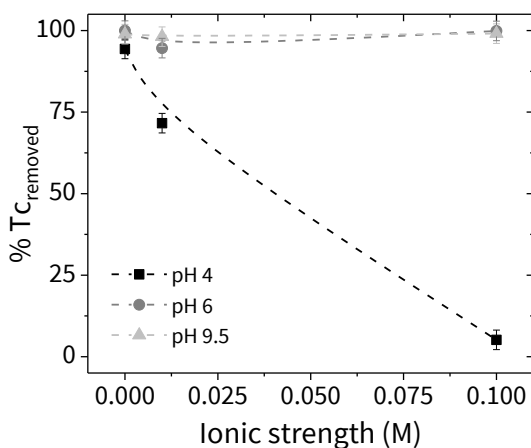


Fig. 1: Tc retention as a function for various ionic strengths.

To identify the immobile Tc species formed at the LDH phase, we carried out ATR FT-IR (data not shown) and XAS (Fig. 2) measurements.

The IR spectrum of aqueous Tc^{VII}O₄⁻ showed a band at 903 cm⁻¹ representing the stretching mode ($\nu_3(\text{TcO}_4)$) of the tetrahedral anion. This band was also observed at nearly the same frequency (901 cm⁻¹) during the *in situ* IR sorption experiment of Tc^{VII}O₄⁻ onto LDH. With respect to the low band intensity and the high reversibility reflected by the IR spectra of desorption experiments, an anion exchange mecha-

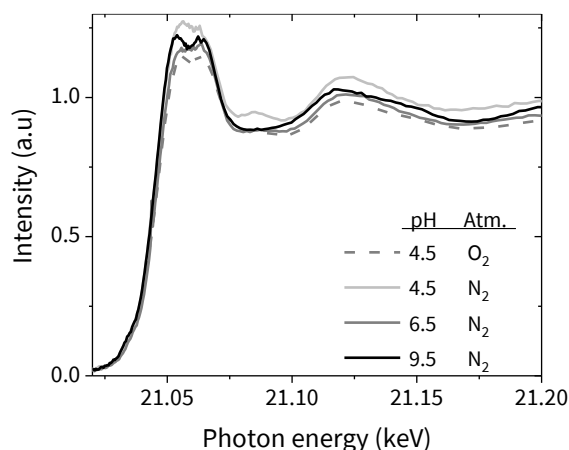


Fig. 2: Tc-K edge XANES spectra of Tc sorbed (600 ppm) on Fe^{II}-Al^{III}-Cl LDH under different pH and atmosphere conditions.

nism or the formation of an outer-sphere complex is suggested.^[3]

The spectra recorded for X-ray absorption near edge structure (XANES) spectroscopy showed a double peak in all samples, independent of the pH or atmospheric conditions (Fig. 2). The absence of the typical pre-edge absorption peak of Tc^{VII} revealed that the oxidation state in the samples was Tc^{IV}.^[4] Consequently, the anion exchange derived from IR data represented either a small contribution or a process kinetically driven at short sorption times. Thus, the main retention mechanism of Tc^{VII} by Fe^{II}-Al^{III}-Cl LDH is the reductive immobilization where Tc^{IV} is formed eventually.

The analysis of the EXAFS (extended X-ray absorption fine structure) spectra revealed two Tc^{IV} species at the Fe^{II}-Al^{III}-Cl LDH phase.^[5] Both species were characterized by the interaction with hematite, which is formed as result of the oxidation of Fe^{II}-Al^{III}-Cl LDH. One component results from monodentate inner-sphere complexation of Tc^{IV} dimers on hematite, whereas the second component from Tc^{IV} incorporation into the hematite structure. More information about the geometries obtained for those components are described in this annual report.^[5]

ACKNOWLEDGEMENTS. This work was financed by the VESPA II project (02E11607B), funded by the German Federal Ministry of Economic Affairs and Energy (BMWi). We thank Jörg Rothe and Kathy Dardenne from the Karlsruhe Research Accelerator (KARA) at KIT for their help during the XAS measurements.

[1] Forano, C. *et al.* (2013) in *Developments in Clay Science*, p. 745–782, Elsevier, Amsterdam.

[2] Müller, K. *et al.* (2009). *Environ. Sci. Technol.* **43**, 7665–7670.

[3] Foerstendorf, H. *et al.* (2012). *J. Colloid Interface Sci.* **377**, 229–306.

[4] Yalçıntaş, E. *et al.* (2016). *Dalton Trans.* **19**, 17874–17885.

[5] Rossberg, A *et al.* (2019) this report, p. 16.

On the chemistry and diffusion of hydrogen in the interstitial space of layered crystals h-BN, MoS₂, and graphite

Y. An,^{1,2} A. Kuc,² P. Petkov,³ M. Lozada-Hidalgo,⁴ T. Heine^{2,5}

¹Universität Leipzig, Leipzig, Germany; ²HZDR, Institute of Resource Ecology, Leipzig, Germany; ³University of Sofia, Sofia, Bulgaria; ⁴University of Manchester, Manchester, U.K.; ⁵Technische Universität Dresden, Dresden, Germany

Recent experiments have demonstrated transport and separation of hydrogen isotopes through the van der Waals gap in hexagonal boron nitride and molybdenum disulfide bulk layered materials. However, the experiments cannot distinguish if the transported particles are protons (H⁺) or protium (H) atoms. Here, reported are the theoretical studies, which indicate that protium atoms, rather than protons, are transported through the gap. First-principles calculations combined with well-tempered metadynamics simulations at finite temperature reveal that for h-BN and MoS₂, the diffusion mechanism of both protons and protium (H) atoms involves a hopping process between adjacent layers. This process is assisted by low-energy phonon shear modes. The extracted diffusion coefficient of protium matches the experiment, while for protons it is several orders of magnitude smaller. This indicates that protium atoms are responsible for the experimental observations. These results allow for a comprehensive interpretation of experimental results on the transport of hydrogen isotopes through van der Waals gaps and can help identify other materials for hydrogen isotope separation applications.

The aim of this study is to answer two open questions regarding the experiment of Hu *et al.*,^[1] namely, (i) which hydrogen species are transported within the layered materials (protons or protium (H) atoms) and (ii) what is the diffusion mechanism of these species in the interstitial space between the layers. The results of this study are published.^[2]

NUMERICAL. All calculations were performed using DFT with PBE functional and D3 van der Waals correction, following the approach of Grimme, as implemented in the CP2K 3.0 package. The Quickstep method was employed with GTH pseudopotentials together with DZVP-MOLOPT-GTH-SR basis set for Mo, S, B, C, and N. Hydrogen was treated with the DZVP-all electron basis set and all-electron potential. The plane-wave energy cutoff was set to 360 Ry. All atomic positions and lattice parameters were fully optimized. The setup of well-tempered metadynamics simulations (WTMetaD) simulations and other details are described elsewhere.^[2]

RESULTS. Free-energy barriers and related self-diffusion coefficients calculated using first-principles Born-Oppenheimer WTMetaD simulations demonstrate high mobility of protium in h-BN and MoS₂. In contrast, H⁺ is highly mobile in MoS₂, but has a low self-diffusion coefficient in h-BN. Hydrogen attached to graphite is essentially immobile. The related overall lattice of the layered materials remains intact. Locally, protons bind to N (S for MoS₂), pick an electron from the lattices, and leave a charged site that extends over a few atoms. At low concentration, this charged state would be maintained. Protium binds to B (S for MoS₂) atoms. The transport of both protium and protons follows a zigzag path where the transported species hop between two adjacent layers (see Fig. 1). The probability of such a hopping is strongly increased by the interlayer shear modes that are typical for these materials. Recombination of protium will

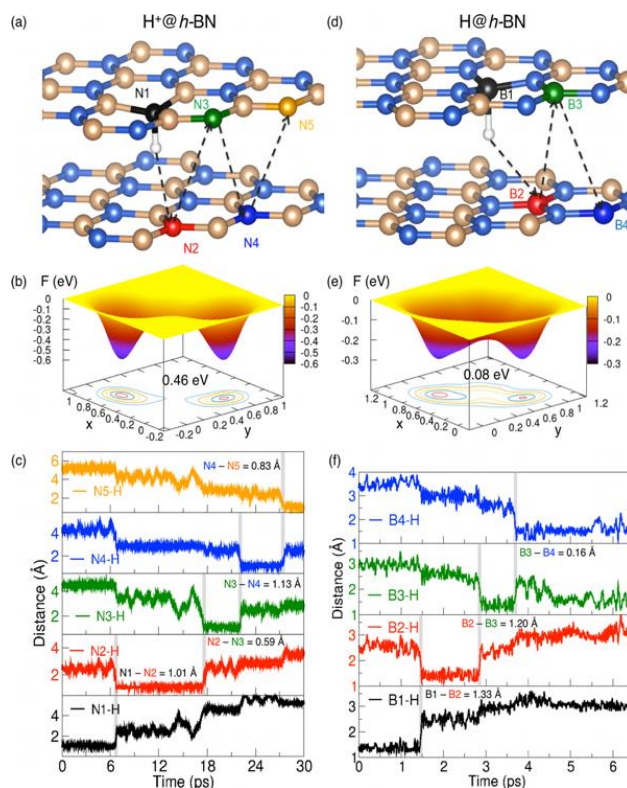


Fig. 1: WTMetaD simulations of H⁺ (a–c) and H (d–f) diffusion in between layers of h-BN. Both species are transported in a zigzag manner between the layers with low free-energy barriers. Transfer paths along the h-BN interstitial space (a, d). Free-energy surface of the H species transfers between layers (b, e). The x- and y-axis correspond to the collective variables, as defined in [2], and the z-axis and color legend refer to the free energy, F (in eV). Change in the bond distances N–H and B–H during the WTMetaD trajectory as function of time (c, f). The vertical gray lines indicate the H or H⁺ jump between the binding sites in neighboring layers as indicated in color in (a) and (d). The N–N and B–B distances indicate the in-plane distance between the neighboring transfer sites (compared with the same distances in the perfect stacking faults: AA' 1.45 Å (staggered stacking), A'B and AB' 0.00 Å (eclipsed stacking)) indicates shearing from AA' toward either A'B or AB' stacking.

always occur, if the species get close to each other, and is avoided only by low concentration and the quasi-2D transport process. Our results should be of interest for hydrogen transport in other layered van der Waals materials, which could be important for applications in hydrogen isotope separation.

ACKNOWLEDGEMENTS. The authors gratefully acknowledge ZIH Dresden for computer time. Y.A. acknowledges China Scholarship Council. Y.A. and A.K. acknowledge Deutsche Forschungsgemeinschaft (DFG) GRK 2247/1 (QM3) for financial support. M.L.H. acknowledges a Leverhulme Early Career Fellowship.

[1] Hu, S. *et al.* (2018) *Nat. Nanotechnol.* **13**, 468–472.
[2] An, Y. *et al.* (2019) *Small*, 1901722–1–7.

Spatially-resolved sorption studies on Bukov diorite

M. Demnitz, K. Molodtsov, A. Schierz, S. Schymura, M. Schmidt, T. Stumpf

Sorption of Eu(III) on diorite from the Bukov Underground Research Facility (URF, CZ) was investigated using Raman-microscopy and μ TRLFS (microscopic time-resolved laser-induced fluorescence spectroscopy). Sorption predominantly occurs on prehnite and apatite with only minor contributions by feldspar and quartz. Luminescence lifetime studies revealed the existence of inner-sphere sorption complexes and incorporation species.

EXPERIMENTAL. Thin sections ($20 \times 20 \text{ mm}^2 \times 150 \mu\text{m}$) were cut and polished from a drill core obtained from the Bukov URF (CZ). The mineralogy of a $3 \times 4 \text{ mm}^2$ area was determined using a Raman-microscope based on the RRUFF database.^[1] The thin section was washed with deionized water and ethanol, after which $[^{152}\text{Eu}] = 0.01 \text{ mM}$ in 0.1 M NaCl at $\text{pH} 7.5$ was sorbed on the surface over seven days. Excess ^{152}Eu was washed off the surface using a 0.1 M NaCl washing solution at $\text{pH} 7.5$. Following, μ TRLFS measurements were performed.

RESULTS. Raman measurements revealed that the Bukov diorite mineral composition is complex, consisting out of feldspar, amphibole, quartz, chlorite, apatite, prehnite, muscovite, titanite, pyrite, and epidote (Fig. 1). Three different regions of interest (A1, A2, A3), each $1 \times 1 \text{ mm}^2$, were measured using μ TRLFS. The Eu(III) luminescence intensity shows the sorption uptake of the different mineral areas (Fig. 2).

High homogeneous luminescence intensities can be seen on apatite and prehnite. In comparison the intensities on feldspar and quartz are far lower, even though feldspar showed the highest uptake in previous studies with granitic rock.^[2] On quartz, luminescence intensities vary strongly often within small distances, indicating varied uptake on the same mineral grain. On feldspar areas higher luminescence intensities are located primarily at the mineral grain boundaries to other minerals. Chlorite and amphibole show almost no luminescence intensity due to the high iron content of those minerals.

Feldspar (plagioclase) shows two existing species derived from luminescence lifetime measurements, similar to previous μ TRLFS investigations on Eibenstock granite.^[2] Shorter lifetimes correspond to inner-sphere complexes with 2 to 3 remaining H_2O bound to Eu(III) while longer lifetimes indicate intrinsic incorporated Eu(III). In comparison to Eibenstock less H_2O remains bound to Eu(III) most likely due to Ca^{2+} being the counter ion in plagioclase and Na^+/K^+ in Eibenstock alkali feldspar. Therefore the higher negatively charged surface is prone to complex Eu(III) stronger. The loading of Eu(III) on diorite feldspar is lower in comparison to studies with Eibenstock granite, most likely due to strong sorption on accessory minerals like apatite and prehnite. Both show high sorption uptake and lifetime studies suggest relatively strong inner-sphere complexation on both minerals. For the safety assessment of nuclear waste disposal in a crystalline host rock, this finding is of great interest, since especially prehnite is a fracture filling mineral in crystalline rocks. It is in direct contact with the water flow path, where in worst case scenarios radionuclides might migrate.^[3-5] However, sorption of radionuclides on prehnite has not yet been studied thoroughly.

The spatially resolved spectroscopic study was able to characterize sorption processes on a heterogeneous material on

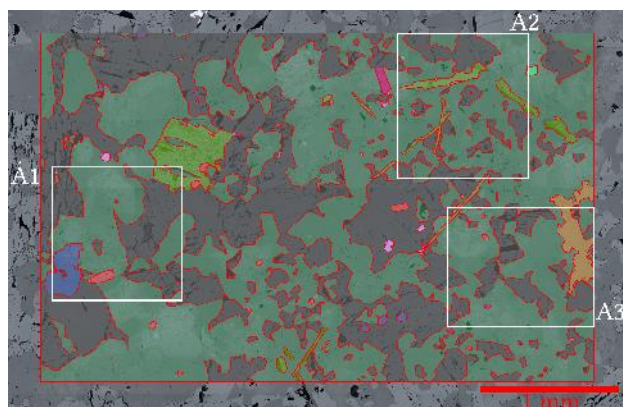


Fig. 1: Mineral composition of an area measured using Raman-microscopy: feldspar, amphibole, quartz, chlorite, apatite, prehnite, muscovite, titanite, pyrite und epidote.

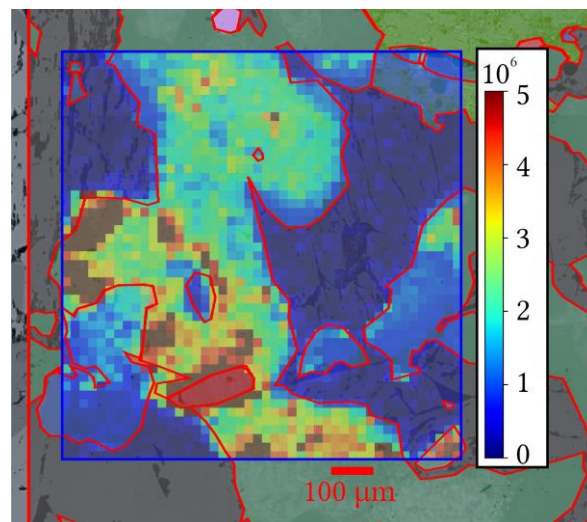


Fig. 2: Luminescence intensity of Eu(III) in A1 on Bukov diorite thin section.

the molecular level. The results show that many aspects influence the sorption behavior, which cannot be assessed in single mineral studies or studies with powdered material. For example, the heterogeneous distribution within single mineral grains or the competitive adsorption on the large number of minerals present simultaneously. These information will have significant impact on our understanding of the migration of radionuclides in the geosphere.

ACKNOWLEDGEMENTS. We gratefully acknowledge the funding provided by the German Federal Ministry of Education and Research (BMBF) (Grant 02NUK053E) and The Helmholtz Association (Grant SO-093) and UJV Rez for providing the Bukov diorite drill core.

- [1] Lafuente, B. *et al.* (2016) *Highlights in Mineralogical Crystallography*, 1–29.
- [2] Molodtsov, K. *et al.* (2019) *Scientific Reports* **9**, 6287.
- [3] Allard, N. *et al.* (1982) Report (Chalmers University of Technology – Department of Nuclear Chemistry).
- [4] Andersson, K. *et al.* (1983) Report (Chalmers University of Technology – Department of Nuclear Chemistry).
- [5] Huber, M. *et al.* (2007) *Geologija* **1**, 1–7.

Flow field characterization in an unaltered granite fracture from the geothermal project Soultz-sous-forets

J. Pingel,¹ J. Kulenkampff, C. Fischer, M. Stoll,² T. Schäfer^{1,2}

¹Institut für Geowissenschaften, Friedrich-Schiller-Universität Jena; ²Institute for Nuclear Disposal, KIT, Karlsruhe, Germany

Comprehension of fluid flow and transport of reactive and inert species in fractured rocks is essential for many applications of geoen지니어ing, in particular for sustainable use of geothermal reservoirs in crystalline rocks. Numerous studies are based on fracture geometry and break-through analysis, but direct observations of these processes are rare, but crucial for the validation of reactive transport modeling (RTM) results. In order to directly characterize the flow field in a granite fracture, we applied positron emission tomography (PET). The results suggest the existence of flow path heterogeneity, thus helping to interpret existing and to improve new simulation calculations.

EXPERIMENTAL. A drill core from the geothermal project Soultz-sous-forets without indications for alteration had been prepared, characterized and analyzed at KIT-INE using μ CT-imaging and break-through curve experiments.^[1] Fluid ports distributed along the fracture section allowed studying the effect of the positions (1, 2, 3) of the input-output dipoles (Fig. 1). Out of these, three different configurations were investigated in this study. We applied positron emission tomography (PET) technique for the analysis of the flow field.^[2]

Although disadvantageous for PET-imaging, we applied high flow rates (6 and 12 mL h⁻¹) corresponding to realistic conditions in the geothermal reservoir. The sample was pre-conditioned with synthetic formation water, and then a 1 mL tracer-pulse labelled with ca 100 MBq ¹⁸F was injected. The propagation of the pulse was imaged with a frame rate of 1 min. From the suite of ca. 60 PET images we reconstructed the flow field (Figs. 2, 3). Details of the procedure are already reported.^[3,4]

RESULTS. An influence of the injection configuration on the shape of the flow field was observed, but exceeded by the impact of fracture topography. We attribute the complex, dissected distribution of the flow field to the combination of aperture and fracture curvature, e.g. flow decreasing with increasing curvature at fixed aperture. Independent from the injection configuration, a considerable portion of the fracture volume is excluded from the flow field and thus only accessible by slow diffusional transport. Overall, the PET data suggest the existence of flow field heterogeneities and channeling that provides critical insight into the transport behavior of fractured rocks. Potential applications include an improved parametrization of numerical approaches.

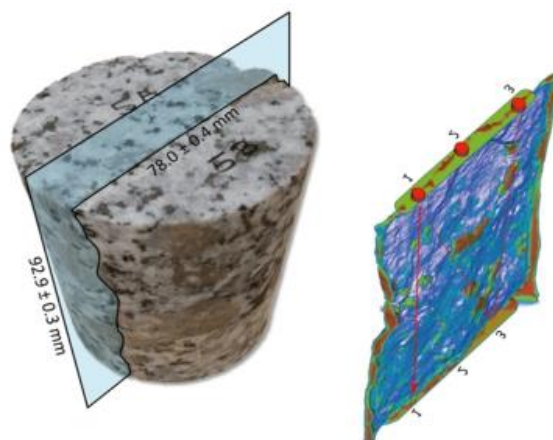


Fig. 1: Sample (photograph taken from [1]) and fracture geometry (from μ CT), also showing the positions of the fluid ports (1-3).

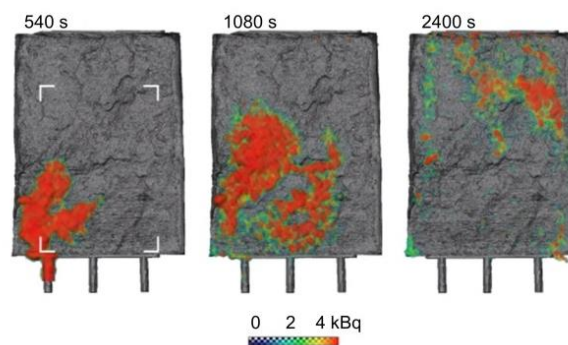


Fig. 2: Three PET-frames out of the sequence of 60 with frame length of 60 s. Although the high frame rate causes images prone to noise, the tracer pattern is clearly traceable (grey: fracture geometry, color: tracer activity).

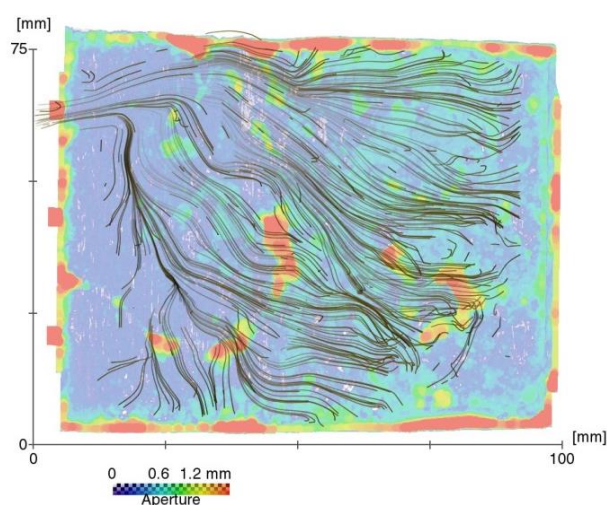


Fig. 3: Streamlines, reconstructed from the suite of PET frames, overlaid on the aperture distribution from μ CT (color coded).

[1] Stoll, M *et al.* (2019) *J. Contaminant Hydrology*, 221, 82–97.

[2] Kulenkampff, J. *et al.* (2016) *Solid Earth* 7, 1217–1231.

[3] Pingel, J. (2019) Master Thesis, Inst. f. Geowissenschaften, FSU Jena.

[4] Pingel, J. *et al.* (2019) Abstract, GeoMünster.

Coupled transport processes across a claystone-concrete interface: results of a combined X-ray CT and PET experiment

J. Kulenkampff, U. Mäder,¹ E. Bernard,¹ A. Jenni¹

¹Institute of Geological Sciences, University of Bern, Switzerland

Interfaces between tight clay materials and cementitious materials (concrete) are studied in the context of deep disposal of radioactive waste. A major motivation is the occurrence of mineral reactions due to chemical gradients with consequences on the pore network porosity and, *via* permeability, the transport of water, solutes, and gas. A thorough understanding of such processes by experimental approaches was one major objective of the Cebama project. In collaboration with the University of Bern, we conducted a study that aimed at insights into the effect of mineralogical-physical changes at such an interface on the transport of water and solutes, and linking mineralogical-physical characterization, X-ray computed tomography, and positron emission tomography (PET).

EXPERIMENTAL. An X-ray transparent core infiltration apparatus was developed at Bern University, maintaining a hydraulic confining pressure and a pressure gradient driving fluid flow over a period of several months.^[1] The pressurized fluid reservoir was lead-shielded for PET tracer application (Fig. 1).

The sample is a 50×50 mm cylindrical subsample from a 14-year-old core sample that was recovered by stabilized drilling from a long-term *in situ* experiment (CI) at the Mont Terri rock laboratory, containing a physically preserved interface between Opalinus Clay and OPC concrete (ordinary portland cement).^[1] The sample was comprehensively characterized using μ CT techniques and high-resolution 2D microscopy methods, SEM/EDX mapping, etc.

During the course of a long-term transport experiment with synthetic claystone pore water, the running experiment was transferred to Leipzig. Here, a portion of the synthetic pore fluid was labelled with ¹²⁴I and monitored with PET over a period of two weeks, while the tracer propagated through the sample.

RESULTS. First results based on 2D interface characterization (SEM/EDX mapping, etc.) and time-resolved 3D μ CT and PET data suggest an initial self-sealing effect of the joint system in the Opalinus Clay, permeation into the diffusion-controlled pore network in claystone and cement matrix, and partial filling of gas-bearing pores. The PET data further suggest (i) preferential flow within the claystone due to joint planes, (ii) spreading of the tracer plume at the clay/cement interface, and some moderate preferential flow across OPC (Fig. 2). The flow rate field – and thus residence times – are estimated from the suite of PET frames (Fig. 3).

Overall, this approach provides new and detailed information of coupled transport processes at the interface of two types of materials, important for nuclear waste management. The successful imaging of both the stationary and the mobile phase offers new applications. Finally, compared to sum parameters, such as tracer breakthrough, there is significantly new information obtained about the localization of flow and the properties of the pore network and its temporal evolution.

ACKNOWLEDGEMENTS. The research leading to these results has also received funding from the European Union's European Atomic Energy Community's (Euratom) Horizon 2020 Programme (NFRP-2014/2015) under grant agreement, 662147 – Cebama

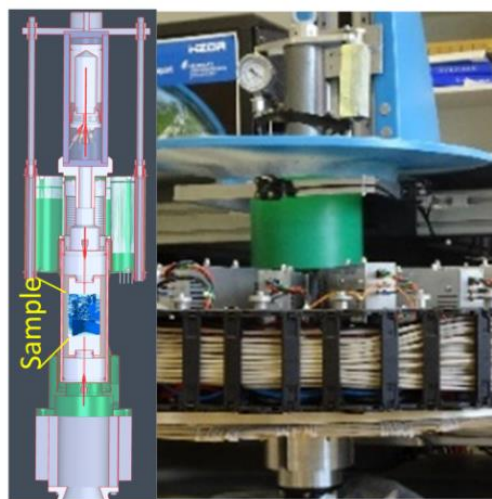


Fig. 1: X-ray transparent pressure vessel for core flow-through experiments with μ CT and PET monitoring, developed at Bern Univ. Longitudinal drawing (left), vessel installed in the tilted PET scanner (right).^[4]

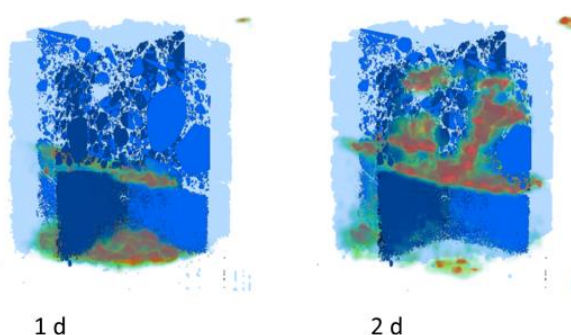


Fig. 2: Overlay of the PET (green-red) and μ CT (blue) images, showing PET frames after one and two days. Lower section: Opalinus clay rock, upper section: OPC concrete.

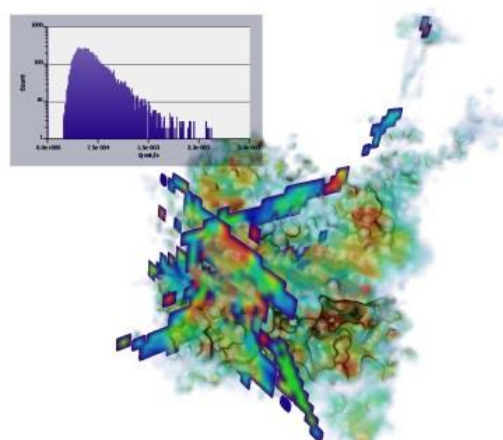


Fig. 3: Flow rate field and magnitude histogram reconstructed from the suite of PET frames. Rate range: 0.1–1.0 $\mu\text{L s}^{-1}$ (blue to red).

- [1] Mäder U. (2018) Geofluids, ID 8198762.
- [2] Mäder, U. *et al.* (2018) *Swiss J. Geosci.* **110**, 307–327.
- [3] Mäder, U. *et al.* (2019) DECOVALEX 2019 Symp. Abstr.
- [4] Kulenkampff, J. *et al.* (2019) *Report HZDR-096*, p. 26.

Dissolution rate maps and rate spectra based on X-ray micro-computed tomography data quantify transport- and surface-controlled rate portions

W.-A. Kahl,¹ T. Yuan, T. Bollermann, W. Bach,^{1,2} C. Fischer

¹Department of Geosciences, Universität Bremen, Bremen, Germany; ²MARUM Center for Marine Environmental Sciences, Universität Bremen, Bremen, Germany

The competing effect of both transport and surface control are responsible for the observed dissolution rates of porous crystalline materials. Mechanistically, the parameters saturation of the ambient fluid and distribution of surface energy control the surface rates. The spatio-temporal heterogeneity of surface rates is analyzed using the rate map and rate spectra concept. In a combined study,^[1] we quantified the dissolution rate variability covering the nm- to mm-scale of dissolving single crystal and polycrystalline calcite samples, using a combined approach of X-ray micro-computed tomography (μ -CT) and vertical scanning interferometry (VSI). Here, we report rate map data based on μ -CT measurements collected during a long-term experiment of several weeks that underscore the concurrent and superimposing impact of surface- vs. fluid flow-controlled rate portions. The impact of fluid flow on reactivity at the mm-scale in the transport-controlled system is confirmed by 2-D reactive transport modeling (RTM). However, current RTM approaches are unable to simulate the impact of heterogeneous surface reactivity.^[1]

EXPERIMENTAL. Polycrystalline marble samples were reacted using 2.2 mMol Na₂CO₃ solution, equilibrated with air to obtain constant pCO₂ at pH 9.2, percolating at a flow rate of 0.05 mL min⁻¹ and 45 bar (4.5 MPa) fluid pressure. The X-ray μ -CT scans were performed using the ProCon CT-ALPHA (FB5, Bremen Univ.). Samples were scanned before and after the dissolution experiment (54 days) with a beam energy of 120 kV, an energy flux of 350 μ A, and using a thin copper filter in 360° rotation scans conducted with a step size of 0.225°. All subsequent processing of volume data was done using Avizo 9.5. Details about the experimental setup and the rate map and rate spectra analysis of this experiment are provided in the literature.^[1,2]

RESULTS. The observed rate ranges for surface-controlled conditions are remarkably consistent over the reaction period but include a variability of about two orders of magnitude (10⁻⁹–10⁻⁷ mol m⁻² s⁻¹; equivalent to the measured rates in units of nm s⁻¹). The sub-mm spatial heterogeneity of low vs. high reactivity surface portions of polycrystalline calcite is clearly below the mean crystal size of several hundreds of micrometers. This suggests the dominant impact of highly-reactive surface portions irrespective of the orientation of larger crystals on the overall surface reactivity. Correspondingly, the overall range of intrinsic reactivity heterogeneity as observed using single crystal material is not further expanded for polycrystalline material. Figure 1 shows the spatial rate distribution and illustrates the combined effect of surface- and transport-controlled conditions. Note, the intrinsic rate heterogeneity is also observed for transport-controlled rate map portions, cf. Fig. 2, FWHM range of the spectra. A simple RTM approach utilized three parameter combinations, according to literature data;^[3] specific surface areas, mean reaction rates: (1) A_{SSA} = 0.19 m² g⁻¹, log Rn = -5.8 mol m⁻² s⁻¹; (2) A_{SSA} = 0.019 m² g⁻¹, log Rn = -6.8 mol m⁻² s⁻¹; (3) A_{SSA} = 0.19 m² g⁻¹, log R = -6.25 mol m⁻² s⁻¹; for modeling the range of measured data. Note the discrepancy of mod-

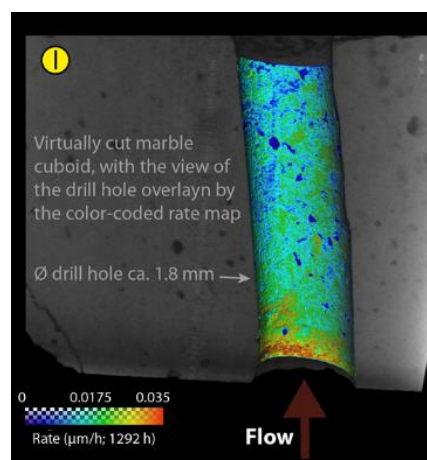


Fig. 1: Visualization of the gradient in the μ -CT-derived reaction rates observed on the calcite surface of a cylindrical channel in a 54 days flow-through experiment. The inlet section of the sample exhibits the highest surface rates (red and yellow colors). Increasing impact of transport-controlled conditions is observed towards the upper section of the percolated cylinder.

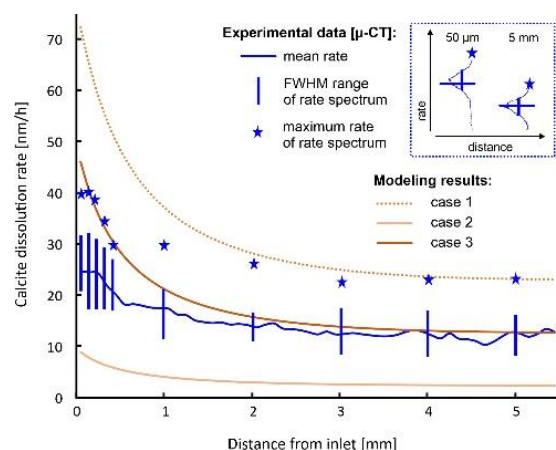


Fig. 2: Comparison of measured dissolution rate data (blue-colored) with results of RTM (orange-colored) using three parameter combinations (cases 1–3) of surface area and reaction rate “constants”.

eled mean rates: While the parameter combination of case 3 describes the observed maximum rates in the experiment close to the inlet, the parameter combination of case 1 simulates the maximum rates close to the outlet. As a general conclusion, numerical reactive transport concepts would benefit from the implementation of a reactivity term resembling the experimentally observed existence of multiple rate components.^[1]

ACKNOWLEDGEMENT. W. B. gratefully acknowledges financial support by DFG, grant no. BA 1605/10-1], C. F. gratefully acknowledges financial support by DFG, grant FI1212-7 as well as by the BMBF, grant 02NUK053B and the Helmholtz Association (Grant SO-093).

- [1] Kahl, W.-A. et al. (2020) *Am. J. Sci.* **320**, DOI: 10.2475/01.2020.03.
- [2] Fischer, C. et al. (2012) *Geochim. Cosmochim. Acta* **98**, 177–185.
- [3] Yuan, T. et al. (2016) *Transp. Porous Media* **114**, 747–775.

Modelling radionuclide transport through a sedimentary rock system with the reactive transport code OpenGeoSys#Phreeqc-3.5.0

M. Stockmann, R. Lu,¹ V. Brendler

¹Helmholtz Centre for Environmental Research—UFZ, Department of Environmental Informatics, Leipzig, Germany

In the framework of the iCross project, the radionuclide transport through the far-field of a repository system has to be simulated with the reactive transport code OpenGeoSys (OGS-6) integrated with PHREEQC-3.5.0 to calculate geochemical reactions.^[1,2] However, there will be unaffordable expensive computational costs for large-scale simulations because of the time and repository scales covered by such predictions: up to one million years and dozens of kilometers. As an effective way to integrate important geochemical processes (e.g. sorption and desorption) at affordable costs, the smart K_d -concept should be implemented in OGS-6.^[3] In a first step, a full reactive transport model was developed based on a well-defined 2D test case for a typical sedimentary rock system in Northern Germany and compared to simulations with the reactive transport code PHAST to verify the OGS-6 model.^[4,5]

MODEL SETUP. To keep the model simple and to reduce the computational effort, a reduced set of chemical components is considered in the test case calculations. Thus, the transport of H^+ , OH^- , Na^+ , Cl^- , Ca^{2+} , dissolved inorganic carbon, and several radionuclides is simulated through an initially saturated column of 20 meters in length and 3 meters in width (Fig. 1), since these geochemical input parameters may strongly influence the sorption capacity of the rock-forming minerals with respect to radionuclides. It is assumed that calcite is present in the entire model domain and may be dissolved in or precipitate from the solution at any time. The influx is held constant at the left side of the column, whereby the chemical composition of the solution changes over time. The right side of the model is open to flow out.

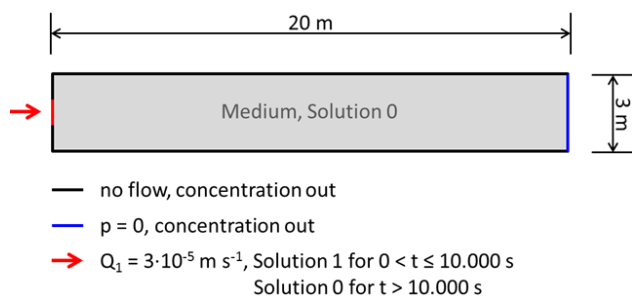


Fig. 1: Model domain with boundary conditions.

The model domain contains a homogeneous medium that owns the reactive surfaces. The hydraulic parameters of the medium are set to typical values for aquifers. The Darcy velocity is $2 \times 10^{-4} \text{ m s}^{-1}$, the porosity 0.2, the dispersion length 0.2m and the diffusion coefficient $10^{-9} \text{ m}^2 \text{ s}^{-1}$. Initially, the model domain is filled with Solution 0 and during the first 10,000 s, the Solution 1 containing additionally radionuclides (Cs, Ra, Ni, Am, Th, Np, U) enters the model domain. After that, Solution 0 flows into the model domain again until the end of the simulation.

RESULTS. The calculations were done step wise: First, a tracer transport was simulated with consideration of the processes advection, diffusion and dispersion. Similar re-

sults were obtained for the flow and tracer calculations and verified the model setup. Second, the transport of radionuclides that underlie sorption and desorption was simulated. The spatial distribution of the different radionuclides is simulated based on following the sequential chemical reactions:

- $Soln_{prev-init-calc} + \text{sorption reaction}$
- $Soln_{cur}$
- $Soln_{cur} + EquilPhase_{cur} + \text{absorbed mass}$

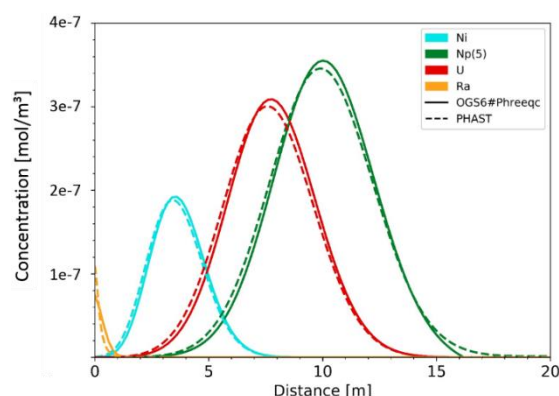


Fig. 2: Spatial distribution of the radionuclides after 500,000 s simulation time.

The spatial distributions after 500,000 s (Fig. 2) reflect a radionuclide-specific retardation effect. Neptunium has the weakest sorption, whose peak lies at a distance of 10m away from the injection boundary. Cesium, Americium and Thorium have the strongest sorption and accumulated nearby the injection boundary (therefore not shown in Fig. 2). For most of the radionuclides, the results of OGS-6 and PHAST agree quite well. In most cases the position of the peak matches reasonably well but its height differs slightly.

ACKNOWLEDGEMENTS. This project is funded by the German Federal Ministry of Education and Research (BMBF) (Grant 02NUK053B) and the Helmholtz Association (Grant SO-093).

[1] Jang, E. et al. (2018) *OpenGeoSys Tutorial III*, p. 103.
 [2] Kolditz, O. et al. (2012) *Environ. Earth Sciences* **67**, 589–599.
 [3] Stockmann, M. et al. (2017) *Chemosphere* **187**, 277–285.
 [4] Noseck, U. et al. (2018) *Report GRS-500*.
 [5] Parkhurst, D. L. et al. (2010) *U.S.G.S. Report 6-A35*, p. 235.

Thermodynamic reference database THEREDA: 9. Solubility of selenate compounds in ternary systems at high ionic strengths

F. Bok

Selenium (with the isotope Se-79 being an important fission product) in its oxidation state +VI is usually highly soluble and therefore very mobile in ground-water. For a correct calculation of the solubilities of alkaline selenate phases at high ionic strengths, the Pitzer ion-ion interaction model is indispensable.

A consistent thermodynamic dataset has been determined for the calculation of selenium compounds' solubility in chloride or sulfate media using the Pitzer ion-ion interaction approach.^[1] In order to be able to apply the data set also to more complex models for realistic final disposal scenarios (hyper-alkaline pH through cement phase dissolution, dissolved inorganic carbonate since ubiquitous in nature), the parameters for describing these influences were added to the data set.

CALCULATION. The experimental solubility data sets of sodium selenates in ternary solutions ($\text{Na}_2\text{SeO}_4\text{-Na}_2\text{CO}_3\text{-H}_2\text{O(l)}$ and $\text{Na}_2\text{SeO}_4\text{-NaOH-H}_2\text{O(l)}$) at various temperatures have been collected from literature.^[2,3] The temperature function's (1) parameters of the Pitzer model binary anion-anion interaction coefficients θ were fitted to these solubility data. For this purpose, the geochemical speciation code PHREEQC was coupled with the parameter estimation software Ucode2014.^[4,5] The thermodynamic database used was THEREDA.^[6] Following this procedure, the obtained data are consistent with the Pitzer model implemented in THEREDA.

$$\theta_{i,j}(T) = A_1 + A_2(T_K - T_{298.15K}) \quad (1)$$

RESULTS. Temperature function's parameters for the interaction coefficients $\theta(\text{SeO}_4^{2-}, \text{CO}_3^{2-})$ and $\theta(\text{SeO}_4^{2-}, \text{OH}^-)$ could be obtained (Tab. 1).

Tab. 1: Temperature function's parameters A_1 and A_2 (Eq. 1) for the binary anion-anion interaction coefficients θ in the chemical systems $\text{Na}_2\text{SeO}_4\text{-Na}_2\text{CO}_3\text{-H}_2\text{O(l)}$ and $\text{Na}_2\text{SeO}_4\text{-NaOH-H}_2\text{O(l)}$.

Anion combination i,j	A_1	A_2	Temperature validity range
$\text{SeO}_4^{2-}, \text{CO}_3^{2-}$	0.02077	-0.0008308	25–50 °C
$\text{SeO}_4^{2-}, \text{OH}^-$	-0.06227	-0.001113	18–25 °C

With this extension of the selenate Pitzer model it is now possible to calculate the solubility of the sodium selenate phases ($\text{Na}_2\text{SeO}_4 \cdot 10\text{H}_2\text{O}(\text{cr})$ and $\text{Na}_2\text{SeO}_4(\text{cr})$) as well as the corresponding solubility changes of the sodium carbonate phases Natron ($\text{Na}_2\text{CO}_3 \cdot 10\text{H}_2\text{O}(\text{cr})$) and Thermonatrite ($\text{Na}_2\text{CO}_3(\text{cr})$) under the complex chemical conditions that might be relevant for the future nuclear waste repository in Germany.

ACKNOWLEDGEMENTS. This work was funded by the BGE with contract number 45162393(8998-3).

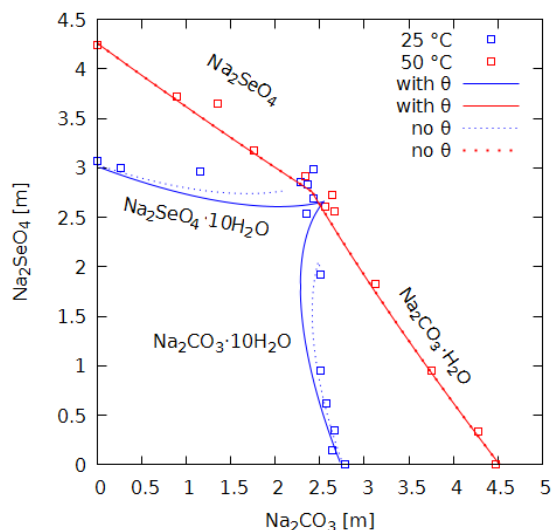


Fig. 1: The ternary system $\text{Na}_2\text{SeO}_4\text{-Na}_2\text{CO}_3\text{-H}_2\text{O(l)}$, Points: experimental data from [2], Solid lines: calculation with the new model parameter, Broken lines: calculation without the θ parameter.

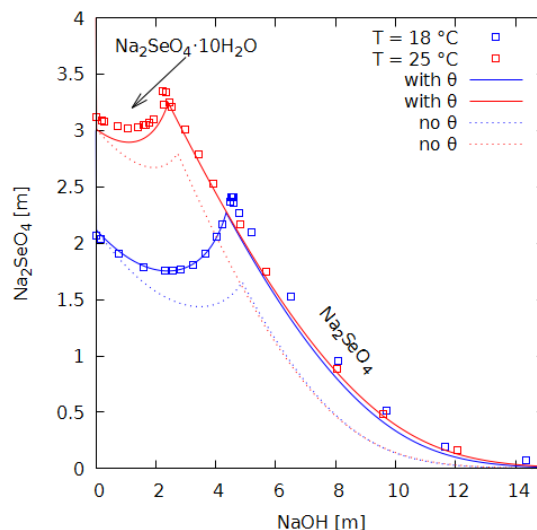


Fig. 2: The ternary system $\text{Na}_2\text{SeO}_4\text{-NaOH-H}_2\text{O(l)}$, Points: experimental data from [3], Solid lines: calculation with the new model parameter, Broken lines: calculation without the θ parameter.

[1] Bok, F. (2019) Report HZDR-096, p. 30.
 [2] Korf, D. M. et al. (1962) *Russ. J. Inorg. Chem.*, **7**, 356–357.
 [3] Windmaisser, F. et al. (1951) *Monatsh. Chem.*, **81**, 287–294.
 [4] Poeter, E. P. et al. (2005) *IGWMC report GWMI 2014-02*.
 [5] Parkhurst, D. L. et al. (2013) *U.S.G.S. report 6-A43*.
 [6] THEREDA – Thermodynamic Reference Database (<http://www.thereda.de>).

Detection of manufactured nanomaterials in complex environmental compartments – An expert review

S. Schymura, H. Hildebrand,¹ K. Franke, C. Fischer

¹Umweltbundesamt, Dessau-Roßlau, Germany

The detection of manufactured nanomaterials in environmental compartments remains a crucial challenge for nanosafety assessment. An expert review of the literature has been conducted to identify relevant methods for nanomaterial detection in complex media in the context of environmental monitoring and a need for action was concluded from the existing body of work. This review serves as a basis for future funding actions by the German Environment Agency (UBA).

Manufactured nanomaterials (NMs) are materials in which 50% or more of the particles have one or more dimensions between 1 nm and 100 nm.^[1] These NMs show interesting properties, e.g. photocatalytical, biocidal, electrical properties, etc. However, the same properties that motivate their use in applications are also reason for concern, as NMs can cause toxic reactions and have mobilities in the environment different from bulk materials of the same elements. Despite considerable scientific efforts, the selective detection of manufactured NMs in environmental compartments is still a very complex and challenging task.

METHODOLOGY. A literature review was performed using predominantly “Web of Science”. More than 150 scientific publications which themselves refer to more than 10,000 sources were evaluated concerning nanoparticle detection methods. The techniques identified through the literature review were evaluated for their capability to detect the relevant NM-related properties such as size, concentration, composition, shape, etc. of arbitrary NMs in environmental samples.^[2]

RESULTS. Evaluating the relevant literature quickly led to the conclusion that while some detection methods will lend themselves more easily towards detection of NMs in a specific compartment, there is no strictly compartment specific method. NMs can be detected with any of the different methods after application of suitable sample preparation techniques. Consequently, a generalized method for NM detection in environmental samples would consist of standardized sampling procedures followed by an extraction step that serves to largely remove the complex matrix, followed by a size fractionation step which would then lead into a multi-method analysis depending on the desired information depth (Fig. 1). An all-encompassing method that allows for the detection and identification as well as measurement of the concentration of NMs without prior

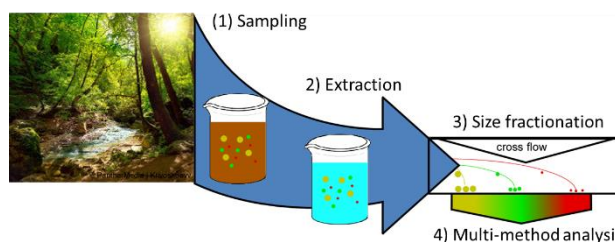


Fig. 1: Scheme of general workflow for NM detection in environmental samples.

knowledge/specification on what to expect, i. e. the detection of unspecified NMs in an environmental monitoring scenario, would need to provide information about NM size, concentration, composition, and shape. An overview of the different techniques that can be used to detect these different properties of NMs is given in Tab. 1.

The need for action for the establishment of routine environmental monitoring of manufactured NMs is thus the development, validation and coupling of suitable extraction, pre-sorting and if necessary pre-concentration procedures, as well, as analysis techniques. A general scheme consists of:

- (i) validated sampling procedures for the different environmental compartments and NMs
- (ii) validated extraction techniques to separate NMs or specific NMs (e. g. organic vs. inorganic) from the matrix
- (iii) validated size separation techniques
- (iv) a multi-method analysis which provides information about NM size, concentration, composition and shape.

One promising combined approach would consist of: CPE, AF⁴, MALS and sp-ICP-TOF-MS.

Techniques such as (radio-)isotopic labeling may provide valuable independent reference measurements for such procedure development.

ACKNOWLEDGEMENTS. This report was conducted on behalf of the German Environment Agency (Project No. 97417). We kindly acknowledge the help and input by Dr. Doris Völker and Dr. Kathrin Schwirn.

[1] Scientific Committee on Emerging and Newly Identified Health Risks (SCENIHR) (2006) *The appropriateness of existing methodologies to assess the potential risks associated with engineered and adventitious products of nanotechnologies*, European Commission, Health and Consumer Protection Directorate-General.

[2] Hildebrand, H. et. al (2019) UBA Texte, 133/2019.

Tab. 1: NM detection techniques according to relevant properties.*

NM property	Method/technique
Size	DLS, MALS, NTA, electron microscopy, sp-ICP-MS
Concentration	ICP-AES/MS (overall conc.), sp-ICP-MS (sp level)
Composition	EM-EDX, ICP-AES/MS (overall comp.), sp-ICP-TOF-MS
Shape	electron microscopy, MALS

*: The most promising methods for a combined approach are in **bold**.

Mobility of radionuclides enhanced by complexants used in a repository: full description by reactive transport modeling

L. Karimzadeh, H. Lippold, M. Stockmann, C. Fischer

Among the organic inventory of a nuclear waste repository, aminopolycarboxylic acids, which are used as decontamination agents during operation, are of particular concern in view of their chelating properties and high persistence, but there is a lack of data regarding their effect on the mobility of radionuclides in geological barriers. Using $^{152}\text{Eu}(\text{III})$ as a tracer analogue of trivalent actinides, we performed batch and column experiments with the complexant diethylenetriaminepentaacetic acid (DTPA) and quartz sand. Based on an improved surface complexation model calibrated for the batch system, the effect of the organic ligand on breakthrough of $\text{Eu}(\text{III})$ was successfully described by 1D reactive transport modeling.

Results of batch adsorption experiments and surface complexation modeling (SCM) were presented in the previous Annual Report.^[1] As a follow-up study, column experiments were carried out in order to examine as to whether the SCM parameters are compatible with the flow conditions of a dynamic system. Besides non-equilibrium conditions due to slow kinetics, heterogeneity effects can cause considerable inconsistencies.^[2]

EXPERIMENTAL. Up- and downflooding experiments were performed with a 70×8 mm glass column, filled with 7.5 g quartz sand (grain size: 0.2–0.8 mm, porosity: 0.37). Feed solutions, adjusted to pH 6.5, were supplied by a syringe pump at a flow rate of 0.02 mL min^{-1} . 0.01 M NaClO_4 was used as a background electrolyte. After conditioning the column, solutions of 10^{-6} M DTPA and/or $10^{-6} \text{ M } [^{152}\text{Eu}]\text{Eu}(\text{NO}_3)_3$ in 0.01 M NaClO_4 were injected as a continuous step input, followed by elution with 0.01 M NaClO_4 . Hydrodynamic characteristics were evaluated by means of tritiated water (HTO) as a non-reactive tracer (0.3 MBq L^{-1} in 0.01 M NaClO_4). Collected fractions (0.4 mL) were analyzed by gamma counting (^{152}Eu) or by liquid scintillation counting (^3T).

RESULTS. As illustrated in Fig. 1, mobility of $\text{Eu}(\text{III})$ is considerably enhanced in the presence of DTPA. The breakthrough curve is shifted to a position close to that of HTO, indicating nearly unretarded transport. Breakthrough and elution curves were simulated on the basis of the 1D advection-dispersion-reaction equation using the transport routine implemented in the speciation program

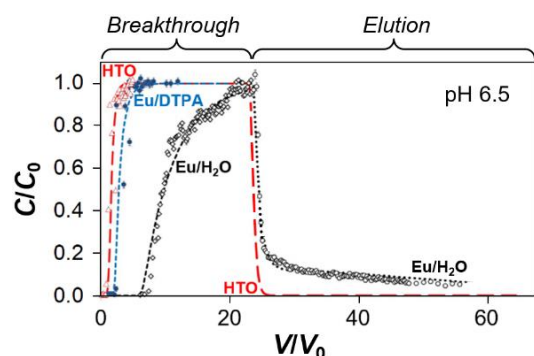


Fig. 1: Breakthrough and elution curves (symbols: experimental data, dashed lines: non-reactive transport calculated with hydrodynamic parameters fitted to HTO breakthrough, dotted lines: reactive transport calculated with SCM parameters derived from batch studies).

PHREEQC (v. 3). Equilibrium constants for aqueous speciation and surface complexation, optimized for the batch system to describe the effect of DTPA on adsorption of $\text{Eu}(\text{III})$ as a function of pH, were adopted without any re-adjustments.^[3]

The perfect agreement of experimental and model results shows that the proposed one-site SCM (based on the Diffuse Double Layer Model by Dzombak and Morel) is capable of describing both static and (homogeneous) dynamic systems.^[3,4] Obviously, there are no kinetic constraints under the present hydrodynamic conditions.

Given the adequateness of the reactive transport model, breakthrough curves for $\text{Eu}(\text{III})$ in the absence and presence of DTPA were simulated for different pH values. The results are shown in Fig. 2.

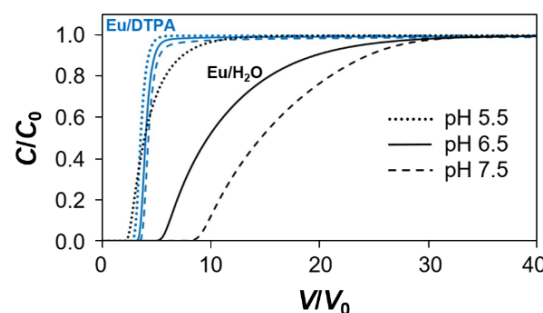


Fig. 2: Effect of pH on breakthrough curves, predicted by means of the SCM-based reactive transport model.

While a strong influence of pH on breakthrough is predicted for aqueous $\text{Eu}(\text{III})$, variations in the presence of the organic ligand are very minor, *i.e.*, the strong mobilizing effect is nearly independent of pH within the circumneutral range. Even though metal adsorption in reservoir rock is dominated by high-affinity minerals such as Al or Fe oxides, it may be concluded that mobility of actinides can be substantially increased in case of concomitant release of complexants like DTPA. If their usage in repositories cannot be avoided, they should be removed during the operation phase to the maximum feasible extent.

ACKNOWLEDGEMENT. This work was part of the FENABIUM project funded by BMBF, support code 02NUK046.

[1] Karimzadeh, L. et al. (2018) Report HZDR-096, p. 19.

[2] Lippold, H. et al. (2018) Appl. Geochem. **98**, 345–350.

[3] Karimzadeh, L. et al. (2020) Chemosphere **239**, 124771.

[4] Dzombak, D. A. et al. (1990) Surface Complexation Modeling: Hydrous Ferric Oxide, Wiley, New York, U.S.A.

SCIENTIFIC CONTRIBUTIONS (PART III)

Long-Lived Radionuclides in
**BIOLOGICAL
SYSTEMS**

Lanthanide-induced folding of an intrinsically disordered protein

E. Hoyer,¹ J. Knöppel, M. Liebmann,¹ M. Steppert,² M. Raiwa,² O. Herczynski,¹ E. Hanspach,¹ S. Zehner,³ M. Göttfert,¹ S. Tsushima, K. Fahmy, J. Oertel

¹Technische Universität Dresden, Dresden, Germany; ²Institut für Radioökologie und Strahlenschutz, Leibniz-Universität Hannover, Hannover, Germany; ³Technische Universität Kaiserslautern, Kaiserslautern, Germany

The Gram-negative bacterium *Vibrio coralliilyticus* causes bleaching of corals due to decomposition of symbiotic microalgae. Within a gene cluster of a type3 secretion system (T3SS) the protein VIC_001052 with sequence homology to the T3SS-secreted nodulation proteins NopE1 and NopE2 of *Bradyrhizobium japonicum* USDA110) is encoded. VIC_001052 has been shown to undergo auto-cleavage in the presence of Ca²⁺ similar to the NopE proteins. We have studied the hitherto unknown secondary structure, Ca²⁺-binding affinity and stoichiometry of the “metal ion-inducible autocleavage” (MIIA) domain which does not possess a classical Ca²⁺-binding motif.^[1]

The regulation of protein function by Ca²⁺-dependent structural transitions provides a ubiquitous mechanism for cellular signaling. In contrast to the canonical helix-turn-helix Ca²⁺-binding EF-hand motif, the MIIA domain does not exhibit substantial secondary structure. However, this intrinsic disorder is reduced by binding of Ca²⁺ or lanthanides. We have addressed the conformation, energetics, binding stoichiometry of the MIIA domain and the putative structure of its ion-binding sites.

EXPERIMENTAL. The MIIA domain was expressed in *E. coli* BL21 (DE3) (NEB) as a fusion protein with Maltose-binding protein (MBP) using plasmids derived from pVCD019. The protein was purified by affinity chromatography using an MBPTrapTM HP column (GE Healthcare) and eluted in TKE buffer containing 10 mM maltose. To prevent autocleavage, the D116A amino acid replacement was introduced which did not affect metal binding but abolished enzymatic activity.

RESULTS. In the absence of metal ions, the MIIA domain exhibited largely random structure. Ca²⁺ and Eu³⁺ (not shown) reduced randomness, whereas Mg²⁺ had no effect on secondary structure as revealed by CD-spectra (Fig. 1). The stoichiometry of 2:1 for Ca²⁺ binding to the MIIA-domain was determined by isothermal titration calorimetry

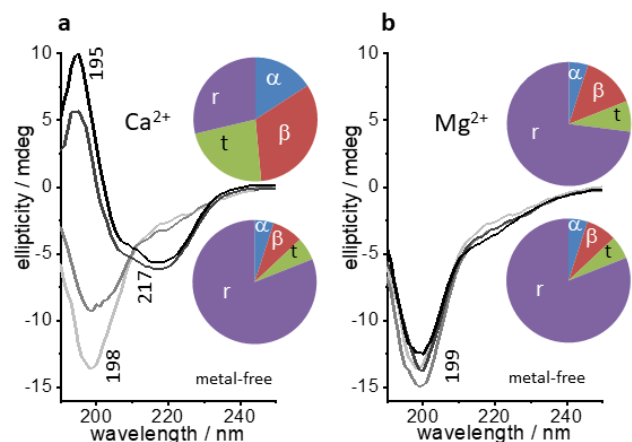


Fig. 1: Circular Dichroism spectra of the D116A-MIIA domain as a function of metal cation binding and thermal unfolding. CD spectra in the absence of metal ions (light gray) and in the presence of increasing concentrations of Ca²⁺ (100, 250, 500 μ M from gray to black) (a). Data as in (a) for Mg²⁺ (b). Pie charts represent per cent structure content as α : α -helical, β : β -sheet, t: turn, r: random.

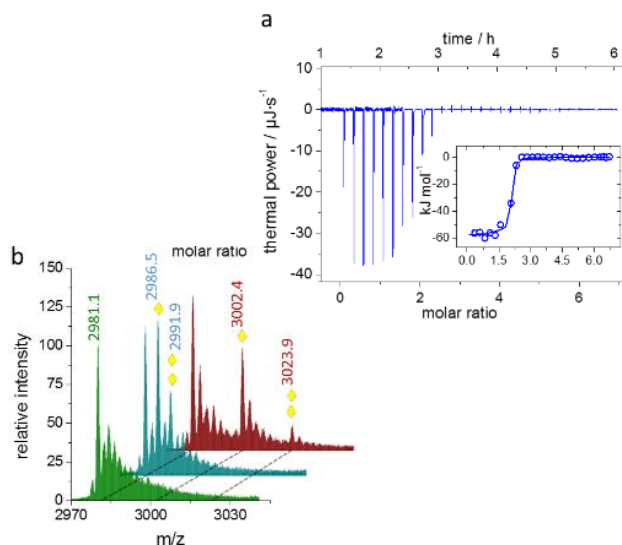


Fig. 2: Ca²⁺-binding energy and stoichiometry. Isothermal Titration Calorimetry of Ca²⁺ binding to the D116A-MIIA domain at 25 °C, 54 μ M of protein and injection of 10 μ L aliquots of 2 mM Ca²⁺ in the presence of 20 mM Tris-SO₄, pH 7 (a). Mass spectra representing the +7 charge states of the metal-free D116AMIIA domain (green) and of the Ca²⁺- (blue) and Eu³⁺- (red) containing samples (b). Yellow diamonds indicate the shifted main peaks containing one or two bound metal ions.

(ITC) with molar binding enthalpies of 54 and 57 \pm 1.1 kJ, and χ^2 /(degree of freedom) = 1.1) and binding entropies between -38 and -59 J mol⁻¹ K⁻¹, corresponding to a $K_d \leq 3.6 \pm 1.2 \mu$ M (Fig. 2a). The binding stoichiometry was confirmed by mass-spectrometry (Fig. 2b) and found to be the same for Ca²⁺ and Eu³⁺, *i. e.*, in agreement with the well-known recognition of canonical Ca-binding sites by lanthanides.^[2] Therefore, a structural model was derived from the most relevant local sequence similarity of the MIIA domain with the canonical EF-hand motif from human calmodulin site 1 (Fig. 3)

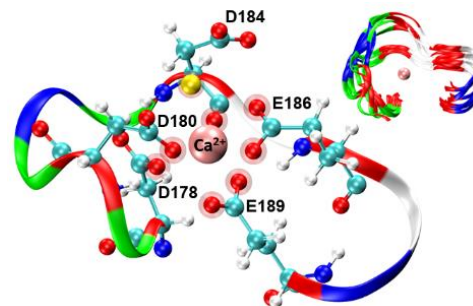


Fig. 3: Hypothetic structural model of Ca²⁺ coordination by site 1 of the MIIA domain (yellow sphere: a single Ca²⁺-coordinating water molecule). The inset shows the superposition of 10 snapshots (at 40 ns) of the backbone dynamics with largest fluctuations occurring at position 184.

ACKNOWLEDGEMENTS. We acknowledge technical help by Jenny Philipp in performing CD and ITC experiments. M.S. and M.R. acknowledge the financial support by the German Federal Ministry of Education and Research (BMBF) in the joint project SIRIUS (02NUK044A).

[1] Hoyer, E. *et al.* (2019) *Sci. Rep.* **9**, 7115.

[2] Bruno, J. *et al.* (1996) *Biophys. Chem.* **63**, 1–16.

Interaction of Eu(III) with calmodulin

B. Drobot, M. Schmidt, Y. Mochizuk,^{1,2} T. Abe,¹ K. Okuwaki,¹ F. Brulfert,³ S. Falke,⁴ S. A. Samsonov,⁵ Y. Komeiji,⁶ C. Betzel,⁴ T. Stumpf, J. Raff, S. Tsushima⁷

¹Department of Chemistry and Research Center for Smart Molecules, Rikkyo University, Tokyo, Japan; ²Institute of Industrial Science, The University of Tokyo, Tokyo, Japan; ³Institut de Physique Nucléaire d'Orsay, Université Paris-Sud, Orsay, France; ⁴Laboratory for Structural Biology of Infection and Inflammation c/o DESY, Universität Hamburg, Hamburg, Germany; ⁵Department of Chemistry, University of Gdańsk, Gdańsk, Poland; ⁶Biomedical Research Institute, National Institute of Advanced Industrial Science and Technology (AIST), Tsukuba, Japan; ⁷Tokyo Tech World Research Hub Initiative (WRHI), Institute of Innovative Research, Tokyo Institute of Technology, Tokyo, Japan

The interaction of Eu(III) with calmodulin – an ubiquitous calcium signaling protein – were investigated by a multi-technique approach including time resolved laser induced fluorescence spectroscopy (TRLFS) and isothermal titration calorimetry (ITC), sophisticated data processing (PARAFAC combined with a Monte Carlo approach), and computational chemistry. A consistent picture of Eu(III) binding modes and of the underlying molecular mechanisms were achieved. Possible effects on protein function were assessed by an enzyme activity assay.

It is known that trivalent f-elements can efficiently substitute Ca(II) in biological systems. We thoroughly investigated the interaction of Eu(III) with calmodulin using a multi-technique approach. In addition, computational chemistry, *i.e.* Molecular Dynamics (MD) and Fragment Molecular Orbital (FMO) methods, indicated minor changes in the protein structure. Impact on the protein function were assessed by an enzyme activity assay.

This report presents highlights of the publication “Cm³⁺/Eu³⁺ induced structural, mechanistic and functional implications for calmodulin”.^[1]

EXPERIMENTAL. Experimental details (TRLFS and ITC) and details of computational techniques (MD and FMO) are given elsewhere and in the associated supporting information.^[1]

RESULTS. Our results from ITC proved high affinity binding of Eu(III) to calmodulin (CaM). Data deconvolution provided four binding sites. The overall binding process was endothermic, which we assigned to the stripping of europium's hydration shell. Interestingly, the highest affinity binding site differed from the remaining three sides. The binding reaction to this side was slightly exothermic (see Fig. 1).

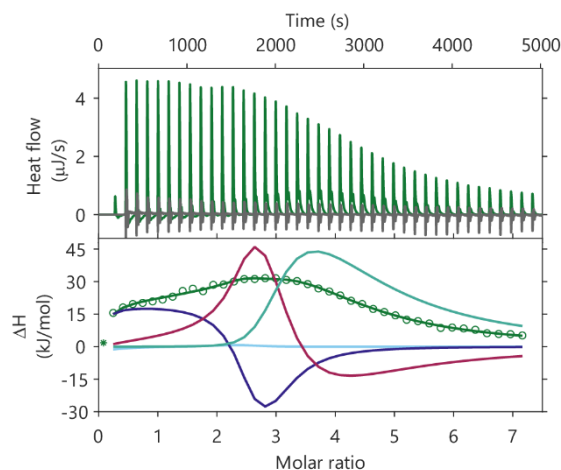


Fig. 1: ITC studies of Eu(III) binding to CaM. Top: Thermograms of Eu(III) titrations to CaM (green) and to electrolyte solution (grey). Bottom: Integrated thermogram and fit (green) and the enthalpic contribution of formed complexes.

We then used time resolved laser induced fluorescence spectroscopy to study series of CaM titration to a Eu(III) solution. We could identify two different environments of Eu(III) in calmodulin by factor analysis (PARAFAC).^[2,3] We grouped the binding sites according to the findings from ITC (one side different from the others). This enabled us to extract thermodynamic data from this series, as previously described (speciation in Fig. 2).^[4] Generally, the extracted affinity of Eu(III) binding by CaM (10^{-7} to 10^{-6}) was about one order of magnitude higher than for Ca(II) (10^{-6} to 10^{-5}) and results from TRLFS were in excellent agreement with ITC.

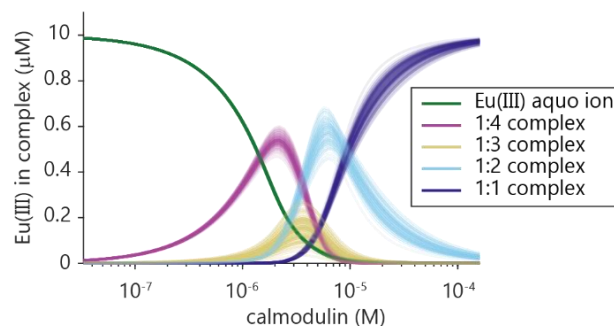


Fig. 2: Speciation of Eu(III) in TRLFS series. Overlaid curves are from different Monte Carlo runs.

We found the luminescence lifetime of the highest affinity binding site to be shorter than the others, which corresponds to an additional water molecule in this site. This is in line with the enthalpic differences observed by ITC and further confirmed by MD simulations.

Moreover, computational chemistry found small differences in the global structures of Ca(II)-CaM and Eu(III)-CaM. Such modifications could alter the protein function. We addressed this question with an enzyme activity assay, based on phosphodiesterase (PDE1) activation by CaM. This revealed that Eu(III)-CaM is able to activate PDE1 but the activity was slightly reduced compared to Ca(II)-CaM (see Fig. 3).

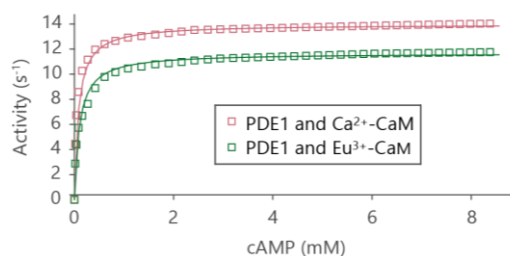


Fig. 3: Comparison of PDE1 activation by Ca-CaM and Eu-CaM.

- [1] Drobot, B. *et al.* (2019) *Phys. Chem. Chem. Phys.* **21**, 21213–21222.
- [2] Andersson C. *et al.* (2000) *Chemom. Intell. Lab. Syst.* **52**, 1–4.
- [3] Drobot, B. *et al.* (2015) *Chem. Sci.* **6**, 964–972.
- [4] Drobot, B. *et al.* (2016) *Anal. Chem.* **88**, 3548–3555.

Transport studies of uranium, europium, caesium and strontium in the mycelium of *S. commune* by microcosm experiments

A. Wollenberg, L. Freitag, A. Günther, J. Raff

Large amounts of radioactive caesium and strontium were measured in the fruiting bodies of various Basidiomycota in the Chernobyl area.^[1-3] However, the accumulation pathways of the radioactive isotopes in the fruiting bodies have not yet been clarified. An extraction of radioactive isotopes from contaminated soil into fungal hyphae with subsequent transport through them, up to the fruiting body, is conceivable. With the help of microcosm experiments the transport of uranium, europium, caesium and strontium from contaminated forest soil into the fungal hyphae of the Basidiomycete *Schizophyllum commune* will be investigated and the results will be compared with transport investigations in sandy soil.

EXPERIMENTAL. As inoculum for the experiments, *S. commune* was cultivated for 2 weeks at 15 °C on minimal medium plates (aspartic acid 2 g L⁻¹, thiamine hydrochloride 120 µg L⁻¹, MgSO₄ 0.5 g L⁻¹, K₂HPO₄ 1 g L⁻¹, KH₂PO₄ 0.45 g L⁻¹, tryptophan 1 g L⁻¹, glucose 20 g L⁻¹) with gelatine (120 g L⁻¹). Sterile forest soil (origin: forest of Tharandt) was mixed with a metal solution containing uranium, europium, caesium and strontium so that the metal concentration in the soil was 21 µM per kg for each of the metals. 100 g of soil with and without metal contamination was filled into sterile magenta boxes, type GA-7. On the soil a cotton pad was placed, previously impregnated with CYM-T and agar (20 g L⁻¹), to avoid possible capillary effects due to the aspiration of liquid in the cotton pad. A nylon mesh bag containing the inoculum was placed on the cotton pad. After an incubation period of three months the mycelium, which had no direct contact with the soil, was harvested from the nylon mesh bag. The biomass was incinerated, disrupted with concentrated nitric acid and analysed by ICP-MS.

RESULTS. Figure 1 shows the amount of metal in the biomass that had no direct contact with the soil. The results from the experiments with forest soil, shown in µmol per gram dry biomass, will be compared to results from the microcosm experiments with *S. commune* and sandy soil.^[4] The results from the microcosm experiments with forest soil show that concentrations of U(VI) of 0.11 ± 0.05 µmol g⁻¹, Eu(III) of 0.08 ± 0.04 µmol g⁻¹ and Sr(II) of 0.28 ± 0.15 µmol g⁻¹ are detectable in the biomass with no direct contact to the forest soil. Also, small amounts of Cs(I) of 0.02 ± 0.01 µmol g⁻¹ can be detected in the biomass. Compared to the metal concentration of the biomass from microcosm experiments with uncontaminated soil, it becomes clear that fungi are able to extract metals from the soil and transport them through the cells of their hyphae. In comparison to the results from the microcosm experiments with sandy soil, it becomes clear that the organic components of the soil play a role, especially for the uranium uptake and transport. Compared to the results from the microcosm experiments with sandy soil, the experiments with forest soil showed lower uranium concentrations in the biomass without soil contact despite a longer incubation period. However, Europium was better transported in the microcosm experiment with forest soil. This tendency is supported by the results of batch experiments with corresponding soil extract media.^[5] While in the microcosm experiment with sandy soil the europium

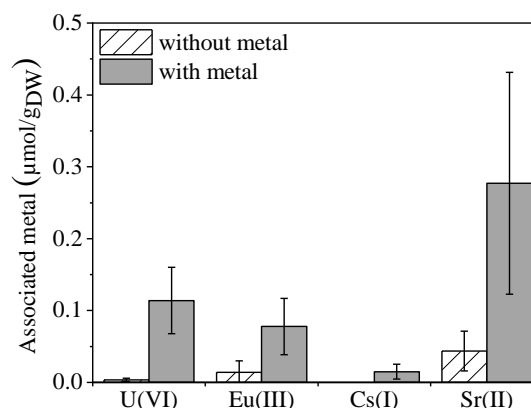


Fig. 1: Amount of U(VI), Eu(III), Cs(I) and Sr(II) in fungal biomass, which was extracted from forest soil.

concentration in the biomass was comparable to the amount of caesium, the microcosm experiments with forest soil show a significantly higher europium than caesium concentration in the biomass. The reason for this could be a higher organic content of the forest soil compared to sandy soil. Europium can complex with organic components of the soil, which allows a better uptake into the cell.

In summary, the microcosm experiments with forest soil confirmed the extraction of metals from soil and their transport through the hyphae to a possible fruiting body. In addition to the influencing factors identified in the microcosm experiments with sandy soil, namely type of metal and fungal species,^[4] the content of organic substances in soil could be identified as another factor influencing the transport of metals in the hyphae.

The microcosm experiments have shown that this is a good method to study the influence of fungi on the cycle of radionuclides and metals in contaminated soils and also to better understand the factors that influence the extraction of metals from soil by biomass and their subsequent transport through the fungal mycelium up to the fruiting bodies.

ACKNOWLEDGEMENTS. The authors kindly acknowledge the funding of the project BioVeStRa by the BMBF under contract No. 15S9276A and thank to Sabrina Beutner and Stephanie Bachmann for elemental analyses.

- [1] Battiston, G. A. et al. (1989) *J. Environ. Radioactivity* **9**, 53–60.
- [2] Berreck, M. et al. (2003) *Int. J. Med. Mushrooms* **5**, 61–86.
- [3] Byrne, A. R. (1988) *J. Environ. Radioactivity* **6**, 177–183.
- [4] Wollenberg, A. et al. (2019) *Report HZDR-096*, p. 39.
- [5] Günther, A. et al. (2020) *BMBF-project BioVeStRa*, final report, p. 36

Interactions of an extremely halophilic archaeon with Eu(III)

M. Bader, H. Moll, R. Steudtner, H. Lösch, B. Drobot, T. Stumpf, A. Cherkouk

Halobacterium noricense DSM15987^T, which is common in rock salt, was used to investigate its interactions with europium as a function of time. Time-resolved laser-induced fluorescence spectroscopy (TRLFS) was applied to characterize formed species in the micromolar europium concentration range. The data revealed the association of Eu(III) to a phosphate compound released by the cells and a solid phosphate species.^[1]

Microorganisms, which are common in rock salt can potentially impact the retardation or mobility of radionuclides by e. g. biosorption, bioaccumulation, biotransformation or biomineralization.^[2] *Halobacterium noricense* DSM15987^T is a representative of such extremely halophilic archaea and was isolated from rock salt of a salt mine in Altausee, Austria.^[3] This microorganism was chosen to investigate its interactions with europium as a function of time by applying TRLFS to characterize the formed species.

EXPERIMENTAL. *H. noricense* DSM15987^T was purchased from the Leibniz Institute DSMZ-German Collection of Microorganisms and Cell Cultures (DSMZ, Braunschweig, Germany) and cultivated in DSM372 medium as described.^[1] Europium bioassociation in batch systems was performed as outlined.^[1] TRLFS was chosen to get information about the formed cell-europium species as well as species that were in the supernatant provoked by released compounds. Therefore, supernatants, as well as washed and resuspended cells, were investigated separately in a quartz glass cuvette at room temperature as described earlier.^[1]

RESULTS. The association of Eu(III) on *H. noricense* DSM15987^T cells was investigated as function of time at 30 μ M europium (Fig. 1). Figure 1 shows that an increasing amount of europium is associated to the cells with increasing incubation time: after 3 h $37 \pm 12\%$ and after 24 h $56 \pm 13\%$ of Eu(III) were associated with the cells.

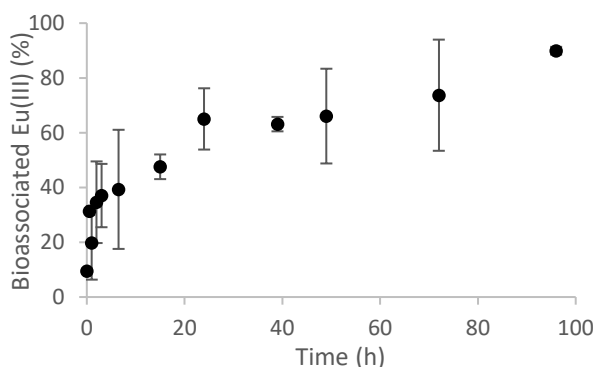


Fig. 1: Kinetic of europium bioassociation on *H. noricense* DSM15987^T cells at 30 μ M Eu(III), [NaCl] = 3 M, dry biomass = 0.5 mg mL⁻¹, pC_{H+} 5.5.

The data that were retrieved from the TRLFS studies performed at 30 μ M europium were analyzed by PARAFAC (Fig. 2). In total three different spectra were extracted.^[1] The initial Eu(III) in 3 M NaCl, defined as blank, showed two intensive local maxima at 592 nm and 616 nm along with less intensive emission bands at 652 and 698 nm. Given the emission lifetime of $112 \pm 6 \mu$ s and the intensity ratio of 0.4, the extracted spectrum 1 can be assigned to the free Eu(III) aqueous ion. The extracted spectrum 2 has a higher lumines-

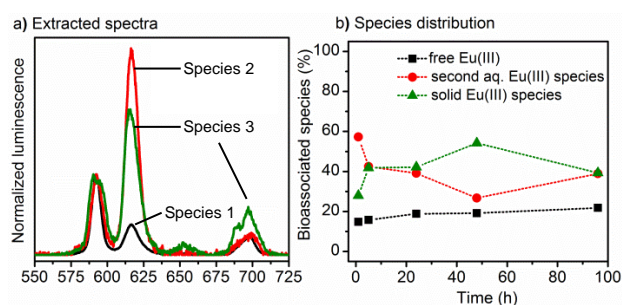


Fig. 2: PARAFAC results from TRLFS spectra analysis from Eu(III) association on *H. noricense* DSM15987^T cells (30 μ M Eu(III), [NaCl] = 3 M, dry biomass = 0.5 mg mL⁻¹, pC_{H+} 5.5).

cence lifetime of $430 \pm 22 \mu$ s and a significantly higher intensity ratio of 7F_2 to 7F_1 of 2.5. This spectrum was isolated from the supernatant and from the cell data. It is difficult to make an assignment based on the comparison of 7F_2 to 7F_1 ratios, the luminescence lifetime, or the coordinated water molecules with the limited number of corresponding references or literature data. Based on luminescence measurements with relevant reference compounds,^[1] it is unclear whether it is an inorganic or organic phosphate species, but it is clearly a phosphate species. The extracted spectrum 3 dominates the Eu(III) speciation in the presences of the cells and could be a cell-associated Eu(III) species or an Eu(III) biomineralization product. The very short lifetime of 48 μ s indicates that ligand-specific quenching processes might occur.^[4]

In conclusion, the amount of bioassociated Eu(III) increased rapidly and then continued to increase even after a few hours, which means that no pure biosorption process occurred. In case of an accidental release of trivalent actinides, these hazardous metals could be bound by the microorganism which would result in a mobilization as cells may act as biocolloids. But when the *H. noricense* cells form a biofilm the actinides can be held back. Moreover, a cell response to the exposure of Eu(III) is the formation of a phosphate containing compound, which can contribute to their retention after a potential release.

MISCELLANEOUS. This work is licensed under Journal of Environmental Science and Pollution Research. Figures have been edited. <https://doi.org/10.1007/s11356-019-04165-7>.

[1] Bader, M. et al. (2019) *Environ Sci Pollut R.* **26**, 9352–9364.

[2] Lloyd, J. R.; Macaskie, L. (2002) in: *Interactions of microorganisms with radionuclides. Radioactivity in the environment*, p. 313–342, Elsevier.

[3] Gruber, C. et al. (2004) *Extremophiles* **8**, 431–439.

[4] Kuke, S. et al. (2010) *Spectroc. Acta Part. A-Molec. Bio Molec. Spectr.* **75**, 1333–1340.

Cm(III) interaction with a Spanish bentonite yeast isolate

M. Lopez-Fernandez, H. Moll, M. L. Merroun¹

¹Department of Microbiology, University of Granada, Granada, Spain

Bentonites considered as an artificial barrier for future deep geological repositories (DRG) of nuclear waste host indigenous microorganisms, e.g. the yeast *Rhodotorula mucilaginosa* BII-R8. Time-resolved Laser-induced Fluorescence Spectroscopy (TRLFS) demonstrated the reversible and pH-dependent biosorption of Cm(III) by *R. mucilaginosa* BII-R8 cells. Eu(III) used as analogue is accumulated as phosphate at the cell membrane, which also proves its involvement in the Cm(III) sorption. In addition, this study showed that the interaction of Cm(III) with the yeast *R. mucilaginosa* BII-R8 cells at pH > 6.5 values will make this radionuclide more mobile and thus can reach the biosphere.

Bentonite formations from Almeria (Spain) were intensely studied and selected as a natural analogue for the engineered barrier in the future DGRs.^[1] A high microbial diversity has been described in these bentonite formations, which might compromise the repository safety through different processes.^[2] Actinide interactions with isolated bacteria from different host environments have been widely studied. However, although yeasts are widely distributed in the environment most of the studies were focused on *Saccharomyces cerevisiae*. To our knowledge, this is the first study describing the use of TRLFS to determine the speciation of Cm(III) associated with a bentonite yeast isolate at a very low metal concentration.^[3]

EXPERIMENTAL. Yeast strain *R. mucilaginosa* BII-R8 was isolated from a bentonite sample recovered from Almeria, Spain.^[4] Cell growth, experimental details on Cm(III) and Eu(III) sample preparation, TRLFS and microscopically techniques (STEM-HAADF and EDX) are summarized elsewhere.^[3] Eu(III) was used as inactive analogue of Cm(III).

RESULTS. TRLFS spectra showed that there are two coordination environments of Cm(III) due to interactions with functional groups of the cell membrane and possibly with released metabolites (Fig. 1).

Cm(III)-*R. mucilaginosa* BII-R8 species 1 was characterized by an emission maximum at 599.6 ± 1 nm and an average luminescence lifetime of $240 \pm 50 \mu\text{s}$, which can be assigned to a Cm(III) species bound to phosphoryl sites; while Cm(III)-*R.*

mucilaginosa BII-R8 species 2 showed a more red shifted emission maximum at 601.5 ± 0.5 nm and a shorter average luminescence lifetime of $123 \pm 11 \mu\text{s}$, assigned to a Cm(III) species bound to carboxyl sites of the cell membrane. In addition, TRLFS of the supernatants and the Cm(III) loaded biomass after washing with 0.1 M NaClO₄ showed that 30 and 82% of the total Cm(III) luminescence intensity remained in solution at pH 6.2. and 8.1, respectively. This suggests a pH-dependent release of complexing agents, possibly phosphates by the cells.

STEM-HAADF micrographs of thin sections showed electron-dense accumulates mainly composed of Eu and phosphorus at the yeast cell surface (Fig. 2). This points to the biosorption of Eu(III) as the main interaction mechanisms with *R. mucilaginosa*-R8 cells, which is in agreement with the Cm-TRLFS results.

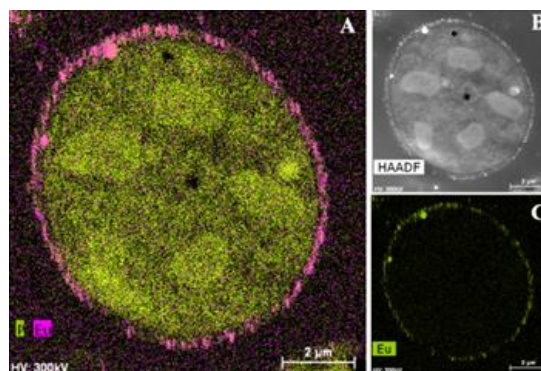


Fig. 2: Mapping image of thin sections of *R. mucilaginosa* BII-R8 treated with 1 mM Eu (III) for 48 h at pH < 6.5.

In conclusion, this work presents the interaction mechanisms of Cm(III)/Eu(III) with *R. mucilaginosa* BII-R8, a natural yeast isolated from Spanish bentonites. The biosorption of Cm(III) by the yeast cells is a reversible and pH-dependent process, where organic carboxyl and phosphates groups are involved, as confirmed by the Eu(III)-phosphate complexes observed at the cell membrane. Our results indicate that this Cm(III)-yeast interaction can affect the mobility of Cm(III), with a negative effect at circumneutral and alkaline pH in a future repository.

MISCELLANEOUS. This work is licensed under a CC BY-NC-ND license. Journal of Hazardous Materials. <https://doi.org/10.1016/j.jhazmat.2018.06.054>. Figures have been edited.

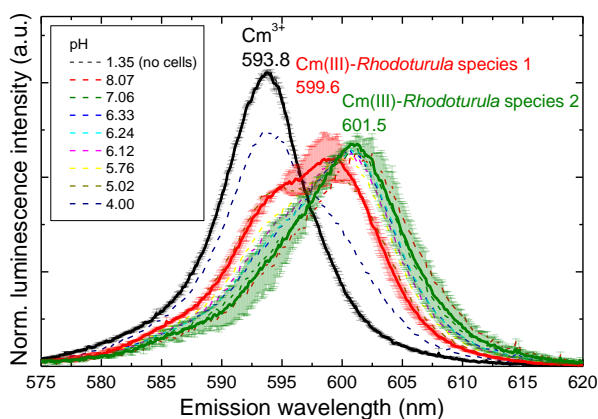


Fig. 1: Luminescence emission spectra of 0.3 μM Cm(III) in 0.1M NaClO₄ measured as a function of pH at a fixed biomass concentration of 0.45 g_{dry weight} L⁻¹.

- [1] Villar, M. V. et al. (2006) *J. Iber. Geol.* **32**, 15–36.
- [2] Lopez-Fernandez, M. et al. (2015) *Microb. Ecol.* **70**, 922–935.
- [3] Lopez-Fernandez, M. et al. (2019) *J. Hazard. Mater.* **370**, 156–163.
- [4] Lopez-Fernandez, M. et al. (2014) *Appl. Geochem.* **49**, 77–86.

Antibacterial activity of selenium nanoparticles studied by microcalorimetry and electron microscopy

S. Schäfer, K. Fahmy, M. L. Merroun¹

¹Universidad de Granada, Departamento de Microbiología, Granada, Spain

Metabolic monitoring of two bacterial strains by microcalorimetry demonstrates the antibacterial activity of selenium nanoparticles after 3–8 h. Extracellular interactions of the selenium nanoparticles with the bacterial cell wall and extracellular proteins are observed by environmental scanning electron microscopy.

The dramatic rise of antibiotic-resistant microorganisms has been defined as a major concern by the world health organization in 2015. Both resistance mechanisms and alternative antibiotics need to be investigated. For the latter, metallic nanoparticles (NPs) have attracted attention. Silver NPs exhibit potential in medical applications as antibacterial coatings for implantable devices or catheter.^[1,2] Although other metals, such as selenium (Se), show antibacterial activity as well, their interaction mechanisms with microorganisms are insufficiently addressed. Besides the equally low toxicity of Se ions to the human body, Se is cheaper compared to silver which improves its applicability. Here, the antibacterial activity of SeNPs has been studied by isothermal microcalorimetry and environmental scanning electron microscopy (ESEM).

EXPERIMENTAL. The bacterial strains *Lysinibacillus sphaericus* NCTC 9602 and *Stenotrophomonas bentonitica* JG-A12 were cultivated for 24 h in LB-medium (30 °C, 120 rpm) and then washed thrice with PBS (pH 7.2). SeNPs were ordered from Nanocs Inc. (USA) with a diameter of 50 nm and a stock concentration of 1.3 mM. For isothermal microcalorimetry measurements, a washed bacterial culture was exposed to SeNPs (0–100 µM) in PBS (pH 7.2) and an optical density of 0.3 at 600 nm. The metabolic heat flow from twelve samples of 2 mL culture were simultaneously monitored by a TAM III (Waters GmbH, Germany) over 48 h. All measurements were performed in triplicates. Maximal metabolic activities were calculated and normalized by the value of the control (0 µM SeNPs).^[3] For ESEM, the washed bacterial cultures were diluted to an optical density of 0.3 at 600 nm in PBS (pH 7.2) and SeNPs were added (100 µM final concentration) to a 1 mL sample for incubation for 24 h at 30 °C and 120 rpm. Sample preparation and measurement with a Quanta 400 instrument (FEI, USA) were performed by the Centro de Instrumentación Científica (Universidad de Granada, Spain).

RESULTS. Microcalorimetry results (Fig. 1) indicate an increasing toxicity of SeNPs with increasing concentration on both bacterial species, displayed by a decrease in maximal metabolic activity which was detected between 2 and 8 h after exposure. Surprisingly, ESEM of *L. sphaericus* (Fig. 2) revealed extracellular interactions of the SeNPs with extracellular polymers, putatively flagella-like proteins, fimbriae or pili, and with the bacterial cell wall (data not shown). Those proteins are hypothesized to be involved in detoxification of SeNPs by biotransformation.^[4] Similar interactions were observed for the gram-negative bacterium *S. bentonitica* (data not shown). In sum, microcalorimetry has proven to be a sensitive tool to detect antimicrobial action of SeNPs, however, an influence of the bacterial cell wall composition on antibacterial activity of SeNPs was not detected. This sug-

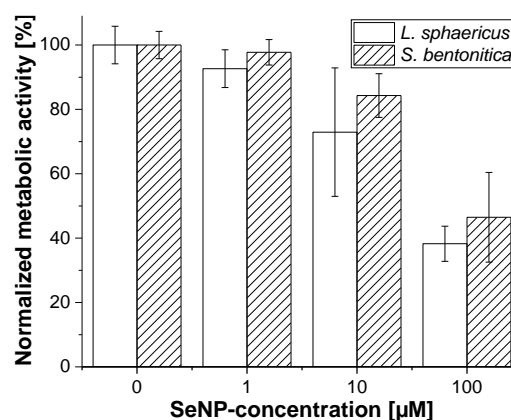


Fig. 1: Normalized metabolic activity of *L. sphaericus* and *S. bentonitica* after exposure to SeNPs.

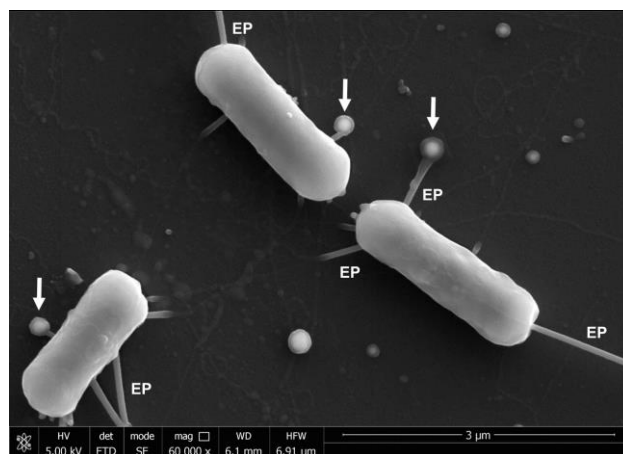


Fig. 2: ESEM micrograph of *L. sphaericus* after 24 h exposure to 100 µM SeNPs. Arrows highlight SeNPs interacting with extracellular polymers (EP). The scale bar represents 3 µm.

gests that cell wall-independent processes such as extracellular metabolite SeNP interactions or SeNP-mediated oxidation reactions at cell surfaces underly the observed toxicity. Future studies will focus on differentially coated and therefore differentially charged SeNPs which may influence the toxicity on specific bacterial species. Since calorimetry does not distinguish reduced metabolic activity from partial cell death, flow cytometry measurements with suitable fluorescent dyes will be performed. Finally, the uptake and biotransformations of SeNPs will be studied by transmission electron microscopy.

ACKNOWLEDGEMENTS. The authors thank Daniel García Muñoz Baustista Cerro and Concepción Hernández Castillo for ESEM sample preparation and Isabel Sánchez Almazo for her professional assistance with ESEM measurements at Centro de Instrumentación Científica (Universidad de Granada, Spain). S. Schäfer acknowledges financial support of his research stay at the Universidad de Granada (Spain) by ERASMUS+.

[1] Antonelli, M. et al. (2012) *J. Hosp. Infect.* **82**, 101–107.
[2] Furno, F. et al. (2004) *J. Antimicrob. Chemother.* **54**, 1019–1024.
[3] Sachs, S. et al. (2017) *Environ. Sci. Technol.* **51**, 10843–10849.
[4] Ruiz Fresneda, M.A. et al. (2018) *Environ. Sci. Nano* **9**, 2103–2116.

First results of U retention studies on *Magnetospirillum magneticum* AMB-1

E. Krawczyk-Bärsch, S. Kluge, J. Raff

Kinetic uranium sorption experiments and cryo-time resolved laser-induced fluorescence spectroscopy were performed for the first time on the Gram-negative, magnetotactic, facultative anaerobic bacterium *Magnetospirillum magneticum* AMB-1. The results show a fast sorption of U during the first 8 hours of incubation. Almost 87% of the initial U amount was removed from the solution. The U removal capacity was determined with 23 mg U/g dry biomass after 24 h. TRLFS studies indicate that U is bound to carboxyl complexes such as malonate within the first hours of incubation.

EXPERIMENTAL. The strain of *Magnetospirillum magneticum* AMB-1 were kindly provided by the Molecular and Environmental Microbiology Department of the Institute of Biosciences and Biotechnologies from CEA Cadarache in France. The cells were grown in our laboratory in 150 mL flasks in 1.5 mM MagMin medium after [1], modified by CEA Cardarache with the addition of iron malate (1:2,000) and vitamin elixir (1:2,000). The flasks were kept at 30 °C on a rotary shaker at 100 rpm. An inoculation of the bacteria was carried out every 4–5 days. For sorption experiments the cells were taken with an OD_{600nm} of 0.1–0.2 and washed three times with sterilized tap water with a pH adjusted to 6.0. The washed cells were suspended in a flask with sterilized tap water pH6.0 and a 0.1 M stock solution of $UO_2(NO_3)_2$ was added to a final concentration of 0.1 mM. The cell suspensions were incubated at room temperature and 130 rpm on a rotary shaker. After distinct times, 0.5 mL samples were taken to determine the residual U concentrations in the supernatant. Each sample was centrifuged for 5 min at $16,000 \times g$ at room temperature. The supernatants were acidified and used for Inductively Coupled Plasma Mass Spectrometry measurements (ICP-MS).

For cryo-time resolved laser-induced fluorescence spectroscopy (cryo-TRLFS) the suspensions were centrifuged 4 h after incubation with U. The pellets were washed twice with sterilized tap water pH6 and the dried solid samples were transferred into a copper sample holder and covered with a quartz plate. For reference a cell suspension in sterilized tap water without U was used. The U(VI) luminescence was measured at 153 K after excitation with laser pulses at 266 nm and an average pulse energy of 300 μ J. The emission of the samples was recorded using an iHR550 spectrograph and an ICCD camera in the 370–670 nm wavelength ranges by averaging 100 laser pulses and using a gate time of 2,000 μ s.

RESULTS. The U removal capacity of *Magnetospirillum magneticum* AMB-1 cells at 0.1 mM U was determined in mg U per g dry biomass and it was found, that 23 mg U was removed after 24 hours. As shown in Fig. 1, U was sorbed very fast. Almost 87% of the initial U amount was already removed from the solution after 8 hours of incubation. The measured TRLFS emission spectrum of the U complexes formed by the *Magnetospirillum magneticum* AMB-1 cells at 0.1 mM U concentration and incubation time of 4 hours indicates the formation of strong inner-sphere complexes of U(VI) with the bacteria. The luminescence band positions (Tab. 1) are in a good agreement with the band positions of *Acidithiobacillus ferrooxidans* ATCC 33020 (formerly *Thiobacillus ferrooxidans*), which was recovered from a uranium mine.^[2] The peak maxima of the *Magnetospirillum magneticum* AMB-1 cells show also similarities to reference spectra of the uranyl

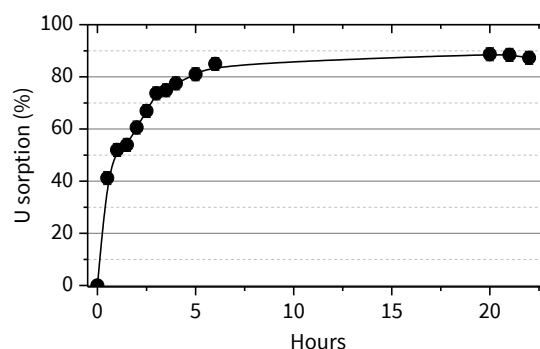


Fig. 1: U removal by *Magnetospirillum magneticum* (AMB-1) under aerobic conditions; initial U conc. = 0.1 mM, 24 h incubation.

Tab. 1: Luminescence band positions of *Magnetospirillum magneticum* AMB-1 cells exposed to 0.1 mM U for 4 h compared to band positions of complexation of U(VI) with cells of *Acidithiobacillus ferrooxidans* and uranyl malonate.^[2,3]

Samples	Luminescence emission bands (nm)			
	<i>Magnetospirillum magneticum</i> AMB-1	476.9	493.5	514.9
<i>T. ferrooxidans</i> ^[2]	–	493.6	514.9	537.1
$UO_2C_3H_2O_4^0_{(aq)}$ ^[3]	477	494	515	540
$UO_2(C_3H_2O_4)_3^{2-}$ ^[3]	479	496	517	542

malonate complexes $UO_2C_3H_2O_4^0_{(aq)}$ and $UO_2(C_3H_2O_4)_3^{2-}$ indicating that UO_2^{2+} is bound as uranyl carboxyl complexes.^[3] However, further studies have to proof if uranyl phosphoryl coordination is additionally formed.

ACKNOWLEDGEMENTS. The authors are grateful to D. Faivre and S. Prévèral (CEA Cardarache, France) for providing the strain of *Magnetospirillum magneticum* AMB-1. We would like to thank H. Neubert for TRLFS as well as S. Gurlit and S. Schubert (all HZDR, Germany) for ICP-MS measurements.

[1] Komeili, A. et al. (2004) *Proc. Natl. Acad. Sci.* **101**, 3839–3844.

[2] Panak, P. et al. (1999) *Radiochim. Acta* **84**, 183–190.

[3] Brachmann, A. et al. (2002) *Radiochim. Acta* **90**, 147–153.

Interaction of *Brassica napus* with U(VI): Extension of the experiments from plant cell cultures to plants

J. Jessat, S. Sachs

Based on the investigations with *Brassica napus* suspension cell cultures, first hydroponic experiments with young *B. napus* plants were performed. The experiments showed that U(VI) was taken up by the plants from the hydroponic solution. A slight translocation of U(VI) within the plant was observed.

For a safety assessment of repositories, it is necessary to consider accident scenarios in which water enters the repository. In this case, the radionuclides can be transported *via* near-surface groundwater and soil and can be absorbed by plants thus entering the food chain. This creates a health risk for humans and animals. Previous studies have shown that radionuclides such as uranium can be immobilized (*i.e.* bio-associated) by interaction with *B. napus* suspension cell cultures. However, in some cases mobility can also be improved.^[1] Therefore, the studies on the interaction of *B. napus* with U(VI) have been extended to experiments with whole plants. The aim was to investigate the heavy metal uptake by the plant as well as the composition of the nutrient solution after plant exposure with U(VI) with regard to the released metabolites. The investigations will be completed by measurements with time-resolved laser-induced fluorescence spectroscopy (TRLFS) to characterize the U(VI) speciation in the plant and the hydroponic solution.

EXPERIMENTAL. Plants were cultivated in hydroponic cultivation boxes (Araponics, Belgium) starting from seeds of *B. napus* from existing stocks. After stratification for five days, the seeds were planted at 7°C in water-permeable plastic inserts containing agar (0.5% in Milli-Q-water). The plants then grew for about 2 months under laboratory conditions. A nutrient solution with a salt mixture (Hoagland Medium, Basalt No. 2, Sigma Aldrich, Germany) was used for the hydroponics and the oxygen supply was ensured by the use of aquarium pumps. For the experiment, three of the plants were placed in an Erlenmeyer flask and fixed in position. 100 mL of Hoagland nutrient solution containing 20 µM U(VI) was added (see Fig. 1). The nutrient solution was filled daily to 100 mL (exception: 96, 144 h) during the exposure period. At the exposure times of 1, 4, 24, 48, 72, and 168 h, samples were taken from the nutrient solution for ICP-MS and TRLFS measurements. The remaining nutrient solution after 168 h of exposure will be used for HPLC measurements to analyse released plant metabolites. After exposure, the plants were washed twice with Milli-Q water and the individual compartments (root, stem, leaves) were separated and ashed. The ashed residues were dissolved in concentrated HNO₃ (≥ 65%, p. a., Roth, Germany) and the uranium concentration in the diluted solutions was determined by ICP-MS. A part of the biomass was stored for TRLFS measurements.

RESULTS. The results of the ICP-MS measurements show that about 85% of the uranium was bio-associated at the end of the exposure period. A large part of the uranium can be found at the root (81.21%), only traces of uranium could be found in the stem (0.02%) and the leaves (0.17%). The evaluation of the ICP-MS measurements of the nutrient solution at the different exposure times results in a time-dependent bio-association profile. This shows that the bio-association in-

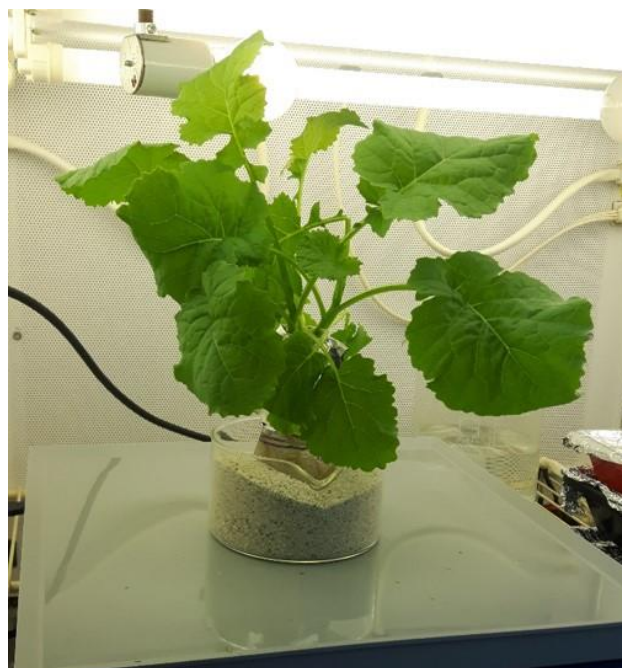


Fig. 1: Exposure of a young *B. napus* plant to a nutrient solution of 20 µM U(VI) for one week.

creases rapidly for an initial concentration of 20 µM U(VI). The bioassociation reaches the already mentioned maximum value of about 85% after 24 to 48 h. After that, there is an equilibrium adjustment, *i.e.* there is no further increase in the amount of bio-associated uranium. Due to the rapid increase in bioassociation, it can be assumed that a large part of the uranium is immobilized at the roots by sorption processes. However, since uranium has also been found in the other compartments of the plant, bioaccumulation and translocation must also take place with increasing exposure times. These results are in good agreement with the experiments carried out for the exposure of *B. napus* plant cells in suspension.^[1] These were also exposed to 20 µM U(VI) and the time-dependent bioassociation was investigated. The behavior was comparable to that of the young plants: first an increase in bioassociation and then an equilibrium adjustment after about 24 h exposure. This underlines the relevance of the *B. napus* suspension cell cultures used as model systems. The TRLFS measurements of biomass and supernatants under cryogenic conditions (-120°C) as well as the HPLC measurements for identification of metabolites will be performed in the future.

ACKNOWLEDGEMENTS. The authors thank J. Seibt, S. Heller, S. Beutner and S. Bachmann for experimental support. This work was funded by the Federal Ministry of Education and Research under contract number 02NUK051B.

[1] Jessat, J. et al. (2019) Report HZDR-096, p. 37.

Initiation and establishment of a *Daucus carota* callus cell culture for the study of the interaction of radionuclides with plants

S. Sachs, J. Jessat

A callus cell culture of *Daucus carota* was successfully initiated and established. These cells are used as model system to study the U(VI) bioassociation with carrots on a molecular level.

To obtain molecular information on the interaction of radionuclides with plants, *in vitro* suspension cell cultures can be used. With such cells, the physiological and biochemical response of plants to heavy metals can be studied more easily at the cellular level. Suspension cell cultures can be initiated starting from friable *in vitro* grown callus cells representing undifferentiated cells.^[1] Compared to non-callus cells they show a simpler organization and their growth conditions are better to control. Additionally, they retain the ability to synthesize typical secondary metabolites of intact tissue, which makes them a suitable model system for metabolic studies.^[2] In the present work we initiated and established a callus cell culture of carrot (*Daucus carota*) for the study of the interaction of crop plants with radionuclides on the molecular level. First experiments were performed to investigate the interaction of these cells with uranium.

EXPERIMENTAL. For initiation of the callus cell culture explants from a carrot were used. Referring to protocols given in the literature, the upper and lower ends of the carrot were cut.^[1,3] After that, the carrot was thoroughly washed with water. The plant material was sterilized for 20 minutes with 14% NaOCl (VWR) containing a few drops of Triton X-100 (Roth). To remove contaminants, the surface material was cut off subsequently with a sterile scalpel. The sterilization and cutting procedure was repeated. The resulting pieces were washed three times for 5 minutes with sterile water. After washing, the outer layers were removed again and the remaining tissue of the carrot was cut in small pieces that were placed on a solid cell culture medium. Petri dishes were sealed with Parafilm® (Bemis) and incubated in the dark at 25 °C. After initiation of the callus formation, the formed callus material was sub-divided and transferred onto fresh medium. Sub-cultivation to fresh medium B5C2 was performed in a time interval of four weeks to maintain the culture.^[4] To establish a *D. carota* suspension cell culture, fragments of the friable callus (Fig. 1A) were transferred to liquid medium B5C2 and the cells were grown with agitation (150 rpm) at 25 °C in the dark. Every seven days the cell suspension was sub-cultivated until the culture reached the desired density and was actively growing. Applying this suspension cells, first experiments were performed to study the time- and concentration-dependent U(VI) bioassociation of *D. carota*. For that, *D. carota* cells were exposed to 20 or 200 µM U(VI) up to 168 h in a phosphate reduced medium B5C2_{red}. After the end of the exposure time, the bioassociated amount of U(VI) as well as the cell vitality was analyzed as described in the literature.^[5]

RESULTS. Figure 1B exemplarily shows a growth curve of a *D. carota* cell suspension established from friable callus cells (Fig. 1A). The entire growth cycle involving a lag, exponential and linear phase ends after about two weeks, when the cells go into the stationary phase. A doubling of the initial cell amount is observed after about six days. This growth

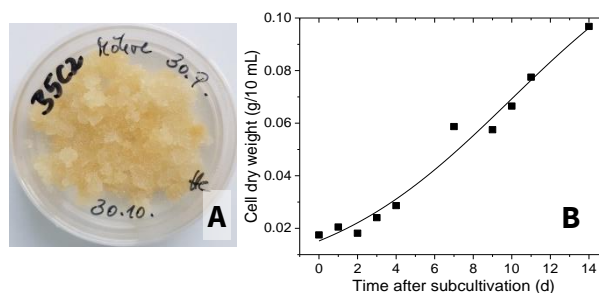


Fig. 1: Callus cells of *Daucus carota* (A) and growth curve of carrot cells in suspension cell culture (B).

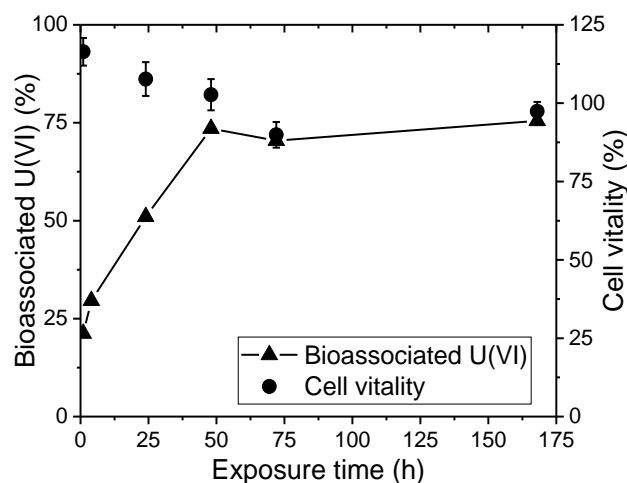


Fig. 2: U(VI) bioassociation and cell vitality of *Daucus carota* cells in the presence of 20 µM U(VI).

curve is in good agreement with those given in the literature.^[1]

In the presence of 20 or 200 µM U(VI) a time-dependent U(VI) bioassociation by *D. carota* cells was found, which is exemplary shown for 20 µM U(VI) in Fig. 2. After an initial increase of the bioassociation an equilibrium is observed after about 48 h, where up to 75 % of the total U(VI) is immobilized. The cell vitality is slightly higher or around 100 % compared to those of control cells. This indicates a slight increase of the metabolic activity of *D. carota* cells as response to the heavy metal stress. Furthermore, the cells are able to tolerate U(VI) under the studied conditions. In future, the U(VI) speciation in the presence of *D. carota* cells will be studied and released cell metabolites will be identified.

ACKNOWLEDGEMENTS. The authors thank J. Seibt, S. Heller, S. Beutner and S. Bachmann for experimental support. This work was funded by Federal Ministry of Education and Research (contract number 02NUK051B).

- [1] Evans, D. E. *et al.* (2003) *Plant Cell Culture*, Taylor & Francis, New York.
- [2] Zagoskina, N. V. *et al.* (2007) *Russ. J. Plant Physiol.* **54**, 237–243.
- [3] Lindl, T., Gstraunthaler, G. (2008) *Zell- und Gewebekultur*, Spektrum Akademischer Verlag, Heidelberg.
- [4] www.dsmz.de/fileadmin/Bereiche/PlantCellLines/Dateien/B5C2.pdf, last viewed Feb. 02, 2018.
- [5] Jessat, J. *et al.* (2019) *Report HZDR-096*, p. 37.

Microcosms as tool for analyzing the microbial influence on metal corrosion

M. Dressler, S. Kluge, A. Schierz, N. Matschiavelli

Microcosms are suitable small-scale experiments for analyzing the evolution of microbial diversity and correlated changes in bio-geochemical parameters within a selected environment. For simulating a “worst-case scenario” in a repository for high-level radioactive waste (HLW), bentonite, which represents the buffering material in between the canister containing the HLW and the host rock, was supplied with a synthetic pore water solution. In order to imitate potential canister materials, cast iron or copper plates were added as well as possible microbial electron sources like H_2 or lactate. After one month incubation at 37 °C with H_2 , cast iron containing microcosms indicated the formation of black precipitates and gas bubbles. Light microscopic analysis showed the formation of black precipitates and voids on the respective plates.

EXPERIMENTAL. Anaerobic bentonite microcosms were set up as described.^[1] For the stimulation of microbial processes, 5 mM lactate or 50 kPa H_2 (0.33 vol.-%) were added. Metal plates were rinsed with acid (copper with 20 vol.-% H_2SO_4 ; cast iron with 2N HCl), deionized water and pure Methanol, dried and added to microcosms.^[2] The well-mixed slurries were incubated at 37 °C in the dark for four months without shaking. Sampling took place at five time points. Geochemical parameters, metabolites, microbial diversity and corrosion processes on metal- and copper surfaces were analyzed as described.^[2,3] For the enrichment of sulfate reducers, 1 mL of incubated, homogenized slurry was transferred into sulfate-reducer medium.^[4]

RESULTS AND DISCUSSION. Microcosms containing cast iron and H_2 showed the formation of black precipitates around the plates and black spots in the bentonite slurry after one month. Furthermore, the formation of gases was observed (Fig. 1B). After four months under the respective conditions, light microscopic studies of incubated cast iron plates indicated the formation of voids and black precipitates on the cast iron surface (Fig. 1D). Analysis of geochemical parameters in the respective microcosms revealed an accelerated decrease of redox potential within the bentonite slurry as well as a significant increase of HCl-extractable ferrous iron and elemental iron (data not shown), pointing to an accelerated corrosion process of cast iron plates in these batches.^[2] Corrosion of the plates was determined gravimetrically and reached after four months incubation 0.12 mm/a (cast iron), 0.16 mm/a (cast iron and lactate) and 0.10 mm/a (cast iron and H_2).^[2]

On the contrary, copper containing microcosms, showed no significant effects on the here analyzed parameters (Fig. 1A).^[2] In general, the corrosion of copper-bentonite systems differs from the iron-bentonite systems, but both metals may react with corrosive sulfides.^[5] A major sulfide source within the bentonite buffer might be the activity of sulfate-reducing bacteria (SRB).^[6–8] In similar bentonite slurry experiments, the presence of microorganisms on an iron surface was reported.^[9] The microbial diversity in the here analyzed microcosms is under investigation. So far, no significant abundance of SRBs can be reported for the first sampling points, but we were successful in isolating a spore-forming SRB from cast iron containing microcosms that were incubated with lactate for four months.^[2] Thus, indigenous SRBs are present in bentonite B25 and can become viable in the

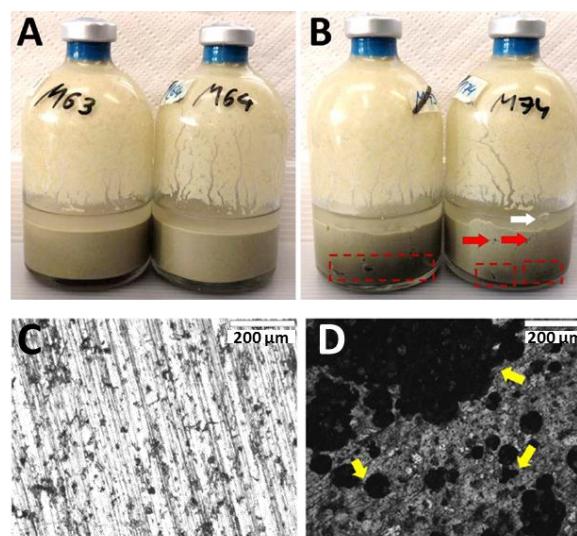


Fig. 1: Development of bentonite microcosms after one month incubation with H_2 at 37 °C. Microcosms with copper (A). Microcosms with cast iron (B). Red dashed lines: location of cast iron plates; red arrows indicate black precipitates; white arrow indicates gas formation. Light microscopic picture of a native cast iron plate (C). Light microscopic picture of a cast iron plate after four months incubation at 37 °C in a H_2 -supplemented microcosm (D). Yellow arrows indicate black precipitates and voids on the metal surface.^[2]

here simulated “worst case scenario”, potentially affecting materials used in a HLW repository. Further analysis regarding the characterization of the corrosion process, corrosion products and the potentially formed patina as well as the involvement of microorganisms in these processes are ongoing.^[9]

This study illustrates the importance of using microcosm experiments in order to analyze bentonites regarding their inherent microbial potential as well as their correlated influence on materials like the here applied metal plates, used in future HLW repositories.

ACKNOWLEDGEMENTS. We thank F. Lehmann for HPLC-analysis, C. Eckardt for IC-measurements and S. Beutner for ICP-MS measurements. Furthermore, we thank S. Kaufhold (BGR, Hannover, Germany) for providing B25 Bavarian bentonite. Cast iron (GGG40) and copper plates were provided by the GRS gGmbH (Braunschweig, Germany). This work was partially funded by the BMBF (Grant 02NUK053B) and HGF (Grant SO-093).

- [1] Matschiavelli, N. *et al.* (2019) *Environ. Sci. Technol.* **53**, 10514–10524.
- [2] Dressler, M. (2019) Master Thesis, TU Dresden.
- [3] Caporaso, J. G. *et al.* (2010) *Proc. Natl. Acad. Sci. U.S.A.* **108**, 4516–4522.
- [4] Postgate, J. R. (1963) *Appl. Microbiol.* **11**, 265–267.
- [5] Kaufhold, S. *et al.* (2017) *Corros. Eng. Sci. Technol.* **5**, 349–358.
- [6] Pedersen, K. (1997) *SKB Technical Report TR 97–22*.
- [7] Pedersen, K. (2010) *J. Appl. Microbiol.* **108**, 1094–1104.
- [8] Muyzer G.; Stams, A. J. M. (2008) *Nat. Microbiol.* **6**, 441–454.
- [9] Kaufhold, S. *et al.* (2015) *J. Hazard Mater.* **285**, 464–473.

Thickness of polyelectrolyte layers of separately confined bacteria alters key physiological parameters on a single cell level

I. Rybkin, D. Gorin,¹ G. Sukhorukov,² A. Lapanje³

¹Institute of Science and Technology, Skolkovo, Russian Federation; ²Queen Mary University of London, London, U.K.; ³Jožef Stefan Institute, Ljubljana, Slovenia

Confinement of bacterial cells in matrix or capsules is an integral part of many biotechnological applications. Here, we adapted the method for deposition of polyelectrolyte layers to entrap separated bacterial cells in a strong and permeable shell, a few nanometers thick. This enabled the investigation of effects of mechanical forces against the mass gain and cell division. Using the method of time-lapse confocal microscopy, we observed a prolonged lag phase, dependent on the confinement strength. In such a constraint both the GFP fluorescent signal from the leaking T7 promoter and cell size were increased by more than five and two times, respectively. We postulate that the observed effects could be caused by the perturbation of the sensing of the cell size, resulting in disproportional synthesis of the cell envelope against the intracellular material, which compels cells to grow rapidly.

EXPERIMENTAL. In our experiments we used cells of *Escherichia coli* top 10 transformed with pRSET-emGFP plasmid which were grown overnight in nutrient broth media. Optical density of the bacteria was adjusted to 1.2 after washing three times in saline solution of 0.9% NaCl. According to prepared modified protocol of LBL covering bacteria, we deposited PEI on cells by adding 0.25% solution of PEI (Poly(Ethyleneimine)) at pH7 to the cells in a 1:1 v/v ratio. This suspension was incubated for 5 min. Unattached PEI was removed by centrifugation at 900 × g for 2 min, discarding supernatant and gentle washing two times and resuspending in a saline solution. 0.25% PSS (Poly(Styrene Sulfonate)) at pH7 layer was added to the PEI covered in the same ratio. The washing step was the same, except 3 min centrifugation at 1,500 × g was used to obtain a sufficiently firm pellet. By repetition of these two steps, we were able to deposit up to four of such bilayers on the bacteria. The separately confined bacteria were analyzed under time lapse confocal microscopy and spectrophotometer, where we observed the changes in the speed of growth and expression of green fluorescent protein (GFP) over time.

RESULTS. The polyelectrolytes are not toxic to *E. coli*, but due to the high mechanical strength of the capsule wall, the physiological properties of the cell such as lag phase, colony formation and leakage expression are affected. Accordingly, measurements at a single cell level showed that the number of polyelectrolyte layers correlates positively with the duration of the lag phase. Over time, cells can escape from weaker capsules at the distal position. For stronger capsules the cracking process of the polymer wall is randomly distributed. Due to the intracellular electrostatic interactions, the escaped bacteria formed more spherical microcolonies than nonencapsulated bacteria. The mechanical stalling of the division also effects the cellular molecular physiology and biochemistry. We observed a high increase in the GFP fluorescent signal from the leaking operon. Furthermore encapsulated cells showed a 2–3 times increased length and width. We can conclude that the encapsulation of cells can be a versatile tool for the modification of the cell surface without ap-

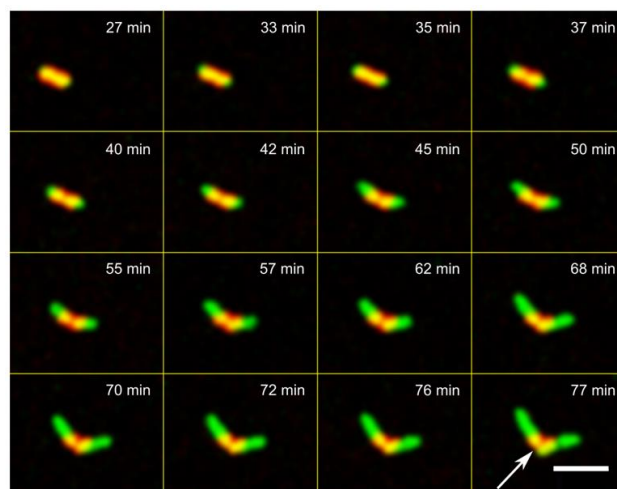


Fig. 1: Escape of *E. coli* cells from the polymer capsules being entrapped in low amount of layers (up to 6), scale bar = 5 μm.

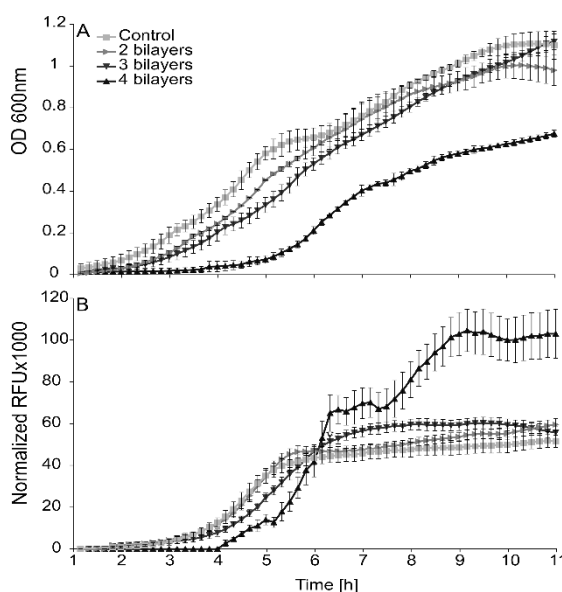


Fig. 2: Effects of the entrapment of cells in layers of polyelectrolytes on growth (A) and GFP fluorescence produced from the promoter leakage without induction (B) of the bulk population of bacterial cells.

plying genetic tools and might be suitable when the genetically modified organisms may not be used.

ACKNOWLEDGEMENTS. The research was performed at Jožef Stefan Institute and Saratov State University in collaboration with HZDR.

[1] Rybkin, I. et al. (2019) *Front. Bioeng. Biotechnol.* 7, 378.

SCIENTIFIC CONTRIBUTIONS (PART IV)

Nuclear Reactor
SAFETY
RESEARCH

Grain boundary analysis in a VVER-440 type reactor pressure vessel steel by electron backscatter diffraction

P. Chekhonin, F. Bergner, C. Heintze

Applying electron backscatter diffraction (EBSD) the microstructure of a VVER-440 type reactor pressure vessel (RPV) steel was characterized. A dedicated analysis that separates former austenite grain boundaries from grain boundaries formed by the bainitic transformation has been conducted.

The RPV is a safety relevant component of a nuclear power plant which determines its maximal potential operation time span. In RPV steels the neutron irradiation leads to a particle induced yield strength increase which results in an increase of the ductile to brittle transition temperature. Previous publications indicate that in the ductile to brittle transition temperature range, the size distributions of microstructural features, such as precipitates, inclusion and spacing of grain boundaries determine the fracture toughness.

The grain boundaries in bainitic steels can be either boundaries already existing before the bainitic transformation (prior austenite grain boundaries, PAGBs) or boundaries between bainitic blocks and packets that formed during the bainitic transformation. While conventional EBSD in a scanning electron microscope is easily applicable to detect grain boundaries in general, a distinction between PAGBs and block/packeted boundaries is not straight forward and requires additional analysis of the EBSD data. The structural transformation from austenite to bainite follows a certain orientation relationship,^[1,2] while different observable bainitic orientations (variants) within one prior austenite grain are related to the symmetry of the cubic lattice. In case of a VVER-440 base metal steel, such a distinction provides detailed statistics on the type of boundaries and the identification of variants occurring during the bainitic transformation. This may be relevant for the understanding of fracture initiation.

EXPERIMENTAL. An unirradiated sample of a VVER-440 base metal from the Greifswald Unit 8 was polished and analyzed in a Zeiss NVision 40 SEM equipped with a Bruker EBSD system. An in-house written EBSD evaluation software was applied to find the orientation relationship of the bainitic transformation and test the orientation relationship for each detected grain boundary.

RESULTS. The EBSD mapping (Figs. 1 (a) and (b)) reveals a bainitic microstructure. In Fig. 1 (a) the PAGBs are highlighted in red. The prior austenite grains are subdivided in packets (packet boundaries colored yellow) which again are subdivided in blocks (block boundaries colored black). The prior austenite grain size is evaluated to be 110 μm , while the packet and block size are 30 μm and 9.2 μm , respectively. Clearly, this analysis is a viable alternative to metallographic approaches where the etched boundaries are rather difficult to differentiate and small prior austenite grains can remain undetected. The size differences indicate that the majority of all grain boundaries originate from the bainitic transformation. Consequently, as demonstrated in Fig. 2 the grain boundary distribution shows a clear preference towards specific misorientation angles of 50° and higher. The peak at $\approx 60^\circ$ corresponds to a particularly preferred variant selection between adjacent blocks during the bainitic transformation. In fact, due to this preference, about 71 % of all grain boundaries have a similar misorientation angle of about 60.2° and a

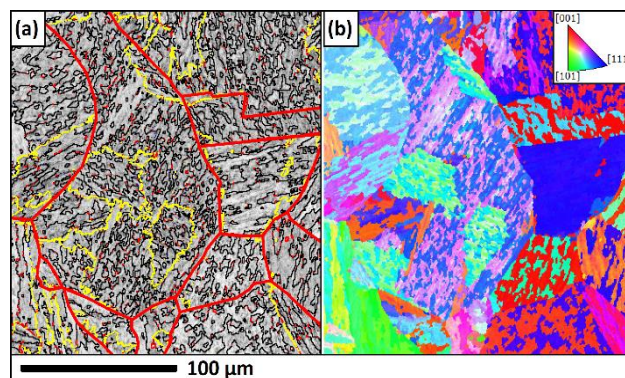


Fig. 1: EBSD mapping (subset) of the same area on a VVER-440 type RPV steel. PAGBs are colored red, packet boundaries yellow and block boundaries black (a). The inverse pole figure mapping with respect to the horizontal specimen direction is presented in (b).

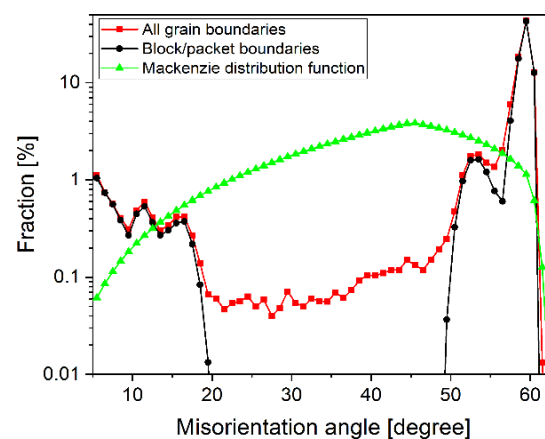


Fig. 2: Fraction of grain boundaries as a function of the misorientation angle. The theoretical Mackenzie distribution describes the case for grain boundaries aligned between randomly oriented grains in a cube lattice.

rotation axis close to $\langle 10 \ 13 \ 11 \rangle$. This is a stark contrast to a case with randomly oriented grains which would result in the Mackenzie misorientation angle distribution for the grain boundaries (green line in Fig. 2). This new information may be of great importance for future research, since there is a correlation between the locations of different types of precipitates and block, packet and prior austenite grain boundaries.

In summary, EBSD was successfully applied to study the grain boundary structure in a VVER-440 type steel. Prior austenite grains, packets and blocks are detected. The strong variant selection between adjacent blocks leads to just one type of grain boundaries predominating.

[1] Miyamoto, G. et al. (2010) *Acta Mater.* **58**, 6393–6403.
[2] Takayama, N. et al. (2012) *Acta Mater.* **60**, 2387–2396.

On the role of Ni, Si, and P on the microstructural evolution of FeCr alloys under irradiation

C. Heintze, B. Gómez-Ferrer,¹ C. Pareige¹

¹Normandie Université et INSA de Rouen, CNRS, Groupe de Physique des Matériaux, Rouen, France

Ni, Si, and P constitute typical impurities or minor alloying elements in ferritic/martensitic steels for nuclear applications. They are known to affect embrittlement and hardening under neutron irradiation by the formation of irradiation-induced or -enhanced solute-rich clusters (SRC) enriched with Ni, Si, P, and Cr.^[1-3] The present work was focused on the analysis of these clusters with the aim to elucidate the influence of the individual chemical species on the cluster formation and evolution with emphasis on early stages of irradiation. The study made use of ion-irradiation as a tool to emulate the effect of neutron irradiation.

EXPERIMENTAL. A set of tailored fully ferritic Fe-15Cr-X model alloys (X = Ni, Si, P, NiSiP in dilute concentration) was ion-irradiated with 5 MeV Fe²⁺ ions up to 0.1 and 0.5 dpa at a depth of 500 nm at 300 °C at the Ion Beam Center of HZDR. The samples including unirradiated reference samples of the same alloys were characterized by means of atom probe tomography (APT) employing a Local Electrode Atom Probe LEAP 4000 XHR from CAMECA. APT samples of the irradiated conditions were extracted by Focused Ion Beam method (FIB) such that the analysed volume corresponded to a depths range of 500 ± 100 nm. The obtained 3D atom maps were analyzed using statistical tools based on the 1st nearest neighbor distance distribution (1NN method) to detect early stages of clustering and by means of iso-concentration algorithms (IPM) to identify and quantify SRC with respect to their volume fraction, number density, size and composition.

RESULTS. An example for the solute distribution obtained by APT is shown in Fig. 1 for Fe15CrNiSiP after ion irradiation to 0.5 dpa at 300 °C. In that specific case, already visual inspection directly confirms that SRC enriched in Ni, Si and P were formed. 1NN frequency distributions of equal (X-X) and mixed (X-Y) element pairs were determined for all APT volumes and compared to the 1NN distance distribution for a corresponding random elemental distributions to detect even early stages of clustering (e. g. Fig. 1). On this basis the so-called V parameter was calculated as a measure on how far the spatial distribution of the present species deviates from a random distribution. The 1NN distance distributions in the unirradiated samples confirmed that the solutes are randomly distributed before ion irradiation. P atoms exhibit the strongest tendency to cluster under irradiation. They are the fastest diffusers forming clusters already at the lowest dose (0.1 dpa). No significant further increase of the V parameter is measured at 0.5 dpa indicating a saturation of P clustering around 0.1 dpa. In contrast to P, Ni and Si atom distributions only slightly deviate from a random distribution at 0.1 dpa, indicating a tendency to cluster, but at slower diffusion. Even at low dose, P, Ni and Si cluster together. The volume fraction, number density and size as well as the enrichment of the SRCs with Ni and Si increase with the irradiation dose.

It is worth to note, that for the Cr concentration present in this work, which is beyond the solubility limit for Cr in bcc Fe, Cr also forms irradiation-enhanced clusters (bcc Cr-rich alpha prime phase), not related to the SRC.

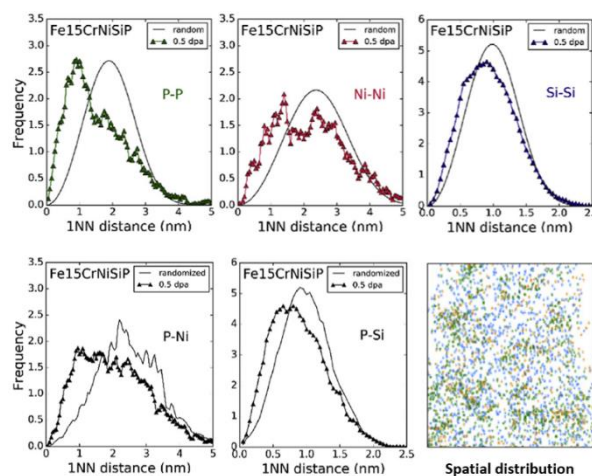


Fig. 1: Spatial distribution map of Fe9CrNiSiP after irradiation to 0.5 dpa at 300 °C and normalized frequency distributions of 1NN distances of X-X and X-Y pairs. (P in green, Ni in orange, Si in blue)

CONCLUSIONS. The results indicate an absence of synergistic effects among Ni, Si, and P in the formation of the SRCs and support the idea of an irradiation-induced rather than irradiation-enhanced formation mechanism of SRC by interstitial or vacancy dragging and decoration of small point defect clusters. Further experiments at higher doses are underway.

ACKNOWLEDGEMENTS. This research was partly funded by the European Commission, grant agreement no. 604862 (MatiSSE project). The use of the HZDR IBC facilities and the support by the staff is gratefully acknowledged.

- [1] Pareige, C. *et al.* (2015) *J. Nucl. Mater.* **456**, 471–476.
- [2] Kuksenkov, V. *et al.* (2013) *J. Nucl. Mater.* **432**, 160–165.
- [3] Bergner, F. *et al.* (2009) *Scr. Mater.* **61**, 1060–1063.
- [4] Gómez-Ferrer, B. *et al.* (2019) *J. Nucl. Mater.* **517**, 35–44.

Effect of anisotropic microstructure of ODS steels on small punch test results

E. Altstadt, F. Bergner, A. Das, M. Houska

Hot rolling and hot extrusion of oxide-dispersion strengthened (ODS) ferritic steels give rise to anisotropic microstructures and mechanical properties and may provoke related phenomena such as secondary cracking. In this study, we consider the small punch (SP) test – a method, applicable in the case of small amounts of available material and well established for isotropic materials. The effect of sample orientation on deformation and cracking was investigated. The applicability of the empirical conversion of SP-based into Charpy-based transition temperatures is evaluated. The fractographic manifestation of load drops in SP curves is identified.

EXPERIMENTAL. Three ODS steels were selected for testing, one hot-rolled and two hot-extruded (denominated as HR, HE1, HE2). HR is a hot-rolled plate with following main production steps: mechanical alloying in an attritor ball mill, encapsulation of the powder, hot isostatic pressing at 1,100 °C/100 MPa and rolling at 1,100 °C from a diameter of 80 mm to a plate of 7 mm thickness in 5 runs. The powder composition was 0.028 C, 0.051 Si, 0.01 P, 0.138 Ti, 12.99 Cr, 0.101 Ni, 1.01 W, 0.3 Y₂O₃, bal. Fe (wt.-%). HE1 is a hot-extruded steel round bar fabricated from the same primary powder batch as ODS-HR (hot extrusion at 1,100 °C). HE2 is a hot-extruded steel round bar from gas atomized pre-alloyed steel powder. Direct hot extrusion was performed at 1,150 °C with an extrusion ratio of 22.5. A final heat treatment at 1,050 °C/1h was applied (furnace cooling). The powder composition was 0.01 C, 0.37 Si, 0.006 P, 0.238 Ti, 13.76 Cr, 0.239 Ni, 0.84 W, 0.3 Y₂O₃, bal. Fe (wt.-%).^[1-3]

Small punch tests were executed in three orientations for HR (S-thickness direction, L-rolling direction and T-transverse direction) and in two orientations for HE-1 and HE-2 (L-extrusion direction, R/C-radial/circumferential direction). The orientation refers to the normal direction of the SP disc. In case of HE1 and HE2, the directions R and C are equivalent because of the axial symmetry of the extrusion process. The SP based ductile-to-brittle transition temperature T_{SP} was determined on the basis of normalized energies $E_n = E_{SP}/F_m$ of the different tests. E_{SP} is the area under the $F(v)$ curve up to the displacement v_m at maximum force F_m . In case of discontinuous load drops (pop-ins) in the $F(v)$ curve, the procedure for the energy calculation is modified so that the area under the force-displacement curve up to the first significant pop-in is used for the calculation of E_{SP} . Subsequent fractographic analysis of selected tested SP specimens was done by SEM using a Zeiss EVO 50 device.

RESULTS. For the hot-rolled ODS steel, pop-ins in the $F(v)$ curves (Fig.1) were found to be associated with liftings (flakes) in the fracture surface (Fig. 2). Such liftings were observed in cases of pop-ins with $\Delta F/F_m > 0.05$. The occurrence of pop-ins in the SP $F(v)$ curves and associated flakes correspond with the susceptibility to secondary cracks in fracture mechanics testing.^[1,2] These effects could not be observed in the hot-extruded materials.

The DBTTs are given in Tab. 1. The established correlation between DBTTs from SP test and Charpy impact test ($T_{SP} = \alpha T_{CVN}$) is questionable for L/T-oriented specimens of hot-rolled ODS material, which exhibit pop-ins in the load-displacement curves. This is due to the different load situations of the weak zones in SP and KLST samples. In contrast, for S-oriented SP samples the correlation is applicable. In

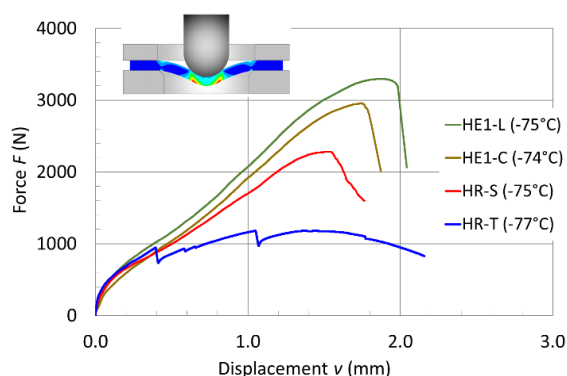


Fig. 1: Force-displacement curves for materials ODS-HR and ODS-HE1, test temperature –75 °C.

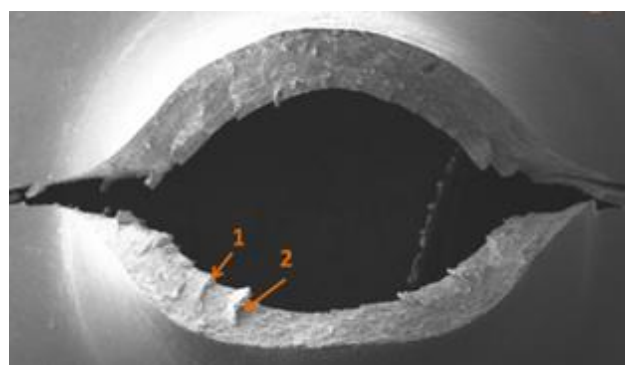


Fig. 2: SEM pictures of the fracture surface of a sample from HR tested at –150 °C, orientation T, flakes indicated by 1 and 2.

Tab. 1: Ductile-to-brittle transitions temperatures.

Mat.	HR	HR	HR	HE-1	HE-1	HE-2	HE-2
Orient.	L	T	S	L	C/R	L	C/R
T_{SP}	-96	-70	-157	-147	-130	-150	-154
T_{CVN}^*	+139	+199	-2	+21	+59	+13	+4

* Recalculated from: $T_{SP}[K] = 0.43 \cdot T_{CVN}[K]$.

hot-extruded ODS steels, the effect of anisotropy on the DBTT is significantly smaller as compared to hot-rolled materials. Therefore, the correlation is applicable for hot-extruded ODS steels irrespective of the sample orientation.

[1] Altstadt, E. et al. (2019) *Theor. Appl. Fract. Mech.* **100**, 191–199.

[2] Das, A. et al. (2017) *J. Nucl. Mater.* **491**, 83–93.

[3] Das, A. et al. (2017) *J. Nucl. Mater.* **497**, 60–75.

Novel and established applications of magnetic small-angle neutron scattering

A. Ulbricht, F. Bergner

The outstanding role of magnetic small-angle neutron scattering (SANS) in condensed matter physics and materials science has been substantiated in a recent review. Two selected cases of established applications in the field of structural materials for future nuclear fission and fusion devices are addressed in some detail and new insight is reported.

NOVEL APPLICATIONS. In a recent review on applications of magnetic SANS, the following topics of interest were identified:^[1]

- Nd-Fe-B-based permanent magnets,
- magnetic steels,
- magnetic nanoparticles and ferrofluids,
- skyrmion lattices and noncollinear spin structures,
- vortex lattices in superconductors.

Some of these topics, such as magnetic skyrmion lattices recently discovered at FRM II Munich, opened up new fields of basic and applied research.^[2] Moreover, emerging micro-magnetic simulation techniques contribute to an improved understanding of experimental findings. Other applications of magnetic SANS are now well established with respect to the basics, but receive continued attention as an avenue to ensembles of nanofeatures in macroscopic volumes. For example, magnetic SANS turned out to add an indispensable contribution to the understanding of irradiation effects on the nanostructure and mechanical properties of ferromagnetic Fe-based nuclear fission and fusion materials. New insight obtained by means of magnetic SANS include, but is not limited to,^[1]

- the effects of the impurity element Cu, the alloying elements Mn and Ni, the neutron fluence and the neutron flux on hardening and embrittlement of reactor pressure vessel (RPV) steels,
- the detrimental role of Cr-rich α' -phase particles on neutron-irradiated ferritic/martensitic high-Cr steels,
- the type and size distribution of oxide nanoparticles in oxide dispersion strengthened nanostructured steels.

SELECTED APPLICATIONS OF SANS. The irradiation-induced nanostructure of neutron-irradiated RPV steels was found to depend on the rate (flux) at which a given neutron fluence is accumulated, as shown in Fig. 1 for the volume fraction and size of irradiation-induced solute atom clusters in a low-Cu RPV steel.^[1,3]

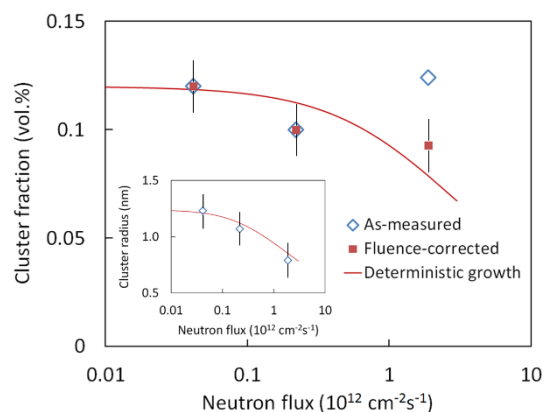


Fig. 1: Volume fraction and size (inset) of irradiation-induced solute atom clusters as function of flux for irradiated 22NiMoCr3-7 type RPV base material.

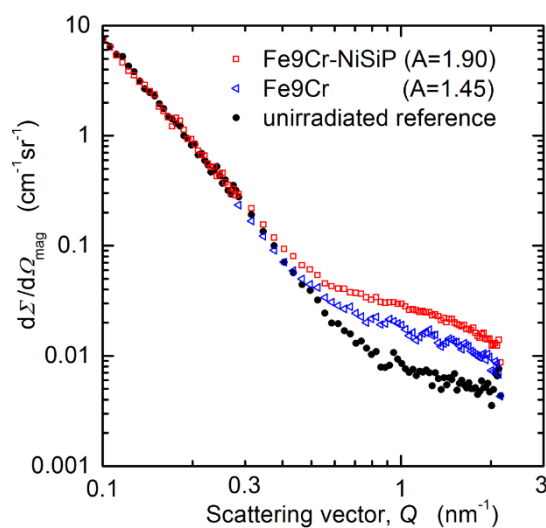


Fig. 2: Magnetic scattering cross sections as function of the scattering vector for neutron-irradiated NiSiP-free and NiSiP-containing Fe-9Cr model alloys.

A model based on the notion of deterministic growth describes the flux dependence of volume fraction and size simultaneously reasonably well.^[3] It is important to note that variations of the primary irradiation parameter, neutron fluence, give rise to major changes of the volume fraction, but only minor changes of the cluster size. Therefore, the former effect has to be considered by introducing a fluence-dependent correction of the volume fraction derived from the SANS experiment (Fig. 1).

Fe-9Cr-based ferritic/martensitic steels are of cross-cutting interest for future nuclear fission and fusion applications. The role of alloying and impurity elements on the formation of irradiation-induced nanofeatures is, however, not yet well understood. Therefore, a set of model alloys was exposed to neutron irradiation (0.1 displacements per atom, 300 °C) in the BR-2 reactor at Mol (Belgium). The SANS samples were placed in a saturation magnetic field allowing magnetic and nuclear scattering contributions to be separated. The magnetic scattering cross sections are plotted in Fig. 2, while the magnetic-to-nuclear scattering ratios A are given in parentheses. If the scatterers are nanovoids, $A = 1.4$ is expected. It can be concluded that the dominant type of scatterers are indeed nanovoids for a Ni-Si-P-free model alloy. Neutron irradiation (same conditions) of a Ni-Si-P-containing model alloy gives rise to the formation of solute atom clusters of higher volume fraction. These findings are integral part of ongoing research within European collaboration using complementary techniques of nm-scale sensitivity such as magnetic SANS, (scanning) transmission electron microscopy and atom probe tomography.

[1] Mühlbauer, S. *et al.* (2019) *Rev. Mod. Phys.* **91**, 015004.

[2] Mühlbauer, S. *et al.* (2009) *Science* **323**, 915–919.

[3] Wagner, A. *et al.* (2016) *Acta Materialia* **104**, 131–142.

Neutron fluence calculations and experimental validation for the dismantling of a German PWR

R. Rachamin, A. Barkleit, J. Konheiser

The German Atomic Energy Act was amended in 2011 to phase out the use of nuclear energy for the commercial production of electricity. Consequently, all German nuclear power plants (NPPs) will have been shut down by the end of 2022. Hence, the decommissioning and dismantling of the NPPs in a safe, economical, and timely manner will be an essential challenge in the next decades. Decommissioning studies have to be performed for each of the shutdown NPPs. The planning and implementation of the decommissioning strategy for an NPP require knowledge of the neutron activation and contamination levels, which have emerged during its operation. The extent and levels of activation in an NPP depend on the neutron fluence distribution within the NPP components. The present work is, therefore, aimed to estimate precisely the neutron fluence within the reactor and the nearby components of a German pressurised-water reactor (PWR).

MONTE-CARLO CALCULATIONS. The calculations of the neutron fluence distribution within the German PWR components are performed using the MCNP6 code.^[1] A detailed 3D MCNP geometrical model of the reactor was developed based on original technical drawings. A schematic view of the model is shown in Fig. 1. The neutron source for the calculations is specified as a fixed source and it is based on real German PWR operating conditions. The source was defined pin-by-pin, whereas each pin is divided into 32 axial layers. To achieve reliable statistical neutron fluence results in a reasonable computational time, the mesh-based weight windows technique is applied in the calculations.

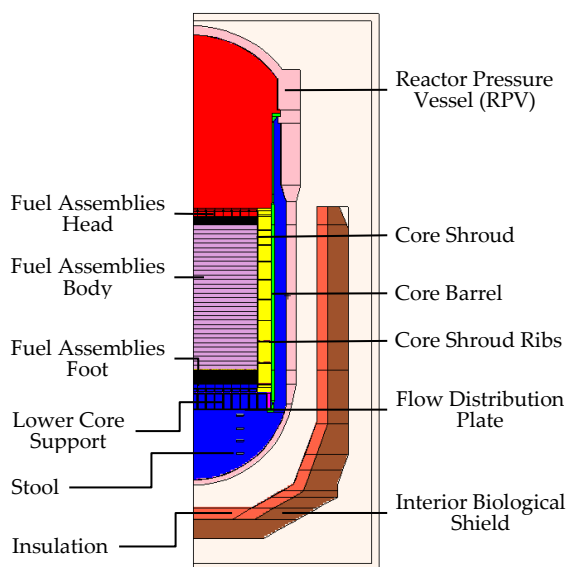


Fig. 1: 3D MCNP model of a German PWR.

EXPERIMENTS. To validate the Monte-Carlo calculation results, neutron fluence measurements are carried out in two still running German PWRs. The measurements are based on activation monitors, which are irradiated during a reactor cycle (approximately one year) at different construction components. Each monitor (see Fig. 2) is composed of nine thin metal foils (Ti, Fe, Ni, Cu, Zn, Nb, In, Sn, Ta) that are located in an aluminum box. The metal foils have a thickness

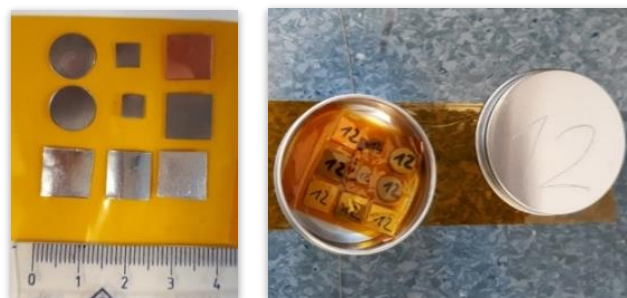


Fig. 2: Activation monitor: Nine metal foils packed in Kapton foil and located in an aluminum box.

of 0.1 mm and a size of 5 × 5 mm to 10 × 10 mm or 10 mm diameter. The monitors are placed and removed during the annual revision of the reactors. After recovery, the neutron activation products are analyzed by gamma spectroscopy and liquid scintillation counting (LSC).

RESULTS AND DISCUSSION. Figure 3 presents the calculated neutron fluence spectrum in the RPV, core barrel, and the inside biological shield. The fluence values were averaged over the segment parallel to the fuel assembly's active length.

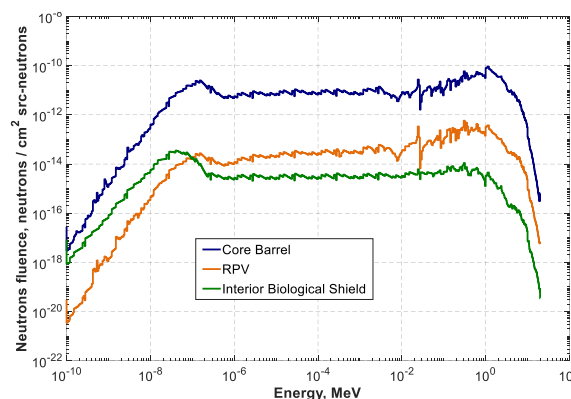


Fig. 3: Neutron fluence spectrum in selected components (relative error less than 1%).

Currently, the activities from the irradiated monitors are being analyzed, and the activities at the location, where the monitors were placed, are calculated based on the calculated neutron fluence rates. The comparison between the calculated and measured values will validate the accuracy of the MCNP model. The MCNP model will be used, then, for a detailed estimation of neutron fluence distribution within the PWR components for the ensuing activation calculations.

ACKNOWLEDGEMENTS. This work is funded by the Federal Ministry of Education and Research (BMBF) under contract number 15S9409A and supported by PreussenElektra GmbH.

[1] Goorley, T. et al. (2012) *Nucl. Technol.* **180**, 298–315.

Uniform fission source method in coupled Monte Carlo/Thermo-Hydraulic calculation

Y. Bilodid

One of challenges of the Monte Carlo full core simulations is to obtain acceptable statistical variance of local parameters throughout the whole reactor core at a reasonable computation cost. The statistical variance tends to be larger in low-power regions. To tackle this problem, the Uniform-Fission-Site method was implemented in Monte Carlo code MC21 and its effectiveness was demonstrated on NEA Monte Carlo performance benchmark.^[1-3] The very similar method is also implemented in Monte Carlo code Serpent under the name Uniform Fission Source (UFS) method.^[4] In this work the effect of UFS method implemented in Serpent is studied on the BEAVRS benchmark which is based on a real PWR core with relatively flat radial power distribution. It is shown that the application of the Uniform Fission Source method has no significant effect on radial power variance but equalizes axial distribution of variance of local power.

The idea of the UFS method is to get more source points in regions where fission power is low, and eventually improve statistics in the outermost fuel pins in full-core calculations. In the original implementation, the core geometry is covered by a mesh in which the code collects the fission source distribution during the inactive neutron cycles. This distribution is then used to adjust the number of emitted fission neutrons during the active cycles. The fission number is increased or decreased by a factor proportional to the inverse of the local fission rate, and the statistical weights are adjusted accordingly to avoid biasing the transport simulation. Recently a fission source convergence acceleration (SCA) routine based on the response matrix method was implemented in the Serpent code.^[5] The method provides a spatial distribution in a super-imposed mesh that approximates the converged fission source. It was shown that the SCA method greatly improves the initial guess for the fission source, and reduces the number of inactive cycles needed for source convergence.

In this work, the combination of SCA and UFS methods is implemented and applied to obtain faster source convergence and improved statistics for the outermost fuel pins in a full-core calculation. This is accomplished by obtaining the spatial fission source distribution for the UFS directly from the response matrix solver. Since the approximated fission source distribution is also used to accelerate source convergence, the weighting factors for the UFS are obtained without additional computational cost.

TEST. To evaluate effects of UFS method on a coupled calculation, the 3×3 PWR mini-core was simulated at the full power with thermo-hydraulic and thermo-mechanic feedbacks by coupled system Serpent-Subchanflow-Transuranus.^[6] The mini-core model was chosen to reduce computation costs of a coupled calculation. The steady-state was simulated without burnup, with critical boron concentration search and equilibrium xenon concentration. For each coupled calculation 20 neutronics – thermo-hydraulic iterations were performed.

RESULTS. The UFS method implemented in Serpent redistributes fission source to equalize variance of the local tallies throughout the reactor core. The implementation in Serpent al-

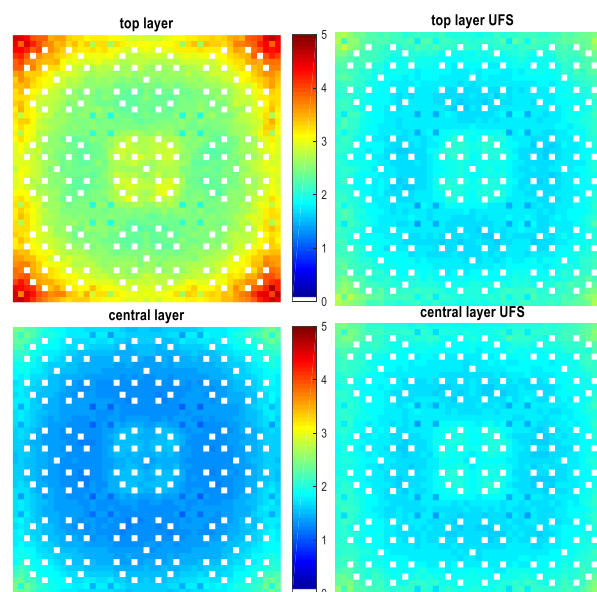


Fig. 1: UFS effect on uncertainties in periphery.

lows to use UFS method together with source convergence acceleration without additional computational costs. The application of UFS method to a coupled neutronic/thermo-hydraulic solution of a 3×3 mini-core test resulted in significant unification of the error in local power (see Fig. 1) and thus the reduction of the maximal relative error, which appears in low-power regions on the core periphery. No significant influence on iteration convergence was found, other than improvement of the local power convergence.

ACKNOWLEDGEMENTS. This work has been funded from the McSAFE project which is receiving funding from the Euratom research and training program 20142018 under grant agreement No 755097.

- [1] Kelly, D. J. *et al.* (2012) in *Proc. of PHYSOR-2012*.
- [2] Griesheimer, D. P. *et al.* (2015) *Ann. Nucl. Energy* **82**, 29–40.
- [3] Hoogenboom, J. E. *et al.* (2009) in *Proc. of M&C-2009*.
- [4] Leppänen, J. *et al.* (2015) *Ann. Nucl. Energy* **82**, 142–150.
- [5] Leppänen, J. (2019) *Ann. Nucl. Energy* **128**, 63–68.
- [6] Ferraro, D. *et al.* (2020) *Ann. Nucl. Energy* **137**, 107090.

Analysis of In-Vessel Melt Retention for Konvoi Pressurized Water Reactor for selected severe accident scenarios

M. Jobst

Further enhancing the nuclear safety in the accident management domain received a substantial reflection after the Fukushima accident. One of such accident management measures is the In-Vessel Melt Retention (IVMR) of molten corium. The applicability of IVMR for German Pressurized Water Reactor (PWR) of type Konvoi was assessed by means of analyses with the severe accident code ATHLET-CD.

IVMR strategy is already implemented in the Severe Accident Management Guidelines for several operating small size light water reactors (such as VVER-440). In the framework of the EU H2020 “In-Vessel Melt Retention Severe Accident Strategy for Existing and Future NPPs” project, the applicability and technical feasibility of IVMR for high power reactors is assessed. HZDR contribution to the project was the investigation of IVMR strategy for German PWR type Konvoi (high power reactor with 1,300 MW).^[1]

INVESTIGATED SCENARIOS. Four different severe accident scenarios with core material relocation to the lower head have been investigated: Station Blackout (SBO), and three Loss-of-coolant-accidents (LOCA) of different sizes: Small break LOCA (SBLOCA) with 20 cm² leak in cold leg, medium break LOCA (MBLOCA) with break of the pressurizer surge line, and large break LOCA (LBLOCA) with double-ended guillotine break of one cold leg. For all LOCAs the unavailability of any active safety injection system and only passive injection by the accumulators was assumed. For all scenarios, the complete flooding of the reactor cavity before the first relocation of molten core material to the lower head is assumed. Further assumptions have been defined in the framework of the project in order to make results obtained for different types of PWR comparable (e. g. the same power density for each type of reactor, defined heat transfer coefficient on the outer surface of the vessel = 10,000 W m⁻² K⁻¹).

PERFORMED ANALYSES. The four scenarios have been studied with the severe accident code ATHLET-CD 3.1A, developed by GRS and the input model of a generic German PWR has been applied.^[2-5] The current version of the ATHLET-CD code can simulate a two-layer configuration (oxidic pool with metal layer on-top) with continuous relocation of molten material from the core region. Such configuration is expected to occur for high corium oxidation degree with high iron to corium ratio.^[6] Due to high heat conductivity of the metal, an increased heat flux (HF) is observed in the metal layer (focusing effect), which leads to melting of the vessel wall and possible melt through. With the previous ATHLET-CD version 3.0A, it was possible to investigate a homogenous pool configuration only, which resulted in unrealistic low maximum HF of ≈ 550 kW m⁻² for the LBLOCA scenario, neglecting any focusing effect.^[7] Furthermore, the ablation of the vessel wall is now taken into account, which was not the case with the previous version. Consequently, the current simulations describe a more realistic behavior of the investigated scenarios.

RESULTS. The observed maximum HF (on the outer wall surface) and minimum residual wall thicknesses calculated by ATHLET-CD are shown in Tab. 1. The time evolution of

the minimum wall thickness is depicted by Fig. 1. As the primary pressure is low for these scenarios (due to large leak in case of LBLOCA and MBLOCA, or due to depressurization of the primary circuit if the coolant temperature exceeds 650 °C in case of SBO and SBLOCA), the integrity of the vessel can be maintained and no failure of the vessel is observed.

Tab. 1: Results of ATHLET-CD simulations.

Scenario	Relocation to lower head (min)	Max. heat flux (MW m ⁻²)	Min. residual wall thickness (mm)
LBLOCA	24	1.64	21
MBLOCA	66	1.67	21
SBLOCA	222	1.67	21
SBO	271	1.47	25

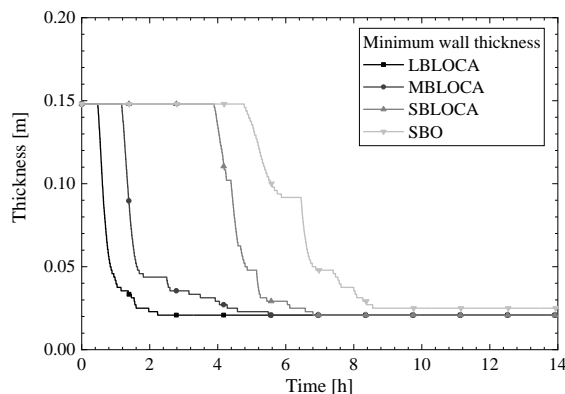


Fig. 1: Evolution of minimum RPV wall thickness.

DISCUSSION. The simulations showed that with the assumptions made IVMR seems to be possible without vessel failure. It has to be mentioned, that the calculated max. HF on the outer surfaces are high due to the focusing effect (up to 1.67 MW m⁻²). However, experiments with flow optimization outside the vessel revealed a critical HF of up to 1.8 MW m⁻².^[8] Furthermore, ATHLET-CD neglects the melting and relocation of several metal components, e. g. fuel rod plugs, or core support plate, which would increase the metal layer thickness and decrease the HF.

ACKNOWLEDGEMENTS. This work was funded by the IVMR grant agreement number 662157 (H2020).

[1] Jobst, M. (2019) Report IVMR project deliverable D2.6. Appendix 2.6.
 [2] Austregesilo, H. et al. (2016). ATHLET-CD 3.1A User's Manual.
 [3] Tushcheva, P. et al. (2015) *atw* **60**, 442–447.
 [4] Jobst, M. et al. (2017) Report HZDR-080.
 [5] Wilhelm, P. et al. (2018) *Ann. Nucl. Energy* **122**, 217–228.
 [6] Asmolov, V. G. et al. (2004) MASA Seminar.
 [7] Wilhelm, P. et al. (2016) IVMR project deliverable D.2.5, p. 155–177.
 [8] Dinh, T. et al. (2003) Report University of California CRSS-03/06.

The efficiency of sequential accident management measures for a German PWR under prolonged station blackout conditions

Y. Kozmenkov, M. Jobst, S. Kliem, K. Kosowski,¹ F. Schäfer, P. Wilhelm

¹PreussenElektra GmbH, Germany

The model of a German Siemens KWU-type PWR is used in a series of calculations to evaluate station blackout (SBO) coping time provided by a set of the countermeasures relevant to the defense-in-depth level four. The analyzed accident management measures (AMMs) cover a sequence of the bleed and feed procedures, starting/ending with secondary/primary side depressurization followed by the feeding of steam generators (SGs) in the passive or active mode and coolant injection from hydro-accumulators (HAs) to the primary system.

ACCIDENT SCENARIO. The accident is initiated by the loss of offsite power under nominal conditions of the plant operation (100% power). The emergency diesel power supply is completely lost. The reactor protection system is powered by batteries for a short term period. All active safety emergency core cooling systems are unavailable, while a passive safety injection from HAs remains available. Feedwater supply to the SGs is completely lost. The pressurizer (PRZ) relief and safety valves as well as SG safety valves are available. A mobile pump is available to feed SGs after their depressurization.

RESULTS. Four SBO cases have been simulated with the code ATHLET-CD starting from the same initial state but differing in the applied AMMs:^[1–3]

Case 1: AMM-1; **Case 1a:** AMM-1+AMM-3; **Case 2:** AMM-1+AMM-2; **Case 2a:** AMM-1+AMM-2+AMM-3. Where: AMM-1 – secondary bleed by main steam safety valve and passive feed by feedwater system; AMM-2 – secondary bleed by main steam safety valve and active feed by a mobile pump; AMM-3 – primary bleed by pressurizer valves and passive feed by hydro-accumulators.

Main results of the analysis are summarized in Fig. 1 and Tab. 1, where they are compared to the simulation without AMMs (**Case 0**).

Each of the two implemented secondary bleed and feed procedures (AMM-1 and AMM-2) provides nearly equal contributions to the coping time, increasing it (compared to **Case 0**) by 10–11 hours, so that the cumulative time window reaches 24 hours. In contrast, the primary bleed and feed countermeasure (AMM-3) is significantly less efficient (in particular due to a limited amount of available coolant in HAs), being able to extend SBO coping time by slightly more than half an hour. With the coping time as long as 24 hours, the recovery

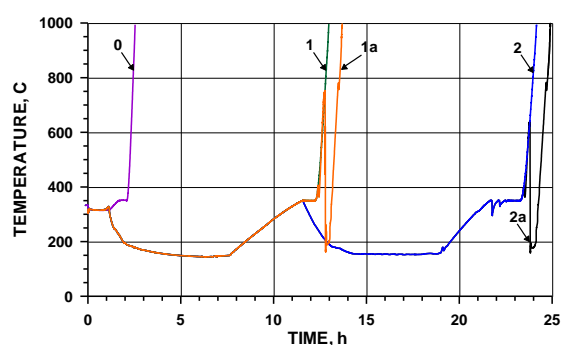


Fig. 1: Core outlet temperature.

Tab. 1: AMM-related sequence of events and their impact on core degradation onset.

Event	Elapsed time since SBO initiation (h:min)				
	0	1	1a	2	2a
Coolant level in SGs < 4.4 m			00:35		
Depletion of SGs at high pressure			01:00		
Initiation of AMM-1	–		01:05		
Start of feedwater tank depletion	–		01:25		
Disconnection of HAs from cold legs	–		01:30		
Start of coolant injection from HAs to hot legs (HLs)	–		01:40		
End of feedwater tank (FWT) depletion	–		02:20		
Termination of coolant injection from HAs to HLs	–		07:20		
Depletion of SGs after AMM-1	–		07:40		
Initiation of AMM-2	–	–	–	11:30	
Complete depletion of emergency feedwater tank (EFT)	–	–	–	17:20	
Depletion of the single SG after AMM-2	–	–	–	19:10	
Initiation of AMM-3	–	–	12:20	–	23:30
Disconnection of HAs from HLs	–	–	12:50	–	23:50
Core degradation onset	02:30	12:50	13:25	24:00	24:35

of AC power for the Siemens KWU plant before reaching core degradation onset (CDO) becomes more likely. For comparison reasons, only one of four EFTs has been depleted (by the operating mobile pump) in the simulations. Depletion of all four EFTs extends the coping time more than twice.

[1] Austregesilo, H. et al. (2014) ATHLET-CD Mod. 3.0 – Cycle B. User’s Manual, GRS.

[2] Wilhelm, P. et al. (2018) Ann. Nucl. Energy **122**, 217–228.

[3] Sonnenkalb, M.; Mertins, M. (2012) Severe Accident Mitigation in German NPP–Status and Future Activities. EUROSAFE Forum 2012.

Neutronic modeling of the FFTF isothermal physics tests with DYN3D

E. Nikitin, E. Fridman

The isothermal physics tests performed on the small core of Fast Flux Test Facility were analyzed with DYN3D. The selected tests comprise a multitude of reactivity measurements. The obtained numerical results were in a very good agreement as compared to the experimental data. This study provided an additional contribution to the validation of DYN3D for neutronic analyses of Sodium cooled Fast Reactors.

Recently, the capabilities of the reactor dynamics code DYN3D were extended with new models to perform static and time-dependent reactor analyses of Sodium cooled Fast Reactor (SFR) cores.^[1] As additional testing against experiments ensures the consistency of the code, the isothermal physics tests performed on the Fast Flux Test Facility (FFTF) core in February 09, 1980 were selected for the succeeding code validation.^[2]

DESCRIPTION OF THE FFTF CORE. The FFTF has a 400 MWth core loaded with 73 U-Pu mixed oxide fuel assemblies. The core is divided into an inner and outer zone with different Pu content of 22.43 and 27.37 wt.-%, respectively. Radially, the active core is surrounded by 106 reflector and 114 shielding assemblies. Twelve identical absorber assemblies with three different roles controlled the reactor: three primaries for safety, six secondaries for control, and three fixed and fully inserted ones on core periphery. The experiments were conducted at zero power while the core was maintained at temperature of around 478 K. A more detailed description can be found in the technical report of Idaho National Laboratory.^[3]

SELECTED ISOTHERMAL PHYSICS TESTS. The 32 control rod related reactivity measurements and the experiment to identify the isothermal temperature coefficient were chosen for the validation of DYN3D. In this report, only a fraction of the tests are presented, as they sufficiently demonstrate the code performance. These comprise the evaluation of eleven control rod worth values as well as the isothermal temperature coefficient. The rest of the simulations and a more profound assessment can be found in the corresponding paper of the authors.^[4]

The rod worth values were obtained by dropping individual or group of control rods from a reference subcritical state. In this state, four of nine moveable control rods remained completely inserted in the core. Only the remaining rods were dropped one by one or in groups. A more exact description of rod positions are available in the technical report.^[3]

The isothermal temperature coefficient was measured for the critical isothermal state while the reactor core temperature was increased from 468 K to 487 K with the help of the secondary systems.

NUMERICAL RESULTS. The numerical results of the control rod worth tests are summarized in Tab. 1. As compared to the experiment, in all cases, the numerical solutions of DYN3D were in a very good agreement while not exceeding the measurement uncertainty of 5–6%.

In order to obtain the isothermal temperature coefficient, the critical core configuration was adjusted by ± 5 K from the reference 478 K. The corresponding Doppler broadening of the microscopic cross sections was considered in all materials. A uniform thermal expansion of core structures including the

Tab. 1: Control rod worth values (\$).

Index of dropped rod(s)*	Experiment	DYN3D
1	6.04 ± 0.32	6.24
2	5.89 ± 0.31	5.94
3	4.65 ± 0.25	4.68
5	3.84 ± 0.20	3.81
7	2.90 ± 0.15	2.99
1+2	12.45 ± 0.69	12.72
1+3	11.01 ± 0.60	11.19
1+5	9.00 ± 0.48	9.05
3+5	8.80 ± 0.46	8.96
1+2+5	15.84 ± 0.87	15.88
2+3+5	15.22 ± 0.86	15.76

*: the exact position of these rods is defined in the technical report.^[3]

expansion of the assembly pitch was considered in this study. In this case, the linear dimensions of the solid geometry were expanded by about $\pm 0.04\%$. In the sake of mass preservation, the solid material densities were adjusted inversely proportional to the volumetric change. The density of the liquid sodium was set according to the benchmark specification. As compared to the experimental value of -1.26 ± 0.19 c/K , DYN3D value of -1.50 c/K is in a good agreement when considering the relatively high uncertainty of the measurements.

CONCLUSIONS. The isothermal temperature coefficient estimated with DYN3D as well as some other results only presented in the full paper of this study were within 2σ experiment uncertainty.^[4] However, the remaining majority of DYN3D estimates, including the presented rod worth values, agreed well within 1σ .

In summary, the reported study provided an additional contribution to the validation of DYN3D for neutronic analyses of small-size SFR cores.

- [1] Rohde, U. et al. (2016) *Prog. Nucl. Energy*, **89**, 170–190.
- [2] Rothrock, R. B. (1981) *FFTF isothermal physics tests*, Hanford Engineering Development Laboratory, Richland, WA, U.S.A.
- [3] Bess, J. D. (2019) *NEA/NSC/DOC(2006)1, FFTF-LMFR-RESR-001, rev. 2*, OECD NEA.
- [4] Nikitin, E. et al. (2019) *Ann. Nucl. Energy* **132**, 679–685.

Extension of the DYN3D/ATHLET code system to SFR applications

V. A. Di Nora, E. Fridman

To extend the DYN3D applicability to safety analyses of sodium fast reactor (SFR) systems, a coupling with a thermal-hydraulics (TH) code capable of sodium flow modeling is needed. At HZDR, the TH system code ATHLET has been already coupled with DYN3D for light-water reactors (LWRs), the code system has now to be extended to SFR applications. The report provides an overview of the steps necessary for the extension of the coupled tool. Subsequently, the main progresses achieved and the ongoing developments are briefly exposed. Finally, an outlook on future steps of the code system extension is proposed.

BACKGROUND & MOTIVATION. The DYN3D code is a multi-group neutron kinetics (NK) solver, initially developed for LWRs.^[1] Recently, the code is being extended to SFRs applications. The extension includes the development of the Monte Carlo based few-group cross sections (XSs) generation methodology, the updating of the TH database with thermal-physical properties of sodium, and the development of a thermal-mechanical (TM) model to account for radial thermal expansion of diagrid and axial thermal expansion of fuel.^[2] The extended version of DYN3D has been validated against the IAEA benchmarks devoted to the Phénix reactor, and in particular, against the control rods (CR) withdrawal tests and the natural circulation test.^[3,4] Currently, the modeling capabilities of DYN3D are limited to the core analyses. In order to extend its applicability beyond the core level, a coupling with a TH system code capable of sodium flow modeling is needed. At HZDR, the TH system code ATHLET has been considered for this purpose. The coupled code system DYN3D/ATHLET already exists for LWRs and it has to be properly extended to account for the modeling peculiarities characterizing SFRs.^[5]

COUPLING EXTENSION, PLAN & OBJECTIVES. The code system extension is currently under development. In the following are listed the steps planned for upgrading the DYN3D/ATHLET code system.

As a first step, improvements on the stand-alone mono-physics modeling are expected to be made, namely on the modeling of neutron kinetics (NK) and of the TH:

- Under the NK modeling profile, some arrangements turned out being necessary to speed up the calculations. To achieve such an objective, it has been chosen to take action on the reduction of the number of groups employed for the characterization of the XSs.
- From the TH perspective, for SFRs the modeling of the out-of-core metallic structures and their thermal-expansion is of remarkable importance. In fact, whenever the out-of-core structures expand, the relative position of the core and control rods (CR) changes affecting the core reactivity. To catch the out-of-core feedback effects correctly, thermal expansions of vessel, strong back, diagrid and CRs-driveline have to be modeled.
- As SFR systems are characterized by three-dimensional regions, additional improvements of the TH modeling could be made by employing an ATHLET 3D option, which accounts for fully 3D momentum equations.

Once all the modeling improvements are implemented, the code system should be able to predict the behavior of SFRs properly. As a final step, the capabilities of the code system will be validated and demonstrated by exploiting data avail-

able from SFR experiments (*e. g.* the Phénix natural convection test).

PROGRESS & ONGOING DEVELOPMENTS. Among the objectives of the coupling extension, the following progresses have been accomplished.

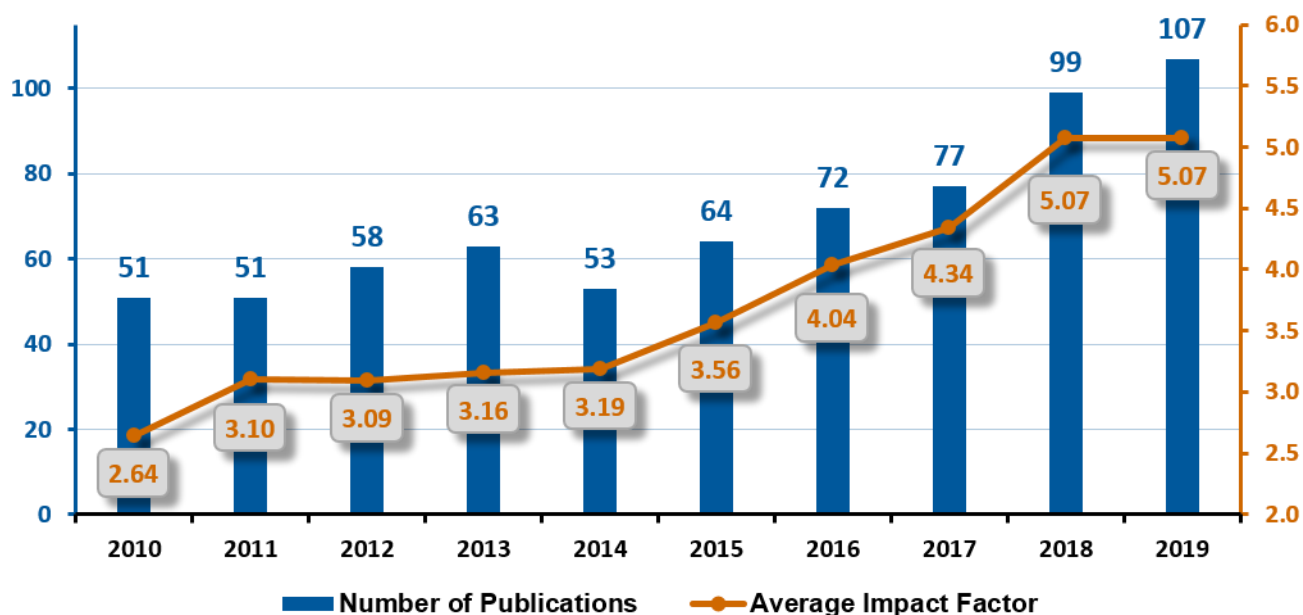
- For the reduction of the computational time in neutronics calculations, a new methodology based on heuristic search techniques has been developed. Such procedure condenses the energy bins characterizing the XSs, preserves as much as possible the quality of the solutions, and significantly decreasing the computational times. The methodology has been successfully tested on stationary conditions and it is meant to be tested soon under transient conditions.
- Initial simplified TH models of the out-of-core structures have been implemented and are being verified in the framework of the Superphénix (SPX) TH benchmark on six different transients. Furthermore, more complete and detailed mockups of the ex-core structures are being developed for the modeling of the ESFR-SMART.^[6]
- Again, within the scope of the ESFR-SMART modeling, also the exploration of the 3D ATHLET option has been implemented and is currently under the testing phase. Additionally, in support of the coupling extension, verification and calibration activities have been carried out on ATHLET stand-alone. For instance, ATHLET has been verified successfully against TRACE on SPX start-up tests,^[7] and it is being now benchmarked on the ESFR-SMART on the protected station blackout (PSBO) and the protected loss of flow (PLOF) tests.

NEAR FUTURE OUTLOOK. Once NK and TH improvements are implemented and the supportive related investigation performed, further efforts will be focused on the development of an ATHLET TH model for the Phénix reactor. The model has to include the core and the primary circuit, and it has to be coupled with the existing correspondent DYN3D model. The coupled model should be then applied for validating and demonstrating the capabilities of the code system on the Phénix natural convection test, at the core level first and then at the full primary circuit level.

-
- [1] Rohde, U *et al.* (2016) *Prog. Nucl. Energy* **89**, 170–190.
 - [2] Nikitin, E. *et al.* (2018) *Ann. Nucl. Energy* **119**, 382–389.
 - [3] Nikitin, E. *et al.* (2018) *Ann. Nucl. Energy* **119**, 411–418.
 - [3] Nikitin, E. *et al.* (2018) *Ann. Nucl. Energy* **119**, 390–395.
 - [5] Kozmenkov, Y. *et al.* (2015) *Ann. Nucl. Energy* **84**, 153–165.
 - [6] Mikityuk, K. *et al.* (2017) IAEA-CN-245–450.
 - [7] Di Nora, V. A. *et al.* (2019) ICAPP2019.

- ARTICLES (PEER-REVIEWED)
- ORAL PRESENTATIONS
- REPORTS
- THESES

ARTICLES (PEER-REVIEWED)



Statistics on the publication activity of the Institute of Resource Ecology (IRE) within the last 10 years. The diagram considers peer-reviewed articles that were published under primary responsibility of the institute. The following compilation provides peer-reviewed articles published in 2019 representing any contribution of members of the IRE.

Alam, F.; Wegner, K. D.; Pouget, S.; Amidani, L.; Kvashnina, K.; Aldakov, D.; Reiss, P.
Eu²⁺: A suitable substituent for Pb²⁺ in CsPbX₃ perovskite nanocrystals?
The Journal of Chemical Physics 151, 231101 (2019).

Altstadt, E.; Bergner, F.; Das, A.; Houska, M.
Effect of anisotropic microstructure of ODS steels on small punch test results
Theoretical and Applied Fracture Mechanics 100, 191–199 (2019).

Amidani, L.; Plakhova, T. V.; Romanchuk, A. Y.; Gerber, E.; Weiss, S.; Efimenko, A.; Sahle, C. J.; Butorin, S. M.; Kalmykov, S. N.; Kvashnina, K. O.
Understanding the size effects on the electronic structure of ThO₂ nanoparticles
Physical Chemistry Chemical Physics 21, 10635–10643 (2019).

An, Y.; Kuc, A. B.; Petkov, P.; Lozada-Hidalgo, M.; Heine, T.
On the Chemistry and Diffusion of Hydrogen in the Interstitial Space of Layered Crystals h-BN, MoS₂, and Graphite
Small 15, 1901722 (2019).

Bachran, M.; Kluge, S.; Lopez-Fernandez, M.; Cherkouk, A.
Microbial diversity in an arid, naturally saline environment
Microbial Ecology 78, 494–505 (2019).

Back, M.; Ueda, J.; Xu, J.; Asami, K.; Amidani, L.; Trave, E.; Tanabe, S.
Uncovering the Origin of the Emitting States in Bi³⁺-Activated CaMO₃ (M=Zr, Sn, Ti) Perovskites: Metal-to-Metal Charge Transfer versus s-p Transitions
Journal of Physical Chemistry C 123, 14677–14688 (2019).

Bader, M.; Moll, H.; Steudtner, R.; Lösch, H.; Drobot, B.; Stumpf, T.; Cherkouk, A.
Association of Eu(III) and Cm(III) onto an extremely halophilic archaeon
Environmental Science and Pollution Research 26, 9352–9364 (2019).

Baranowski, M.; Zelewski, S. J.; Kepenekian, M.; Traoré, B.; Urban, J. M.; Surrente, A.; Maude, D. K.; Kuc, A. B.; Booker, E. P.; Stranks, S. D.; Plochocka, P.
Phase Transition Induced Carrier Mass Enhancement in 2D Ruddlesden-Popper Perovskites
ACS Energy Letters 4, 2386 (2019).

Bauer, A.; Jäschke, A.; Shams Aldin Azzam, S.; Glasneck, F.; Ullmann, S.; Kersting, B.; Brendler, V.; Schmeide, K.; Stumpf, T.
Multidentate extracting agents based on calix[4]arene scaffold – U^{VI}/Eu^{III} separation studies
Separation and Purification Technology 213, 246–254 (2019).

- Belskaya, O. B.; Stepanova, L. N.; Nizovskii, A. I.; Kalinkin, A. V.; Erenburg, S. B.; Trubina, S. V.; Kvashnina, K. O.; Leont'eva, N. N.; Gulyaeva, T. I.; Trenikhin, M. V.; Bukhtiyarov, V. I.; Likholobov, V. A.
The Effect of Tin on the Formation and Properties of Pt/MgAl(Sn)O_x Catalysts for Dehydrogenation of Alkanes
Catalysis Today 329, 187–196 (2019).
- Besold, J.; Eberle, A.; Noël, V.; Kujala, K.; Kumar, N.; Scheinost, A.; Lezama Pacheco, J.; Fendorf, S.; Planer-Friedrich, B.
Antimonite binding to natural organic matter: Spectroscopic evidence from a mine water impacted peatland
Environmental Science & Technology 53, 10782–10802 (2019).
- Besold, J.; Kumar, N.; Scheinost, A. C.; Lezama Pacheco, J.; Fendorf, S.; Planer-Friedrich, B.
Antimonite complexation with thiol and carboxyl/phenol groups of particulate organic matter
Environmental Science & Technology 53, 5005–5015 (2019).
- Biswas, A.; Besold, J.; Sjöstedt, C.; Gustafsson, J. P.; Scheinost, A. C.; Planer-Friedrich, B.
Complexation of arsenite, arsenate, and monothioarsenate with oxygen-containing functional groups of natural organic matter: An XAS study
Environmental Science & Technology 53, 10723–10731 (2019).
- Bonato, L.; Virost, M.; Dumas, T.; Mesbah, A.; Lecante, P.; Prieur, D.; Le Goff, X.; Hennig, C.; Dacheux, N.; Moisy, P.; Nikitenko, S.
Deciphering the Crystal Structure of a Scarce 1D Polymeric Thorium Peroxo Sulfate
Chemistry – A European Journal 25, 9580–9585 (2019).
- Brinkmann, H.; Patzschke, M.; Kaden, P.; Raiwa, M.; Rossberg, A.; Kloditz, R.; Heim, K.; Moll, H.; Stumpf, T.
Complex formation between UO₂²⁺ and α-isosaccharinic acid: insights on a molecular level
Dalton Transactions 48, 13440–13457 (2019).
- Cametti, G.; Scheinost, A. C.; Churakov, S. V.
Structural modifications and thermal stability of Cd²⁺-exchanged stellerite, a zeolite with STI framework-type
Journal of Physical Chemistry C 123, 25236–25245 (2019).
- Cametti, G.; Scheinost, A. C.; Giordani, M.; Churakov, S. V.
Framework modifications and dehydration path of a Ag⁺-modified, STI-type zeolite
Journal of Physical Chemistry C 123, 13651–13663 (2019).
- Chekxonin, P.; Zöllner, D.; Zimmer, E.; Scharnweber, J.; Romberg, J.; Skrotzki, W.
Microstructure of accumulative roll bonded high purity aluminium laminates
Materialia 5, 100236 (2019).
- Cristino, V.; Pasti, L.; Marchetti, N.; Berardi, S.; Bignozzi, C. A.; Molinari, A.; Passabi, F.; Caramori, S.; Amidani, L.; Orlandi, M.; Bazzanella, N.; Piccioni, A.; Kesavan, J. K.; Boscherini, F.; Pasquini, L.
Photoelectrocatalytic degradation of emerging contaminants at WO₃/BiVO₄ photoanodes in aqueous solution
Photochemical & Photobiological Sciences 18, 2150–2163 (2019).
- Daniels, N.; Franzen, C.; Kvashnina, K.; Petrov, V.; Torapava, N.; Bukaemskiy, A.; Kowalski, P.; Hölzer, A.; Walther, C.
Application of Layered Double Hydroxides for ⁹⁹Tc remediation
Applied Clay Science 176, 1–10 (2019).
- Diaz Pescador, E.; Schäfer, F.; Kliem, S.
Thermal-hydraulic insights during a main steam line break in a generic PWR KONVOI reactor with ATHLET 3.1A
Kerntechnik 84, 367–374 (2019).
- Doronkin, D. E.; Benzi, F.; Zheng, L.; Sharapa, D. I.; Amidani, L.; Studt, F.; Roesky, P. W.; Casapu, M.; Deutschmann, O.; Grunwaldt, J. D.
NH₃-SCR over V–W/TiO₂ Investigated by Operando X-ray Absorption and Emission Spectroscopy
Journal of Physical Chemistry C 123, 14338–14349 (2019).
- Drobot, B.; Schmidt, M.; Mochizuki, Y.; Abe, T.; Okuwaki, K.; Brulfert, F.; Falke, S.; Samsonov, S.; Komeiji, Y.; Betzel, C.; Stumpf, T.; Raff, J.; Tsushima, S.
Cm³⁺/Eu³⁺ Induced Structural, Mechanistic and Functional Implications for Calmodulin
Physical Chemistry Chemical Physics 21, 21213–21222 (2019).
- Dumas, T.; Fellhauer, D.; Schild, D.; Gaona, X.; Altmaier, M.; Scheinost, A.
Plutonium retention mechanisms by magnetite under anoxic conditions: Entrapment versus sorption
ACS Earth and Space Chemistry 3, 2197–2206 (2019).
- Ehrling, S.; Senkovska, I.; Bon, V.; Evans, J. D.; Petkov, P.; Krupskaya, Y.; Kataev, V.; Wulf, T.; Krylov, A.; Vtyurin, A.; Krylova, S.; Adichtchev, S.; Slyusareva, E.; Weiss, M. S.; Büchner, B.; Heine, T.; Kaskel, S.
Crystal size versus paddle wheel deformability: selective gated adsorption transitions of the switchable metal–organic frameworks DUT-8(Co) and DUT-8(Ni)
Journal of Materials Chemistry A 7, 21459–21475 (2019).
- Eibl, M.; Virtanen, S.; Pischel, F.; Bok, F.; Lönnrot, S.; Shaw, S.; Huittinen, N.
A spectroscopic study of trivalent cation (Cm³⁺ and Eu³⁺) sorption on monoclinic zirconia (ZrO₂)
Applied Surface Science 487, 1316–1328 (2019).

- Elo, O.; Hölttä, P.; Kekäläinen, P.; Voutilainen, M.; Huittinen, N.
Neptunium(V) transport in granitic rock: A laboratory scale study on the influence of bentonite colloids
Applied Geochemistry 10331, 31–39 (2019).
- Epifano, E.; Naji, M.; Manara, D.; Scheinost, A. C.; Hennig, C.; Lechelle, J.; Konings, R. J. M.; Gueneau, C.; Prieur, D.; Vitova, T.; Dardenne, K.; Rothe, J.; Martin, P. M.
Extreme multi-valence states in mixed actinide oxides
Communications Chemistry 2, 59 (2019).
- Erenburg, S. B.; Trubina, S. V.; Zvereva, A.; Zinoviev, A.; Katsyuba, V.; Dvurechenskii, V.; Kvashnina, K. O.; Voelskow, M.
XAFS Spectroscopy Study of Microstructure and Electronic Structure of Heterosystems Containing Si/GeMn Quantum Dots
Journal of Experimental and Theoretical Physics 128, 303–311 (2019).
- Eswayaha, A. S.; Hondow, N.; Scheinost, A. C.; Merroun, M.; Romero-Gonzalez, M.; Smith, T. J.; Gardiner, P. H. E.
Methyl selenol as precursor in selenite reduction to Se/S species by methane-oxidizing bacteria
Applied and Environmental Microbiology 85, e01379–01319 (2019).
- Filimonova, O. N.; Nickolsky, M. S.; Trigub, A. L.; Chareev, P. V.; Kvashnina, K. O.; Kovalchuk, E. V.; Vikentyev, I. V.; Tagirov, B. R.
The State of Platinum in Pyrite Studied by X-Ray Absorption Spectroscopy of Synthetic Crystals
Economic Geology 114, 1649–1663 (2019).
- Filimonova, O. N.; Trigub, A. L.; Tonkacheev, D. E.; Nickolsky, M. S.; Kvashnina, K. O.; Chareev, D. A.; Chaplygin, I. V.; Kovalchuk, E. V.; Lafuerza, S.; Tagirov, B. R.
Substitution mechanisms in In, Au, and Cu-bearing sphalerites studied by X-ray absorption spectroscopy of synthetic and natural minerals
Mineralogical Magazine 83, 435–451 (2019).
- Flipo, S.; Kohut, M.; Roth, F.; Weigel, T.; Schnelle, W.; Bobnar, M.; Ormeci, A.; Burkhardt, U.; Hennig, C.; Leisegang, T.; Meyer, D. C.; Leithe-Jasper, A.; Gumeniuk, R.
CeMo₂B₃: a new type of arrangement of puckered boron hexagonal rings
European Journal of Inorganic Chemistry, 3572–3580 (2019).
- Fridman, E.; Valtavirta, V.; Aufiero, M.
Nuclear Data Sensitivity and Uncertainty Analysis of Critical VENUS-F Cores with the Serpent Monte Carlo Code
Annals of Nuclear Energy 138, 107196 (2019).
- Gao, D.; Sinev, I.; Scholten, F.; Arán-Ais, R. M.; Divins, N. J.; Kvashnina, K.; Timoshenko, J.; Roldan Cuenya, B.
Selective CO₂ Electroreduction to Ethylene and Multicarbon Alcohols via Electrolyte-Driven Nanostructuring
Angewandte Chemie – International Edition 58, 17047–17053 (2019).
- Gómez-Ferrer, B.; Heintze, C.; Pareige, C.
On the role of Ni, Si and P on the microstructural evolution of FeCr alloys under irradiation
Journal of Nuclear Materials 517, 35–44 (2019).
- Götzke, L.; Schaper, G.; März, J.; Kaden, P.; Huittinen, N.; Stumpf, T.; Kammerlander, K. K. K.; Brunner, E.; Hahn, P.; Mehnert, A.; Kersting, B.; Henle, T.; Lindoy, L. F.; Zanoni, G.; Weigand, J. J.
Coordination chemistry of f-block metal ions with ligands bearing bio-relevant functional groups
Coordination Chemistry Reviews 386, 267–309 (2019).
- Gräning, T.; Klimenkov, M.; Rieth, M.; Heintze, C.; Möslang, A.
Long-term stability of the microstructure of austenitic ODS steel rods produced with a carbon-containing process control agent
Journal of Nuclear Materials 523, 111–120 (2019).
- Haldar, R.; Batra, K.; Marschner, S. M.; Kuc, A. B.; Zahn, S.; Fischer, R. A.; Bräse, S.; Heine, T.; Wöll, C.
Bridging the Green Gap: Metal–Organic Framework Heteromultilayers Assembled from Porphyrinic Linkers Identified by Using Computational Screening
Chemistry – A European Journal 25, 7847–7851 (2019).
- Heintze, C.; Hilger, I.; Bergner, F.; Weissgärber, T.; Kieback, B.
Nanoindentation of single- (Fe) and dual-beam (Fe and He) ion-irradiated ODS Fe-14Cr-based alloys: Effect of the initial microstructure on irradiation-induced hardening
Journal of Nuclear Materials 518, 1–10 (2019).
- Heller, A.; Barkleit, A.; Bok, F.; Wober, J.
Effect of four lanthanides onto the viability of two mammalian kidney cell lines
Ecotoxicology and Environmental Safety 173, 469–481 (2019).
- Herzog, S. D.; Kvashnina, K.; Persson, P.; Kritzberg, E.
Organic Iron Complexes Enhance Iron Transport Capacity along Estuarine Salinity Gradients
Biogeosciences Discuss., <https://doi.org/10.5194/bg-2019-234>, in review (2019).
- Holmström, S.; Simonovski, I.; Baraldi, D.; Bruchhausen, M.; Altstadt, E.; Delville, R.
Developments in the estimation of tensile strength by small punch testing
Theoretical and Applied Fracture Mechanics 101, 25–34 (2019).

- Hoyer, E.; Knöppel, J.; Liebmann, M.; Steppert, M.; Raiwa, M.; Herczynski, O.; Hanspach, E.; Zehner, S.; Göttfert, M.; Tsushima, S.; Fahmy, K.; Oertel, J.
Calcium binding to a disordered domain of a type III-secreted protein from a coral pathogen promotes secondary structure formation and catalytic activity
Scientific Reports 9, 7115 (2019).
- Ionescu, C.; Fischer, C.; Hoeck, V.; Lutge, A.
Discrimination of ceramic surface finishing by vertical scanning interferometry
Archaeometry 61, 31–42 (2019).
- Jain, R.; Fan, S.; Kaden, P.; Tsushima, S.; Foerstendorf, H.; Barthen, R.; Lehmann, F.; Pollmann, K.
Recovery of gallium from wafer fabrication industry wastewaters by Desferrioxamine B and E using reversed-phase chromatography approach
Water Research 158, 203–212 (2019).
- Ji, Y.; Kowalski, P. M.; Kegler, P.; Huittinen, N.; Marks, N.; Vinograd, V.; Arinicheva, Y.; Neumeier, S.; Bosbach, D.
Rare-Earth orthophosphates from atomistic simulations
Frontiers in Chemistry 7, 197 (2019).
- Jing, Y.; Heine, T.
Two-Dimensional Kagome Lattices Made of Hetero Triangulenes Are Dirac Semimetals or Single-Band Semiconductors
Journal of the American Chemical Society 141, 743–747 (2019).
- Juhin, A.; Collins, S. P.; Joly, Y.; Diaz-Lopez, M.; Kvashnina, K.; Glatzel, P.; Brouder, C.; de Groot, F.
Measurement of f orbital hybridization in rare earths through electric dipole-octupole interference in X-ray Absorption Spectroscopy
Physical Review Materials 3, 120801(R) (2019).
- Jung, J.; Lakatos, M.; Bengs, S.; Matys, S.; Raff, J.; Blüher, A.; Cuniberti, G.
S-layer protein-AuNP systems for the colorimetric detection of metal and metalloid ions in water
Colloids and Surfaces B: Biointerfaces 183, 110284 (2019).
- Kazama, H.; Tsushima, S.; Takao, K.
Crystallization of Anhydrous Proton from Acidic Aqueous Solution with Diamide Building Block
Crystal Growth & Design 19, 6048–6052 (2019).
- Kiani, M.; Du, N.; Vogel, M.; Raff, J.; Hübner, U.; Skorupa, I.; Bürger, D.; Schulz, S. E.; Schmidt, O. G.; Schmidt, H.
P-N Junction-Based Si Biochips with Ring Electrodes for Novel Biosensing Applications
Biosensors 9, 120 (2019).
- Kliem, S.; Grahn, A.; Bilodid, Y.; Höhne, T.
A realistic approach for the assessment of the consequences of heterogeneous boron dilution events in pressurized water reactors
Nuclear Engineering and Design 349, 150–161 (2019).
- Köhler, F.; Riebe, B.; Scheinost, A. C.; König, C.; Hölzer, A.; Walther, C.
Sorption of iodine in soils: insight from selective sequential extractions and X-ray absorption spectroscopy
Environmental Science and Pollution Research 23, 23850–23860 (2019).
- Konheiser, J.; Müller, S. E.; Magin, A.; Naumann, B.; Ferrari, A.
Source term calculation and validation for F-18 production with a cyclotron for medical applications at HZDR
Journal of Radiological Protection 39, 906–919 (2019).
- Kumar, S.; Creff, G.; Hennig, C.; Rossberg, A.; Steudtner, R.; Raff, J.; Vidaud, C.; Oberhaensli, F. R.; Bottein, Y.; Den Auwer, C.
How do actinyls interact with hyperphosphorylated yolk protein Phosvitin ?
Chemistry – A European Journal 25, 12332–12341 (2019).
- Kumar, A.; Naumenko, D.; Rossi, G.; Magnano, E.; Nappini, S.; Bondino, F.; Segoloni, E.; Amidani, L.; D’Acapito, F.; Boscherini, F.; Barba, L.; Pace, E.; Benfatto, M.; Casassa, S.; Pedio, M.
The effect of long-range order on intermolecular interactions in organic semiconductors: zinc octaethyl porphyrin molecular thin film model systems
Physical Chemistry Chemical Physics 21, 22966–22975 (2019).
- Kuzenkova, A.; Romanchuk, A.; Trigub, A.; Maslakov, K.; Egorov, A.; Amidani, L.; Kittrelle, C.; Kvashnina, K.; Toure, J.; Talyzin, A.; Kalmykov, S.
New insights into the mechanism of graphene oxide and radionuclide interaction through vacancy defects
Carbon, DOI: 10.1016/j.carbon.2019.10.003 (2019).
- Kvashnina, K.; Romanchuk, A.; Pidchenko, I.; Amidani, L.; Gerber, E.; Trigub, A.; Roßberg, A.; Weiß, S.; Popa, K.; Walter, O.; Caciuffo, R.; Scheinost, A.; Butorin, S.; Kalmykov, S.
A novel metastable pentavalent plutonium solid phase on the pathway from aqueous Pu(VI) to PuO₂ nanoparticles
Angewandte Chemie – International Edition 58, 17558–17562 (2019).
- Lee, S. S.; Schmidt, M.; Sturchio, N. C.; Nagy, K. L.; Fenter, P.
Effect of pH on the Formation of Gibbsite-Layer Films at the Muscovite (001)–Water Interface
Journal of Physical Chemistry C 123, 6560–6571 (2019).
- Lehmann, S.; Foerstendorf, H.; Zimmermann, T.; Patzschke, M.; Bok, F.; Brendler, V.; Stumpf, T.; Steudtner, R.
Thermodynamic and structural aspects of the aqueous uranium(IV) system – hydrolysis vs. sulfate complexation
Dalton Transactions 48, 17898–17907 (2019).

- Liu, J.; Luo, X.; Sun, Y.; Tsang, D. C. W.; Qi, J.; Zhang, W.; Li, N.; Yin, M.; Wang, J.; Lippold, H.; Chen, Y.; Sheng, G.
Thallium pollution in China and removal technologies for waters: A review
Environment International 126, 771–790 (2019).
- Liu, J.; Ren, S.; Zhou, Y.; Tsang, D. C. W.; Lippold, H.; Wang, J.; Yin, M.; Xiao, T.; Luo, X.; Chen, Y.
High contamination risks of thallium and associated metal(loid)s in fluvial sediments from a steel-making area and implications for environmental management
Journal of Environmental Management 250, 109513 (2019).
- Liu, J.; Yin, M.; Luo, X.; Xiao, T.; Wu, Z.; Li, N.; Wang, J.; Zhang, W.; Lippold, H.; Belshaw, N.; Feng, Y.; Chen, Y.
The mobility of thallium in sediments and source apportionment by lead isotopes
Chemosphere 219, 864–874 (2019).
- Lopez-Fernandez, M.; Moll, H.; Merroun, M. L.
Reversible pH-dependent curium(III) biosorption by the bentonite yeast isolate *Rhodotorula mucilaginosa* BII-R8
Journal of Hazardous Materials 370, 156–163 (2019).
- Lopez Fernandez, M.; Broman, E.; Simone, D.; Bertilsson, S.; Dopson, M.
Statistical Analysis of Community RNA Transcripts between Organic Carbon and Geogas-Fed Continental Deep Biosphere Groundwaters
mBio 10, e01470–01419 (2019).
- Lösch, H.; Hirsch, A.; Holthausen, J.; Peters, L.; Xiao, B.; Neumeier, S.; Schmidt, M.; Huittinen, N.
A spectroscopic investigation of Eu³⁺ incorporation in LnPO₄ (Ln = Tb, Gd_{1-x}Lu_x, x = 0.3, 0.5, 0.7, 1) ceramics
Frontiers in Chemistry 7, 94 (2019).
- Löser, R.; Bader, M.; Kuchar, M.; Wodtke, R.; Lenk, J.; Wodtke, J.; Kuhne, K.; Bergmann, R.; Haase-Kohn, C.; Urbanová, M.; Steinbach, J.; Pietzsch, J.
Synthesis, ¹⁸F-labelling and radiopharmacological characterisation of the C-terminal 30mer of *Clostridium perfringens* enterotoxin as a potential claudin-targeting peptide
Amino Acids 51, 219–244 (2019).
- Lüttge, A.; Arvidson, R. S.; Fischer, C.; Kurganskaya, I.
Kinetic concepts for quantitative prediction of fluid-solid interactions
Chemical Geology 504, 216–235 (2019).
- Mashita, T.; Tsushima, S.; Takao, K.
Photocatalytic Oxygenation of Cyclohexene Initiated by Excitation of [UO₂(OPCyPh₂)₄]²⁺ under Visible Light
ACS Omega 4, 7194–7199 (2019).
- Matschiavelli, N.; Kluge, S.; Podlech, C.; Standhaft, D.; Grathoff, G.; Ikeda-Ohno, A.; Warr, L.; Chukharkina, A.; Arnold, T.; Cherkouk, A.
The year-long development of microorganisms in uncompact Bavarian bentonite slurries at 30 °C and 60 °C
Environmental Science & Technology 53, 10514–10524 (2019).
- Mayordomo, N.; Alonso, U.; Missana, T.
Effects of gamma-alumina nanoparticles on strontium sorption in smectite: additive model approach
Applied Geochemistry 100, 121–130 (2019).
- Merchel, S.; Gärtner, A.; Beutner, S.; Bookhagen, B.; Chabilan, A.
Attempts to understand potential deficiencies in chemical procedures for AMS: Cleaning and dissolving quartz for ¹⁰Be and ²⁶Al analysis
Nuclear Instruments and Methods in Physics Research B 455, 293–299 (2019).
- Merchel, S.; Gurlit, S.; Opel, T.; Rugel, G.; Scharf, A.; Tiessen, C.; Weiß, S.; Wetterich, S.
Attempts to understand potential deficiencies in chemical procedures for AMS
Nuclear Instruments and Methods in Physics Research B 456, 186–192 (2019).
- Mingchao, W.; Marco, B.; Wang, M.; Hung-Hsuan, L.; Bishnu, P. B.; Xiaocang, H.; Silvia, P.; Eike, B.; Pan, L.; Mingwei, C.; Mischa, B.; Heine, T.; Zhou, S.; Enrique, C.; Renhao, D.; Xinliang, F.
Unveiling Electronic Properties in Metal-Phthalocyanine-Based Pyrazine-Linked Conjugated Two-Dimensional Covalent Organic Frameworks
Journal of the American Chemical Society 141, 16810–16816 (2019).
- Molodtsov, K.; Schymura, S.; Rothe, J.; Dardenne, K.; Schmidt, M.
Sorption of Eu(III) on Eibenstock granite studied by μ TRLFS: A novel spatially-resolved luminescence-spectroscopic technique
Scientific Reports 9, 6287 (2019).
- Mühlbauer, S.; Honecker, D.; Perigo, E. A.; Bergner, F.; Disch, S.; Heinemann, A.; Erokhin, S.; Berkov, D.; Leighton, C.; Eskildsen, M. R.; Michels, A.
Magnetic small-angle neutron scattering
Reviews of Modern Physics 91, 015004 (2019).

- Müller, K.; Foerstendorf, H.; Steudtner, R.; Tsushima, S.; Kumke, M. U.; Lefèvre, G.; Rothe, J.; Mason, H.; Szabó, Z.; Yang, P.; Adam, C.; André, R.; Brennenstuhl, K.; Cho, H.; Creff, G.; Coppin, F.; Dardenne, K.; Den Auwer, C.; Drobot, B.; Eidner, S.; Hess, N. J.; Kaden, P.; Kremleva, A.; Kretzschmar, J.; Krüger, S.; Platts, J. A.; Panak, P. J.; Polly, R.; Powell, B. A.; Rabung, T.; Redon, R.; Reiller, P. E.; Rösch, N.; Rossberg, A.; Scheinost, A. C.; Schimmelpfennig, B.; Schreckenbach, G.; Skerencak-Frech, A.; Sladkov, V.; Solari, P. L.; Wang, Z.; Washton, N. M.; Zhang, X.
Interdisciplinary round-robin test on molecular spectroscopy of the U(VI) acetate system
ACS Omega 4, 8167–8177 (2019).
- Nikitin, E.; Fridman, E.
Modeling of the FFTF isothermal physics tests with the Serpent and DYN3D codes
Annals of Nuclear Energy 132, 679–685 (2019).
- Pedrosa, E. P.; Kurganskaya, I.; Fischer, C.; Lüttge, A.
A Statistical Approach for Analysis of Dissolution Rates Including Surface Morphology
Minerals 2019, 458 (2019).
- Pereira, G.; Johnson, A. E.; Bilodid, Y.; Fridman, E.; Kotlyar, D.
Applying the Serpent-DYN3D Code Sequence for the Decay Heat Analysis of Metallic Fuel Sodium Fast Reactor
Annals of Nuclear Energy 125, 291–306 (2019).
- Petkov, P. S.; Bon, V.; Hobday, C. L.; Kuc, A.; Melix, P.; Kaskel, S.; Düren, T.; Heine, T.
Conformational isomerism controls collective flexibility in metal-organic framework DUT-8(Ni)
Physical Chemistry Chemical Physics 21, 674–680 (2019).
- Philipp, T.; Shams Aldin Azzam, S.; Rossberg, A.; Huittinen, N.; Schmeide, K.; Stumpf, T.
U(VI) sorption on Ca-bentonite at (hyper)alkaline conditions – Spectroscopic investigations of retention mechanisms
Science of the Total Environment 676, 469–481 (2019).
- Plakhova, T.; Romanchuk, A.; Lykshostova, D.; Baranchikov, A.; Dorovatovskii, P.; Svetogorov, R.; Shatalova, T.; Egorova, T.; Trigub, A.; Kvashnina, K.; Ivanov, V.; Kalmykov, S.
Size effects in nanocrystalline thoria
Journal of Physical Chemistry C 123, 23167–23176 (2019).
- Plakhova, T. V.; Romanchuk, A. Y.; Butorin, S. M.; Konyukhova, A. D.; Egorov, A. V.; Shiryaev, A. A.; Baranchikov, A. E.; Dorovatovskii, P. V.; Huthwelker, T.; Gerber, E.; Bauters, S.; Sozarukova, M. M.; Scheinost, A.; Ivanov, V.; Kalmykov, S. N.; Kvashnina, K.
Towards the surface hydroxyl species in CeO₂ nanoparticles
Nanoscale 11, 18142–18149 (2019).
- Povedano-Priego, C.; Jroundi, F.; Lopez Fernandez, M.; Sánchez-Castro, I.; Martín-Sánchez, I.; Huertas, F. J.; Merroun, M. L.
Shifts in bentonite bacterial community and mineralogy in response to uranium and glycerol-2-phosphate exposure
Science of the Total Environment 692, 219–232 (2019).
- Prieur, D.; Popa, K.; Vigier, J. F.; Scheinost, A.; Martin, P.
Crystallographic structure and charge distribution of AUO₄ and A₃UO₆ uranates (A=Ca, Sr, Ba or Pb)
Journal of Nuclear Materials 516, 303–308 (2019).
- Pushkarev, R.; Fainer, N.; Kirienko, V.; Matsynin, A.; Nadolinnyy, V.; Merenkov, I.; Trubina, S.; Ehrenburg, S.; Kvashnina, K.
SiC_xN_y:Fe films as a tunable ferromagnetic material with tailored conductivity
Journal of Materials Chemistry C 7, 4250–4258 (2019).
- Rammelt, T.; Kuc, A.; Böhm, J.; Heine, T.; Gläser, R.
Nature and Surface Interactions of Sulfur-Containing Deposits on V₂O₅-WO₃/TiO₂- Catalysts for SCR-DeNO_x
Emission Control Science and Technology 5, 297–306 (2019).
- Ramzan, M. S.; Bacic, V.; Jing, Y.; Kuc, A.
Electronic Properties of a New Family of Layered Materials from Groups 14-15: First-Principles Simulations
Journal of Physical Chemistry C 123, 25470–25476 (2019).
- Rossberg, A.; Abe, T.; Okuwaki, K.; Barkleit, A.; Fukuzawa, K.; Nakano, T.; Mochizuki, Y.; Tsushima, S.
Destabilization of DNA through interstrand crosslinking by UO₂²⁺
Chemical Communications 55, 2015–2018 (2019).
- Rothe, J.; Altmaier, M.; Dagan, R.; Dardenne, K.; Fellhauer, D.; Gaona, X.; González-Robles Corrales, E.; Herm, M.; Kvashnina, K.; Metz, V.; Pidchenko, I.; Schild, D.; Vitova, T.; Geckeis, H.
Fifteen Years of Radionuclide Research at the KIT Synchrotron Source in the Context of the Nuclear Waste Disposal Safety Case
Geosciences 9, 91 (2019).
- Rybkin, I.; Gorin, D.; Sukhorukov, G.; Lapanje, A.
Thickness of Polyelectrolyte Layers of Separately Confined Bacteria Alters Key Physiological Parameters on a Single Cell Level
Frontiers in Bioengineering and Biotechnology 7, 378 (2019).
- Schönberger, N.; Braun, R.; Matys, S.; Lederer, F. L.; Lehmann, F.; Flemming, K.; Pollmann, K.
Chromatopanning for the identification of gallium binding peptides
Journal of Chromatography A 1600, 158–166 (2019).

- Schöne, S.; März, J.; Stumpf, T.; Ikeda-Ohno, A.
Mixed-valent neptunium oligomer complexes based on cation-cation interactions
Dalton Transactions 48, 6700–6703 (2019).
- Sturm, S.; Sigleitmeier, M.; Wolf, D.; Vogel, K.; Gratz, M.; Faivre, D.; Lubk, A.; Büchner, B.; Sturm, E.; Cölfen, H.
Magnetic Nanoparticle Chains in Gelatin Ferrogels: Bioinspiration from Magnetotactic Bacteria
Advanced Functional Materials, 1905996 (2019).
- Tagirov, B. R.; Filimonova, O.; Trigub, A. L.; Akinfiev, N. N.; Nickolsky, M. S.; Kvashnina, K. O.; Chareev, D. A.; Zotov, A. V.
Platinum transport in chloride-bearing fluids and melts: Insights from in situ X-ray absorption spectroscopy and thermodynamic modeling
Geochimica et Cosmochimica Acta 254, 86–101 (2019).
- Tagirov, B. R.; Trigub, A. L.; Filimonova, O. N.; Kvashnina, K. O.; Nickolsky, M. S.; Lafuerza, S.; Chareev, D. A.
Gold transport in hydrothermal chloride-bearing fluids: Insights from in situ X-ray absorption spectroscopy and ab initio molecular dynamics
ACS Earth and Space Chemistry 3, 240–261 (2019).
- Takao, K.; Kazama, H.; Ikeda, Y.; Tsushima, S.
Crystal Structure of Regularly Th-Symmetric $[U(NO_3)_6]^{2-}$ Salts with Hydrogen Bond Polymers of Diamide Building Blocks
Angewandte Chemie – International Edition 58, 240–243 (2019).
- Taube, F.; Drobot, B.; Roßberg, A.; Foerstendorf, H.; Acker, M.; Patzschke, M.; Trumm, M.; Taut, S.; Stumpf, T.
Thermodynamic and structural studies on the Ln(III)/An(III) malate complexation
Inorganic Chemistry 58, 368–381 (2019).
- Thommen, A.; Werner, S.; Frank, O.; Philipp, J.; Knittelfelder, O.; Quek, Y.; Fahmy, K.; Shevchenko, A.; Friedrich, B. M.; Jülicher, F.; Rink, J. C.
Body size-dependent energy storage causes Kleiber's law scaling of the metabolic rate in planarians
eLife 8, e38187 (2019).
- Tsushima, S.
Lanthanide-induced conformational change of methanol dehydrogenase involving coordination change of cofactor pyrroloquinoline quinone
Physical Chemistry Chemical Physics 21, 21979–21983 (2019).
- Vivas, J.; Capdevila, C.; Altstadt, E.; Houska, M.; Sabirov, I.; San-Martín, D.
Microstructural degradation and creep fracture behavior of conventionally and thermomechanically treated 9% Chromium Heat Resistant steel
Metals and Materials International 25, 343–352 (2019).
- Willms, T.; Kryk, H.; Oertel, J.; Hempel, C.; Hampel, U.; Knitt, F.
On the thermal decomposition of tert.-butyl hydroperoxide, its sensitivity to metals and its kinetics, studied by thermoanalytic methods
Thermochimica Acta 672, 25–42 (2019).
- Winde, F.; Geipel, G.; Espina, C.; Schütz, J.
Human exposure to uranium in South African gold mining areas using barber-based hair sampling
PlosOne 14, e0219059 (2019).
- Wolter, J. M.; Schmeide, K.; Huittinen, N.; Stumpf, T.
Cm(III) retention by calcium silicate hydrate (C-S-H) gel and secondary alteration phases in carbonate solutions with high ionic strength: A site-selective TRIFS study
Scientific Reports 9, 14255 (2019).
- Wolter, J. M.; Schmeide, K.; Weiss, S.; Bok, F.; Brendler, V.; Stumpf, T.
Stability of U(VI) doped calcium silicate hydrate gel in repository-relevant brines studied by leaching experiments and spectroscopy
Chemosphere 218, 241–251 (2019).
- Wyźga, P.; Veremchuk, I.; Himcinsi, C.; Burkhardt, U.; Carrillo-Cabrera, W.; Bobnar, M.; Hennig, C.; Leithe-Jasper, A.; Kortus, J.; Gumeniuk, R.
Indium thiospinel $In_{1-x}□_xIn_2S_4$ – structural characterization and thermoelectric properties
Dalton Transactions 48, 8350–8360 (2019).
- Younes, A.; Creff, G.; Beccia, M. R.; Moisy, P.; Roques, J.; Aupiais, J.; Hennig, C.; Solari, P. L.; Den Auwer, C.; Vitaud, C.
Is hydroxypyridonate 3,4,3-LI(1,2-HOPO) a good competitor of fetuin for uranyl metabolism?
Metallomics 11, 496–507 (2019).
- Yu, C.; Drake, H.; Lopez Fernandez, M.; Whitehouse, M.; Dopson, M.; Åström, M. E.
Micro-scale isotopic variability of low-temperature pyrite in fractured crystalline bedrock — A large Fe isotope fractionation between $Fe(II)_{aq}$ /pyrite and absence of Fe-S isotope co-variation
Chemical Geology 522, 192–207 (2019).
- Yuan, K.; Bracco, J. N.; Schmidt, M.; Soderholm, L.; Fenter, P.; Lee, S. S.
Effect of Anions on the Changes in the Structure and Adsorption Mechanism of Zirconium Species at the Muscovite (001) – Water Interface
Journal of Physical Chemistry C 123, 16699–16710 (2019).
- Yuan, T.; Wei, C.; Zhang, C. S.; Qin, G.
A numerical simulator for modeling the coupling processes of subsurface fluid flow and reactive transport processes in fractured carbonate rocks
Water 11, 1957 (2019).

Zänker, H.; Heine, K.; Weiss, S.; Brendler, V.; Husar, R.; Bernhard, G.; Gloe, K.; Henle, T.; Barkleit, A.
Strong Uranium(VI) Binding onto Bovine Milk Proteins, Selected Protein Sequences and Model Peptides
Inorganic Chemistry 58, 4173–4189 (2019).

Zelewski, S. J.; Urban, J. M.; Surrente, A.; Maude, D. K.; Kuc, A.; Schade, L.; Johnson, R. D.; Dollmann, M.; Nayak, P. K.; Snaith, H. J.; Radaelli, P. G.; Kudrawiec, R.; Nicholas, R. J.; Plochocka, P.; Baranowski, M.
Revealing the Nature of Photoluminescence Emission in Metal-Halide Double Perovskites
Journal of Materials Chemistry C 7, 8350–8356 (2019).

Zibouche, N.; Philipsen, P.; Kuc, A.
Strong Variation Of Electronic Properties Of MoS₂ And WS₂ Nanotubes In Presence Of External Electric Fields
Journal of Physical Chemistry C 123, 3892–3899 (2019).

Zuñiga-Puelles, E.; Cardoso-Gil, R.; Bobnar, M.; Veremchuk, I.; Himcinschi, C.; Hennig, C.; Kortus, J.; Heide, G.; Gumeniuk, R.
Structural stability and thermoelectric performance of high quality synthetic and natural pyrites (FeS₂)
Dalton Transactions 48, 10703–10713 (2019).

ORAL PRESENTATIONS

Amidani, L.; Pidchenko, I.; Kvashnina, K.
Modeling XANES of U⁵⁺ and U⁶⁺ in different local coordination geometries
49^{èmes} Journées des Actinides, April 14–17, 2019, Erice, Italy (2019).

Amidani, L.; Pidchenko, I.; Kvashnina, K.
Modelling high resolution XANES for nuclear materials
E-MRS Spring Meeting, May 27–31, 2019, Nice, France (2019).

Arnold, T.
NORM research and strategy at the HZDR, Germany
Cores Symposium on Radon and NORM – regulatory aspects, scientific achievements and research needs, September 03–04, 2019, Helsinki, Finland (2019).

Bader, M.
Interactions of halophilic microorganisms with radionuclides
GDCh Jahrestagung der Fachgruppe Nuklearchemie 2019, September 25–27, 2019, Dresden, Germany (2019).

Bader, M.; Hilpmann, S.; Swanson, J. S.; Steudtner, R.; Drobot, B.; Schmidt, M.; Roßberg, A.; Ikeda-Ohno, A.; Stumpf, T.; Cherkouk, A.
Interaction of uranium with halophilic microorganisms
Halophiles 2019, June 24–28, 2019, Cluj-Napoca, Romania (2019).

Barkleit, A.; Heller, A.
Influence of common decorporation agents on the speciation of trivalent f-elements in serum – a luminescence spectroscopic study
ENVIRA 2019 – 5th International Conference on Environmental Radioactivity, September 08–13, 2019, Prague, Czech Republic (2019).

Bergner, F.; Ulbricht, A.
Small-angle neutron scattering (SANS): Overview on principles and best practices
OECD/NEA Nuclear Science Committee Preparatory meeting: Best practices for nuclear materials characterisation techniques, February 11–12, 2019, Boulogne-Billancourt, France (2019).

Bok, F.; Moog, H. C.
Solubility of Se in saline solutions – towards a consistent polythermal Pitzer dataset
Workshop on Actinide-Brine-Chemistry and Workshop on High Temperature Aqueous Chemistry, June 25–27, 2019, Karlsruhe, Germany (2019).

Chekhonin, P.; Röder, F.; Müller, G.; Roßner, M.; Heintze, C.; Bergner, F.
Microstructural Characterization of a VVER-440 type Reactor Pressure Vessel Steel by Electron Microscopy
IGRDM-21 – 21th meeting of International Group on Radiation Damage Mechanism, May 19–24, 2019, Gifu, Japan (2019).

Demnitz, M.; Molodtsov, K.; Bollermann, T.; Schymura, S.; Schierz, A.; Schmidt, M.
Spatially-resolved speciation of Eu(III) and Cm(III) on granite surfaces
GDCh Jahrestagung der Fachgruppe Nuklearchemie 2019, September 25–27, 2019, Dresden, Germany (2019).

Demnitz, M.; Molodtsov, K.; Bollermann, T.; Schymura, S.; Schierz, A.; Schmidt, M.
Spatially-resolved speciation of Eu(III) and Cm(III) on granite surfaces
Goldschmidt 2019, August 18–23, 2019, Barcelona, Spain (2019).

- Diaz Pescador, E.
Modelling of fluid mixing in reactor circuits with the thermal-hydraulic system code ATHLET
Kraftwerkstechnisches Kolloquium, October 23, 2019, Dresden, Germany (2019).
- Diaz Pescador, E.; Schäfer, F.; Kliem, S.
Multidimensional fluid mixing study during an asymmetric injection of cold water in the primary side of a generic PWR KONVOI with ATHLET 3.1A
50th Annual meeting on Nuclear Technology (AMNT) 2019, May 07–08, 2019, Berlin, Germany (2019).
- Diaz Pescador, E.; Schäfer, F.; Wilhelm, P.; Kliem, S.
Investigations on the thermal-hydraulic behavior of a generic PWR KONVOI during a 1% cold leg small-break loss of coolant accident using the system code ATHLET
ICONE 27 – 27th International Conference on Nuclear Engineering, May 19–24, 2019, Ibaraki, Japan (2019).
- Drobot, B.
Spektroskopische Methoden für die Endlagerforschung
Kraftwerkstechnisches Kolloquium, October 23, 2019, Dresden, Germany (2019).
- Drobot, B.; Steudtner, R.; Raff, J.; Brendler, V.; Bauer, A.; Bok, F.; Patzschke, M.; Tsushima, S.
What we can learn from the 'f' in f-elements
14th PhD seminar Kompetenzverbundes für Kerntechnik Ost, December 05, 2019, Dresden, Germany (2019).
- Eibl, M.; Shaw, S.; Hennig, C.; Morris, K.; Stumpf, T.; Huittinen, N. M.
Trivalent Lanthanide and Actinide Incorporation into Zirconium(IV) Oxide – Spectroscopic Investigations of Defect Fluorite Structures
GDCh Jahrestagung der Fachgruppe Nuklearchemie 2019, September 25–27, 2019, Dresden, Germany (2019).
- Eibl, M.; Shaw, S.; Hennig, C.; Morris, K.; Stumpf, T.; Huittinen, N. M.
Trivalent Lanthanide and Actinide Incorporation into Zirconium(IV) Oxide – Spectroscopic Investigations of Defect Fluorite Structures
Migration 2019 – 17th International Conference on the Chemistry and Migration Behaviour of Actinides and Fission Products in the Geosphere, September 15–20, 2019, Kyoto, Japan (2019).
- Fichter, S.
Synthesis and Characterization of Tri- and Tetravalent Actinide Amidinates
FENABIUM Projekttreffen, November 12, 2019, Dresden, Germany (2019).
- Foerstendorf, H.
Pathways to a nuclear waste repository in Germany
The Chemistry of f-Elements Autumn School, November 12–16, 2019, Dresden, Germany (2019).
- Fridman, E.
Initial solution of the SFR-UAM Exercises I-1 and I-2 with Serpent
OECD/NEA UAM Workshop 2019, May 13–17, 2019, Oak Ridge National Laboratory, U.S.A. (2019).
- Fridman, E.; Jiménez-Carrascosa, A.; García-Herranz, N.; Alvarez-Velarde, F.; Romojaro, P.; Bostelmann, F.
Benchmarking KENO-VI against MCNP/Serpent using a simplified SFR pin cell problem
OECD/NEA UAM Workshop 2019, May 13–17, 2019, Oak Ridge National Laboratory, U.S.A. (2019).
- Gueye, P. M.; Gomez-Ferrer, B.; Heintze, C.; Pareige, C.
Behaviour of C, Ni, Si, P under ion irradiation at different doses in model FeCr(Ni, Si, P) alloys
M4F PhD and post-doc event, June 23–25, 2019, Miraflores de la Sierra, Madrid, Spain (2019).
- Heintze, C.; Olsson, P.; Konstantinovic, M.; Caturla, M. J.
M4F - Materials Modelling For Fusion and Fission Materials - Domain 1
M4F PhD and post-doc event, June 23–25, 2019, Miraflores de la Sierra, Madrid, Spain (2019).
- Heller, A.; Acker, M.; Barkleit, A.; Bok, F.; Wober, J.
Comparative effect of trivalent lanthanides and actinides on a rat kidney cell line
GDCh Jahrestagung der Fachgruppe Nuklearchemie 2019, September 25–27, 2019, Dresden, Germany (2019).
- Heller, A.; Acker, M.; Barkleit, A.; Bok, F.; Wober, J.
Effect of trivalent lanthanides and actinides on a rat kidney cell line
ENVIRA 2019 – 5th International Conference on Environmental Radioactivity, September 08–13, 2019, Prague, Czech Republic (2019).
- Hennig, C.; Ikeda-Ohno, A.; Radoske, T.; Scheinost, A. C.
A new single crystal diffractometer at BM20/ESRF
27th Annual Meeting of the German Crystallographic Society (DGK), March 25–28, 2019, Leipzig, Germany (2019).
- Hernández Mayoral, M.; Onorbe, E.; Gómez-Ferrer, B.; Heintze, C.; Malerba, L.; Gueye, P. M.; Pareige, C.
Neutron irradiated microstructure of FeCr alloys investigated by TEM
MINES – Materials in Nuclear Energy Systems, October 06–10, 2019, Baltimore, Maryland, U.S.A. (2019).
- Hildebrand, H.; Franke, K.; Fischer, C.; Schymura, S.
Analysis of studies and research projects regarding the detection of nanomaterials in different environmental compartments and deduction of need for action regarding method development
Abschlusspräsentation des Sachverständigengutachtens „NanoExperte“, April 17, 2019, Dessau-Roßlau, Germany (2019).

- Hilpmann, S.; Bader, M.; Bachran, M.; Steudtner, R.; Schmidt, M.; Stumpf, T.; Cherkouk, A.
Microscopic and spectroscopic investigations of the interactions of a Halobacterium-isolate with uranium
Migration 2019 – 17th International Conference on the Chemistry and Migration Behaviour of Actinides and Fission Products in the Geosphere, September 15–20, 2019, Kyoto, Japan (2019).
- Huittinen, N.; Lösch, H.; Hirsch, A.; Holthausen, J.; Peters, L.; Xiao, B.; Neumeier, S.; Schmidt, M.
A spectroscopic investigation of Eu³⁺ incorporation in LnPO₄ (Ln = Tb, Gd_{1-x}Lu_x, x = 0.3, 0.5, 0.7, 1) ceramics
27th Annual Meeting of the German Crystallographic Society (DGK), March 25–28, 2019, Leipzig, Germany (2019).
- Jessat, J.
Studies on the interaction of plant cells with U(VI) and Eu(III) and on stress-induced metabolite release
Finale der WiN Preisverleihung, October 11, 2019, Karlstein/Main, Germany (2019).
- Jessat, J.; Sachs, S.; Moll, H.; Steudtner, R.; Bok, F.; Stumpf, T.
Time dependence of the bioassociation behavior of U(VI) and Eu(III) with *Brassica napus* cells
Goldschmidt 2019, August 18–23, 2019, Barcelona, Spain (2019).
- Jessat, J.; Sachs, S.; Moll, H.; Steudtner, R.; Bok, F.; Stumpf, T.
Zeit- und Konzentrationsabhängigkeit des Bioassoziationsverhaltens von U(VI) und Eu(III) mit *Brassica napus*-Zellen
GDCh Jahrestagung der Fachgruppe Nuklearchemie 2019, September 25–27, 2019, Dresden, Germany (2019).
- Kloditz, R.; Patzschke, M.; Stumpf, T.
Insights into the excited states of 5f systems: Protactinium and Uranium
Arbeitsgruppenseminar des AK Markus Reiher (ETH Zürich), July 10, 2019, Zürich, Switzerland (2019).
- Kloditz, R.; Patzschke, M.; Stumpf, T.
Multiconfigurational calculations of ground and excited states of actinide complexes
Arbeitsgruppenseminar des AK Thomas Heine (TU Dresden), November 26, 2019, Dresden, Germany (2019).
- Kloditz, R.; Radoske, T.; Patzschke, M.; Stumpf, T.
Comprehensive real space bonding analysis of tetravalent f-element complexes with Schiff-base ligands
49^{emes} Journées des Actinides, April 14–17, 2019, Erice, Italy (2019).
- Köhler, L.; März, J.; Patzschke, M.; Kloditz, R.; Stumpf, T.
The Inverse Trans Effect in Uranium complexes containing N-heterocyclic Carbenes
Bilaterales Treffen mit AK Roesky (KIT), January 10–11, 2019, Karlsruhe, Germany (2019).
- Köhler, L.; Patzschke, M.; März, J.; Stumpf, T.
Actinid-Komplexe mit N-heterocyclischen Carbenen
Finale der WiN Preisverleihung, October 11, 2019, Karlstein/Main, Germany (2019).
- Köhler, L.; Patzschke, M.; März, J.; Stumpf, T.
The Inverse Trans Influence in a novel Uranium(IV)bis(carbene) Complex
GDCh Jahrestagung der Fachgruppe Nuklearchemie 2019, September 25–27, 2019, Dresden, Germany (2019).
- Köhler, L.; Patzschke, M.; März, J.; Stumpf, T.
The Inverse Trans Influence in U(IV/V) complexes
49^{emes} Journées des Actinides, April 14–17, 2019, Erice, Italy (2019).
- Krawczyk-Bärsch, E.; Gerber, U.; Müller, K.; Rossberg, A.; Merroun, M. L.
Microorganisms for biological remediation of uranium contaminated sites – a microscopic and spectroscopic approach
3rd International Caparica Conference on Pollutant Toxic Ions and Molecules, November 04–07, 2019, Costa da Caparica, Portugal (2019).
- Krawczyk-Bärsch, E.; Lehtinen, A.; Pedersen, K.
Biofilms as a sink for radionuclides in future granitic nuclear waste repositories
18. Sanierungskolloquium, Jena, October 01–02, 2019, Jena, Germany (2019).
- Kretzschmar, J.; Tsushima, S.; Jäckel, E.; Meyer, R.; Steudtner, R.; Müller, K.; Schmeide, K.; Brendler, V.; Stumpf, T.
Dimeric Uranium(VI)–Citrate Complexes: Structures and Dynamics
GDCh Jahrestagung der Fachgruppe Nuklearchemie 2019, September 25–27, 2019, Dresden, Germany (2019).
- Kvashnina, K.
An expanding view on actinide oxide nanoparticles
43rd Symposium on Scientific Basis for Nuclear Waste Management, October 21–24, 2019, Vienna, Austria (2019).
- Kvashnina, K.
Fundamentals of Actinide Chemistry by Cutting Edge X-ray Methods and Models
E-MRS Spring Meeting, May 27–31, 2019, Nice, France (2019).
- Kvashnina, K.
Towards the electronic structure of actinide oxides nanoparticles
Goldschmidt 2019, August 18–23, 2019, Barcelona, Spain (2019).
- Lopez-Fernandez, M.; Drozdowski, J.; Kluge, S.; Cherkouk, A.
Microorganisms present in bentonites from a deep underground experiment
Goldschmidt 2019, August 18–23, 2019, Barcelona, Spain (2019).

- Lösch, H.; Tits, J.; Marques-Fernandes, M.; Baeyens, B.; Chiorescu, I.; Krüger, S.; Stumpf, T.; Huittinen, N. M.
Uranium(VI) complexation with aqueous silicates in the acidic to alkaline pH-range
Migration 2019 – 17th International Conference on the Chemistry and Migration Behaviour of Actinides and Fission Products in the Geosphere, September 15–20, 2019, Kyoto, Japan (2019).
- Lösch, H.; Tits, J.; Marques-Fernandes, M.; Baeyens, B.; Krüger, S.; Chiorescu, I.; Stumpf, T.; Huittinen, N. M.
Uranium(VI) complexation with aqueous silicates in the acidic to alkaline pH-range
GDCh Jahrestagung der Fachgruppe Nuklearchemie 2019, September 25–27, 2019, Dresden, Germany (2019).
- Mäder, U.; Bernard, E.; Kulenkampff, J.; Jenni, A.
Coupled processes across a claystone-concrete interface: results of a combined X-ray CT and PET transport experiment
Decovalex 2019 – Development of Coupled Models and their Validation Against Experiments, November 04–05, 2019, Brugg, Switzerland (2019).
- Mansel, A.; Franke, K.
Recent application of the solid targetry system
14th CYCLEUR workshop 2019, May 08–10, 2019, Dresden, Germany (2019).
- Marques Fernandes, M.; Scheinost, A. C.; Baeyens, B.
Reduction of NpO_2^+ and TcO_4^- at the Fe(II)-montmorillonite-water interface
Goldschmidt 2019, August 18–23, 2019, Barcelona, Spain (2019).
- Marques Fernandes, M.; Scheinost, A. C.; Huittinen, N.; Baeyens, B.
Adsorption of U(VI) and Eu(III) on illite: The important role of accessory minerals
Migration 2019 – 17th International Conference on the Chemistry and Migration Behaviour of Actinides and Fission Products in the Geosphere, September 15–20, 2019, Kyoto, Japan (2019).
- Matschiavelli, N.
Deutschlands Ausstieg aus der Atomkraft – Was passiert mit dem Müll und welche Rolle spielen dabei Mikroorganismen
Veranstaltung der Dresdner Seniorenakademie, October 08, 2019, Deutsches Hygienemuseum, Germany (2019).
- Matschiavelli, N.
Mikroorganismen und deren Relevanz in einem Endlager
Radioaktivität – Forschung, Schule, Praxis, October 09, 2019, Schülerlabor DeltaX, HZDR, Dresden, Germany (2019).
- Matschiavelli, N.; Kluge, S.; Podlech, C.; Standhaft, D.; Grathoff, G.; Ikeda-Ohno, A.; Warr, L. N.; Chukharkina, A.; Arnold, T.; Cherkouk, A.
Natural occurring spore-forming sulfate reducers and their influence on the bentonite barrier
MIND Project, Annual Meeting 2019, May 07–09, 2019, Stockholm, Sweden (2019).
- Mayordomo Herranz, N.; Rodriguez Hernandez, D. M.; Molodtsov, K.; Johnstone, E. V.; Roßberg, A.; Heim, K.; Foerstendorf, H.; Schild, D.; Brendler, V.; Müller, K.
 ^{99}Tc immobilization by aluminum solids containing Fe(II) moieties
The 43rd Symposium on Scientific Basis for Nuclear Waste Management, October 21–24, 2019, Vienna, Austria (2019).
- Mayordomo Herranz, N.; Rodriguez Hernandez, D. M.; Roßberg, A.; Scheinost, A.; Foerstendorf, H.; Heim, K.; Brendler, V.; Müller, K.
Tc immobilization by Fe(II)-Al(III)-Cl layered double hydroxide phase
GDCh Jahrestagung der Fachgruppe Nuklearchemie 2019, September 25–27, 2019, Dresden, Germany (2019).
- Mayordomo Herranz, N.; Rodriguez Hernandez, D. M.; Scheinost, A.; Roßberg, A.; Brendler, V.; Müller, K.
 ^{99}Tc retention on Fe(II)Al(III)-Cl layered double hydroxides
Goldschmidt 2019, August 18–23, 2019, Barcelona, Spain (2019).
- Moll, H.; Raff, J.; Stumpf, T.
Spectroscopic characterization of curium(III) protein interactions
GDCh Jahrestagung der Fachgruppe Nuklearchemie 2019, September 25–27, 2019, Dresden, Germany (2019).
- Moll, H.; Sachs, S.; Raff, J.
Interaction of curium(III) with plant cells (*Brassica napus*)
ENVIRA 2019 – 5th International Conference on Environmental Radioactivity, September 08–13, 2019, Prague, Czech Republic (2019).
- Moog, H. C.; Altmaier, M.; Bok, F.; Brendler, V.; Freyer, D.; Gaona, X.; Marquardt, C.; Richter, A.; Schrage, T.; Seher, H.; Thoenen, T.; Voigt, W.
THEREDA – Achievements, present activities, and future developments
Workshop on Actinide-Brine-Chemistry and Workshop on High Temperature Aqueous Chemistry, June 25–27, 2019, Karlsruhe, Germany (2019).
- Müller, S.; Ferrari, A.; Rachamin, R.
Updates on the FLUKA geometry for the MU2E experiment
Mu2e Collaboration Meeting, October 16–19, 2019, Fermilab, Batavia, U.S.A. (2019).

- Neumann, J.; Qiu, C.; Hellebrandt, S.; Eng, P.; Skanthakumar, S.; Steppert, M.; Soderholm, L.; Stumpf, T.; Schmidt, M.
Effect of Background Electrolyte Composition on the Interfacial Formation of Th(IV) Nanoparticles
Goldschmidt 2019, August 18–23, 2019, Barcelona, Spain (2019).
- Pareige, C.; Gómez-Ferrer, B.; Heintze, C.; Oñorbe, E.; Hernandez-Mayoral, M.; Gueye, P. M.; Malerba, L.
Influence of impurities in microstructural evolution of FeCr alloys under ion irradiation – link with hardening
MINES – Materials in Nuclear Energy Systems, October 06–10, 2019, Baltimore, Maryland, U.S.A. (2019).
- Pareige, C.; Gómez-Ferrer, B.; Heintze, C.; Oñorbe, E.; Hernandez-Mayoral, M.; Desgardin, P.; Malerba, L.
On the role of Ni, Si and P on the nanostructural evolution of FeCr alloys under irradiation – link with hardening
SMINS 5 – NEA International Workshop on Structural Materials for Innovative Nuclear Systems, July 08–11, 2019, Kyoto, Japan (2019).
- Philipp, T.; Schmeide, K.; Rossberg, A.; Huittinen, N.; Stumpf, T.
Influence of pH, carbonate and calcium concentration on U(VI) retention by clay minerals at (hyper)alkaline conditions – A batch sorption and spectroscopy study
EUROCLAY 2019 – International Conference on Clay Science and Technology, July 01–05, 2019, Paris, France (2019).
- Philipp, T.; Schmeide, K.; Stumpf, T.
Influence of calcium on uranium and neptunium sorption on clay minerals at (hyper)alkaline conditions
2nd International Conference on Radioanalytical and Nuclear Chemistry, May 05–10, 2019, Budapest, Hungary (2019).
- Radoske, T.
Tetravalent Actinide Complexes with Schiff bases: Comparison with Isostructural Transition Metal and 4f Element Compounds
FENABIUM Projekttreffen, February 27, 2019, Dresden, Germany (2019).
- Radoske, T.
Tetravalent Actinide N-Donor Affinity in Monosalen Complexes
FENABIUM Projekttreffen, June 28, 2019, Leipzig, Germany (2019).
- Radoske, T.; Kaden, P.; Walter, O.; Kloditz, R.; Patzschke, M.; Stumpf, T.; März, J.
A series of tetravalent Pu, Np, U and Th complexes of a salen type ligand
49^{èmes} Journées des Actinides, April 14–17, 2019, Erice, Italy (2019).
- Radoske, T.; Schöne, S.; Kloditz, R.; März, J.; Stumpf, T.; Ikeda-Ohno, A.
Relative Stability of Actinide(IV) Bissalen Complexes
GDCh Jahrestagung der Fachgruppe Nuklearchemie 2019, September 25–27, 2019, Dresden, Germany (2019).
- Raff, J.
Anforderungen an Materialien zur definierten Immobilisierung von Biomolekülen und Zellen
PolCarr-Innovationsforum, March 28–29, 2019, Leipzig, Germany (2019).
- Raff, J.; Wollenberg, A.; Traxler, L.; Schulz, W.; Freitag, L.; Günther, A.; Gupta, D.; Steinhauser, G.; Großmann, S.; Lehmann, F.; Köhler, M.; Walther, C.; Kothe, E.
None is like the other: the interaction of selected fungi with radionuclides
18. Jenaer Sanierungskolloquium, October 01–02, 2019, Jena, Germany (2019).
- Rossberg, A.; Scheinost, A. C.
Factor Analysis, Monte Carlo Modeling and Landweber Iteration: advanced approaches to EXAFS analysis
Demi-journée de l'Atelier de l'OSUG sur le Traitement du Signal pour la Spectroscopie et l'imagerie Hyperspectrale, January 25, 2019, Grenoble, France (2019).
- Sachs, S.; Oertel, J.; Fahmy, K.
Uranium toxicity on plant cells: Isothermal microcalorimetric studies for the differentiation between chemotoxic and radiotoxic effects of uranium
ENVIRA 2019 – 5th International Conference on Environmental Radioactivity, September 08–13, 2019, Prague, Czech Republic (2019).
- Schäfer, S.; Fahmy, K.; Merroun, M. L.
Antibacterial activity of selenium nanoparticles studied by calorimetry, flow cytometry and electron microscopy
Goldschmidt 2019, August 18–23, 2019, Barcelona, Spain (2019).
- Schäfer, S.; Fahmy, K.; Merroun, M. L.
Antibacterial activity of selenium nanoparticles studied by calorimetry, flow cytometry and electron microscopy
Congreso Nacional de Microbiología, July 01–05, 2019, Málaga, Spain (2019).
- Schmidt, M.; Lösch, H.; Hirsch, A.; Holthausen, J.; Peters, L.; Xiao, B.; Neumeier, S.; Huittinen, N.
Eu³⁺ incorporation into xenotime LnPO₄: the effect of local distortion on long term stability
Goldschmidt 2019, August 18–23, 2019, Barcelona, Spain (2019).

- Schmidt, M.; Qiu, C.; Hellebrandt, S.; Eng, P. J.; Skanthakumar, S.; Steppert, M.; Soderholm, L.
Effect of background electrolyte composition on the formation of Th(IV) nanoparticles on the muscovite (001) basal plane
49^{èmes} Journées des Actinides, April 14–17, 2019, Erice, Italy (2019).
- Schöne, S.; Kloditz, R.; März, J.; Kaden, P.; Patzschke, M.; Roesky, P. W.; Stumpf, T.
Amidates – Versatile Ligands for Tetravalent Actinides
GDCh Jahrestagung der Fachgruppe Nuklearchemie 2019, September 25–27, 2019, Dresden, Germany (2019).
- Schöne, S.; Kloditz, R.; März, J.; Kaden, P.; Patzschke, M.; Roesky, P. W.; Stumpf, T.
Enantiopure Tetravalent Actinide Amidates – Synthesis and Reactivity
49^{èmes} Journées des Actinides, April 14–17, 2019, Erice, Italy (2019).
- Schöne, S.; März, J.; Kaden, P.
Amidates as Versatile Ligands for Tetravalent Actinides
FENABIUM Projekttreffen, June 28, 2019, Leipzig, Germany (2019).
- Schöne, S.; März, J.; Kaden, P.
Synthesis and Reactivity of Tetravalent Actinide Amidates
FENABIUM Projekttreffen März 2019, February 27, 2019, Dresden, Germany (2019).
- Schymura, S.; Hildebrand, H.; Neugebauer, M.; Lange, T.; Franke, K.
Investigating the fate of manufactured nanoparticles in waste water treatment by the use of radiolabeled nanoparticles
Cycleur Workshop, May 08–09, 2019, Dresden, Germany (2019).
- Shimojo, K.; Sasanuki, T.; Schöne, S.; Sugita, T.; Okamura, H.; Ikeda-Ohno, A.
Solvent extraction and separation of rare earth elements by diamide type ligands and the complex structure of extracted species
The 84th Annual Meeting of the Society of Chemical Engineering, Japan, March 13–15, 2019, Tokyo, Japan (2019).
- Tsushima, S.
Recent progress in application of computational chemistry to actinide interaction with biomolecules
Engineering Physics Seminar Series at the Department of Engineering Physics of the McMaster University, October 04, 2019, Hamilton, Canada (2019).
- Ulbricht, A.
Flux effect on RPV materials
SOTERIA Final Workshop, June 25–27, 2019, Miraflores de la Sierra, Spain (2019).
- Wollenberg, A.; Freitag, L.; Hübner, R.; Günther, A.; Raff, J.; Stumpf, T.
Investigation of the potential of fungi for precautionary radiation protection in soil
GDCh Jahrestagung der Fachgruppe Nuklearchemie 2019, September 25–27, 2019, Dresden, Germany (2019).
- Yuan, T.; Bollermann, T.; Fischer, C.
Heterogeneous adsorption of actinides on host rocks at the pore scale: Application of an improved surface complexation model
GDCh Jahrestagung der Fachgruppe Nuklearchemie 2019, September 25–27, 2019, Dresden, Germany (2019).
- Yuan, L.; Zheng, B.; Kunstmann, J.; Brumme, T.; Kuc, A. B.; Ma, C.; Deng, S.; Blach, D.; Pan, A.; Huang, L.
Interlayer Exciton Transport Modulated by Twist-Angle-Dependent Moiré Potentials in WS₂-WSe₂ Heterobilayers
XX. Brazilian Symposium on Theoretical Chemistry, November 10–14, 2019, Joao Pessoa, Brazil (2019).

In addition, about 40 posters were presented at international conferences and workshops.

○ REPORTS

Arnold, T.; Barkleit, A.; Gerber, U.; Krawczyk-Bärsch, E.; Wilke, C.

Untersuchungen zu den Wechselwirkungen zwischen unter Tage lebenden Mikroorganismen mit Uran und deren Einfluss auf das Migrationsverhalten von Uran in gefluteten Urangruben und Spektroskopische Bestimmung der Bindungsform (Speziation) trivalenter Actinide/Lanthanide in Biofluiden des menschlichen Gastrointestinaltraktes und im Blut
Wissenschaftlich-Technische Berichte / Helmholtz-Zentrum Dresden-Rossendorf; HZDR-098 (2019).

Hennig, C.; Ikeda-Ohno, A.; Radoske, T.; Scheinost, A. C.
A new single crystal diffractometer at BM20/ESRF
Zeitschrift für Kristallographie Supplement (2019).

Matschiavelli, N.; Drozdowski, J.; Kluge, S.; Arnold, T.; Cherkouk, A.

Joint project: Umwandlungsmechanismen in Bentonitbarrieren - Subproject B: Einfluss von mikrobiellen Prozessen auf die Bentonitumwandlung
Wissenschaftlich-Technische Berichte / Helmholtz-Zentrum Dresden-Rossendorf; HZDR-103 (2019).

○ THESES

(Technische Universität Dresden, 2019, except where noted)

DOCTORAL THESES

Gerber, U.

Investigations on indigenous microorganisms isolated from a former uranium mine and their interaction mechanisms with uranium - a possible bioremediation study
Friedrich-Schiller-Universität Jena, 2019.

Kretzschmar, J.

NMR Spectroscopic Investigation of Lanthanide, Actinide, and Selenium Containing Complexes Related to the Environment or Nuclear Waste Disposals

Sporn, M.

Entwicklung einer Best-Estimate-Methode mit Unsicherheitsanalyse für DWR-Störfalluntersuchungen basierend auf dem Störfallanalyseprogramm TRACE

Taube, F.

Komplexe trivalenter Actinide und Lanthanide mit organischen Liganden und deren Retention an CSH-Phasen

MASTER THESES

Dressler, M.

Einfluss der metabolischen Aktivität einer natürlich vorkommenden mikrobiellen Gemeinschaft im Tonmineral Bentonit auf Gusseisen- und Kupferoberflächen
Universität Greifswald, 2019

Dullies, P.

Untersuchungen zum Einfluss von Isosaccharinsäure auf die U(VI)- Rückhaltung an Ca-Bentonit unter alkalischen Bedingungen"
University of Applied Sciences, Dresden, 2019.

Galanzew, J.

Electronic structure studies of Th systems by High Energy X-Ray spectroscopy and computational methods

Garimella, J. N.

Uranium(VI) interaction with plant cells: a physiological perspective
Hochschule Offenburg, 2019

Jessat, I.

Komplexierung von Eu(III) und Cm(III) mit Phosphat bei höheren Temperaturen

Pingel, J. L.

4D Geo-Positronen-Emissions-Tomographie (GeoPET) Anwendung an einem Granitbohrkern aus der Bohrung EPS-1, Soultz-sous-Forets (Frankreich)
Friedrich-Schiller-Universität Jena, 2019

Schäfer, S.

**Antibacterial activity of selenium nanoparticles:
Calorimetric, flow-cytometric and microscopic
studies**

Vincon, I.

**Synthesis and characterization of U(VI)-complexes
with organic ligands by spectroscopy and quantum
chemical methods**

DIPLOMA THESIS

Freitag, L.

**Untersuchungen der molekularen
Wechselwirkungen von Pilzen mit Uran und
Europium**

BACHELOR THESIS

Henka, A.

**Bindungsstudien von FUS-Protein und RNA unter
Nutzung der abgeschwächten Totalreflexions-
Fourier-Transform-Infrarotspektroskopie**

○ WORKSHOPS

○ SESSIONS

○ SEMINARS

○ AWARDS

○ TEACHING ACTIVITIES

○ FURTHER EVENTS

○ 14TH WORKSHOP OF THE EUROPEAN CYCLOTRON NETWORK – CYCLEUR 2019

HZDR, Germany, May 08–10, 2019

The CYCLEUR workshop is an outstanding platform for networking and developing collaborations within the European cyclotron research community. The 14th CYCLEUR workshop took place at the HZDR, Dresden, Germany, on May 8–10, 2019. The workshop was jointly organized by the Institute of Resource Ecology and the Institute of Radiopharmaceutical Cancer Research.

The agenda enclosed general cyclotron research as well as critical application in research, nuclear medicine and industry, and facility reports. The 14th CYCLEUR attracted 22 presentations from 15 different countries, ranging from the exchange on future trends to the deconstruction of long running cyclotron sites.

For discussions about the practical experience, three cyclotron facilities belonging to the HZDR have been visited during the workshop in Dresden. The participants had access to the Cyclone 18/9 (IBA) in Rossendorf (Fig. 1), the cyclotron TR-FLEX (ACSI) at the Center for Radiopharmaceutical Tumor Research (ZRT) in Rossendorf (Fig. 2) and the proton facility (IBA) at the OncoRay Center in Dresden (Fig. 3). The visit provided a platform to share opinions and knowledge about the operation of cyclotrons, the targetry, the related radiochemical procedures and about the regulatory issues. The 14th CYCLEUR workshop contributed to an improved collaboration between cyclotron facilities and to an exchange of expertise on issues of common concern within the cyclotron research community in Europe.

LINK: → <http://old.lhep.unibe.ch/cycleurnetwork>

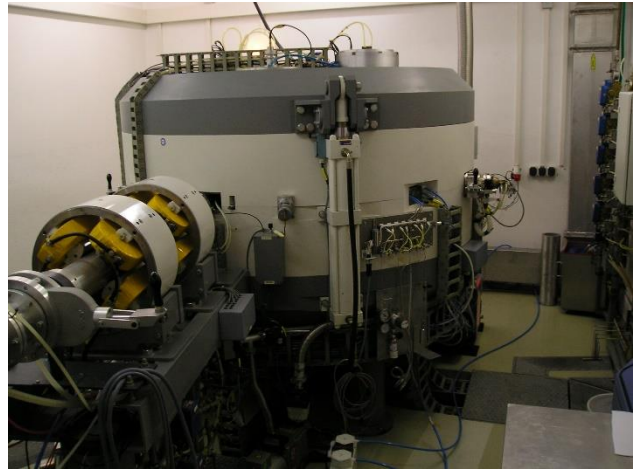


Fig. 1. Cyclone 18/9 (IBA), Institute of Radiopharmaceutical Cancer Research, Department of Radiopharmaceuticals Production, Dresden.



Fig. 2. Cyclotron TR-Flex (ACSI), Institute of Radiopharmaceutical Cancer Research, Department of Radiopharmaceuticals Production, Dresden (Image: 54401 HZDR).

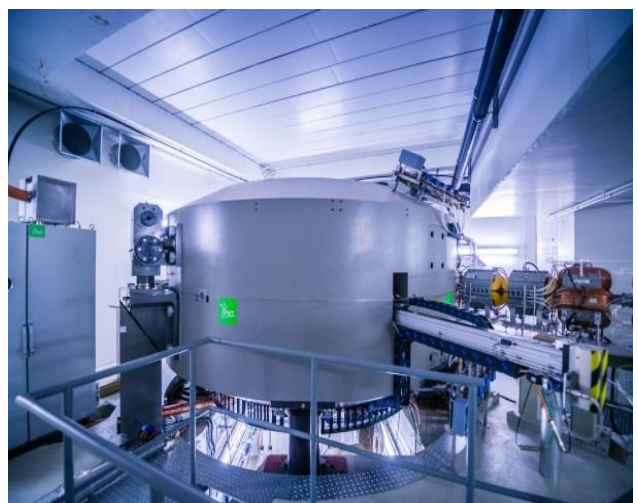


Fig. 3. Proton facility (IBA) at the OncoRay Center – Institute of Radiooncology (Image: 40738 OncoRay/André Wirsig).

WORKSHOP OF THE ALLIANCE TOPICAL ROADMAP WORKING GROUP NORM

HZDR, Germany, June 18–19, 2019



Working group (WG) Natural Occurring Radioactive Materials (NORM) is one of five topical roadmap WGs of the European Radioecological Alliance (ALLIANCE). The ALLIANCE promotes research in radioecology and acts as a research platform.

Objective of the workshop was to foster collaboration and cooperation within WG NORM, to develop ideas for joint projects and to compile a contribution of WG NORM to the update of the ALLIANCE strategic research agenda (SRA) in radioecology. 27 participants from 16 organisations coming from 9 countries were attending the workshop. The workshop was divided into four topical sessions as shown below:
Session 1: “Current activities of WG NORM members in national and international projects”

Session 2: “Modelling and molecular process understanding”

Session 3: “Funding opportunities” and

Session 4: “Discussion on SRA update and possible web presence of WG NORM”

Each organisation presented its NORM activities in national and international projects. The main topical session of the workshop session 2 “Modelling and molecular process understanding” focused on the development of biogeochemical models for the description of the naturally occurring radionuclide (NOR) transfer in the environment and the following presentations were given:

Arnold, T.; Sachs, S.

HZDR, Germany

Introduction into modelling

Bok, F.

HZDR, Germany

Smart- K_d values as realistic distribution coefficient

Chapon, V.

CEA, France

Potential influence of microorganisms on radionuclide transport

Fischer, C.

HZDR, Germany

Hydro-bio-geochemical models

Grambow, B.

SUBATECH, Nantes, France

Classification of radioactive waste in France

Law, G.

University of Helsinki, Finland

NORM situation in Finland – NORM problems

Merroun, M.

University of Granada, Spain

Influence of microorganisms on the oxidation state of radionuclides/metals – Consequences for the mobilization and immobilization behavior of radionuclides

Montavon, G.

SUBATECH, Nantes, France

Radionuclide transport processes in the vicinity of an old uranium mine – Studies at the ZATU site

Popic, J.

DSA, Norway

NORM situation in Norway – NORM problems

Sachs, S.

HZDR, Germany

Interaction of radionuclides with plants

Vanhoudt, N.

SCK•CEN, Belgium

Practical approach to environmental dose assessment – The ERICA tool

Transfer factors – A measure to describe the interaction of radionuclides with plants

ACKNOWLEDGMENT:

The organisation of this workshop was financially supported by the ALLIANCE.

GDCh – JAHRESTAGUNG DER FACHGRUPPE NUKLEARCHEMIE 2019

Penck Hotel, Dresden, Germany, September 25–27, 2019

The Annual Meeting of the Section Nuclear Chemistry of the GDCh provided a unique insight into the interdisciplinary research field of Nuclear Chemistry. It addressed to all scientists working with radionuclides and ionizing radiation. The meeting took place from September 25 to 27, 2019 at the Penck Hotel, Dresden, Germany, with about 115 attendees. The program included 39 lectures and 42 posters, which was organized by the chairman Prof. T. Stumpf and the members of the director's board of the Section Nuclear Chemistry. It was a particular pleasure to welcome experts giving plenary lectures during the meeting as follows:

Churakov, S. V.

Multiscale mechanistic modelling of reactive transport phenomena in nuclear waste disposal systems

PSI, Villigen, Switzerland

Müller, C.

Radiotheragnostik in der Krebsforschung: „From Bench-to-Bedside“

PSI, Villigen, Switzerland

Montavon, G.; Galland, N.

Astatine: Halogen or Metal?

*Laboratoire SUBATECH, IN2P3/CNRS/EMN
Nantes/UniVersite ´ de Nantes, Nantes, France*

Law, G. *et al.*

Fukushima Daiichi's Microscopic Environmental Legacy

Dept. of Chemistry, University Helsinki, Helsinki, Finland

During this event the Fritz-Straßmann Ph.D. prizes were awarded to the following persons:

Dr. Karolin Wagener, Johannes Gutenberg-Universität, Mainz, Germany.

Dr. Miriam Bader, HZDR, Dresden, Germany

Dr. Katharina Domnanich, Universität Bern, Switzerland (upper photo, from left to right)

Poster prizes were awarded to:

M. Sachs, Philipps-Universität Marburg, Germany,

J. Neumann, HZDR, Dresden, Germany,

P. Hanemann, Leibniz Universität Hannover, Germany, and

T. Kieck, Johannes Gutenberg-Universität Mainz, Germany by the head of the director's board Prof. C. Walther (lower photo, from left to right).



GESELLSCHAFT DEUTSCHER CHEMIKER



Jahrestagung der Fachgruppe Nuklearchemie 2019

25. – 27. September 2019
Dresden



AWARDS

Bader, M.

Wechselwirkung halophiler Mikroorganismen mit Radionukliden

Ph.D. Prize

GDCh Jahrestagung der Fachgruppe Nuklearchemie 2019, September 25–27, 2019, Dresden, Germany (2019).

Anerkennungspreis 2018

March 14, 2019, HZDR, Dresden, Germany (2019).

Diaz Pescador, E.; Schäfer, F.; Wilhelm, P.; Kliem, S.

Investigations on the thermal-hydraulic behavior of a generic PWR KONVOI during a 1% cold leg small-break loss of coolant accident using the system code ATHLET

Best Paper from Europe

ICONE 27 – 27th International Conference on Nuclear Engineering, May 19–24, 2019, Ibaraki, Japan (2019).

Gerber, E.

Examination of plutonium nanoparticles with manifold synchrotron methods

Poster Prize

Migration 2019 – 17th International Conference on the Chemistry and Migration Behaviour of Actinides and Fission Products in the Geosphere, September 15–20, 2019, Kyoto, Japan (2019).

Jessat, J.

Studies on the interaction of plant cells with U(VI) and Eu(III) and on stress-induced metabolite release

WIN-Germany-Prize 2019

Women in Nuclear Germany, October 11, 2019, Karlstein, Germany (2019).

Mayordomo Herranz, N.

Experimental and theoretical studies of mixed smectite and Al₂O₃ nanoparticles to improve pollutant retention in geochemical barriers

Outstanding Thesis Prize

Universidad de Alcalá, July 5, 2019, Alcalá de Henares, Spain (2019).

Neumann, J.

Effect of background electrolyte composition on the formation of Th(IV) nanoparticles on the muscovite (001) basal plane

Poster Prize

GDCh Jahrestagung der Fachgruppe Nuklearchemie 2019, September 25–27, 2019, Dresden, Germany (2019).

SESSIONS (CO)ORGANIZED BY IRE

Bilateral meeting: HZDR-IRE – AK Roesky, Institute of Inorganic Chemistry, KIT

Karlsruhe Institute of Technology, Karlsruhe, Germany, January 10–11, 2019.

Hauser, A.

Towards the synthesis of novel group 13-lanthanide compounds

Kaden, P.

Paramagnetic NMR investigations of metal-organic complexes of soft donor ligands and the tetravalent actinides

Köhler, L.

ITI in U-complexes containing N-heterocyclic carbenes

Patzschke, M.

Computational Actinide Spectroscopy

Reinhardt, N.

Reaction pathways for the reduction chemistry of classical and non-classical divalent lanthanoid compounds

Schmidt, M.

Luminescence spectroscopy at IRE

Schöne, S.

Tetravalent Actinide and Transition Metal Amidinates-Trends and Perspectives

Schoo, C.

Reactivity of divalent lanthanide complexes towards group 15/16 elements and compounds

Simmler, T.

Redox-transmetallation to access divalent lanthanide NHC complexes

European Geosciences Union General Assembly 2019

Vienna, Austria, April 07–12, 2019.

Convener: Meister, P.

Co-Conveners: Fischer, C.; Frisia, S.; Gebauer, D.
Hippler, D.

SSP3.12/BG4.3/GMPV3.7:

Nucleation and growth of sedimentary/diagenetic minerals

Goldschmidt 2019

Barcelona, Spain, August 18–23, 2019.

Poonoosamy, J.; Deng, H.; Fischer, C.; Chapon, V.;
Havlova, V.; Raff, J.

Session 13a:

**Cross-Scale Understanding of Geochemical,
Biological, and Mechanical Processes in the
Subsurface and their Coupling to Solute Transport:
Experimental and Numerical Approaches**

Mehta, N.; Benzerara, K.; Dittrich, M.; Matschiavelli, N.;
Rodriguez-Escales, P.; Valhondo, C.

Session 13i:

**Microbial Controls on Contaminant
Transformations in Different Environments: Bio-
Mineralization, Bioweathering and Bioremediation**

Bilateral meeting: HZDR-IRE – University of Helsinki, Dept. of Chemistry

HZDR, Dresden, Germany, October 02, 2019.

18th Bilateral meeting: HZDR-IRE – PSI-LES, Villigen, Switzerland

HZDR, Dresden, Germany, October 28–29, 2019.

Barkleit, A.

Forka: Research for the decommissioning of nuclear facilities

Brendler, V.

iCross: Integrity of nuclear waste repository systems – Cross-scale system understanding and analysis

Churakov, S.

Atomistic modelling of mineral dissolution

Curti, E.

Thermodynamic modelling of the oxygen potential in Cr-doped UO₂ fuel under in-pile conditions

Eibl, M.

The incorporation of Ln³⁺ into zirconia - studies of bulk and molecular structures of zirconia solid-solutions

Fischer, C.

Reactive transport processes and the project Crossing

Mancini, A.

Uptake of Fe in cement phases

Marques Fernandes, M.

U(VI)/Eu(III) sorption on illite

Matschiavelli, N.

Some microbial issues regarding the storage of high-level radioactive waste

Mayordomo Herranz, N.

Tc immobilization by minerals containing Fe(II) moieties

Sachs, S.

Study of the interaction of radionuclides with plants

○ SEMINARS (TALKS OF VISITORS)

Rowland, Darren

Joint Expert Speciation System (JESS), Australia

Thermodynamics of Glycine + H₂O

January 25, 2019

Burns, Peter

Department of Civil & Environmental Engineering & Earth Sciences, University of Notre Dame, Notre Dame, U.S.A.

Nuclear Waste Management in the U.S.A.

New Landscapes of Uranium Mineralogy and Mineral-Inspired Nanomaterials

March 14, 2019

Kalmykov, Stepan

Lomonosov Moscow State University; Moscow, Russia

Nuclear Waste Programs in Russia

March 14, 2019

Konevnik, Yulia

Lomonosov Moscow State University; Moscow, Russia

Research Related to the Repositories in Russia

March 14, 2019

Kielar, Charlotte

Paderborn University, Paderborn, Germany

Atomic force microscopy investigations of DNA origami nanostructures: toward applications in biomedicine

July 4, 2019

Knecht, Stefan

ETH Zürich, Switzerland

Exploration of f-Element Chemistry and Chemical Bonding

July 31, 2019

Scheibe, Benjamin

Department of Chemistry, Philipps Universität Marburg, Marburg, Germany

Fluoridometallates(IV) of the actinoids

August 20, 2019

Kohlgruber, Tsuyoshi Anthony

University of Notre Dame, Indiana, U.S.A.

Sorption of U₆₀ Nanoclusters on Muscovite

September 10, 2019

Mandrova, Natalya

Lomonosov Moscow State University, Moscow, Russia

Green rust: synthesis, characterization and ⁹⁹Tc sorbent properties

September 10, 2019

Joseph, Claudia

KIT, Karlsruhe, Germany

Influence of interlayers on the diffusion of HTO, ³⁶Cl⁻, and ⁸⁵Sr²⁺ through smectites / KIT-INE's activities in the Mont Terri underground rock laboratory (iCross)

September 23, 2019

Özcan, Özlem

Bundesanstalt für Materialforschung und -prüfung (BAM), Berlin, Germany

Coupled electrochemical, microscopic and spectroscopic techniques for the analysis of local corrosion and MIC processes

September 24, 2019

Koerdt, Andrea

Bundesanstalt für Materialforschung und -prüfung (BAM), Berlin, Germany

Investigation of methanogen-induced microbiologically influenced corrosion (Mi-MIC) using simulated marine environments under flowing conditions

September 24, 2019

Konietzky, Heinz

TU Bergakademie Freiberg, Freiberg, Germany

Gesteinsmechanische Forschung an der TU BAF - Laborversuche und numerische Simulationen

October 18, 2019

Réal, Florent

University of Lille, CNRS, France

Molecular Modeling of Electronic Spectroscopic Properties of Solvated Heavy Elements

November 6, 2019

Klemmed, Benjamin

Technische Universität Dresden, Dresden, Germany

Optical properties of modified metal oxide aerogels

November 26, 2019

TEACHING ACTIVITIES

(Winter term: WT; summer term: ST)

Lectures

- Bok, F.
Friedrich-Schiller-Universität, Jena
ST 2019
Geochemische Modellierung mit Geochemist's Workbench®
- Bok, F.
TU Bergakademie Freiberg
ST 2019
Geochemical modelling using PHREEQC
- Brendler, V.
Dresden University of Applied Sciences,
ST 2019
Radiochemistry
- Fahmy, K.
Technische Universität Dresden,
WT 2018/19
Biophysical methods
ST 2019
Biological thermodynamics
- Fischer, C.
Universität Bremen,
ST 2019
Diagenese
- Heine, T.
Technische Universität Dresden,
ST 2019, WT 2019/20
PC II (Theorie der Chemischen Bindung)
PC III (Einführung in die Computerchemie)
Modul MRBO 01 – Quantenchemie
- Huittinen, N.
Technische Universität Dresden,
ST 2019
Radioecology
- Kuc, A. B.
Universität Leipzig,
WT 2018/19
Computational Chemistry of Solids
WT 2019/2020
Spektroskopie (PC)
- Lippold, H.
Universität Leipzig,
ST 2019
Radioanalytik
Entstehung und Eigenschaften ionisierender Strahlung
WT 2019/2020
Radioanalytik
Radiochemische Analysemethoden
- Raff, J.
Dresden University of Applied Sciences,
WT 2018/19, WT 2019/2020
Mikrobiologie

Technische Universität Dresden,
WT 2018/2019, WT 2019/2020
Mikrobielle Laugung

Universität Granada, Spain
ST 2019
Properties and application perspectives of bacterial surface layer proteins
- Schmidt, M.
Technische Universität Dresden,
WT 2018/19
Chemistry of the f-elements
- Schymura, S.
Universität Leipzig
WT 2019/2020
Radioanalytik
- Stumpf, T.
Technische Universität Dresden,
ST 2019, WT 2019/2020
Radiochemistry

Courses

✎ The laboratory course “Radiochemistry” was provided from August 26–September 06, 2019, as a part of a module of the chemistry master degree program at the Technische Universität Dresden.

Advisers:

Brinkmann, H.	Moll, H.
Eibl, M.	Neumann, J.
Demnitz, M.	Patzschke, M.
Foerstendorf, H.	Rodriguez Hernandez, D. M.
Hilpmann, S.	Sachs, S.
Huittinen, N.	Schierz, A.
Jessat, J.	Schmidt, M.
Jordan, N.	Schönberger, N.
Kaden, P.	Schöne, S.
Kloditz, R.	Subramanian, M.
Kretzschmar, J.	Weiss, S.
Lösch, H.	Wollenberg, A.
Mayordomo, N.	

✎ The IRE provided the experiment “Alpha spectrometric isotope dilution analysis of uranium” of the laboratory course “Instrumental Analysis” held by the Institute for Analytical Chemistry, Technische Universität Dresden.

Advisers:

<i>WT 2018/19</i>	<i>WT 2019/20</i>
Demnitz, M.	Hilpmann, S.
Jessat, J.	Köhler, L.
Lösch, H.	Neumann, J.
Neumann, J.	Roode-Gutzmer, Q. I.
Weiss, S.	Weiss, S.

✎ Biophysics course of the Dresden-International-Graduate School.

Advisers:

<i>WT 2018/19 & WT 2019/20</i>
Fahmy, K.
Oertel, J.
Philipp, J.

✎ Courses and seminars were held referring to the following lectures:

Fahmy, K.

*Technische Universität Dresden,
WT 2018/2019, WT 2019/2020*

Biophysics course of the Dresden-International-Graduate School

Kuc, A. B.

*Universität Leipzig,
WT 2019/2020*

Spektroskopie (PC)

Springer, M.

*Technische Universität Dresden,
WT 2019/2020*

Theorie der chemischen Bindung

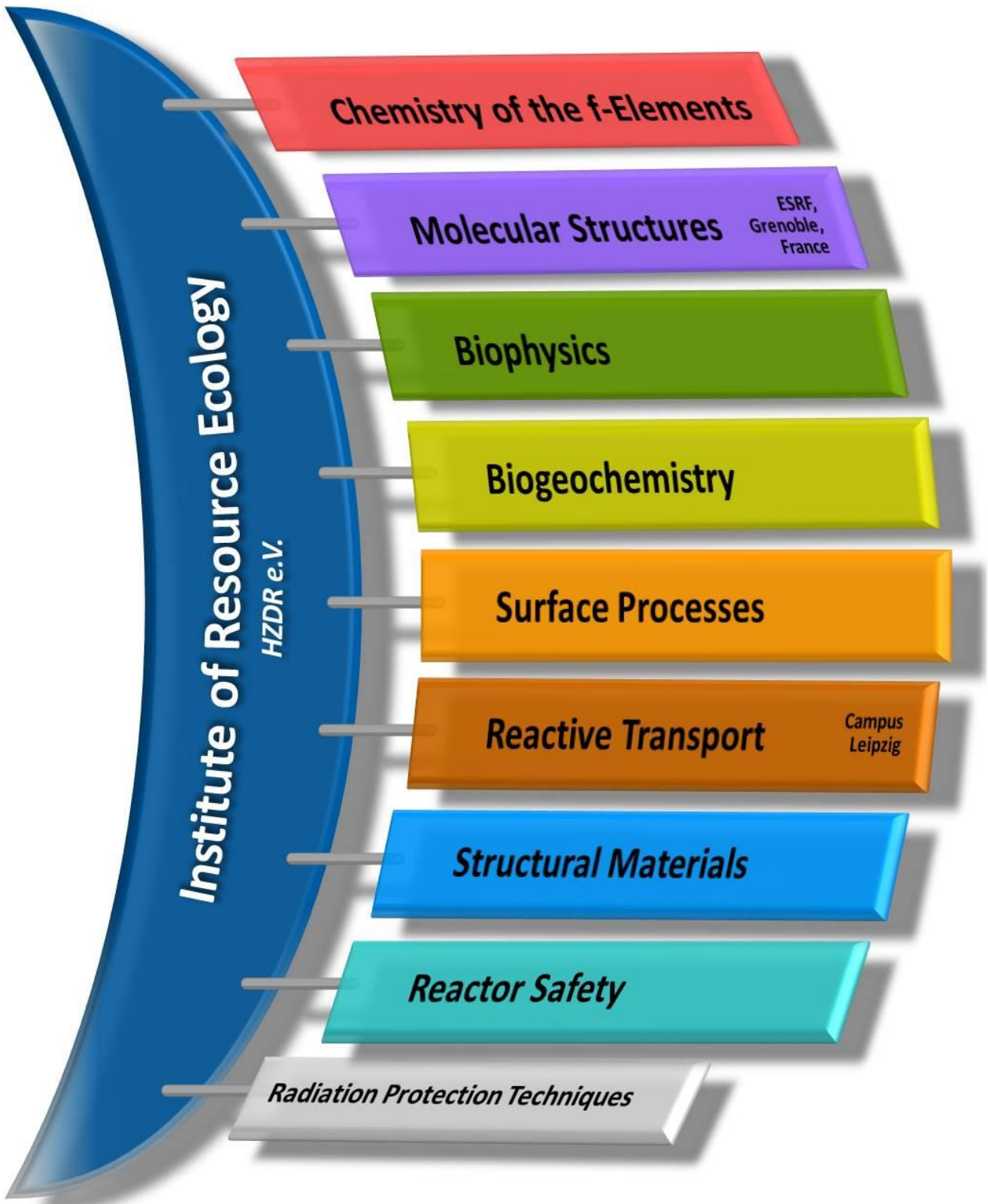
○ FURTHER EVENTS

Impressions from the award ceremonies as they are listed on p. 94, the PhD seminar of the IRE at Scheffau, Austria, the conferences Goldschmidt 2019 at Barcelona, Spain, and Migration at Kyoto, Japan.

Photos provided by: R. Berndt, F. Bok, B. Drobot, J. Gorzitze, S. Hilpmann, L. Köhler, N. Matschiavelli, N. Mayordomo, T. Stumpf, A. Wirsig.



PERSONNEL



Prof. Dr. Thorsten Stumpf (HEAD OF INSTITUTE)

ADMINISTRATION:

Office Dresden: Gorzitze, Jana; Grübner, Manuela; Kovacs, Jenny;

Kurde, Kerstin

Office Leipzig: Gerstner, Katrin; Meinken, Roswitha

Sysad (IT): Berndt, Ronny

PROJECT COORDINATION:

Office Dresden: Dr. Arnold, Thuro

Office Leipzig: Dr. Stedtner, Robin; Falkenberg, Dirk; Henke, Steffen; Jimenez Hernandez, Susana; Nebe, Katrin; Rumpel, Annette; Stalke, Sebastian

*. Ph.D. student (as of 2019/12/31).

BIOGEOCHEMISTRY

Dr. Raff, Johannes

Bachran, Madlen*
Dr. Bader, Miriam
Dr. Cherkouk, Andrea
Drozdzowski, Jennifer*
Dr. Drobot, Björn
Flemming, Katrin
Dr. Günther, Alix
Heller, Sylvia
Hilpmann, Stephan*
Jesat, Jenny*
Dr. John, Warren*

Kluge, Sindy
Dr. Krawczyk-Bärsch, Evelyn
Dr. Lopez Fernandez, Margarita
Dr. Mandal, Poulami
Dr. Matschavelli, Nicole
Dr. Moll, Henry
Dr. Rajabi, Fatemeh
Dr. Sachs, Susanne
Seibt, Jana
Sushko, Vladyslav*
Wollenberg, Anne*

SURFACE PROCESSES

Prof. Dr. Brendler, Vinzenz / Dr. Müller, Katharina

Bachmann, Stefanie
Beutner, Sabrina
Brinkmann, Hannes
Dr. Bok, Frank
Chlupka, Aline
Dennitz, Maximilian*
Eckardt, Carola
Eibl, Manuel*
Dr. Foerstendorf, Harald
Gürtler, Sylvia
Hein, Karsten
Dr. Huittinen, Nina
Dr. Jordan, Norbert
Dr. Kretschmar, Jérôme
Lehmann, Susanne*
Lösch, Henry*

Dr. Mayordomo H., Natalia
Molodtsov, Konrad*
Müller, Christa
Neubert, Heidrun
Philipp, Thimo*
Dr. Richter, Anke
Rodriguez Hernandez, Dana M.*
Roode-Gutzmer, Quirina
Dr. Schierz, Ariette
Dr. Schneide, Katja
Shams Aladin Azzam, Salim
Dr. Stockmann, Madlen
Weiss, Stephan
Wolter, Jan-Martin*
Dr. Yassin, Ghada

STRUCTURAL MATERIALS

Dr. Alstadt, Eberhard / Dr. Heintze, Cornelia

Dr. Bergner, Frank
Dr. Chekroun, Paul
Dr. Das, Aniruddh
Houska, Mario
Dr. Müller, Gudrun
Pietzsch, Jens
Richter, Henry

Roßner, Michaela
Rott, Sonja
Skorpupa, Ulrich
Dr. Ulbricht, Andreas
Dr. Vogel, Karin
Webersinke, Wolfgang

BIOPHYSICS

Prof. Dr. Fahmy, Karim

Iric, Katarina*
Kielar, Charlotte
Nucke, Lisa*
Dr. Oertel, Jana

Philipp, Jenny
Dr. Sayed, Ahmed M. T.
Dr. Tashima, Satoru
Subramania, Madhumalar*

CHEMISTRY OF THE F-ELEMENTS

PD Dr. Schmidt, Moritz / Dr. Ikeda-Ono, Atsushi

Dr. Bansal, Deepak
Dr. Barkleit, Astrid
Fichter, Sebastian*
Dr. Kaden, Peter
Kloditz, Roger*
Köhler, Luisa*
Dr. Lyu, Kai

Dr. März, Juliane
Neumann, Julia
Dr. Patzschke, Michael
Radoske, Thomas*
Schöne, Sebastian*
Dr. Taylor, Corey

REACTIVE TRANSPORT

PD Dr. Fischer, Cornelius

Campus Leipzig

Bolleermann, Till*
Dr. Franke, Karsten
Grubbe, Stefan
Dr. Hildebrand, Heike
Dr. Kamnzadeh, Lottallah
Dr. Kulenkampf, Johannes

Dr. Lippold, Holger
Lösöl, Dagmar
Dr. Mansel, Alexander
Schögler, Claudia
Dr. Schymura, Stefan

Prof. Dr. Heine, Thomas (Chair Theor. Chem. TU Dresden)
PD Dr. Kuc, Agnieszka Beata
Lurz, Christian*
Springer, Maximilian*

Dr. Suyetin, Mikhail
Wulf, Toshiki*

REACTOR SAFETY

Dr. Klem, Sören

Dr. Bilodid, Yuri
Dr. Fridman, Emil
Gomulich, André
Dr. Grahn, Alexander
Jobst, Matthias

Konheiser, Jörg
Dr. Nikitin, Evgeny
Dr. Nora, Vincenzo Antonio*
Dr. Schäfer, Frank
Yadav, Prathiba*

GUEST SCIENTISTS

Baier, Silvio	<i>Technische Universität Dresden, Germany</i>
Bilodid, Yevgen	<i>Scientific-technical Centre for Nuclear and Radiation Safety of the Ukraine, Kiev, Ukraine</i>
Diaz Pescador, Eduard	<i>Technische Universität Dresden, Germany</i>
Formánek, Petr	<i>Leibniz-Institut für Polymerforschung Dresden e.V., Germany</i>
Ieremenko, Maksym	<i>Scientific-technical Centre for Nuclear and Radiation Safety of the Ukraine, Kiev, Ukraine</i>
Manzaneque, Juan Alberto Meza	<i>Universidad Carlos III de Madrid, Madrid, Spain</i>
Oliveira, Augusto Faria	<i>TU Dresden, Jacobs University Bremen, University Leipzig, Germany</i>
Romanchuk, Anna	<i>Moscow State University, Russia</i>
Shimojo, Kojiro	<i>JAEA Japan Atomic Energy Agency, Japan</i>

CO-FUNDED PH.D. STUDENTS

An, Yun	<i>University of Leipzig/ China Scholarship Council, Beijing, China</i>
Fichtner, Andreas	<i>Subatech, Nantes, France</i>
Gerber, Evgeny	<i>Lomonosov Moscow State University, Moscow, Russia</i>
Kempt, Roman	<i>Technische Universität Dresden, Germany</i>
Melix, Patrick	<i>Technische Universität Dresden, Germany</i>
Wöhner, Kevin	<i>Universität Leipzig, Germany</i>

MASTER/DIPLOMA/BACHELOR

Dressler, Magdalena	Henka, Anne	Neubert, Tom	Schabernack, Jonas
Freitag, Leander	Jessat, Isabelle	Pingel, Leon Janis	Schäfer, Sebastian
Garimella, Jawaharlal Nehru	Kliemann, Jonas		

GRADUATE ASSISTANTS, STUDENT ASSISTANTS, TRAINEES

Alchaar, Hussam Alddin	Dullies, Paul	Lessing, Richard	Thömel, Svenja
Arrozi, Ubed Sonai Fahrudie	Kai, Lyo	Mandrova, Natalya	Volkova, Anna
Bilke, Marie-Louise	Kühnel, Luca	Schurig, Paulina	Würth, Maria
Dietze, Alexandra	Kohlgruber, Tsuyoshi Anthony	Talatiya, Adityaraj	Zechel, Susanne

ACKNOWLEDGEMENTS

The Institute of Resource Ecology is one of the eight institutes of the Helmholtz-Zentrum Dresden–Rossendorf e.V. (HZDR). As registered, non-profit institution, the HZDR is supported by the authorities of the Federal Government and the Free State of Saxony. In addition to the basic funding, the financial support of the projects listed below by the given organizations and companies is gratefully acknowledged.

FUNDING ORGANIZATION / COMPANY	PROJECT TITLE	CONTRACT NO. (if applicable)
Commission of the European Communities (EU)	Cebama – Cement-based materials, properties, evolution, barrier functions	H2020-662147
	CONCERT – European Joint Programme for the Integration of Radiation Protection Research	H2020-662287
	ESFR-SMART – European SFR – Safety Measures Assessment and Research Tools	H2020-754501
	EURAD – European Joint Programme on Radioactive Waste Management CORI, DONUT, FUTURE T2 + T3, SFC, UMAN, KMSoK	H2020-847593
	INSIDER	H2020-755554
	IVMR – In-Vessel Melt Retention Severe Accident Management Strategy for Existing and Future NPPs	H2020-662157
	MIND – Microbiology in Nuclear Waste Disposal	H2020-661880
	M4F – Multiscale Modeling for Fusion and Fission Materials	H2020-755039
	McSAFE – High-Performance Monte Carlo Methods for Safety Demonstration	H2020-755097
	R2CA: Reduction of Radiological Consequences of Design Basis and Design Extension Accidents	H2020-847656
SOTERIA – Safe Long Term Operation of Light Water Reactors	H2020-661913	
TOP – ERC Starting Grant - Towards the Bottom of the Periodic Table	H2020-759696	
Bundesministerium für Wirtschaft und Energie (BMWi) & Bundesministerium für Bildung und Forschung (BMBF)	BioVeStRa – Untersuchungen des Potentials biologischer Verfahren zur Strahlenschutzvorsorge bei Radionuklidbelastungen	02S9276A
	EMPRADO – Entwicklung einer Methode zur Pre-Aktivitäts- und Dosisleistungsberechnung von reaktornahen Bauteilen auf Basis von Neutronenfluenzverteilungen	15S9409A
	EDUKEM – Entwicklung und Durchführung experimenteller Methoden zur verbesserten Modellierbarkeit uranhaltiger salinärer Lösungen	02E11334B
	FENABIUM – Struktur-Wirkungsbeziehungen zwischen f-Elementen und organischen Ligandsystemen mit Naturstoff-basierten Bindungsfunktionen in Hinblick auf eine mögliche Mobilisierung in der Umwelt	02NUK046B
	GRaZ – Verbundprojekt Geochemische Radionuklidrückhaltung an Zementalterationsphasen	02E11415B
	iCross – Integrität von Endlagersystemen für radioaktive Abfälle – Skalenübergreifendes Systemverständnis und Systemanalyse	02NUK053B
	MgO-S3 Spritzbeton für Streckenverschlüsse für HAW-Endlager im Steinsalz	02E11769B
	r4 – SEM ² – Seltene-Erden-Metallurgie – fortgeschrittene Methoden für die optimierte Gewinnung und Aufbereitung am Beispiel von Ionenadsorptionstonen	033R127D
	SMILE – Smart-Ka in der Langzeitsicherheitsanalyse – Anwendungen, Teilprojekt B	02E11668B

FUNDING ORGANIZATION / COMPANY	PROJECT TITLE	CONTRACT NO. (if applicable)
	STROEFUN III – Strömungstechnischer Funktionsnachweis für Verschlussbauwerke und flüssigkeitsgestützte Abdichtung des Kontaktbereiches Phase III: Vertiefung Kenntnisstand Kontaktbereich & Injektionsmittel, in situ-Versuche	02E11748B
	ThermAc – Verbundprojekt Aufklärung von Thermodynamik und Speziation von Actiniden bei höheren Temperaturen in Kombination von Schätzmethode, spektroskopischen und quantenmechanischen Methoden, Teilprojekt B	02NUK039B
	TRANS-LARA – Verbundprojekt Transport- und Transferverhalten langlebiger Radionuklide entlang der kausalen Kette Grundwasser-Boden-Oberfläche-Pflanze unter Berücksichtigung langfristiger klimatischer Veränderungen, Teilprojekt B	02NUK051B
	VESPA II – Verbundprojekt Verhalten langlebiger Spalt- und Aktivierungsprodukte im Nahfeld eines Endlagers und Möglichkeiten ihrer Rückhaltung	02E11607B
	WERREBA – Wege zum effizienten Rückbau von Reaktorkomponenten und Betonabschirmung: Berechnung des Aktivitätsinventars und deren Validierung an Bohrkernen sowie Mobilitätsuntersuchungen von Radionukliden	15S9412
DFG	DNA-Struktur Molekulare Mechanismen der Interaktion chaotroper Salze mit natürlichen und künstlichen DNA-Strukturen	FA 248/8-1
Gesellschaft für Anlagen- und Reaktorsicherheit gGmbH (GRS)	Datenbasis 2018/2019	
Helmholtz-Gemeinschaft Deutscher Forschungszentren e.V. (HGF)	CROSSING – Crossing borders an scales - an interdisciplinary approach Exzellenznetzwerk-Phase 3 "Physics of Life" NUSAFE / iCross	PIE-0007 ExNet-0029-Phase2-3 SO-093
JAEA	MESys – JAEA Reimei funding 2018 Solid-state chemistry of multi-element systems composed of actinides and fission products	
PreussenElektra GmbH	Containmentmodell	
EnBW Kernkraft GmbH	Mikroorganismen EnBW	
European Radioecology Alliance	Workshop ALLIANCE WG NORM	
TÜV NORD	Prüfung geologischer Fragen	M.ASS.06.015.01.F70
TÜV SÜD	Gemischte Reaktorkerne	3617R01520
Trumpf Laser GmbH	Untersuchung von Mikroorganismen in Prozesswässern	
Umweltbundesamt	NanoExperte – Gutachten Nachweis von Nanomaterialien	P97417
UJV Rez, a.s.	DYN3D für UJV Wartung 2018/2019 DYN3D für UJV Wartung 2019/2020	

INDEX OF AUTHORS

AUTHOR	PAGE	AUTHOR	PAGE
Abe, T.....	48	Gaona, X.....	12
Altmaier, M.....	12	Gerber, E.....	11, 14
Altstadt, E.....	63	Gómez-Ferrer, B.....	62
Amidani, L.....	11, 32	Gorin, D.....	57
An, Y.....	36	Göttfert, M.....	47
Bach, W.....	40	Günther, A.....	49
Bader, M.....	50	Hanspach, E.....	47
Baranchikov, A. E.....	14	Heim, K.....	35
Barkleit, A.....	65	Heine, T.....	36
Baumann, N.....	27	Heintze, C.....	61, 62
Bauters, S.....	14	Helbig, T.....	24
Bergner, F.....	61, 63, 64	Hennig, C.....	15, 27
Bernard, E.....	39	Herczynski, O.....	47
Betzel, C.....	48	Hildebrand, H.....	43
Bilodid, Y.....	66	Hölttä, P.....	31
Bok, F.....	42	Houska, M.....	63
Bollermann, T.....	40	Hoyer, E.....	47
Bonato, L.....	15	Huittinen, N.....	13, 20, 23, 31
Brendler, V.....	34, 35, 41	Huthwelker, T.....	14
Brinkmann, H.....	22, 33	Ikeda-Ohno, A.....	27
Britz, S.....	33	Ivanov, V. K.....	14
Brulfert, F.....	48	Jenni, A.....	39
Butorin, S. M.....	11, 14	Jessat, I.....	20
Caciuffo, R.....	11	Jessat, J.....	54, 55
Chekhonin, P.....	61	Jobst, M.....	67, 68
Cherkouk, A.....	50	Jordan, N.....	20
Claussner, J.....	27	Kaden, P.....	17, 19, 22
Dacheux, N.....	15	Kahl, W.-A.....	40
Das, A.....	63	Kalmykov, S. N.....	11, 14, 32
Demnitz, M.....	37	Karimzadeh, L.....	44
Di Nora, V. A.....	70	Kekäläinen, P.....	31
Dorovatovskii, P. V.....	14	Kliem, S.....	68
Dressler, M.....	56	Kloditz, R.....	18, 22
Drobot, B.....	48, 50	Kluge, S.....	53, 56
Dullies, P.....	21	Knecht, S.....	18
Dumas, T.....	12, 15	Knöppel, J.....	47
Egorov, A. V.....	14	Köhler, L.....	17
Eibl, M.....	13	Komeiji, Y.....	48
Elo, O.....	31	Konheiser, J.....	65
Exner, J.....	27	Konyukhova, A. D.....	14
Fahmy, K.....	47, 52	Kosowski, K.....	68
Falke, S.....	48	Kozmenkov, Y.....	68
Fellhauer, D.....	12	Krawczyk-Bärsch, E.....	53
Fichter, S.....	19	Kuc, A.....	36
Findeisen, S.....	27	Kulenkampff, J.....	38, 39
Fischer, C.....	38, 40, 43, 44	Kuzenkova, A. S.....	32
Foerstendorf, H.....	21, 35	Kvashnina, K. O.....	11, 14, 32
Franke, K.....	25, 26, 43		
Freitag, L.....	49		
Fridman, E.....	69, 70		

AUTHOR	PAGE
Lapanje, A.	57
Le Goff, X.	15
Lecante, P.	15
Lehmann, S.	21
Liebmann, M.	47
Lippold, H.	44
Lopez-Fernandez, M.	51
Lösch, H.	23, 50
Lozada-Hidalgo, M.	36
Lu, R.	41
Mäder, U.	39
Mansel, A.	24, 25, 26
März, J.	17, 19
Matschiavelli, N.	56
Mayordomo, N.	16, 34, 35
Merroun, M. L.	51, 52
Mesbah, A.	15
Mochizuk, Y.	48
Moisy, P.	15
Moll, H.	22, 50, 51
Molodtsov, K.	37
Müller, K.	34, 35
Naudet, D.	27
Neumann, J.	33
Nikitenko, S. I.	15
Nikitin, E.	69
Oertel, J.	47
Okuwaki, K.	48
Pareige, C.	62
Patzschke, M.	18, 19, 21, 22
Petkov, P.	36
Pidchenko, I.	11
Pingel, J.	38
Plakhova, T. V.	14
Popa, K.	11
Prieur, D.	15
Rachamin, R.	65
Radoske, T.	27
Raff, J.	48, 49, 53

AUTHOR	PAGE
Raiwa, M.	23, 47
Réal, F.	20
Rodríguez, D. M.	34, 35
Romanchuk, A. Y.	11, 14, 32
Rossberg, A.	11, 16, 35
Rybkin, I.	57
Sachs, S.	54, 55
Samsonov, S. A.	48
Schäfer, F.	68
Schäfer, S.	52
Schäfer, T.	38
Scheinost, A. C.	11, 12, 14, 27, 34, 35
Schierz, A.	37, 56
Schild, D.	12
Schmidt, M.	33, 37, 48
Schymura, S.	37, 43
Shiryaev, A. A.	14
Sozarukova, M. M.	14
Steppert, M.	23, 47
Stedtner, R.	21, 50
Stockmann, M.	33, 41, 44
Stoll, M.	38
Stumpf, T.	17, 33, 34, 37, 48, 50
Sukhorukov, G.	57
Talyzin, A. V.	32
Trigub, A. L.	11, 32
Tsushima, S.	47, 48
Ulbricht, A.	64
Vallet, V.	20
Viro, M.	15
Voutilainen, M.	31
Walter, O.	11
Weiss, S.	11
Wilhelm, P.	68
Wollenberg, A.	49
Yuan, T.	40
Zehner, S.	47



Institute of Resource Ecology
Bautzner Landstrasse 400
01328 Dresden/Germany
Phone +49 351 260-3210
Fax +49 351 260-3553
Email contact.resourceecology@hzdr.de
<http://www.hzdr.de>

Member of the Helmholtz Association